Techniques in molecular spectroscopy: from broad bandwidth to high resolution

by

Kevin C. Cossel

B.S., California Institute of Technology, 2007

A thesis submitted to the

Faculty of the Graduate School of the

University of Colorado in partial fulfillment

of the requirements for the degree of

Doctor of Philosophy

Department of Physics

2014

This thesis entitled:
Techniques in molecular spectroscopy: from broad bandwidth to high resolution
written by Kevin C. Cossel
has been approved for the Department of Physics

_____

Prof. Jun Ye

_____

Prof. Eric Cornell

Date _____

The final copy of this thesis has been examined by the signatories, and we find that both the content and the form meet acceptable presentation standards of scholarly work in the above mentioned discipline.

Cossel, Kevin C. (Ph.D., Chemical Physics)

Techniques in molecular spectroscopy: from broad bandwidth to high resolution

Thesis directed by Prof. Jun Ye

This thesis presents a range of different experiments all seeking to extended the capabilities of molecular spectroscopy and enable new applications. The new technique of cavity-enhanced direct frequency comb spectroscopy (CE-DFCS) provides a unique combination of broad bandwidth, high resolution, and high sensitivity that can be useful for a wide range of applications. Previous demonstrations of CE-DFCS were confined to the visible or near-infrared and operated over a limited bandwidth: for many applications it is desirable to increase the spectral coverage and to extend to the mid-infrared where strong, fundamental vibrational modes of molecules occur. There are several key requirements for CE-DFCS: a frequency comb source that provides broad bandwidth and high resolution, an optical cavity for high sensitivity, and a detection system capable of multiplex detection of the comb spectrum transmitted through the cavity. We first discuss comb sources with emphasis on the coherence properties of spectral broadening in nonlinear fiber and the development of a high-power frequency comb source in the mid-infrared based on an optical-parametric oscillator (OPO). To take advantage of this new mid-infrared comb source for spectroscopy, we also discuss the development of a rapid-scan Fourier-transform spectrometer (FTS). We then discuss the first demonstration of CE-DFCS with spectrally broadened light from a highly nonlinear fiber with the application to measurements of impurities in semiconductor manufacturing gases. We also cover our efforts towards extending CE-DFCS to the mid-infrared using the mid-infrared OPO and FTS to measure ppb levels of various gases important for breath analysis and atmospheric chemistry and highlight some future applications of this system.

In addition to the study of neutral molecules, broad-bandwidth and high-resolution spectra of molecular ions are useful for astrochemistry where many of the observed molecules are ionic, for studying molecules such as CH_5^+ with highly non-classical behavior, and for tests of fundamental

physics. We have developed a new technique – frequency comb velocity-modulation spectroscopy – that is the first system to enable rapid, broadband spectroscopy of molecular ions with high resolution. We have demonstrated the ability to record 150 cm^{-1} of spectra consisting of 45,000 points in 30 minutes and have used this system to record over 1000 cm^{-1} of spectra of HfF^+ in the near-infrared around 800 nm. After improvements, the system can now cover more than 3250 cm^{-1} (700-900 nm). We have combined this with standard velocity-modulation spectroscopy to measure and analyze 19 ro-vibronic bands of HfF^+.

These measurements enabled precision spectroscopy of trapped HfF^+ for testing time-reversal symmetry. For this experiment, we perform Ramsey spectroscopy between spin states in the metastable $^3\Delta_1$ level to look for a permanent electric dipole moment of the electron with what we believe is the narrowest line observed in a molecular system (Fourier limited with 500 ms of coherence time). The long coherence time is a major advantage of using ions, but there are also some added complexities. We discuss various aspects metastable state preparation, state detection, and spectroscopy in a rotating frame (due to the necessary rotating electric bias field) that were particular challenging. In addition, we discuss limits to the coherence time – in particular, ion-ion collisions – as well as the sensitivity of the current measurements and provide a path towards a new limit on the electric dipole moment of the electron.

Dedication

To my dad, who was an amazing role model and always encouraged my interest in science. In some way, he probably always knew that I would achieve this.

Acknowledgements

None of this work would have been possible without a lot of help from a great group of people. Both Jun and Eric have been great advisors and have tried to teach my how to think like a physicist. If I only succeed in learning a fraction of this, it will still serve me very well! The members of both Jun and Eric's labs are all extremely talented and it has been a pleasure to work with them. I can't hope to name all of the people who I taught me various tips or who lent me critical optics but I would like to thank in particular Mike Martin, Mike Thorpe, Dylan Yost, Arman Cingöz, Tom Alison, Florian Adler, Matt Swallows, Craig Benko, Piotr Maslowski, Alexsandra Foltynowicz, Bryce Bjork, AJ Fleisher, Laura Sinclair, Dan Gresh, Huanqian Loh, Matt Grau, and Will Cairncross. I wish the best of luck to them and have no doubt that they will all be extremely successful. In addition to all of the graduate students and postdocs in the labs, the JILA staff that I worked with in the electronics shop (Terry, James, Carl) and instrument shop (Hans, Kim, Tracy, Blaine) are all indispensable for all of the experiments. In addition, Pam, Diane, Krista, Lauren, and all of the other staff do a great job keeping everything running smoothly. Outside of JILA, I am grateful to Scott Diddams and Nate Newbury at NIST for many interesting discussions, Axel Ruehl, Ingmar Hartl and the crew at IMRA for help with lasers, Ronald Holzwarth, Tobias Wilken, Thomas Udem and others at MPQ for hosting me for a month, and Mitchio Okumura and Thinh Bui at Caltech for great collaborations. My parents have provided amazing support and always gave me opportunities to learn something new. I would also than Mike Martin, Carly Donahue, Laura Sinclair, and Galen O'Neil for many fun times outside of the lab. Last, but definitely not least, my wife Eleanor has provided immeasurable support, encouragement, and joy.

Contents

Chapter

1 Introduction **1**

2 Frequency comb sources **9**

2.1 Mode-locked lasers 10

2.1.1 Mode-locking Mechanisms 12

2.2 Indirect Sources 15

2.2.1 cw-laser Based Sources 18

2.2.2 Typical comb sources 19

2.3 Nonlinear fiber optics 22

2.3.1 Numerical simulations 25

2.3.2 Broadening mechanisms 28

2.3.3 Coherence measurements 36

2.4 Optical parametric oscillators 43

3 Detection techniques **57**

3.1 Cavity-comb coupling 57

3.1.1 Tight locking scheme 59

3.1.2 Swept coupling scheme 60

3.2 Detection sensitivity 62

3.3 Detection techniques 66

3.3.1 VIPA . . . 67
3.3.2 Fourier-transform spectrometer . . . 75
3.4 Velocity-modulation spectroscopy . . . 83
3.4.1 Background . . . 85
3.4.2 Comb-vms . . . 87
3.4.3 System performance . . . 91
3.4.4 Single-frequency vms . . . 93
3.4.5 Extensions of comb-vms . . . 98

4 Applications of DFCS **100**
4.1 Trace detection in Arsine . . . 101
4.1.1 Experimental Setup . . . 103
4.1.2 Data Analysis . . . 107
4.1.3 Results . . . 108
4.2 Mid-infrared comb spectroscopy . . . 114
4.2.1 Measurement of individual molecular species . . . 116
4.2.2 Instrument performance limits . . . 117
4.2.3 Multi-line fitting advantage . . . 120
4.2.4 Determination of absolute concentrations of a gas mixture . . . 121
4.3 Future applications . . . 122
4.4 Conclusions . . . 132

5 Velocity-modulation spectroscopy of HfF^+ **133**
5.1 Results . . . 134
5.1.1 Diatomic molecular spectra primer . . . 134
5.1.2 Fitting . . . 146
5.1.3 Lambda doubling . . . 156
5.2 Theory . . . 160

5.3 Summary 162

6 Precision spectroscopy of trapped ions **171**

6.1 eEDM Background 171

6.1.1 Measurement Basics 175

6.1.2 Current Limit 178

6.1.3 Overview of JILA eEDM measurement 180

6.2 Experimental Setup 182

6.2.1 Ion Trap 184

6.2.2 Photodissociation 192

6.2.3 Rotating bias fields 199

6.3 Coherent Transfer 203

6.3.1 Laser stabilization 206

6.3.2 Transfer theory 212

6.3.3 Transfer parameters 213

6.3.4 Transfer efficiency and timescale 218

6.3.5 Transfer spectrum 219

6.4 Ramsey Spectroscopy 225

6.4.1 Sensitivity Estimates 232

6.5 Coherence Time 233

6.5.1 Lifetime 233

6.5.2 Field inhomogeneity 236

6.5.3 Collisions 237

6.5.4 Collision background 239

6.5.5 Coherence time from collisions 241

6.6 Systematic Errors 249

6.6.1 Non-reversing magnetic field 250

6.6.2 Perpendicular magnetic fields 253
6.6.3 Field inhomogeneity 254
6.6.4 Other effects 255
6.7 eEDM measurement 257
6.8 Outlook 261
6.9 Useful numbers 265

7 Conclusion **268**

Bibliography **269**

Tables

Table

2.1 Mirror coatings for OPO 51

3.1 Comparison of cavity-enhanced comb systems. 65

4.1 Detection limits for a collection of important molecules within the spectral range of our mid-IR FC-FTS. 119

4.2 Many trace species in human breath. 127

4.3 Atmospheric trace species. 130

5.1 Possible states and configurations arising from s^2 and sd electron configurations. . . 139

5.2 Fitted constants for observed transitions in $^{180}HfF^+$ in cm^{-1}. 150

5.3 Matrix elements for the Λ-doubling in $^3\Delta_1$. 158

5.4 Derived constants for observed states in $^{180}HfF^+$ 164

5.5 Summary of electronic states measured in HfF^+ 165

5.5 Summary of states. 166

5.5 Summary of states. 167

5.6 Calculate dipole matrix elements between states in HfF^+. 168

5.7 Franck-Condon factors (vibrational overlap integrals) for $^3\Pi_{0^+}$ - $^3\Delta_1$. 169

5.8 Franck-Condon factors for $^3\Phi_2$ - $^3\Delta_1$ 169

5.9 Franck-Condon factors for $^3\Pi_{0^+}$ - $^1\Sigma^+$ 169

5.10 Franck-Condon factors for $^3\Pi_1$ - $^1\Sigma^+$ 170

5.11 Franck-Condon factors for $^1\Pi_1$ - $^1\Sigma^+$ 170

5.12 Franck-Condon factors for $^3\Sigma_{0^+}$ - $^1\Sigma^+$ 170

6.1 Trap characterization. 189

6.2 Estimated statistical sensitivity of the first generation measurement using HfF^+ . . . 234

6.3 Systematic error summary. 251

6.4 Useful numbers 266

6.5 $\bar{\Delta}$, $\delta\Delta$, and Stark shift for different values of $\mathcal{E}_{\rm rot}$, from theory 267

Figures

Figure

1.1 Location of fundamental vibrational bands and spectra of some example molecules. . 5

2.1 Comparison of comb sources 11

2.2 Sources based on a Yb:fiber laser 20

2.3 Spectral broadening of a Yb:fiber laser using suspended core fiber. 24

2.4 Raman shifting and broadening of Er:fiber laser. 26

2.5 Pulse propagation in fibers with negative and positive GVD 30

2.6 Soliton dynamics in fibers 31

2.7 Simulation of Raman shifting of an Er:fiber laser in SMF-28 33

2.8 Simulation of supercontinuum generation in highly nonlinear fiber near 1.55 μm . . . 35

2.9 Coherent supercontinuum generation spanning over 1.5 octaves from a Yb:fiber laser 38

2.10 Simulation results for the optical spectrum and coherence properties of a Yb:fiber laser based supercontinuum 40

2.11 Dependence of coherence with Raman gain 42

2.12 Mid-infrared OPO comb based on periodically-poled lithium niobate (PPLN) 47

2.13 OPO crystal Holder 49

2.14 PPLN crystal design. 50

2.15 OPO performance. 52

2.16 Stabilization of mid-IR OPO and measurement of idler-comb linewidth 55

3.1 Detection schemes for CE-DFCS. 68
3.2 VIPA Spectrometer 69
3.3 Setup of Fourier-transform spectrometer. 77
3.4 Circuit diagram for mid-IR auto-balancing detector 81
3.5 Sketch of velocity-modulation spectroscopy (VMS). 86
3.6 Setup for comb-vms. 90
3.7 Setup for cw-vms. 95
3.8 Comparison of coherent subtraction and single-direction measurements. 97

4.1 Sketch of trace detection in arsine 104
4.2 The spectrum of 10 ppm methane (CH_4), 10 ppm carbon dioxide (CO_2), 10 ppm hydrogen sulfide (H_2S), and 2.5 ppm water (H_2O) in nitrogen gas from 1.75-1.95 μm. 110
4.3 Determination of detection limits. 112
4.4 Spectrum of trace water in arsine. 115
4.5 Spectra of several species measured using the mid-IR OPO, FTS, and multi pass cell. 118
4.6 Multispecies detection using mid-IR comb. 123

5.1 All data obtained with cw- and comb-vms. 135
5.2 Molecular orbital diagram for valence orbitals of HfF^+ 138
5.3 Angular momentum coupling in diatomic molecules corresponding to different Hund's cases. 142
5.4 Example transitions with Λ-doubling in one or both states 145
5.5 Loomis-Wood plot showing branches of the $^3\Pi_1 \leftarrow {}^1\Sigma^+$ (3, 1) transition. 148
5.6 Isotope shifts for each observed transition in HfF^+ scaled to approximately group transitions by electronic states 152
5.7 Residuals for three fits to the $\mathbf{^3\Pi_{0^-} \leftarrow {}^3\Delta_1}$ (1, 0) band. 155

6.1 An eEDM violates both parity (P) and time (T) reversal symmetry. The solid black arrows show the effect of a P- or T-reversal operation on an electron with both a spin and an electric dipole moment due to a charge distribution asymmetry. 173

6.2 Sketch of levels used in the JILA eEDM measurement 181

6.3 The eEDM induced Stark splitting (ΔE) for $J = 1$ hyperfine levels of the $^3\Delta_1$ state of HfF^+: between $F = 3/2$ $m_F = \pm 3/2$ levels (solid line), between $F = 3/2$ $m_F = \pm 1/2$ levels (doted line), and between $F = 1/2$ $m_F = \pm 1/2$ (dashed line). . . . 183

6.4 Sketch of eEDM experiment 185

6.5 Histogram of Hf^+ number measured using counting or integrating 193

6.6 $(1+1')$ resonance-enhanced multiphoton photodissociation. 196

6.7 Rotational state distribution of trapped ions in $X^1\Sigma^+ v'' = 0$ state: 20 ms after trapping (blue) and 220 ms after trapping (red). The first REMPD photon is tuned near 35,976 cm^{-1}. We observed a redistribution towards higher rotational states after 220 ms of wait time. 197

6.8 Multiple dissociation pulses. 200

6.9 Population lifetimes in trapped HfF^+. (a) $X^1\Sigma^+ v = 0$, $J = 0$ and (b) $^3\Delta_1 v = 0$, $J = 1$. The $X^1\Sigma^+$ lifetime exceeds many seconds after the initial fast decay (100 ms) due to rotational re-distribution as described in Section IV. The $^3\Delta_1$ lifetime is 2.1(2) s. 201

6.10 Characterization of magnetic field gradient. 204

6.11 Adiabatic transfer from $^1\Sigma^+$ to $^3\Delta_1$. 207

6.12 Stabilization cavity for Raman transfer lasers 209

6.13 Sketch of the laser stabilization setup for the transfer lasers. 210

6.14 Transition dipole moment calibration for the $^3\Pi_{0^+} \leftarrow {}^1\Sigma^+$ $(v = 1, J = 1) \leftarrow (v = 0, J = 0)$ transition. 216

6.15 One photon lineshape for the transfer laser. 217

6.16 Fraction of population remaining in $^1\Sigma^+$ $J = 0$ versus transfer laser on duration. . . 220

6.17 Stark spectroscopy of $^3\Delta_1$ $J = 1$ . . . 221

6.18 Possible two-photon transfer pathways . . . 224

6.19 Ramsey spectroscopy . . . 226

6.20 Depletion from the $^3\Delta_1$ . . . 229

6.21 Coherence time versus fringe frequency. . . . 238

6.22 Ion-ion collision. . . . 240

6.23 Collision trajectory and solid angle . . . 242

6.24 Solid angle versus scattering angle. . . . 244

6.25 Plot of the estimated coherence time limit from collisions as a function of collision energy . . . 245

6.26 Coherence time versus ion number and $\mathcal{E}_{\rm rot}$. . . . 247

6.27 Simulation of Ramsey sequence. . . . 258

6.28 Switches . . . 260

6.29 All eEDM measurements to date. . . . 262

Chapter 1

Introduction

Spectroscopy – loosely defined as the study of the energy levels in atoms and molecules – has existed for over two centuries now, see [1] for an interesting history. Despite the long history, it is still an active area of research. The invention of the grating spectrometer by Fraunhofer in 1814 led to the first high-resolution (at the time) studies of the spectra of molecules. This was later improved upon by Rowland who developed new ways of making gratings – including curved gratings – in the 1880's. These inventions led to quantitative studies of the band structure of molecules by Rowland, Smyth, Herschel and other. Emperical descriptions of the patterns in the spectra were developed by Deslandres in the late 1800's, but there were no good theoretical descriptions. The beginning of the 20th century saw the discovery of resonance fluorescence in iodine by Wood [2, 3] as well as the initial developments of quantum theory. Armed with the added information from resonance fluorescence, a quantum description of the rotational and electronic structure of spectra was accomplished by Heurlinger and Lenz, among others. This shows how spectra could provide information about the structure of molecules, which is still important today. Attempts to fully understand the electronic structure of molecules resulted in the development of molecular orbital theory, spearheaded by Mulliken [4]. The field of molecular spectroscopy continued to advance rapidly with measurements in a variety of molecules with increasing resolution, which led to the observations of many new effects and continued improvements in the theoretical description of spectra, see, for example [5].

Further advances have typically been driven by the development of new technologies. For

example, the introduction of commercial Fourier-transform infrared (FTIR) spectrometers by Digilab (now part of Agilent) in 1969 started the development of bench-top infrared spectroscopy. Because of its ease of use and extremely broad bandwidth, FTIR is now a ubiquitous technique for chemical analysis of mixtures, environmental science, and laboratory studies of molecular spectra [6, 7] and has even been deployed on a satellite for studying earth's atmosphere [8]. Recently, Fourier-transform spectroscopy has even been extended to the vacuum ultraviolet region [9].

Another frontier has been the quest for ever higher resolution. The invention of the laser in 1960 revolutionized the field of high-resolution molecular spectroscopy and further improvements occurred with the development of sub-Doppler saturated absorption spectroscopy and Doppler-free two-photon spectroscopy [10]. Transitions of some molecules were discovered near the emission lines of HeNe (e.g., CH_4 and I_2), Nd:YAG (e.g., I_2) and CO_2 (e.g., SF_6 and OsO_4) lasers, which provide fractional resolutions of better than 10^{-10} [11]. Continued improvement of tunable lasers and frequency stabilization methods, including the transfer of frequency stability using optical frequency combs [12, 13, 14, 15], as well as molecular cooling techniques also enabled this resolution to be achieved in other wavelength regions.

As the resolution continues to improve, more and more effects become visible. In addition to the usual molecular constants for vibration and rotation terms such as spin-spin, spin-vibration, and spin-rotation interactions need to be included to describe high resolution spectra [16]. High resolution spectroscopy can provide insights into the structure of even very large molecules [17, 18]. It can also be used to observe dynamics such as tunneling and interconversion, which in turn can be used to learn about reactive radical species [19, 20], proton exchange [21], and hydrogen bonding [22].

At the highest resolutions, molecular spectroscopy can be used directly – or indirectly via laser stabilization – as a probe of fundamental physics such as observing recoil doublets due to the interaction with light [11], measuring the speed of light [23], testing for parity violation in molecular spectra [24, 25], measuring the Boltzmann constant [26], checking temporal variation of fundamental constants [27], or improving tests of special relativity with new Kennedy-Thorndike

experiments [28]. Variations of Ramsey spectroscopy can also be used to probe microwave – or lower frequency – transitions for tests of time reversal symmetry [29, 30, 31] or temporal variation of fundamental constants [32, 33, 34].

A final direction has been the desire for increased sensitivity to detect of trace species or weak spectral lines. This was achieved with the development modulation techniques such as frequency-modulation spectroscopy [35, 36, 37] as well as the use of cavity-enhanced techniques [38, 39, 40]. The combination of these two techniques led to the development of noise-immune cavity-enhanced spectroscopy (NICE-OHMS) [41, 42], which can provide sensitivity below 1 cm^{-3}. Ultra-sensitive cavity-enhanced spectroscopy has also recently been applied to the detection of $^{14}CO_2$ with the potential to perform radiocarbon dating out to 20,000 years [43].

Recent efforts have attempted to combine these previously separate directions into one system that can provide broad bandwidth, high resolution, and high sensitivity. This led to the development of cavity-enhanced direct frequency comb spectroscopy (CE-DFCS) [44, 45, 46, 47]. The spectrum of a frequency comb consists of a series of regularly space spectral lines underneath a broad spectral envelope; the frequency of one line is given by $\nu_n = nf_{rep} + f_0$, where n is an integer (typically $10^4 - 10^6$, f_{rep} is known as the repetition rate (typically 100 MHz - 10 GHz), and f_0 is an offset frequency that ranges from $-f_{rep}/2$ to $f_{rep}/2$. The spectral envelope can be hundreds or even thousands of nanometers broad while the width of a single line – or comb mode – can be kilohertz or even hertz, which shows the incredible combination of spectral bandwidth and resolution possible.

Initially, CE-DFCS was confined to the visible and near-infrared spectral regions where comb sources were easily obtainable, and the experiments focused on demonstrating various possible combinations of resolution, bandwidth, and sensitivity. The first three chapters of this thesis discuss further developments of CE-DFCS that sought to extend the range and applicability. To do this, we wanted comb sources that could operate over a broad spectral bandwidth and that operated in new spectral regions. Many of the molecular transitions in the near-infrared are overtones and combinations of different vibrational modes. Because of this, the strength of these transitions is considerably weaker than the strength of a fundamental vibrational transition in the mid-infrared,

so the sensitivity can be improved by pushing to the mid-infrared or to the visible/UV where many molecules have strong electronic transitions. Figure 1.1 shows the regions of fundamental vibrational bands and shows spectra from some example molecules, which illustrates the motivation for extending CE-DFCS into the mid-infrared. In particular, we see how a broadband mid-infrared spectroscopy system would enable spectroscopy of many different species.

In Chapter 2, we discuss different comb sources and then discuss our efforts to increase the spectral range of comb sources used for CE-DFCS. In particular, the ultrashort pulses that are typical of most frequency comb sources enable very efficient nonlinear optics. By tightly confining ultrashort pulses in highly nonlinear fiber, it is possible to shift the laser spectrum or to broaden the spectrum to simultaneously cover a wide spectral range. One challenge with this though is that the generated light many not always be fully coherent. We cover some basics of nonlinear effects in fiber and then discuss some of our experimental and theoretical studies of the coherence properties of the generated light, which enabled coherent broadening covering 1.5 octaves of simultaneous spectral bandwidth [49]. We also use nonlinear effects to push comb spectroscopy to the mid-infrared spectral region with the development of a high-power comb source based on an optical parametric oscillator (OPO) [50]. We discuss the development and characterization of our system, which covers the 3-5 μm range. This system enabled a series of measurements, some of which we discuss later, and a system based on the same design is now being constructed to cover the 6-12 μm region.

In order to take advantage of the broad bandwidth and inherent high resolution of the frequency comb source, we need a readout system that is capable of recording many spectral channels rapidly, as discussed in Chapter 3. One option for this is a 2D spectrometer based on a virtually-imaged phased array (VIPA) etalon [51], which provides several thousand simultaneous spectral channels and microsecond time resolution. We have demonstrated a VIPA spectrometer in the mid-infrared to use with the mid-infrared comb source [52]. Unfortunately, the VIPA spectrometer also has several disadvantages for very broad bandwidth spectroscopy: in particular, the total spectral range of a single VIPA etalon is limited by the optical coatings and the simultaneous bandwidth

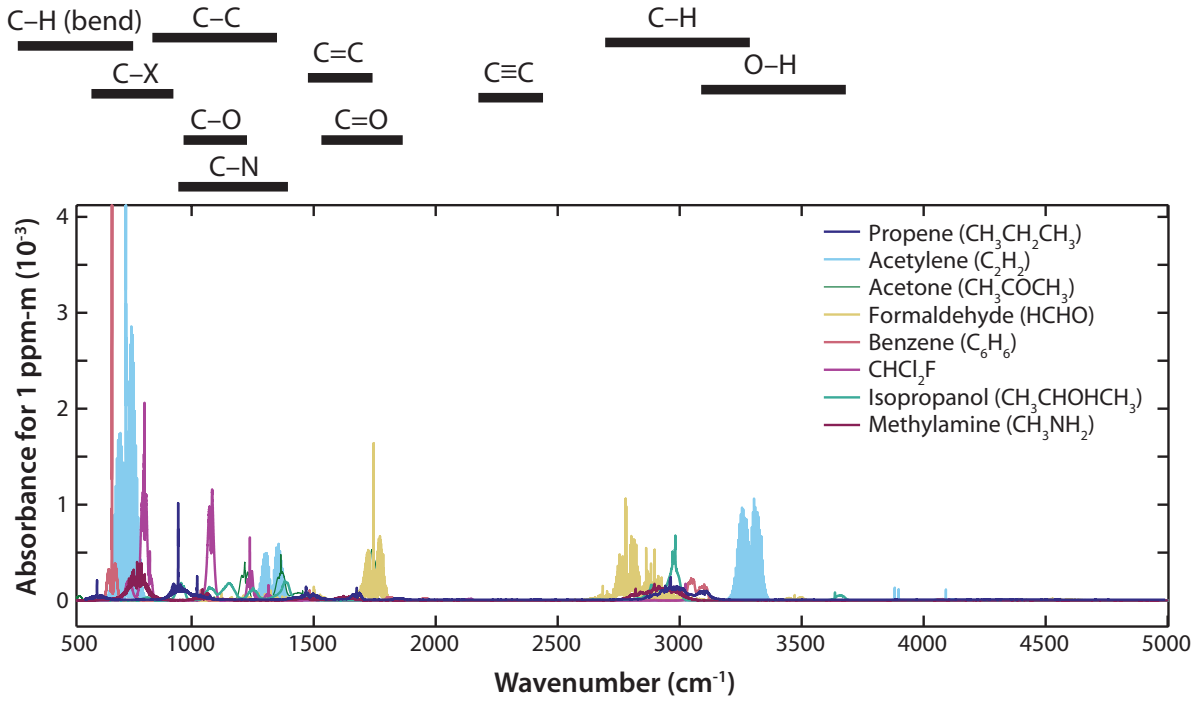

Figure 1.1: Location of fundamental vibrational bands and spectra of some example molecules in the mid-infrared. Spectra from the PNNL Northwest Infrared (NWIR) database [48].

recorded is limited by the camera used for detection. To circumvent these problems, we have developed a scanning Fourier-transform spectrometer (FTS) that is capable of recording spectra in the near- and mid-infrared with below 150 MHz resolution [46].

Chapter 4 covers the results from two different comb spectroscopy systems. One system was designed to test the application of CE-DFCS for the detection of trace water and other contaminants in arsine (AsH_3) [53], which is a critical gas for semiconductor manufacturing. In this system, we demonstrate for the first time direct frequency comb spectroscopy in a region accessed using highly nonlinear fiber – in this case, 1.75-1.95 μm (5710-5130 cm^{-1}). Furthermore, this was the first demonstration of CE-DFCS with a focus on an industrial application (i.e., trace detection in a strongly absorbing process gas), where the bandwidth is critical for distinguishing impurity signals from background absorption, along with high resolution for making unambiguous identifications. Next, we discuss our initial demonstrations of frequency-comb-FTS based on a high power OPO that operates in the important mid-infrared window from 2100 cm^{-1} to 3700 cm^{-1} [50]. The system provided for the first time a combination of resolution, spectral range, sensitivity, and acquisition speed that is sufficient for detecting trace quantities of a wide range of molecules under real-world conditions [46]. This system also provided the basic tools for later demonstrations of shot-noise limited CE-DFCS in the near-IR [54] as well as sensitive detection of hydrogen peroxide in the presence of water in the mid-infrared [55]. Because the FTS only provides time resolution of at best one second, we also used the VIPA spectrometer with mid-infrared CE-DFCS to demonstrate rapid detection of reactive chemical intermediates [56]. We conclude this section with an outlook on potential future applications of comb spectroscopy.

While a nearly uncountable number of neutral molecules have been studied in detail using spectroscopy, the study of molecular ions is much less developed despite their importance in stratospheric chemistry [57] and astrochemistry [58, 59]. We have developed a new technique for broad bandwidth spectroscopy of molecular ions by combining CE-DFCS with velocity-modulation spectroscopy [60]. The description of this system is given in Chapter 3, while a detailed analysis of the spectra of HfF^+ measured with this system [61] is given in Chapter 5. In addition to it's importance

for a test of time-reversal symmetry using trapped ions, HfF^+ is challenging for molecular theory calculations due to the large number of electrons and the inclusion of d and f shell electrons. Our data provided critical information for improving and testing the theory of heavy atoms.

The final chapter covers the application of precision spectroscopy using molecular ions to fundamental physics with a measurement of the electric dipole moment of the electron (eEDM) [62, 63, 64, 65], which is a test of time-reversal symmetry. Trapped molecular ions – in this case HfF^+ – can potentially provide very long coherence times for Ramsey measurements, which in turn enables high precision. Partially for this reason, molecular ions have recently attracted considerable interest for a variety of precision tests of fundamental physics [66, 67, 68, 69, 70]. In this chapter, we first provide a brief introduction to eEDM measurements and then provide some details about our ion trap and ion detection systems. We also discuss state detection using resonance-enhanced multiphoton dissociation and preparation of a desired quantum state using a variation of adiabatic passage that uses trap motion combined with state-sensitive depletion. For the eEDM measurement, we need to apply bias electric and magnetic fields, which we do in a rotating frame. We demonstrate Ramsey spectroscopy between Zeeman sublevels in this rotating frame and discuss limitations to the coherence time from inhomogeneous fields and ion-ion collisions. Finally, we analyze the sensitivity and potential sources of systematic errors and demonstrate an initial measurement of the eEDM.

Overall, the techniques developed here should provide the basis for many exciting new applications. Further developments of CE-DFCS to increase the sensitivity and extend the wavelength coverage further into the mid-infrared could enable studies of many important reactions and reactive intermediates with applications to atmospheric and combustion chemistry as well as fundamental chemical kinetics. The combination of bandwidth, resolution, and sensitivity of CE-DFCS also has exciting prospects for experiments outside of the lab. Our frequency-comb velocity-modulation system is the first system capable of rapid, sensitivity spectroscopy of molecular ions over a broad bandwidth. Extensions of this technique could enable survey spectroscopy of many molecular ion species with applications to astrochemistry, physical chemistry, and fundamental physics. The combination of survey spectroscopy of ions with the techniques pioneered in Chapter 6 for pre-

cision measurements in trapped ion clouds could result in a new limit on the eEDM and could also provide new systems for other tests of fundamental physics such as parity violation, quantum electrodynamics, and variation of fundamental constants.

Chapter 2

Frequency comb sources

In a broad sense, a "frequency comb" [14, 71, 15] can be defined in the frequency domain as a collection of narrow, equally-spaced lines with a well-defined phase relationship between the lines. More specifically, each line or mode in the comb should be at a known, and controllable, frequency. Frequency combs can be generated by a variety of sources; we divide these into three general categories: mode-locked lasers, indirect sources, and cw-laser based sources. Mode-locked lasers can produce frequency combs directly at the output of the laser. Indirect sources use non-linear optical effects to modify or shift the the spectrum of a mode-locked laser. cw-laser based sources use non-linear or electro-optical materials to generate multiple sidebands from a cw-laser. We will provide an overview of how each of these sources work and also briefly discuss some common sources and their advantages and disadvantages. We also provide references to reviews or books with more information whenever possible.

The frequency comb spectrum provides several benefits for spectroscopy applications when compared to more commonly used sources such as incoherent (thermal and LED) light or cw-lasers [44, 46, 72]. First – as we will see – the comb spectrum can be very broad, even matching or exceeding some incoherent sources. At the same time though, under the broad spectral envelope there are many narrow lines at well defined frequencies, thus matching the spectral resolution attainable with cw-lasers. In this respect, a frequency comb can be thought of as an array of many thousands of cw-lasers operating simultaneously, each with a precisely defined frequency. Additionally, the spectrum of a frequency comb can be efficiently matched with the resonances of

an optical Fabry-Perot cavity for significantly increased detection sensitivities. Finally, the high spatial coherence of laser sources enables long path-length beam propagation with little loss of power due to divergence. This can be used for example for multi-kilometer length absorption measurements in the atmosphere [73].

The comb source used in a particular spectroscopic application is chosen based on the requirements of that application. The first consideration is typically the necessary spectral coverage of the comb source. For molecular spectroscopy, the strongest transitions, thus the highest detection sensitivity, exist in the visible to ultraviolet (electronic transitions) and in the mid-infrared above 3 μm (fundamental vibrational modes). Many interesting atomic transitions occur below 200 nm. This has pushed the development of comb sources towards these spectral regions. For multi-species detection capability, typically a broader spectral bandwidth is desired; however, for a given laser power, a broader bandwidth results in less power at any given spectral line, potentially decreasing the signal-to-noise. Another consideration is the spacing between comb lines. This not only affects the power-per-line for a given power and bandwidth, but also presents a tradeoff between instantaneous spectral resolution and the amount of scanning necessary to cover the full spectrum. The necessary power depends also on the efficiency of the read-out method. Finally, for applications outside of the spectroscopy lab, the robustness and portability of the system must also be considered. These considerations have led to the development of a wide range of comb sources. Figure 2.1 shows the spectral coverage and power of a variety of different sources currently demonstrated.

2.1 Mode-locked lasers

A frequency comb in the spectral domain transforms to a train of equally spaced pulses in the time domain. The time between each pulse is given by the inverse of the frequency spacing between adjacent lines in the frequency domain. This frequency is called the repetition rate (f_{rep}), and is typically set by the optical path-length L of the laser resonator. The inverse of the duration of each pulse sets the frequency domain spectral bandwidth. There is one additional degree of freedom, which is the pulse-to-pulse phase shift of the oscillating carrier electric field relative to the

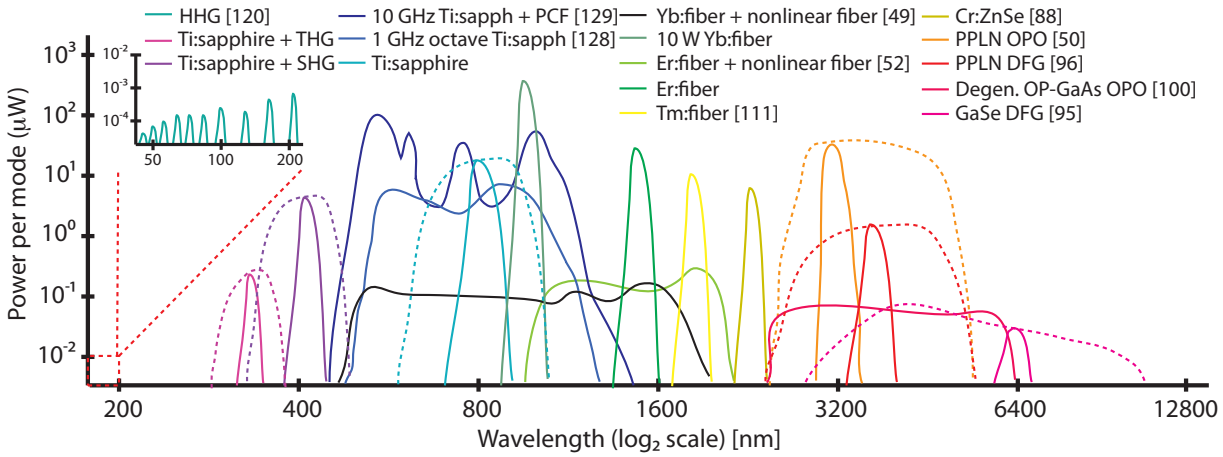

Figure 2.1: Comparison of various comb sources. Solid lines represent example spectra from each source, dotted lines represent the approximate tuning range for tunable sources.

pulse envelope (the carrier-envelope phase shift, $\Delta\phi_{CE}$). The carrier-envelope phase shift arises from cavity dispersion which results in a difference between the group velocity v_g and the phase velocity v_p at the pulse center frequency:

$$\Delta\phi_{CE} = \omega L \left(\frac{1}{v_g} - \frac{1}{v_p} \right). \tag{2.1}$$

This causes in a shift of the comb modes in the frequency domain such that the frequency of the modes is now given by $\nu_m = m * f_{rep} + f_0$. Here m is an integer mode number and f_0 is the offset frequency (also called the carrier-envelope offset frequency) due to the carrier-envelope phase shift, $f_0 = \Delta\phi_{CE}/(2\pi) * f_{rep}$.

Lasers that emit such a train of short pulses are called mode-locked lasers and were originally investigated solely for ultrashort pulse generation. Over the past few decades, mode-locking has been demonstrated by a variety of different methods in many different lasers, including solid-state lasers, dye lasers, fiber lasers, and diode lasers. Twenty years after the initial demonstration of a mode-locked laser, the ability to completely control and stabilize the frequency domain structure of such a laser was achieved, resulting in the first fully phase-stabilized frequency comb [74]. Such precise control has only been reliably accomplished in a small subset of all mode-locked lasers, and we focus our attention on the most common of those gain media: namely Ti^{3+}:sapphire, Yb^{3+}:fiber, Er^{3+}:fiber, Tm^{3+}:fiber, and (to some extent) Cr^{2+}:ZnSe. Several mechanisms exist for mode-locking these lasers [75, 76, 77] and can be broadly divided into active or passive methods.

2.1.1 Mode-locking Mechanisms

2.1.1.1 Active mode-locking

Active mode-locking works by forcing multiple laser resonator modes to have a well-defined phase relation between them [77]. This can be accomplished with an intra-cavity electro-optic or acousto-optic modulator that is driven at f_{rep} (i.e., the laser mode spacing). Thus, laser light at one mode will have sidebands located at adjacent modes. These sidebands will experience gain and will also obtain sidebands, which results in a cascaded generation of laser modes with fixed phase.

While active mode-locking is very robust, it is difficult to produce extremely short pulses using only active mode-locking because there is no strong pulse shortening mechanism [78]. Because of this limitation, most comb sources rely on some form of passive mode-locking possibly in addition to active mode-locking for self-starting.

2.1.1.2 Saturable Absorber

Mode-locking can also be achieved by modifying the temporal response of the laser cavity to favor pulse formation over cw lasing. One way to accomplish this is to incorporate an intra-cavity absorbing medium with an absorption coefficient given by

$$\alpha = \frac{\alpha_0}{1 + \frac{I}{I_s}} \tag{2.2}$$

where α_0 is the zero-power absorption coefficient, I is the intra-cavity intensity, and I_s is the saturation intensity (defined as the point where the absorption coefficient is $\alpha_0/2$). This has the effect of absorbing the leading edge of a pulse and increasing the effective gain for the peak of the pulse. The carrier lifetime of common saturable absorbers is in the range of picoseconds to nanoseconds, which would limit the achievable pulse duration to this range; however, when combined with gain saturation – which lowers the gain for the trailing edge of the pulse – shorter pulses are possible.

The most common saturable absorbers are semiconductor-based quantum wells (such as GaAs or InGaAsP) grown on the surface of Bragg reflecting mirrors [79]. These are called either saturable Bragg reflectors (SBRs) or semiconductor saturable absorber mirrors (SESAMs) and are typically used as an end-mirror in the laser cavity. These saturable absorbers often have a saturation fluence of about 20 μJ/cm^2, which gives a saturation energy of 250 pJ for a beam radius of 20 μm and necessitates tight focusing for effective mode-locking. In order to overcome some of the limitations (such as carrier lifetime) of semiconductor-based saturable absorbers and extend the applicability to other systems, saturable absorbers based on materials such as carbon nanotubes and graphene have been demonstrated [80, 81, 82].

2.1.1.3 Kerr effect

An optical field ($\mathcal{E}$) traveling through a material causes a polarization of the material given by $P = \chi_e \mathcal{E}$, where χ_e is the material susceptibility [83]. For strong fields, χ_e is itself dependent on the field strength and is approximated by $\chi_e \approx \chi^{(1)} + \chi^{(2)}\mathcal{E} + \chi^{(3)}\mathcal{E}^2 + ...$ For a material with inversion symmetry (and amorphous materials), $\chi^{(2)} = 0$. Using $I = (cn_0\epsilon_0|\mathcal{E}|^2)/2$ and $n^2 = 1+\chi_e$, we obtain for small $\chi^{(3)}$ that $n \approx n_0 + n_2 I$, where n_2 is the nonlinear index and is proportional to $\chi^{(3)}$. This (instantaneous) modification of the index of refraction as a function of intensity is known as the Kerr effect.

In solid-state lasers such as Ti:sapphire [84, 85] and Cr:ZnSe [86, 87, 88], the Kerr effect results in a variable nonlinear phase as a function of radial position in the the beam [89, 77]

$$\phi_{nl}(r,t) = \left(\frac{2\pi}{\lambda}\right) n_2 dI(t) e^{-(2r^2/w_0^2)} \approx \left(\frac{2\pi}{\lambda}\right) n_2 dI(t) \left(1 - 2\frac{r^2}{w_0^2}\right) \tag{2.3}$$

for a thin material of thickness d and a Gaussian beam of waist w_0. This parabolic phase front results in an effective lens of focal length

$$f = \frac{w_0^2}{4n_2 dI_0} \tag{2.4}$$

where I_0 is the peak pulse intensity. This lens can be used as an effective saturable absorber for mode-locking (called Kerr-lens mode-locking or KLM) in several ways. First, with a hard aperture, the transmission through the aperture will increase with more lensing, so the net gain will be higher for pulsed operation. Even without a hard aperture, the presence of the Kerr lens modifies the cavity parameters, thus a cavity near the edge of stability can be made more stable for pulsed operation. KLM lasers may not be self-starting; however, typically only small perturbations are necessary to initiate mode-locking. In general, KLM lasers provide the shortest pulse durations achievable directly from the gain medium.

The Kerr effect also occurs in Yb- and Er-doped gain fibers, where it results in a nonlinear rotation of elliptically polarized light. This polarization rotation can be used in a ring cavity with polarization selective elements to achieve mode-locking by increasing the transmission through an

intracavity polarizer for pulsed light relative to cw light [90]. Polarization-rotation mode-locking can be used to create all-fiber lasers with no free-space sections and provides for reliable, self-starting mode-locked operation [91].

2.2 Indirect Sources

The ultrashort pulsed output of a mode-locked laser results in a high peak intensity per pulse. This provides large nonlinear effects in many materials, which can be used to extend or shift the spectrum of a mode-locked laser. Frequency combs can thus be generated in spectral regions that are difficult or impossible to fully cover with cw-lasers such as the extreme ultraviolet (below 100 nm) or the mid-infrared (2-10 μm). In addition, frequency combs can simultaneously cover multiple octaves of spectral bandwidth using non-linear optics, far exceeding the tuning range of any cw-laser, while still maintaining the high resolution of a cw-laser. This flexibility makes indirect comb sources well suited for new applications in spectroscopy.

Many crystals do not possess inversion symmetry and therefore exhibit $\chi^{(2)}$ nonlinearity. This nonlinearity can be used for second-harmonic generation (SHG), sum-frequency generation (SFG), difference-frequency generation (DFG), and parametric generation [83]. In SHG, two pump photons are combined to form one photon at twice the frequency; similarly in SFG, two pump photons at different frequencies are combined to produce one at the sum frequency. DFG again works in the same way, except that the difference frequency is produced. Parametric generation is the reverse of SFG, where one pump photon is down-converted into two lower energy photons (a signal and idler). Phase-matching between all three frequencies must be satisfied in all of these processes; this can be accomplished by using different axes of a birefringent crystal and tuning the input angle and polarization relative to the crystal axes or by periodically poling a crystal such that the phase of the produced light is periodically changed to add coherently (similar to Bragg reflection). The phase matching can be tuned by rotating the crystal, or in the case of periodically-poled materials, it is possible to create a "fan-out" poling-period that varies linearly across one dimension of the crystal so that the crystal just needs to be translated. In addition, longer periodically-poled crystals can

be used without severely limiting the angular acceptance (and thus the phase-matched spectral bandwidth), resulting in higher conversion efficiencies.

The most common approaches for producing mid-infrared frequency combs beyond 3 μm are to use either DFG or an optical parametric oscillator (OPO, see Section 2.4). DFG combs have been demonstrated using the spectrum generated directly from a Ti:sapphire laser [92]; however, the achievable powers were very low. More power can be obtained by using two synchronized Ti:sapphire lasers [93], but this is experimentally more complicated. Multi-branch Er:fiber lasers enable mW-level, tunable DFG with one branch used with nonlinear fiber to provide tunable, shifted light and the second branch used to provide high-power, unshifted light [94, 95]. Up to 100 mW has recently been acheived using a fan-out periodically-poled crystal and a Yb:fiber laser [96]. In this case, some of the light from the fiber laser was sent through nonlinear fiber, and the red-shifted Raman soliton (see Section 2.3 for more information on nonlinear fiber optics) was mixed with the remaining unshifted pump light to generate the difference frequency. DFG systems are convenient and compact, but the power limitations can hinder some applications. For higher power, it is necessary to use an OPO, in which the signal and/or idler light produced by parametric generation is resonant with a cavity containing the nonlinear crystal. This greatly increases the conversion efficiency, but also adds some additional complexity. For comb generation, the cavity is generally pumped synchronously, that is the OPO cavity FSR should match an integer multiple of the laser repetition rate, and the cavity length is actively controlled since this sets the f_0 of the generated comb [97, 50, 98]. It is also possible to run an OPO with the signal and idler degenerate (a "divide-by-two" system), which can be used to produce near-octave spanning spectral bandwidth in the mid-infrared [99, 100]. This broad spectrum presents a drawback though as well, since the power per spectral element is usually low. The upper limit to the attainable spectral range is set partially by the absorption edge of crystals used (commonly lithium niobate), so to reach longer wavelengths, other crystals must be used. These are usually angled-tuned crystals such as $AgGaSe_2$ [101]; however, recently, periodic patterning of GaAs has been developed, which could enable significantly higher powers. In order to use GaAs for mid-infrared generation, the

pump wavelength must be above about 1.6 μm, thus the increased interest in Tm:fiber systems. Very recently, an octave-spanning mid-infrared spectrum up to 6.1 μm was demonstrated with a Tm:fiber laser and degenerate OPO using orientation-patterned GaAs (OP-GaAs) [102], although the average power was only about 30 mW.

Large nonlinear effects can also be obtained by tight confinement in small-core optical fiber [103, 104] (such as photonic crystal fiber [105, 106], microstructure fiber [20, 107], and highly nonlinear fiber [108]). These fibers not only result in high intensities but also provide a long interaction length over which to accumulate effects. In addition, the dispersion profile of the fiber can be tailored by adjusting the mode size and adding dopants, which provides even more control over the nonlinear effects present. Because of the flexibility, nonlinear fibers have found a wide range of applications. In addition to visible light production [109], Er:fiber lasers broadened with nonlinear fiber have also been used to seed a Tm:fiber amplifier, which can produce >3 W average power femtosecond pulses tunable around 2 μm [110, 111]. This source can be used to pump an OP-GaAs OPO in the 5-12 μm spectral region (where sources for comb spectroscopy are lacking) or can be used to generate tunable THz radiation using OP-GaAs [112]. Broadening in nonlinear fiber can also be used to coherently link different wavelength regions. For example, a broadened Yb:fiber comb would perhaps be the ideal source to link a highly stable cw laser at 1.55 μm to the Strontium optical clock transition at 698 nm if the Yb:fiber laser can provide coherent light at both spectral regions simultaneously. Finally, in an application of comb spectroscopy to trace gas analysis in semiconductor processing gases (Section 4.1), an Er:fiber laser can be used to provide tunable 1.8-1.9 μm light with reasonable powers from a compact system. Currently, fibers with large nonlinearities are readily available throughout the visible and near-infrared and have recently been demonstrated in the mid-infrared [113, 114, 115, 116]. Nonlinear fibers enable flexible comb generation in many wavelength regions using robust (fiber-based) pump lasers; however, care must be taken so that the coherence of the pump is preserved in the nonlinear processes, as discussed in Section 2.3.

With extremely high peak electric fields, like those attainable at a tight focus in an optical

cavity, the perturbative expansion to the polarizability breaks down and the material (in this case usually a jet of noble gas) is ionized. The electron is accelerated away from the atom for some period of time, until the electric field reverses and accelerates the electron back toward the atom. The electron can then recombine with the atom, emitting all of the excess energy from the field in high-order (odd) harmonics of the original laser frequency. This process, called high-harmonic generation (HHG), can be used to produce combs in the vacuum ultra-violet (VUV, 100 to 200 nm) and extreme ultra-violet (XUV, below 100 nm) [117, 118, 119] with over 100 μW per harmonic order[120].

2.2.1 cw-laser Based Sources

Currently, cw-laser based comb sources have not seen many applications to spectroscopy and so we only briefly mention them. It is possible to make a frequency comb simply by applying a strong frequency modulation, which results in sidebands at harmonics of the modulation frequency. With very strong modulation it is possible to put optical power into high orders, resulting in a comb in the frequency domain. However, in practice, the achievable spectral bandwidth is small and thus does not provide much of an advantage over cw-laser spectroscopy. A comb can also be generated by driving a Raman transition between rotational levels in a molecule using two (pulsed) laser frequencies. With enough Raman gain, it is possible to cascade this process and produce an octave-spanning comb [121]. Currently these combs have only been demonstrated with large mode spacing (the rotational spacing of the molecules used), which potentially limits the usefulness for spectroscopy.

Recently, frequency combs based on parametric frequency conversion of cw-lasers in microresonators have been been demonstrated [122, 123, 124]. When a cw-laser is injected into a high-finesse microresonator, the high intracavity intensity results in cascaded four-wave mixing (FWM) and can generate a comb with a frequency spacing set by the free-spectral range of the microresonator. These sources show some interesting potential for spectroscopy applications due to their compact size and inherent simplicity; however, they are currently limited to repetition rates

above about 20 GHz, which is a potential drawback. In addition, the inherent noise properties of the generated comb are not yet well understood or controllable [125, 126].

2.2.2 Typical comb sources

Mode-locked Ti:sapphire lasers were used for the first realization of fully stabilized frequency combs, and they are still probably the most widely used comb sources. These are usually Kerr-lens mode-locked and are sometimes actively mode-locked as well. The Ti:sapphire gain bandwidth is extremely broad, which enables the generation of ultrashort (10 femtosecond) pulses and correspondingly large spectral bandwidth (covering about 700 nm to 1050 nm) directly from the laser. It is even possible to generate octave-spanning spectra directly from the laser with intracavity SPM [127, 128]. Ti:sapphire combs can be made with repetition rates ranging from < 100 MHz up to 10 GHz [129], providing large flexibility for different applications. Because the ultrashort pulses result in high-efficiency nonlinear processes, Ti:sapphire lasers also provide the highest power combs in the visible to UV range by using SHG [130] or supercontinuum fiber. One drawback is that the free-space cavity limits the robustness of these lasers. In addition, the pump laser is still expensive and relatively bulky, further limiting the field applicability of the system.

Yb:fiber lasers [75] produce combs directly in the 1000 to 1100 nm spectral region. These lasers are typically mode-locked using a saturable absorber and are limited in spectral bandwidth (and thus pulse duration of about 80 fs) by the gain bandwidth of the fiber. One common cavity configuration consists of a linear cavity with the pump diode coupled to the gain fiber using a wavelength-division multiplexer (WDM), one cavity mirror (the output coupler) being a Bragg grating written into fiber, and a short free-space section containing a waveplate, focusing lens and an SBR as the second cavity mirror (see Figure 2.2). While this design does contain a small free-space section, it is still robust since the pump is entirely fiber-coupled and the cavity is mostly fiber. Additionally, the pump diode is compact and fairly inexpensive. It is also possible to use polarization rotation mode-locking; however, in this case free-space intracavity gratings are required for dispersion compensation. Yb:fiber combs have been built with repetition rates up to 1 GHz.

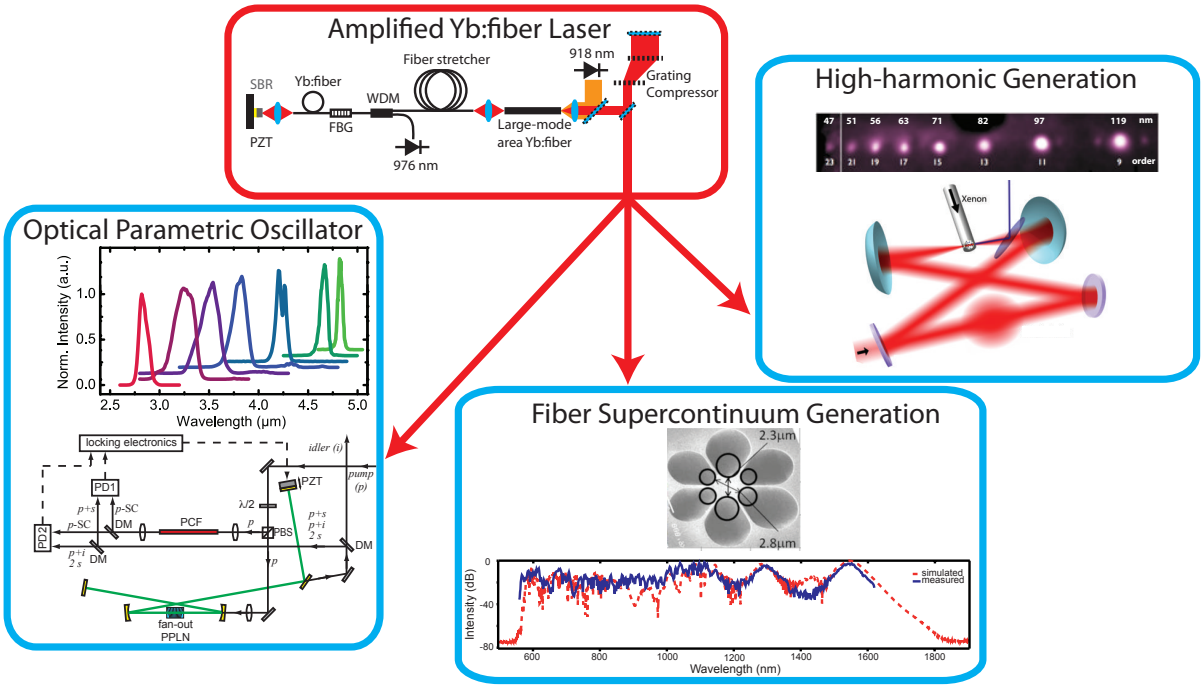

Figure 2.2: Sources based on a Yb:fiber laser. The red-outlined box shows a linear Yb:fiber oscillator and stretched pulsed amplifier. This type of system can be used to produce frequency combs covering many different spectral regions with nonlinear optics. The bottom left box shows a tunable comb in the mid-infrared using an optical parametric oscillator [50]. By using a small core nonlinear fiber (an example cross-section is given in [20]) it is possible to cover over 1.5 octaves coherently (center box) [49]. As shown in the box on the right, an XUV comb down to 50 nm can be produced using cavity-enhanced high-harmonic generation [120]. PZT is a piezo-electric transducer, FBG is a fiber Bragg grating, DBR is distributed Bragg reflector.

Yb:fiber based amplifiers are very power scalable due to the high Yb-doping concentration possible in large mode area fibers. In fact, chirped-pulse amplifiers have been used to produce a comb with 80 W average power at 150 MHz [131]. As shown in Figure 2.2, the high average power capabilities have enabled comb generation spanning over 1.5 octaves in the near-infrared in highly nonlinear fiber (Section 2.3) [49], in the XUV down to 50 nm with high-harmonic generation [120], and in the mid-infrared with parametric generation (Section 2.4) [50]. One drawback of Yb:fiber lasers is that they are not very tunable without external spectral broadening due to the narrow gain bandwidth.

Er:fiber lasers [132, 133] mode-locked (typically) using polarization rotation, have become very popular for a few reasons. First, since they produce combs near 1550 nm they can take advantage of all of the advancements in telecommunications technology. This makes them inexpensive and fairly easy to build. In addition, they can be made entirely out of fiber, without any free-space sections, which makes them very robust and portable [134, 91] even being used in a drop tower experiment with deceleration of 50 g [135]. It is also possible to split the comb output into multiple branches, and amplify each branch separately, which provides a large amount of flexibility. With highly nonlinear fiber, Er:fiber lasers can cover from 1000 nm to over 2100 nm (Section 2.3). When combined with SHG as well, they can be used to provide tunable combs throughout the visible region [109]. They have also been used for mid-infrared comb generation using DFG or an optical parametric oscillator. However, currently Er:fiber lasers are limited to typically 500 mW per branch. Also, for spectroscopy, their spectral coverage without broadening or frequency conversion is not ideal. Due to the low doping concentration of the Er:fiber and the necessary dispersion compensation, the repetition rate is typically 100-250 MHz, although a repetition rate of 1 GHz has been demonstrated [136].

Two new comb sources have recently been developed that push the wavelengths toward the mid-infrared. Tm:fiber combs [137], which operate between 2 to 2.1 μm, function in many ways similarly to Yb:fiber lasers and with many of the same advantages and disadvantages of those lasers. Currently, they can provide about 3 W of power at repetition rates up to about 100 MHz, although the power can be increased with careful thermal management. It is also possible to seed

a Tm:fiber amplifier with the shifted output of an Er:fiber comb [111]. The primary advantage of these lasers is that they allow for the use of new nonlinear crystals for frequency conversion to the mid-infrared. Cr:ZnSe lasers are similar in may respects to Ti:sapphire except that they operate around 2.5 μm. The fractional gain bandwidth is even larger than that of Ti:sapphire, which gives the potential for ultrashort pulse generation in the mid-infrared and thus broad spectral bandwidth directly from the laser. Currently though, challenges such as cavity dispersion control [138] have limited the utility of these lasers.

2.3 Nonlinear fiber optics

The observed spectrum from the nonlinear fiber results from a complex interplay of multiple $\chi^{(3)}$ processes such as self-phase modulation (SPM), cross-phase modulation (XPM), stimulated Raman scattering (SRS), and four-wave mixing (FWM) as well as the interaction of dispersion with each of these [139, 140]. Because of this complexity, fiber super-continuum sources are often modeled numerically using a generalized nonlinear Schrodinger equation [141]. Several comprehensive reviews [104, 142] and books [103, 143] have been written about nonlinear effects in fiber, and we provide a summary in Section 2.3.2. Briefly, the dominant nonlinear process depends on the fiber group-velocity dispersion (GVD, parameterized by the coefficient β_2) near the wavelength of the injected pulse. For normal (i.e., positive) GVD, the primary broadening mechanism initially is SPM, which results in a nearly symmetrical spectral broadening, with some additional contributions from XPM and FWM especially close to the zero-GVD point. SPM and XPM both arise from the Kerr effect discussed before; however, in this case the nonlinear phase shift occurs in the temporal domain. Since a time-varying phase results in an instantaneous frequency shift, this results in a frequency chirp and spectral broadening. This can also be understood as a temporal focusing, i.e., pulse compression. In XPM, electric fields at one frequency cause phase shifts on fields at another frequency. FWM is a general term for a $\chi^{(3)}$ process that converts two input photons (at the same or different frequencies) into two photons at new frequencies with the same total energy. It dominates near the zero-GVD wavelength and also plays a role as the spectrum broadens

and phase-matching becomes more likely. In the anomalous (negative) GVD region, the injected pulse can initially form (quasi-) stable wavepackets called solitons. As these solitons propagate, they shift toward longer wavelengths (i.e., red shift) due to stimulated Raman scattering where a photon from the shorter wavelength portion of the pulse spectrum is converted into a longer wavelength (lower energy) photon and an acoustic phonon. In addition, as the solitons propagate, they emit so-called dispersive waves at short wavelengths (in the normal GVD region) where the phase velocity matches that of the soliton. These dispersive waves are analogs to the Cherenkov radiation emited by charged particles. Finally, the solitons and dispersive waves can couple through XPM, resulting in additional spectral broadening.

Many of these features can be observed in the measured spectra from a broadened Yb:fiber laser shown in Figure 2.3. The fiber used here is the IMRA suspended core fiber [20], and we measure the spectrum as a function of power coupled into the fiber. As the power is increased, we initially see one Raman soliton on the red side of the spectrum and then this soliton progressively shifts to the red and multiple solitons appear. On the blue side, we initially see peaks below 700 nm, which are the dispersive waves. Between 700 and 900 nm the behavior is more complicated: at the highest power, this region is completely filled, but we have found that this region potentially has significant amplitude noise (see below). This fiber setup was used as part of the stabilization of the mid-IR OPO (Section 2.4). We have investigated the coherence properties of a similar broadening setup that covers 1.5 octaves, as discussed in detail below.

Nonlinear fiber optics can also be used for comb spectroscopy around 1.8-2 μm with an Er:fiber laser (Section 4.1). Initially, we used a long piece of single-mode polarization-maintaing fiber (e.g., Fibercore HB-1500, which has a slightly smaller core compared to standard SMF-28) to Raman shift a significant portion (50% or potentially even more) of the initial power to beyond 1.8 μm, as shown in Figure 2.4(a). The final wavelength of the shifted light could be controlled by varying the input power, polarization, or initial chirp (using a prism pair). This has the advantage of providing high power concentrated in a single, controllable spectral region; however, we found some issues with the coherence of the shifted light, as discussed more below. Because of this, we

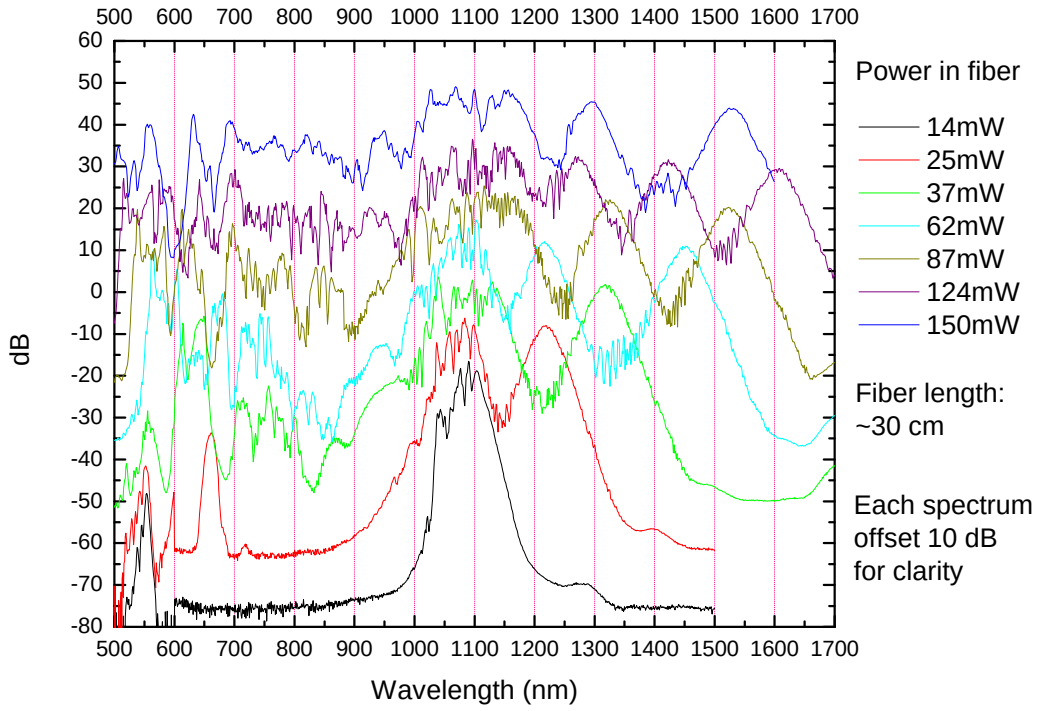

Figure 2.3: Spectral broadening of a Yb:fiber laser using IMRA suspended core fiber.

used supercontinuum generation in highly nonlinear fiber for this project (Figure 2.4(b)).

2.3.1 Numerical simulations

To better understand the spectral broadening process and supercontinuum coherence properties, it is necessary to perform numerical simulations of the pulse dynamics within the nonlinear fiber. The propagation in fiber can be accurately described by a generalized nonlinear Schrödinger equation (GNLSE) [144, 141],

$$\frac{\partial A(z,t)}{\partial z} + \frac{\alpha}{2}A - i\mathcal{F}^{-1}\Big[\big(\beta(\omega) - \omega\beta_1 - \beta_0\big)\tilde{A}(z,\omega)\Big] = i\gamma\left(1 + \frac{i}{\omega_0}\frac{\partial}{\partial t}\right)\left[A(z,t)\int R(t')\left|A\left(z,t-t'\right)\right|^2 dt'\right]. \tag{2.5}$$

The left side describes all linear and dispersive effects where $A(z,t)$ is the field envelope as a function of position z and time t, α is the absorption coefficient, and the inverse Fourier transform accounts for dispersion. In this, $\tilde{A}(z,\omega)$ is the Fourier transform of $A(z,t)$; $\beta_k \equiv \frac{\partial^k}{\partial\omega^k}\beta(\omega)\big|_{\omega_0}$, where $\beta(\omega)$ is the propagation constant, and ω_0 is the carrier frequency. The dispersion term is frequently approximated by a Taylor series, so

$$i\mathcal{F}^{-1}\Big[\big(\beta(\omega) - \omega\beta_1 - \beta_0\big)\tilde{A}(z,\omega)\Big] \approx \sum_{k\geq 2}\frac{i^{k+1}}{k!}\beta_k\frac{\partial^k A}{\partial T^k}. \tag{2.6}$$

The terms on the right side of Equation 2.5 take into account the relevant $\chi^{(3)}$ effects, namely Raman scattering and the Kerr effect, through the nonlinear coefficient $\gamma = \omega_0 n_2(\omega_0)/cA_{eff}(\omega_0)$. Here n_2 is the nonlinear refractive index of the fiber core and A_{eff} is the effective area of the guided mode. The time derivative accounts for intensity dependence of the group velocity, an effect that leads to self-steepening and optical shock formation (steep leading pulse edges). This same formalism can be used to describe the Kerr effect. Shock wave formation occurs on a characteristic time scale given by $\tau_{sh} \approx 1/\omega_0$. The integral term on the right side of Equation 2.5 accounts for the delayed Raman response of the fiber material whose temporal impulse response is given by $R(t) = (1 - f_R)\,\delta(t - t_e) + f_R h_R(t)$ [103], where the Raman fraction, f_R, sets the ratio of Kerr to Raman non-linearity, $h_R(t)$ is the time-domain Raman response function, and t_e is an electric

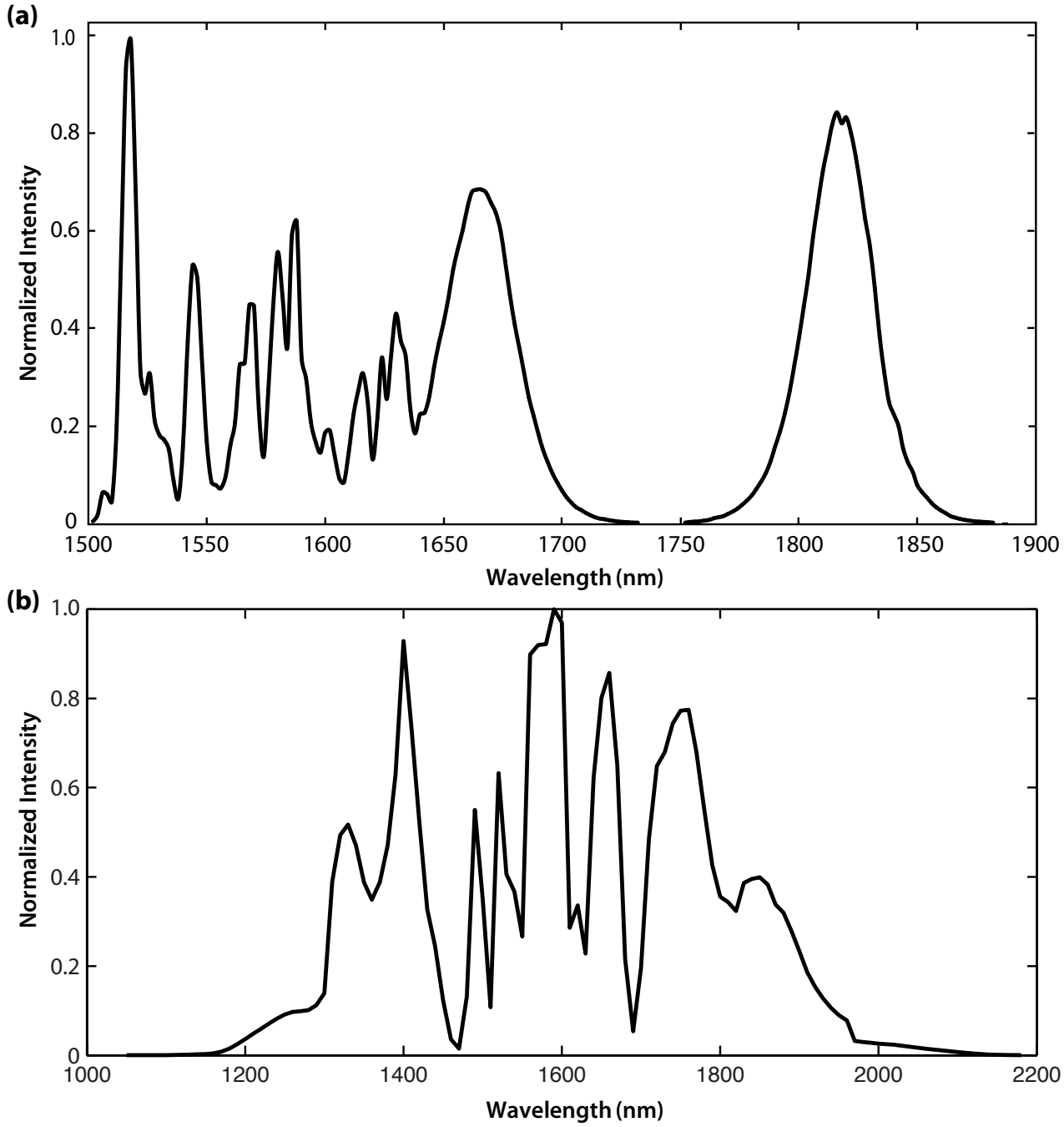

Figure 2.4: Comparison of Raman shifting fiber and highly nonlinear fiber. (a) Raman shifted spectrum from an Er:fiber laser after propagating through ∼8 m of polarization-maintaining fiber. (b) Spectrum after ∼7 cm of highly nonlinear fiber (OFS Specialty Photonics).

delay. In general, it is assumed that the electronic response is instantaneous so that the delay time can be neglected. The response function and Raman fraction ($f_R \approx 0.18$) are determined by fitting the frequency domain Raman gain spectrum [144, 145]. This fit assumes that the gain spectrum can be described by a single Lorentzian model (which assumes that the Raman response is only due to a symmetric Si–O–Si stretch); however, this neglects what is known as the 'Boson peak' in amorphous glasses. A potentially more complete model for h_R is given in [146], which gives a higher fit value of $f_R \approx 0.245$ for silica fiber. For the simulations here we have opted to continue to use the simpler and more frequently used model with $f_R \approx 0.18$ for standard SMF 28. Doping of the fiber core, for example with GeO_2, will increase f_R, which will be important below.

We numerically solved the GNLSE using a symmetric split-step Fourier algorithm. This algorithm assumes that the dispersion and non-linearities act independently of each other, so for each distance step of size h, dispersion acts for the first length $h/2$, then the non-linearity is applied, and then dispersion is applied for the second half step of distance $h/2$. This can be thought of as neglecting the commutator between the dispersion and non-linearity operators, which results in an error of order h^2, thus the algorithm converges by decreasing h. For the dispersion step, we have the following equation (neglecting all non-linearities):

$$\frac{\partial A}{\partial z} = \hat{D}A \tag{2.7}$$

where $\hat{D}$ is the dispersion operator, which can be obtained by comparing with the GNLSE (Equation 2.5). Equation 2.7 can be easily solved by switching to the frequency domain

$$A(z + h/2, T) = \mathcal{F}^{-1}\left[\exp\left(-h/2\hat{D}(-i\omega)\right)\mathcal{F}(A)\right] \tag{2.8}$$

where $\hat{D}(-i\omega)$ is obtained by replacing each time derivative in the dispersion operator with $-i\omega$.

While dispersion is easy to apply, non-linearities are more subtle. There are many possible methods that can be used, each with trade-offs in terms of accuracy and computational difficulty. First, there are several ways of computing the non-linearity operator. Agrawal [103] typically approximates $|A(z, t - t')|^2$ with a Taylor expansion (to first order) about $t' = 0$ which reduces the

convolution integral to just an integral of the Raman response function. Furthermore, second order derivatives are dropped to give three terms. This is the simplest form of the non-linearity operator; however, its accuracy is questionable for ultrashort ($<$ 100 fs) pulses, so it was not used in this study. The method used here is to compute the convolution in the frequency domain as an inverse Fourier transform of a product of Fourier transforms [147]. Note that if the FFT algorithm is used (as it typically is) the convolution will need to be scaled by a factor proportional to $1/N$, where N is the number of frequency/time grid points. Similarly, the time derivative can be evaluated using another inverse Fourier transform/Fourier transform pair, or by using a numerical gradient algorithm.

The simplest way to apply the non-linearity operator is by multiplication with $\exp(h\hat{N})A$; however, this is not the most accurate method. Another method is to say that in reality, the non-linearity should have been integrated over the distance h, and then to approximate this integral as the average value at its endpoints. Now, the value of $A(z+h)$ (which is needed to find the non-linearity operator at that point) is not known, but can be solved iteratively by first using the initial value of A, calculating the final A after applying all dispersion, then using this as the new value of $A(z+h)$ and repeating until the final field converges. This is ideally very accurate, although is potentially computationally intensive. The method used here is to solve the differential equation given by

$$\frac{\partial A}{\partial z} = \hat{N}A \tag{2.9}$$

using a fourth-order Runge-Kutta algorithm. This algorithm seems to be robust while maintaining high accuracy.

2.3.2 Broadening mechanisms

Our first task now is to understand the dynamics of pulse propagation in optical fibers. We first look at an 83 fs FWHM Gaussian pulse with 35.2 kW peak power in standard SMF-28. Additionally, we neglect all dispersion except GVD and assume that γ is $\sim$1 W^{-1}/km. Figure 2.5(a) and (b) show the pulse evolution with -22 ps^2/m dispersion (i.e., in the anomalous dispersion

regime) while (c) and (d) show the propagation with the GVD sign flipped (normal dispersion). From this simple simulation we can see several important features. First, we can see the dramatic difference between dynamics with anomalous and normal dispersion. In the normal dispersion case the dynamics are primarily just the result of GVD induced pulse broadening as well as SPM spectral broadening (which results in a symmetrically broadened frequency spectrum). However, in the anomalous dispersion case the dynamics are clearly different. In this case, the evolution is dominated by the dynamics of solitons.

If we inject a pulse with a given peak power and pulse duration into fiber with anomalous dispersion, the pulse will rapidly evolve into a soliton with order given by

$$N = \sqrt{\frac{P_0 \gamma T_0^2}{|\beta_2|}} \tag{2.10}$$

where P_0 is the peak power and T_0 is the pulse width (not FWHM – with the given parameters T_0 is 50 fs). In Figure 2.5, the power is sufficient to form a second-order soliton ($N = 2$). To confirm that soliton dynamics are important, Figure 2.6(a) and (b) show a similar pulse with peak power high enough to give a third-order soliton, while Figure 2.6(c) and (d) show what happens if $N << 1$ so that soliton dynamics are not relevant.

The most distinctive features of Raman solitons are the strong temporal and frequency shifts seen in Figures 2.5(a)-(b) and 2.6(a)-(b). Each Raman soliton experiences a different group delay and thus temporally separates from the center seed pulse. Furthermore, it continues to experience a frequency shift toward the red from intrapulse Raman scattering (where the blue frequency components of the pulse seed the red frequency components through the Raman gain of the fiber). This frequency shift, $\Delta\nu_R(z)$, is called the Raman induced frequency shift (RIFS) or the soliton self-frequency shift (SSFS). Neglecting higher order dispersion and losses,

$$\Delta\nu_R(z) \approx \frac{-4T_R(\gamma P_0)^2 z}{15\pi|\beta_2|}, \tag{2.11}$$

where T_R is a Raman delay parameter, which is about 3 fs for fused silica [103]. Another noticeable effect is an oscillating spectral and temporal profile. This is further confirmation of soliton dynamics, as these oscillations occur in soliton propagation without non-linear effects.

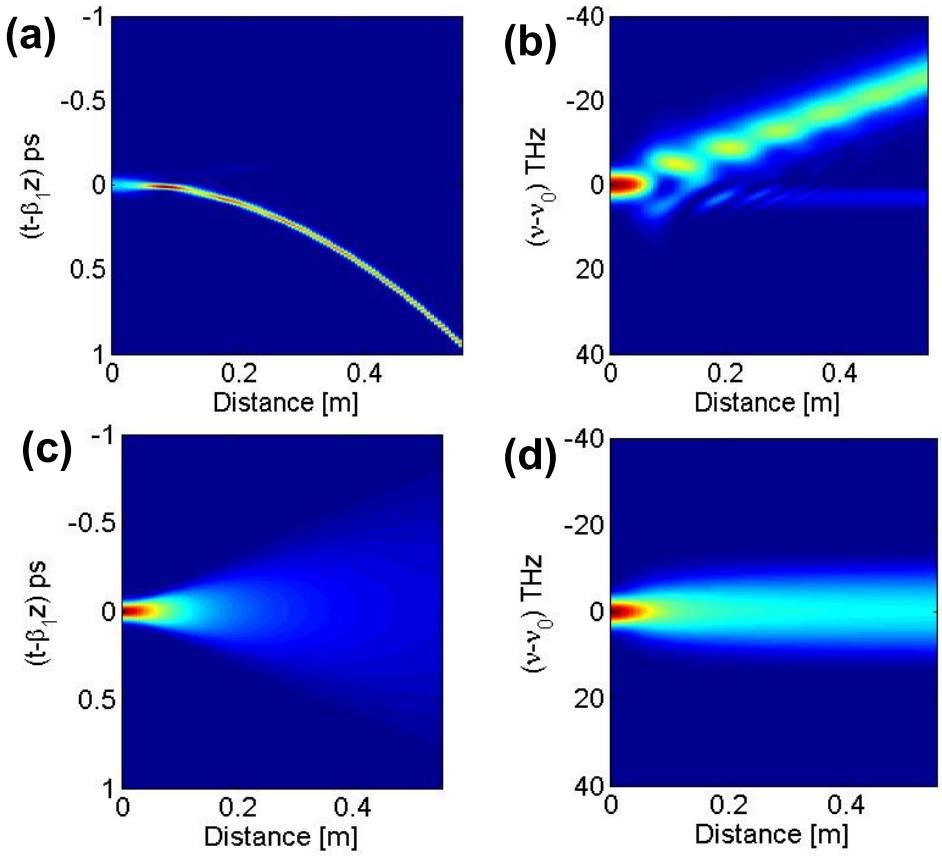

Figure 2.5: $N = 2$ Gaussian pulses propagating in fiber with only GVD and non-linear effects included. (a) and (b) Temporal and spectral profile with -22 ps^2/m GVD. (c) and (d) Temporal and spectral profile with +22 ps^2/m GVD.

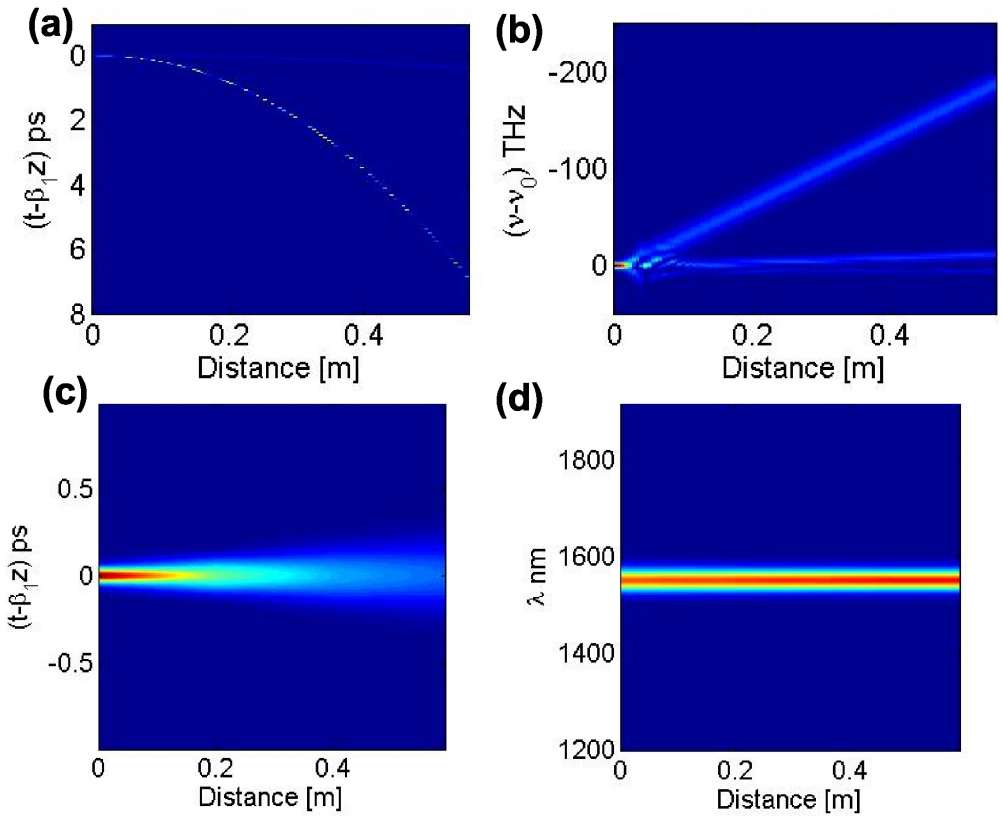

Figure 2.6: Higher and lower power pulses propagating in SMF-28. (a) and (b) Temporal and spectral profiles of an $N = 3$ soliton; (c) and (d) Temporal and spectral profiles of a pulse with $N << 1$.

Within a short distance into the fiber, a higher-order soliton (including one with non-integer N) is believed to break-up into $\bar{N}$ fundamental solitons in a process termed soliton fission [142]. This fission process can be explained by stimulated Raman scattering dumping enough power from the high-order soliton into a frequency shifted component to form a stable fundamental Raman soliton. The temporal width and power of the kth soliton ($k = 1, 2, ..., \bar{N}$) are

$$\begin{aligned} T_k &= \frac{T_0}{2N + 1 - 2k} \text{ and} \\ P_k &= \frac{(2N + 1 - 2k)^2}{N^2} P_0. \end{aligned} \tag{2.12}$$

Each soliton then experience RIFS according to Equation 2.11 with P_0 replaced by P_k. We can see this in the $N = 3$ case, Figure 2.6(a) and (b), where two red-shifted solitons are seen at the longer propagation distances.

While instructive, these calculations did not necessarily use reasonable parameters. For example, third-order and higher dispersion terms were ignored and the peak power was chosen as to satisfy the given soliton number condition without regard to how much peak power was required. We now consider what happens if we use experimentally relevant values. For these simulations we assumed values reasonable for a standard Er:fiber oscillator followed by a single-mode Er:fiber amplifier. In particular, we assumed 400 mW average power at 250 MHz repetition rate and 70 fs FWHM sech^2 pulses. The center wavelength was assumed to be 1550 nm.

We first simulated propagation of this pulse through SMF-28. The result is shown in Figure 2.7. The given pulse parameters correspond to $N \approx 1$ so we would expect to see some soliton dynamics involved. Indeed this is the case, as we see the clear formation of a single Raman soliton, which experiences RIFS along the fiber. After propagating through 8 m of fiber, the wavelength has shifted to around 1850 nm, which is similar to the shift observed in Figure 2.4. As the soliton shifts to longer wavelengths, $|\beta_2|$ increases, which results in an increasing temporal pulse width (according to Equation 2.10). This results in a lower Raman gain and causes the rate of wavelength shifting to decrease at longer wavelengths.

For comparison, we also simulate the propagation of this same pulse in dispersion-shifted

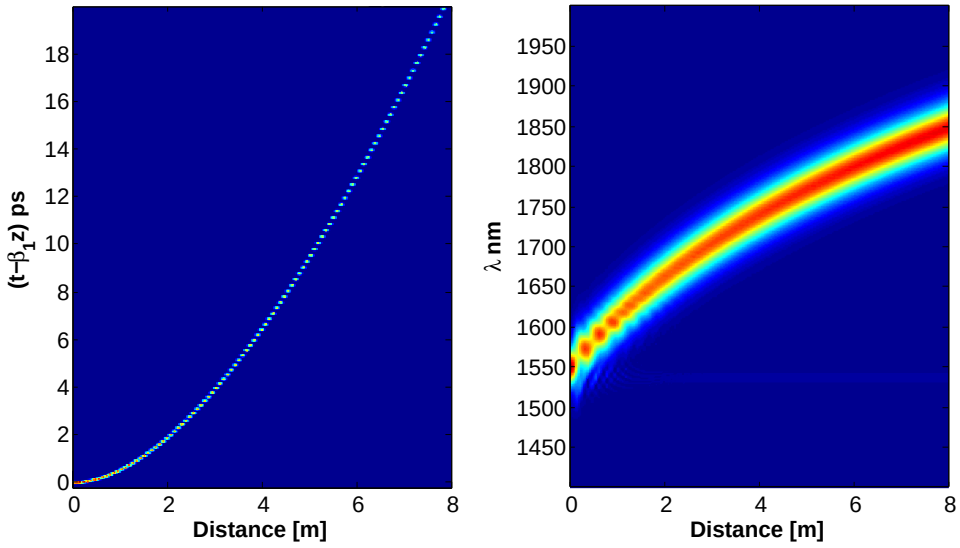

Figure 2.7: Simulation of Raman shifting of an Er:fiber laser in SMF-28.

fiber (i.e., highly nonlinear fiber, HNLF), which has a zero-dispersion wavelength typically above 1500 nm and a smaller core size than SMF 28. This results in $\gamma \approx 21$ W^{-1}/km. We used dispersion parameters from [148]. The results from this simulation are shown in Figure 2.8. Using our knowledge of propagation in SMF-28, we can attempt to deconstruct the dynamics of the supercontinuum formation in HNLF.

Since we are still pumping the HNLF slightly in the anomalous dispersion region, we still expect to see soliton dynamics. If fact, given the small GVD and higher non-linearity of the fiber, we are injecting an $N = 48.7$ soliton into the fiber; however, the distance at which soliton fission occurs is given roughly by L_D/N where $L_D = T_0^2/|\beta_2|$ is the dispersion length. This estimate implies that soliton fission would occur in about 11 cm; therefore, we do not expect to see a large number of ejected solitons. We can however still attribute the long wavelength edge of the spectrum to a Raman soliton undergoing RIFS. Instead of seeing an ejected soliton after the fission distance, which would happen almost immediately in SMF-28, we are instead seeing the high-order soliton just starting to break-up. However, since the fission distance is so long compared to the length over which the non-linearities take to become apparent, the process is distorted because of the non-linearities. In particular, the long wavelength region results from the Raman shifting of the high-order soliton. As this soliton is rapidly shifted due to the RIFS, it is still undergoing a fission process, resulting in further breakup into two pulses with different pulse energies. The higher energy soliton experiences more RIFS, whereas the low energy component would not experience as many nonlinearities. In addition, the initial spectrum broadens rapidly due to SPM, which would serve as a further driving effect for the soliton breakup.

We also see a significant amount of structure on the short wavelength edge. Some of this is certainly due to SPM (note the symmetrical initial broadening); however, SPM would most likely not lead to such a strong edge to the spectrum. An additional source of this is coupling from the Raman soliton components into a dispersive wave. This coupling occurs through a phase resonance

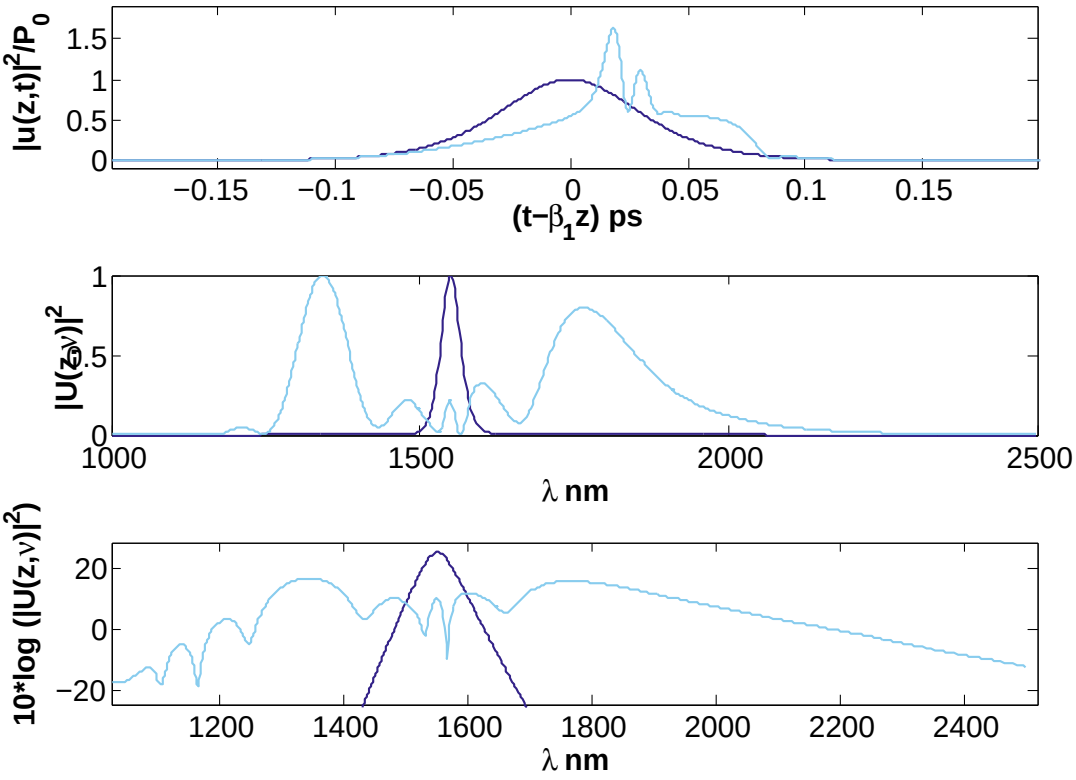

Figure 2.8: Simulated broadening of an Er:fiber laser through 3 cm of HNLF. Dark blue is the initial pulse, light blue is after the fiber. The top panel is the temporal evolution and the bottom two panels are the spectral evolution (normalized, linear scale and log scale, respectively).

where the dispersive wave is formed at frequency ω_{DW} given by [142]

$$\beta(\omega_s) - \omega_s/v_s^g + (1 - f_R)\gamma P_s = \beta(\omega_{DW})\,\omega_{DW}/v_s^g \tag{2.13}$$

where P_s is the peak power of the soliton coupling to the dispersive wave and v_s^g is the group velocity of the soliton. Since these are changing as the soliton propagates, the generated dispersive wave could evolve along with its generating soliton. The temporal profile in the first panel of Figure 2.8 corroborates this explanation. In this, we see two Raman solitons slightly delayed from the main pulse and a broad pedestal around the solitons, which is the dispersive wave.

In addition to understanding the broadening process, we care about the coherence of the generated light. As we will see in the next section, we can use a combination of experiments and simulations to check the coherence of the nonlinear processes occurring in the fiber. This was the first systematic experimental and numerical study of supercontinuum coherence over wide bandwidth.

2.3.3 Coherence measurements

We have tested the coherence properties of the broadened spectra from a Yb:fiber laser by performing free-running beat experiments with several single-frequency lasers. The frequency comb was based on a Fabry-Perot-type Yb-similariton oscillator mode-locked with a sub-ps lifetime saturable absorber mirror, which are known to exhibit excellent passive stability (details about the oscillator are published elsewhere [149]). While it has been demonstrated that fiber oscillators can produce high quality frequency combs [150], pulse durations in the 100 fs range make it challenging to realize super continua with a high degree of coherence over a large spectral region [151], as the sensitivity of the broadening process to noise can lead to large spectral phase fluctuations [152]. Due to this consideration, care was taken to reach near transform-limited nJ-level pulses suitable for supercontinuum generation. The 152 MHz pulse train was amplified in a Yb-doped double-clad phosphosilicate fiber with 12 μm core diameter pumped at 976 nm. To avoid self-phase modulation and hence to minimize amplitude-to-phase noise conversion in the fiber amplifier, a linear

chirped-pulse amplification scheme was chosen, and it has been demonstrated that this amplification scheme is compatible with low-noise phase control [153, 154]. With fiber-based compensation for higher-order dispersion contributions, necessary to reach the Fourier-limit, the pulses could be recompressed to < 80 fs with a grating compressor as characterized by frequency resolved optical gating. After coupling the pulse train with a pulse energy of 1.2 nJ into a highly nonlinear suspended core fiber (SCF), the optical spectrum spanned from 570 nm up to 1.66 μm at the -30 dB-level as shown in Figure 2.9 (a).

We used the measured pulse energy coupled into the fiber, input spectrum, and fiber dispersion in our simulation from Section 2.3.1 (dashed red line in Figure 2.9(a)). The input pulses were modeled as unchirped hyperbolic secant pulses of 80 fs duration (full width at half maximum) with a center wavelength of 1050 nm. The nonlinear fiber used had a nonlinearity (γ) of about 40 $\mathrm{W^{-1}km^{-1}}$ and also an increased f_R, due to germanium doping, from the standard value of 0.18 for fused silica. We found that the simulated spectrum matched measured spectrum best for $f_R = 0.28$. The injected soliton order, N, was about 19.2. Because many of the input and fiber parameters were well known, the simulation was able to very accurately match the measured spectrum.

The measured beat notes are shown in Figures 2.9(b-d). Interestingly, we noticed a significant amount of amplitude noise in certain spectral regions, which was identified with the help of dual-balanced detection to cancel out common mode noise [155]. After balanced detection, we obtained beat notes at 698 nm and 1020 nm with a signal-to-noise ratio (SNR) of > 30 dB at 100 kHz RBW. As shown in Figures 2.9(b) and (c), the amplitude noise floor could be suppressed by up to 20 dB at 698 nm and 8 dB at 1020 nm by using dual-balanced detection compared to the measurement with a single detector. This observation supports the existence of comb amplitude noise without the presence of phase noise in these spectral regions. In other spectral regions (e.g. at 1540 nm) we observed that dual-balanced detection was not necessary to obtain a similar SNR (shown in Figure 2.9(d)). More than 30 dB SNR was also obtained for beat signals at 771 nm and for the $\nu - 2\nu$ heterodyne beat signal representing the carrier-envelope offset frequency, f_0. Self-referencing

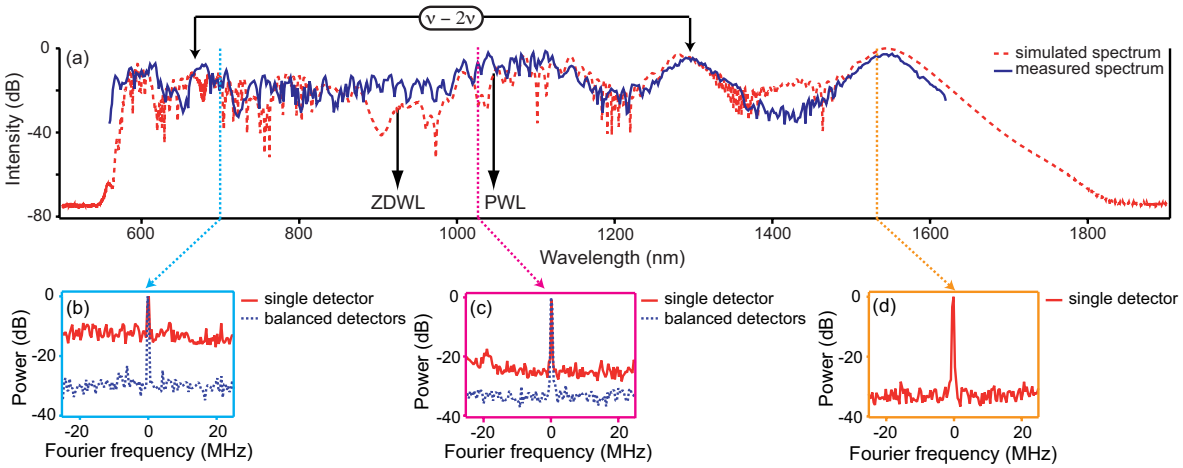

Figure 2.9: Coherent supercontinuum generation spanning over 1.5 octaves from a Yb:fiber laser. (a) Simulated (dashed) and measured (solid) super-continuum spectrum at the output of the suspended core fiber. The zero dispersion wavelength (ZDWL) and pump wavelength (PWL) are shown with arrows. (b) Beat at 698 nm with (dashed) and without (solid) balanced detection. Up to 20 dB suppression of the amplitude noise floor is observed. (c) Beat at 1020 nm with (dashed) and without (solid) balanced detection. (d) Beat at 1.5 μm without balanced detection, exhibiting a signal to noise ratio comparable to the balanced cases.

the comb was possible with $\nu = 1150$ nm to $\nu = 1300$ nm (and the corresponding second harmonic, 2ν) providing the freedom to detect other beat notes in this region.

The optical heterodyne beat signals help demonstrate that the free-running supercontinuum is coherent beyond the 1 μs time scale, permitting coherent beats with high SNR to be observed across the entire spectrum. In addition, a beat frequency between the self-referenced frequency comb stabilized to the Sr clock at 698 nm and a cavity-stabilized 1.54 μm cw laser was recorded for a long duration. By fitting the down-mixed beat signal with a chirped sinusoid, we deduce a coherence time of > 200 ms corresponding to $> 3 \times 10^7$ pulses from our 152 MHz pulse train [49].

In order to model quantum-limited supercontinuum coherence, we performed multiple simulations with a quantum shot-noise seed perturbing the input pulse, $A(t)$, such that $A(t) \rightarrow A(t) + \delta A(t)$. In this case, $\delta A(t)$ is described stochastically by $\langle \delta A^*(t)\, \delta A(t+\tau) \rangle = (h\nu/2)\delta(\tau)$ [156, 157], and we treat it as a Gaussian-distributed random variable in both quadratures. We also include the effects of spontaneous Raman scattering along the fiber according to the procedure of [156]. The first-order coherence, $g(\omega)$, defined as

$$g(\omega) = \frac{\left| \langle \tilde{A}_i(\omega)\, \tilde{A}_j^*(\omega) \rangle_{i \neq j} \right|}{\sqrt{\langle \left| \tilde{A}_i(\omega) \right|^2 \rangle \langle \left| \tilde{A}_j(\omega) \right|^2 \rangle}}, \tag{2.14}$$

was calculated numerically in 50-GHz spectral bins by an ensemble average of 100 independently simulated spectra [151]. Figure 2.10(a) shows $g(\omega)$ along with the calculated spectrum, and it can be seen that there are significant drops in the coherence in isolated spectral regions that still posses significant optical power. Another interesting note is that the coherence degrades smoothly across the first Raman soliton.

We also considered the different contributions to $g(\omega)$ arising from amplitude and phase noise separately by calculating the variance of the argument and amplitude of $\tilde{A}(\omega)$. As evident in Figure 2.10 (b), certain spectral regions feature decreased coherence arising from amplitude noise but exhibit only negligible phase noise contributions, which agrees with the experimental results. Previous experimental studies, where supercontinuum coherence was demonstrated by the use of a modified Young experiment with two sources, could not make such a clear distinction [158].

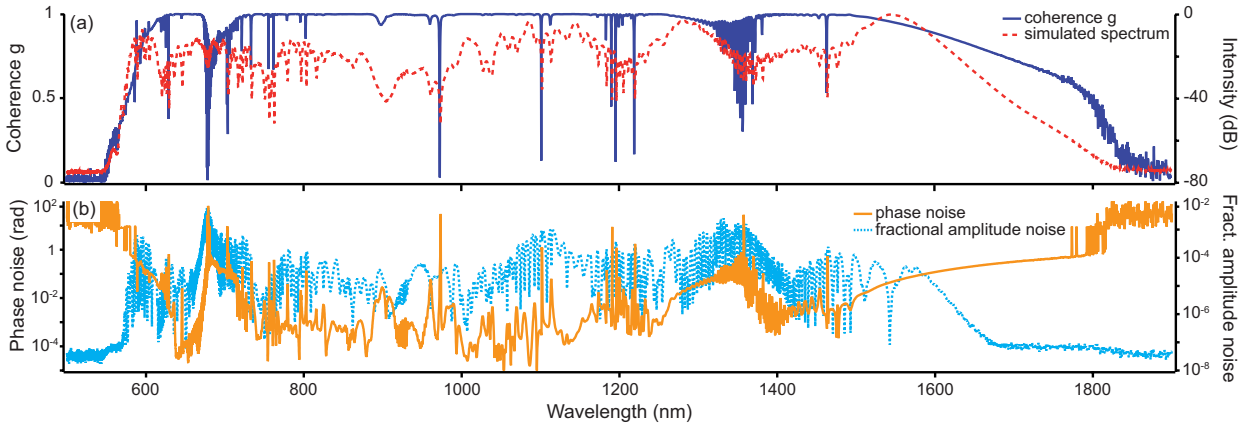

Figure 2.10: Simulation results for the optical spectrum and coherence properties after broadening in the suspended core fiber. (a) Simulated spectrum (dashed, right) and calculated quantum noise-limited pulse-to-pulse coherence (solid, left). There is a significant loss of coherence on the red side of the soliton as well as in narrow spectral regions throughout the spectrum. (b) Contributions of amplitude (dashed, right) and phase (solid, left) noise to the total coherence function. In many spectral regions, the presence of amplitude noise does not presage the presence of phase noise, indicating that degradation of $g(\omega)$ is not necessarily indicative of a loss of phase coherence. In particular, many of the narrow dips are related to amplitude noise, not phase noise.

Numerical simulations of up to 1000 pulses show that the total phase standard deviation does not change, indicating that that the quantum noise-induced phase deviation is bound at some level and is not a random walk, which would degrade relative linewidth. This is consistent with other tests of comb coherence that reach the same conclusion [159]. Supercontinuum generation can thus be seen as a white phase noise process without a random walk so there is no net accumulation of phase noise. This further confirms that the observed linewidth in the out-of-loop comparison was not compromised by the supercontinuum.

Numerically, we identified several parameters responsible for a significant loss of coherence. In particular, we sew a dependence on the fractional Raman contribution (f_R) that had not been studied previously. We calculated the average coherence of the first soliton (i.e., from 1450-1750 nm) and saw a decrease in coherence from 0.9 to 0.7 for f_R varying from 0.28 to 0.2 with the soliton center wavelength fixed by increasing the fiber length, as shown in Figure 2.11. The loss of coherence was most dramatic on the red side of the soliton and was caused primarily by increasing phase noise not amplitude noise. We also noticed reduced coherence with increasing pulse energy and with increasing pulse duration (both increase the soliton order) as has been observed previously [160]; however, we saw a coupling between these parameters and f_R that has not been noted previously. With a higher value of f_R, the coherence was significantly less sensitive to pulse duration (slight loss of coherence in the soliton at 120 fs) and energy than with low values of f_R, where we saw strong loss of coherence in the first soliton and also low coherence across the spectrum with 90 fs pulses. These results demonstrate that in addition to the complex interplay between soliton fission and modulation instability (lower soliton order results in rapid fission and higher coherence) there seems to be a competition between intrapulse stimulated Raman scattering (resulting in coherent red-shifting of the soliton) and amplification of noise (primarily on the red side) due to modulation instability as the fundamental soliton propagates. Overall, these simulations indicate that higher fractional Raman contribution (e.g., by higher Ge-doping) can be used as an additional tool for increasing the coherence of supercontinua, especially in cases where the pulse duration cannot be further decreased.

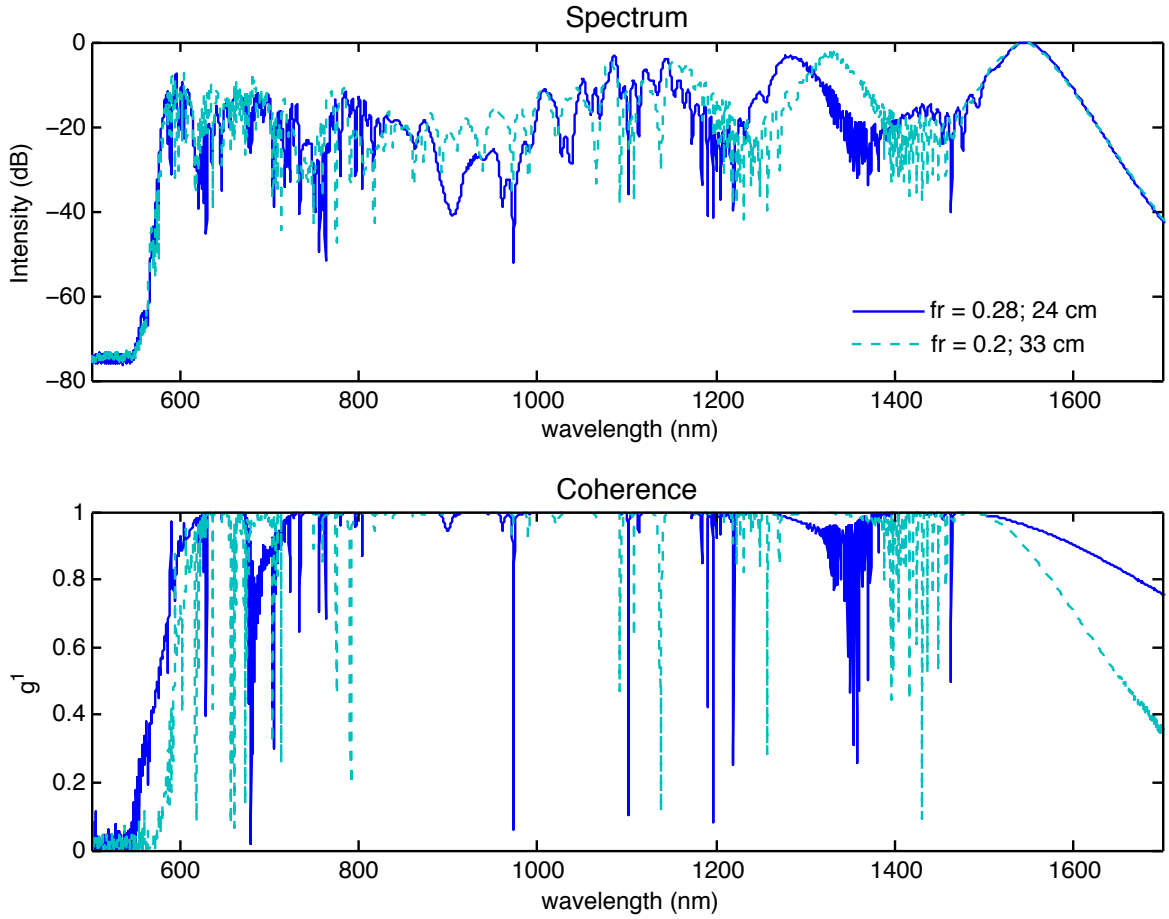

Figure 2.11: Simulations of the spectrum (top panel) and degree of coherence (bottom panel, defined in the text) for two different Raman fractions, $f_R = 0.28$ (solid blue) and $f_R = 0.2$ (dashed gray). The simulations are for a Yb:fiber laser pumping suspended core fiber as discussed in the text. The fiber length was chosen so that the soliton shift of the first soliton was the same in both spectra. The solition shows a significant loss of coherence on the red side of the spectrum; the loss of coherence is worse for a smaller value of f_R.

The simulated loss of coherence on the red side of the Raman soliton shown above was also observed in measurements using an Er:fiber laser. We used two branches of the same Er:fiber laser (one frequency shifted using an AOM) to pump a short piece of HNLF (for supercontinuum generation) and a long piece of polarization-maintaining fiber for Raman shifting. We then observed a spectrally-filtered beat note between the Raman soliton and the supercontinuum after a monochromator. When the Raman-shifting fiber was too long, there was a very noticeable, broadband increase in noise on the beat note, especially on the red side of the soliton (soliton center around 1800 nm). This was true even if the power was decreased so that the total soliton shift was also reduced (soliton center around 1700 nm); however, this was not observed for a shorter fiber length, which resulted in a soliton center of 1750 nm. We believe that the coherence degradation occurs as the RIFS slows down (e.g., above 1800 nm in Figure 2.4). This suggests that it should be possible to use a different Raman-shifting fiber (e.g., with higher Raman gain) or even splice together a combination of Raman-shifting fibers with progressively smaller core diameters to more rapidly shift to longer wavelengths. Preliminary results from R. Holzwarth and co-workers at Menlo Systems indicate that this is indeed the case and that coherent shifting beyond 1900 nm is possible using polarization-maintaining fiber for 1310 nm (OFS Truephase 1310 Sensor), which has a smaller core diameter.

The results of this section show that it is possible to use nonlinear fiber optics to generate coherent light in a variety of wavelength regions using fiber-based pump lasers. However, there can also be a loss of coherence in the nonlinear processes that must be considered. We have seen that numerical models are capable of reproducing many of the experimental results and provide more details into the broadening processes as well as potential issues with coherence.

2.4 Optical parametric oscillators

Two nonlinear systems are important for the generation of light in the mid-infrared: difference-frequency generation and optical parametric oscillators (OPOs). Since we desired a high-power mid-IR comb, we chose to use an OPO. An OPO uses parametric conversion inside of a resonator

to efficiently convert light from one wavelength (the pump, p) to two longer wavelengths (signal s and idler i). This process satisfies both energy conservation, $\omega_p = \omega_s + \omega_i$, and phase matching, $\Delta k = 0$ for maximum conversion efficiency. In a periodically-poled crystal, the phase matching is written as

$$\Delta k = 2\pi \left(\frac{n_p}{\lambda_p} - \frac{n_s}{\lambda_s} - \frac{n_i}{\lambda_i} - \frac{1}{\Lambda} \right), \tag{2.15}$$

where Λ is the poling period of the crystal. The theory of OPOs has been covered in many references [161, 83, 162], so we only reproduce the pertinent results here. If we assume that there is no pump depletion, we can obtain equations for the signal and idler fields (in MKS units) as a function of position, z:

$$\begin{aligned} \mathcal{E}_s(z) &= \left(\mathcal{E}_s(0) \left[\cosh(\Gamma z) + i \frac{\Delta k}{2\Gamma} \sinh(\Gamma z) \right] + i\kappa_s \mathcal{E}_i^*(0) \frac{\sinh(\Gamma z)}{\Gamma} \right) e^{-i\frac{\Delta k z}{2}} \\ \mathcal{E}_i(z) &= \left(\mathcal{E}_i(0) \left[\cosh(\Gamma z) + i \frac{\Delta k}{2\Gamma} \sinh(\Gamma z) \right] + i\kappa_i \mathcal{E}_s^*(0) \frac{\sinh(\Gamma z)}{\Gamma} \right) e^{-i\frac{\Delta k z}{2}}. \end{aligned} \tag{2.16}$$

Here $\Gamma = \sqrt{\kappa_s \kappa_i - \Delta k^2/4}$ is the gain per unit length with κ a coupling constant given by

$$\kappa_{s(i)} = \frac{\omega_{s(i)} d_{eff}}{n_{s(i)} c} \mathcal{E}_p(0), \tag{2.17}$$

where d_{eff} is the effective non-linear coefficient of the material (typically given in picometers per Volt, note that d_{eff} is reduced by a factor of about $\pi/4$ when using periodically-poled crystals). If we now enclose a crystal of length L in a cavity with total round-trip reflectivity of $R_{s(i)}$, the field after one round trip is $\mathcal{E}_{s(i)}(L) e^{i\phi_{s(i)}} R_{s(i)}$, including an additional phase shift due to propagation. To obtain the threshold for steady-state oscillation, these fields must equal $\mathcal{E}_{s(i)}(0)$. Assuming that $\Delta k = 0$ and that the phase shift is an integer multiple of 2π (due to cavity resonance), we can write this set of coupled equations as

$$\begin{bmatrix} \mathcal{E}_s(0) \\ \mathcal{E}_i^*(0) \end{bmatrix} = \mathbf{M} \begin{bmatrix} \mathcal{E}_s(0) \\ \mathcal{E}_i^*(0) \end{bmatrix}, \tag{2.18}$$

with

$$\mathbf{M} = \begin{bmatrix} \cosh(\Gamma L) R_s & i\kappa_s \frac{\sinh(\Gamma L)}{\Gamma} R_s \\ -i\kappa_i \frac{\sinh(\Gamma L)}{\Gamma} R_i & \cosh(\Gamma L) R_i \end{bmatrix}. \tag{2.19}$$

This means that $\mathbf{M}$ must have an eigenvalue of 1, so $\det|\mathbf{M}-\mathbf{I}|=0$ and finally

$$\begin{gathered}(R_s\cosh(\Gamma L)-1)(R_i\cosh(\Gamma L)-1)-R_sR_i\sinh^2(\Gamma L)=0\rightarrow\\ \cosh(\Gamma L)=\frac{1+R_sR_i}{R_s+R_i}=1+\frac{(1-R_i)(1-R_s)}{R_s+R_i}\end{gathered}\tag{2.20}$$

where we used the identity $\cosh^2(x)-\sinh^2(x)=1$. We can now expand $\cosh(\Gamma L)$ for small ΓL to arrive at the threshold condition

$$(\Gamma L)^2=\frac{2(1-R_i)(1-R_s)}{R_s+R_i}.\tag{2.21}$$

This also works for a singly-resonant OPO by taking $R_i\rightarrow 0$. Notice that a singly-resonant OPO will have a threshold that is higher by a factor of about $\frac{2}{1-R_i}$. Finally, we can substitute for Γ, and remembering that $I=nc\epsilon_0|\mathcal{E}|^2/2$, to find the threshold intensity for a singly-resonant OPO,

$$I_{th}^{ideal}=\frac{n_pn_sn_i\epsilon_0c^3}{2\omega_s\omega_id_{eff}^2L^2}\frac{2(1-R_s)}{R_s}.\tag{2.22}$$

This equation can be modified to account for both the spatial and temporal overlap of the pump and signal by replacing L with an effective interaction length L_{eff} and including coupling factors g_s (spatial) and g_t (temporal) [163, 164]

$$I_{th}=\frac{n_pn_sn_i\epsilon_0c^3}{2\omega_s\omega_id_{eff}^2L_{eff}^2g_sg_t}\frac{2(1-R_s)}{R_s}.\tag{2.23}$$

The coupling factors, assuming ideal Gaussian spatial and temporal beams, are given by

$$g_t=\sqrt{\frac{\tau_p^2}{\tau_s^2+\tau_p^2}}\text{ and}\tag{2.24a}$$

$$g_s=\frac{w_p^2}{w_s^2+w_p^2}.\tag{2.24b}$$

Here $\tau_{s(p)}=T_{s(p)}/\sqrt{2\ln 2}$ is the pulse duration for the signal (pump) pulses with FWHM intensity duration $T_{s(p)}$ and $w_{s(p)}$ is the beam radius for the signal (pump). The effective gain length is

$$L_{eff}=L_t\text{erf}\left(\frac{\pi L_c}{2L_t}\right),\tag{2.25}$$

where L_c is the crystal length and

$$L_t=\frac{\sqrt{\pi}}{2}\left[\left(\frac{\delta v_s^2}{\tau_s^2}\right)+\delta v_i^2\left(\frac{1}{\tau_s^2}+\frac{1}{\tau_p^2}\right)-\frac{\left(\frac{\delta v_s^2}{\tau_s^2}\right)+\delta v_i^2\left(\frac{1}{\tau_s^2}+\frac{1}{\tau_p^2}\right)}{2\left(\frac{1}{\tau_s^2}+\frac{1}{\tau_p^2}\right)}\right]^{-1/2}\tag{2.26}$$

is the temporal overlap length. Here $\delta v_{s(i)} = \frac{n^g_{s(i)}}{c} - \frac{n^g_p}{c}$ is the group delay walk-off for the signal (idler) in (velocity)$^{-1}$. The group velocity is given by $\frac{c}{n^g}$ and $n^g = n - \lambda\frac{dn}{d\lambda}$ is the group index. Equation 2.26 simplifies to $L_t \approx \frac{\tau_s}{\delta v_s}$ for short signal pulse durations.

The phases of the pump, signal, and idler fields are related to each other by $\phi_p - \phi_s - \phi_i = -\pi/2$. If we take the time derivative of both sides, we find that $\dot{\phi_p} = \dot{\phi_s} + \dot{\phi_i}$. This expression can also be interpreted as a conservation of energy. Since $\dot{\phi} \sim f_0$, we arrive at a useful relationship

$$f_0^p = f_0^s + f_0^i. \tag{2.27}$$

In order to extend frequency comb spectroscopy to the mid-IR, we built a synchronously-pumped OPO based on a fan-out periodically-poled lithium niobate (PPLN) crystal that covers the 2.8 μm to 4.8 μm spectral region [50], a schematic of which is shown in Figure 2.12(a). The main part of the OPO consists of a five-mirror linear cavity that is singly resonant for the signal. We chose this cavity design because we wanted to have a small retro-reflecting mirror to provide easy cavity-length adjustment (to match the cavity length to the comb f_{rep}) and fast feedback bandwidth to the cavity length with a high-speed PZT. The mirror M4 was added so that there was the option of two output couplers (M1 and M4) and to reduce the overall footprint. M2 and M3 both have a 20-cm radius-of-curvature and are spaced by 20.5 cm. A summary of the cavity mirror coatings in given in Table 2.1.

We can calculate the intracavity mode using ABCD matrices [165, 166]. The beam waist, ω(z), at a given position, z, is given by

$$-Im(q) = \frac{\lambda}{\pi\omega^2(z)} = \frac{1}{B}\sqrt{1 - \left(\frac{A+D}{2}\right)^2} \tag{2.28}$$

where λ is the wavelength of the light. The beam radius of curvature, $R(z)$, is given by

$$Re(q) = \frac{1}{R(z)} = \frac{D-A}{2B}. \tag{2.29}$$

In order to find the q-parameter, the ABCD matrix can be calculated by using the propagation through a medium with index of refraction n with length d, $\begin{pmatrix} 1 & \frac{d}{n} \\ 0 & 1 \end{pmatrix}$, and the reflection from a

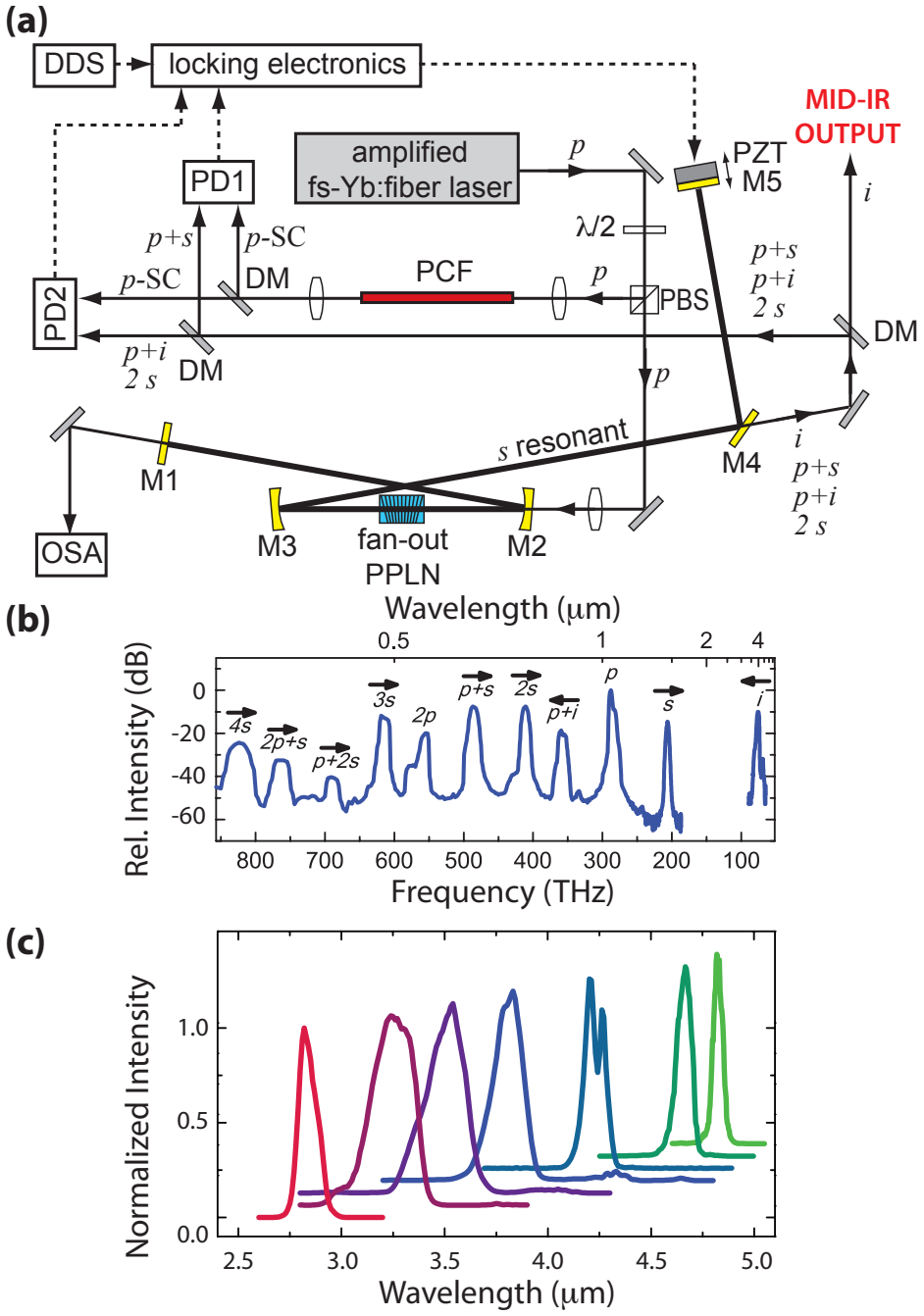

Figure 2.12: Mid-infrared OPO comb based on periodically-poled lithium niobate (PPLN). (a) Schematic of the optics layout, see text for details. p, s, and i indicate pump, signal and idler respectively; M1-M5 (yellow) are the OPO cavity mirrors; DM is dichroic mirror; PD1 and PD2 are photodiodes; PCF is a photonic crystal fiber for pump supercontinuum (p-SC) generation; OSA is an optical spectrum analyzer. (b) A composite spectrum of all outputs (wavelengths shorter than 2 μm were recorded on the OSA, the idler output was measured using a scanning monochromator). Arrows above each peak indicate the tuning direction, labels give the assignment. (c) Individually normalized idler spectra recorded using the scanning monochromator for different crystal positions.

spherical mirror with curvature R, $\begin{pmatrix} 1 & 0 \\ -\frac{2}{R} & 1 \end{pmatrix}$ (in this definition, R is positive for a concave mirror and negative for a convex mirror). The ABCD matrix for the focus between the two curved mirrors, assuming that the center of the crystal is at the focus, is given by:

$$\begin{pmatrix} A & B \\ C & D \end{pmatrix} = \begin{pmatrix} 1 & \frac{L_c}{2n} \\ 0 & 1 \end{pmatrix} \begin{pmatrix} 1 & \frac{L_{2-3}-L_c}{2} \\ 0 & 1 \end{pmatrix} \begin{pmatrix} 1 & 0 \\ \frac{-2}{R} & \end{pmatrix} \begin{pmatrix} 1 & 2L_{2-5}-t \\ 0 & 1 \end{pmatrix}$$
$$\begin{pmatrix} 1 & L_{2-3}-L_c+\frac{L_c}{n} \\ 0 & 1 \end{pmatrix} \begin{pmatrix} 1 & 0 \\ \frac{-2}{R} & \end{pmatrix} \begin{pmatrix} 1 & 2L_{1-3}-t \\ 0 & 1 \end{pmatrix} \begin{pmatrix} 1 & \frac{L_{2-3}-L_c}{2} \\ 0 & 1 \end{pmatrix} \begin{pmatrix} 1 & \frac{L_c}{2n} \\ 0 & 1 \end{pmatrix}.$$

Here L_{a-b} is the length between mirrors Ma and Mb and L_c is the length of the crystal (7 mm). This gives an expected waist of 55 μm.

The OPO is pumped with an amplified Yb:fiber comb (f_{rep} = 136 MHz, 10 W average power, ~100 fs pulse duration) coupled into the cavity through M2 (designed with $T > 97\%$ at the pump wavelength). The MgO-doped PPLN crystal (HC Photonics) is 1 mm high, 10 mm wide, and 7 mm long and has a poling period that varies from 25.5 to 32.5 μm across the width. In order to reduce losses and lower the threshold, the crystal is AR coated for the signal ($R < 3\%$ from 1400-1900 nm) as well as for the pump ($R < 1\%$ at 1080 nm). The crystal is heated to 71 °C to reduce potential photo-refractive damage from the high intensity pump. We hold the crystal in a U-shaped copper mount with indium foil above and below the crystal. The crystal is held in place with a top plate that bolts to both sides of the U mount, see Figure 2.13. The pump laser is focused with a 150 mm lens to a beam waist of ~100 μm. This gives a Rayleigh range of ~3.7 cm, so the length of the crystal is short compared to the Rayleigh range.

The poling period of the crystal was chosen so that the idler covers approximately 3-5 μm. Figure 2.14(a) shows the calculated gain profile (i.e., Γ) as a function of poling period, which was used to determine the correct poling period. The phase matching was calculated using the Sellmeier coefficients for the index of refraction from [167]. The gain and bandwidth both increase as the poling approaches degeneracy (i.e., signal and idler wavelengths both equal to twice the pump

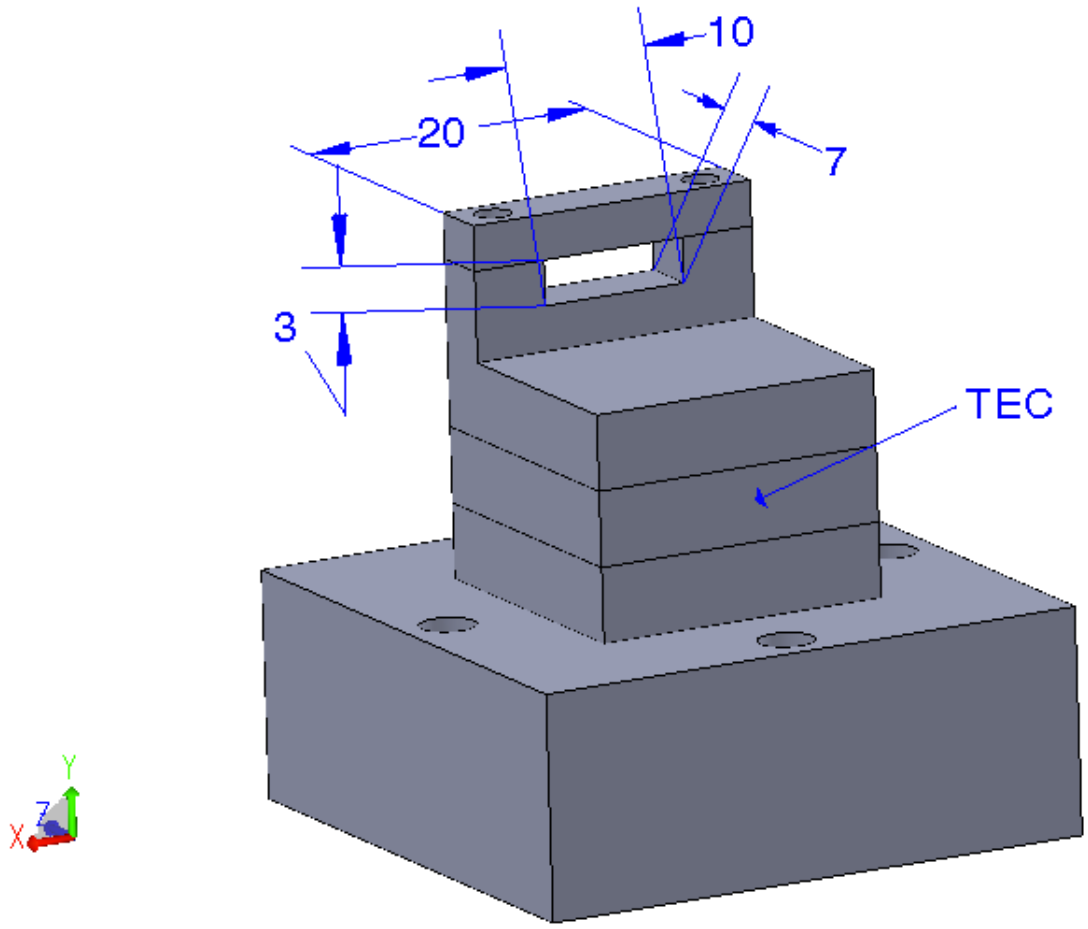

Figure 2.13: OPO crystal holder. A thermo-electric cooler (TEC) is used to heat the crystal. The crystal is clamped in place between two sheets of indium foil. Marked dimension are in mm.

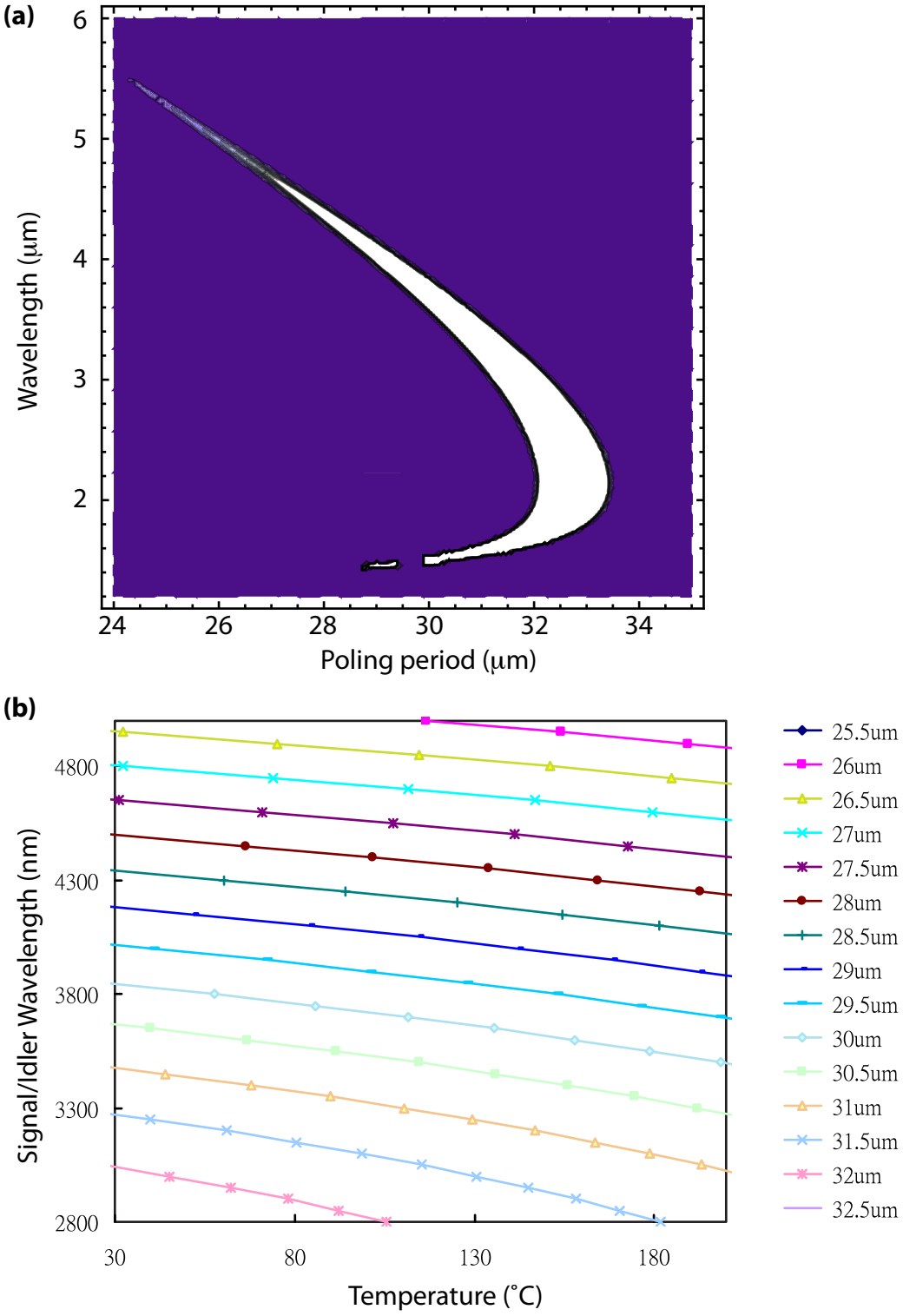

Figure 2.14: Calculations for PPLN OPO. (a) Calculated gain profile as a function of poling period (white is higher gain). The gain and bandwidth both increase as the poling approaches degeneracy (i.e., signal and idler wavelengths both equal to twice the pump wavelength). (b) Phase matching curves provided by HC Photonics for different poling periods as a function of temperature.

Table 2.1: Mirror coatings for OPO

Mirror	Coating	R for signal	Dispersion
M1,3,5	HR signal, GVD optimized	$R > 99.9\%$	$0 \rightarrow -600$ fs^2 1400-1600 nm
			$-600 \rightarrow -100$ fs^2 1600-1800 nm
M2	1064-nm enhanced silver	$\sim$98%	Unknown (assume $\sim$0?)
M4	Output coupler	$R_s \sim 99.9\%$	Unknown
Xtal	AR pump/signal/idler	$R_{s,i} < 3\%$, $R_p < 1\%$	Unknown

wavelength). The temperature dependence of the phase matching is shown in Figure 2.14(b), which was provided by HC Photonics.

Rough alignment of the OPO cavity was accomplished with a 1.55 μm laser coupled in through M1. In addition, a significant amount of doubled pump light is produced in the crystal; this green light can also be used to align the cavity by using it to overlap the retro-reflection from mirrors M1 and M5 and by optimizing the contrast of the observed fringes while scanning the cavity length. Since the green light has the same repetition rate as the pump laser, it can be used to tune the length of the OPO cavity to match the repetition rate by maximizing the fringes. Due to the different index-of-refraction for green versus the signal wavelength, the cavity length needs to be adjusted from the optimum position for the green fringes. Also, care must be taken in the alignment as there are multiple sets of green light fringes caused by various stray reflections. After the alignment is optimized, the pump-laser power can be increased and the cavity length scanned until idler light is observed. Figure 2.15(a) shows the measured output power and photon conversion efficiency as a function of crystal position (i.e., output wavelength) with 8.47 W of pump power. The output power is over 1 W from 3 μm to 4 μm. The normalized output spectrum measured using a scanning monochromator for different crystal positions (corresponding to different idler wavelengths) is shown in Figure 2.12(c). We obtain a simultaneous bandwidth (FWHM) of up to 0.3 μm (300 cm^{-1}).

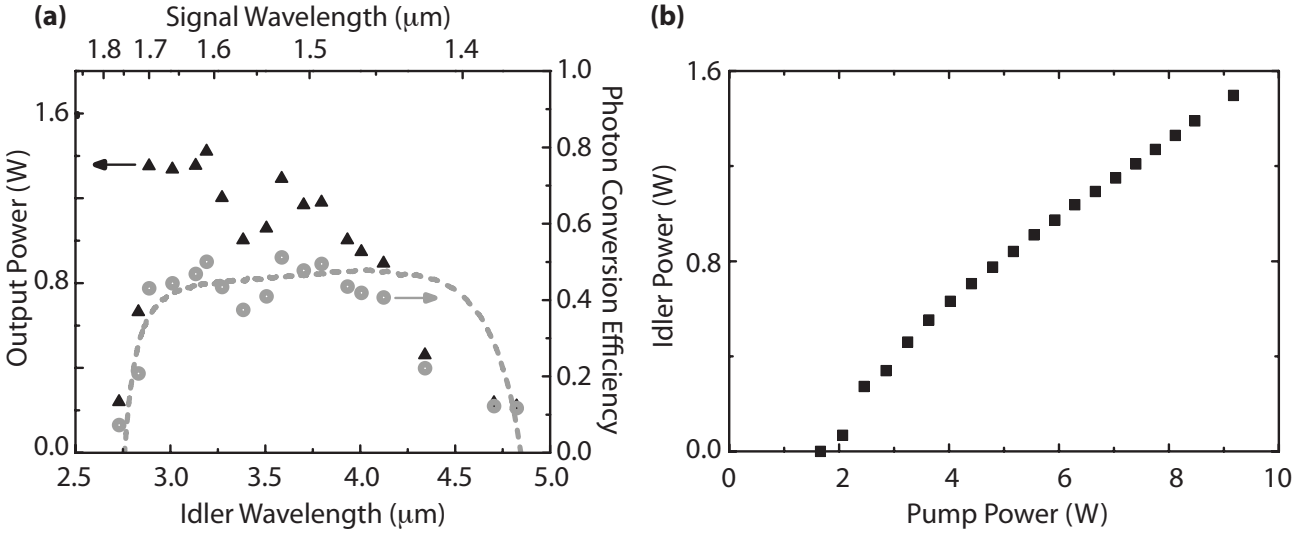

Figure 2.15: OPO performance. (a) Measured output power (black triangles, left axis) and photon conversion efficiency calculated from output power (grey circles, right axis) as function of idler wavelength. The output power peaks at almost 1.5 W near 3 μm. The grey dashed line shows the trend expected from the cavity mirror reflectivity (max level adjusted to match the data). (b) Idler power versus pump power, measured at $\lambda_{\text{idler}} = 3.01$ μm. This gives a threshold of 1.7 W and an initial slope efficiency of 0.29.

To determine the threshold, we measured the output power at 3.01 μm as a function of pump power as shown in Figure 2.15(b). This gives a threshold of 1.7 W and an initial slope efficiency of 0.29. The slope efficiency drops to 0.16 at about 4 W, which we attribute to the onset of an additional (unknown) conversion process; after this, however, we see no further signs of nonlinear losses up to 9.17 W of pump power (yielding an output power of 1.5 W). We estimate the threshold using Equation 2.23 to be $\sim$1.7 W using reasonable parameters. The effective nonlinear coefficient for PPLN is around 14 pm/V [168]. We assume that the pump pulse duration (FWHM) is 120 fs and the signal duration is 200 fs. This duration assumed some uncompensated dispersion in the cavity. Since $L_t = 1.4$ mm (from Equation 2.26) is significantly shorter than the crystal length, the effective interacting length is entirely limited by L_t. This means that a shorter signal pulse duration actually results in an increased threshold.

Now that we can generate mid-infrared light from a synchronously pumped OPO, we want to turn this into a frequency comb, which means that we need to be able to control both f_0 and f_{rep}. Since the OPO is synchronously pumped, f_{rep} is set by the pump laser. There is not an easy way to control f_0^i directly without an additional reference laser in the mid-IR; however, we can make use of Equation 2.27 and control both f_0^p and f_0^s. In order to do this, we need feedback signals for both f_0^p and f_0^s. Luckily, in addition to the signal and idler light, the OPO produces a variety of other colors due to various non-phase-matched conversion processes. Figure 2.12(b) shows an output spectrum from M1 measured with an optical spectrum analyzer, plus the idler spectrum measured with a monochromator. The arrows indicate the relative tuning direction of the corresponding peak, which was essential for identification. Of particular interest are the peaks originating from pump plus signal ($p+s$) and pump plus idler ($p+i$): if we form the beatnote between each of these signals and broadened pump light, we obtain f_0^p and f_0^s. We do this by picking off about 400 mW of pump power before the OPO and sending this to a nonlinear fiber for spectral broadening (see Figure 2.3). This pump supercontinuum (p-SC) is overlapped both spatially and temporally in two separate interferometers with $p+i$ and $p+s$ out of M4 using dichroic mirrors and delay stages. We were able to obtain a high signal-to-noise beatnote on the $p+s$ arm, but have not been able to get

similar results for $p+i$, probably due to the difficulty in broadening with low noise in the spectral region from 700-900 nm as discussed in Section 2.3. We have not implemented balanced detection, which would help reduce amplitude noise from the broadening (see Figure 2.9). However, we can stabilize f_0^p separately with either an f-2f interferometer or an optical lock to a stable cw laser.

Feedback to f_0^s is accomplished by tuning the OPO cavity length via a PZT on M5 since f_0 depends on $\Delta\phi_{CE}$ which in turn depends on the cavity length according to Equation 2.1. To test our ability to stabilize the idler, we compared the idler to a narrow-linewidth cw laser as shown in Figure 2.16. Since we do not have such a laser in the mid-IR, we tuned the idler to 3.09 μm and doubled it using a thin GaSe crystal to 1.545 μm. We could then form a beat note between one doubled idler mode and a $<$ 10 kHz linewidth RIO diode laser. In this test, f_{rep} of the pump was locked with an optical lock to a stable 1.064 μm non-planar ring oscillator (NPRO) laser via feedback to the cavity length (Figure 2.16(a)); since we only wanted to check the idler short-term linewidth, f_0^p was stable enough and was left free running. Interestingly, with the idler at 3.09 μm we observe a beat note between the spectrally overlapping $p+i$ and $2s$, which gives a rf signal at $2f_0^i - f_0^s$. We used this signal to stabilize the OPO cavity length (Figure 2.16(b)). After locking the OPO cavity we see a stable beat note between $2i$ and the RIO (Figure 2.16(c), black versus gray) with a linewidth (at -3 dBc) of 80 kHz, which corresponds to an idler linewidth of 40 kHz in the mid-IR. The pedestal on the beat note is consistent with the servo bumps on the f_{rep} lock. In this test, the idler linewidth was limited by the feedback bandwidth to the OPO cavity length PZT. By fully stabilizing the pump laser and replacing the OPO cavity PZT with a high bandwidth PZT/mirror on a bullet mount [169], we have obtained an idler linewidth of 10 kHz (measured using a high-finesse cavity).

The development of this OPO comb demonstrated the ability to extend frequency comb technology to the mid-infrared, which has enabled high-resolution spectroscopy in the spectral region containing the OH and CH fundamental vibrational modes of many molecules. When originally developed, this source was, to our knowledge, the first fully-stabilized mid-IR frequency comb and also the highest power comb in the mid-IR. Several applications are discussed in the next two

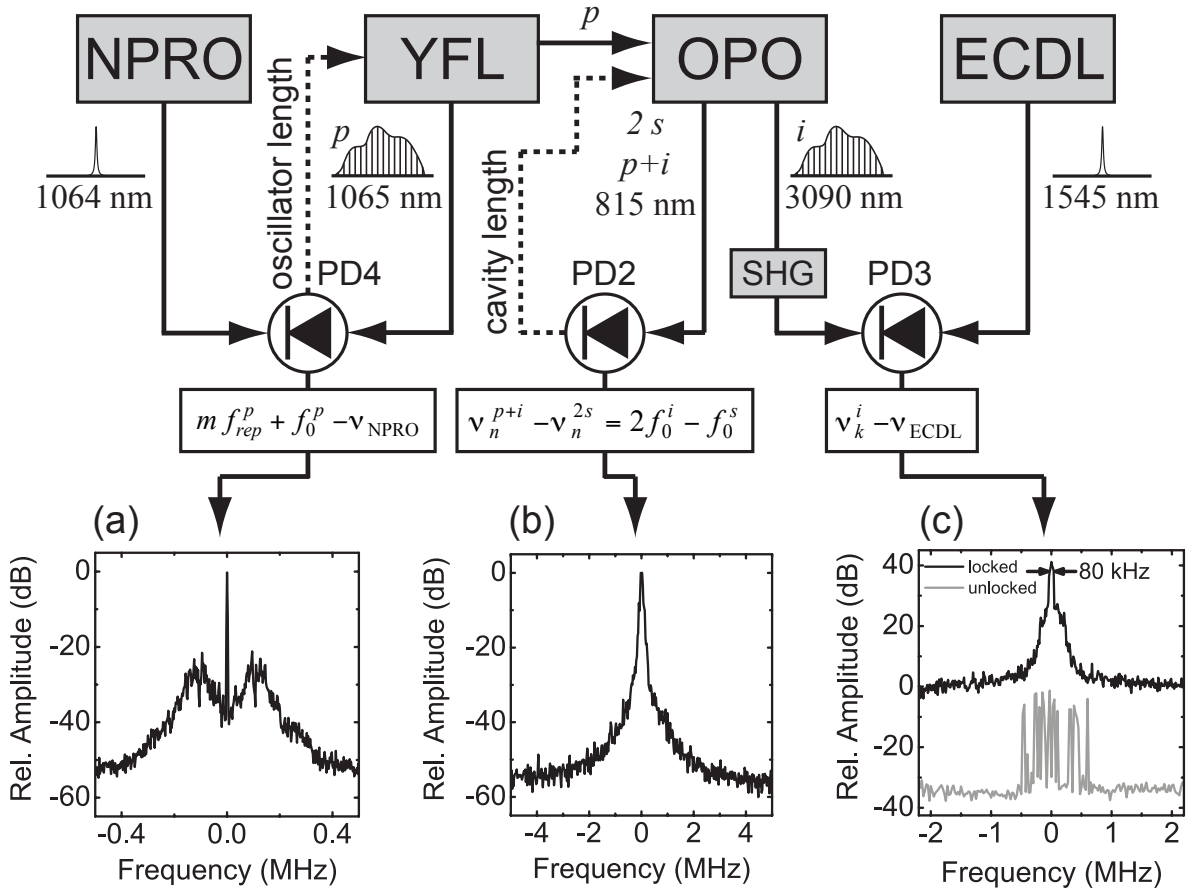

Figure 2.16: Experimental setup and rf signals for stabilization of the OPO and measurement of the idler-comb linewidth. NPRO, non-planar ring oscillator; YFL, Yb:fiber pump laser; ECDL, external-cavity diode laser; PD2-PD4, photodiodes; SHG, second-harmonic generation crystal (GaSe). (a) In-loop signal for stabilization of f_{rep}, 1 kHz RBW. (b) In-loop signal for stabilization of $2f_0^i - f_0^s$, 3 kHz RBW. (c) Out-of-loop beat note between $2i$ and ECDL, with OPO cavity length unlocked (gray; 0.5 s sweep time; 10 kHz RBW) and locked (black; 2 s sweep time, 3 kHz RBW); the traces are offset vertically for clarity.

chapters as well as in [170, 72, 55, 47, 56]. Furthermore, the same basic design can be used with a Tm:fiber laser pump and OP-GaAs to create high-power frequency combs out to 10 μm and beyond.

Chapter 3

Detection techniques

In addition to a comb source operating in the desired spectral region, every comb spectroscopy system needs a detection system for readout. For high sensitivity, we often use an optical cavity to increase the effective path length. We first discuss some details about coupling the frequency comb to the cavity. Then we cover different detection techniques. Finally, in addition to spectroscopy of neutral species, one may want to study the spectra of ions. This was motivated by the search for the electric dipole moment of the electron using molecular ions (Chapter 6). For this, we have developed a frequency comb velocity-modulation spectroscopy system, as described in Section 3.4.

3.1 Cavity-comb coupling

Efficient coupling of the comb light into the cavity is possible because the spectrum of Fabry-Perot cavity resonance modes and that of the comb are similar in structure. However, while the comb-line spacing is constant, the frequencies of the optical cavity resonances are separated from each other by a frequency-dependent free spectral range (FSR), given by

$$FSR(\omega_0) = \frac{c}{2L + \frac{\partial\phi}{\partial\omega}|_{\omega_0}} \tag{3.1}$$

where c is speed of light, L is the length of the cavity, and $\frac{\partial\phi}{\partial\omega}$ represents the intra-cavity dispersion, originating mostly from the cavity mirror coatings and intracavity absorption. This dispersion term means that the separation of consecutive cavity resonant modes is approximately constant only in a limited frequency range. Thus, some care must be taken to minimize the cavity dispersion at

the spectral region of interest, typically by operating as close as possible to the maximum of the mirror reflectivity. In addition, the dispersion is typically reduced for coatings that have a broader bandwidth.

The spectral range of most current CE-DFCS systems is limited by the bandwidth of the optical cavities. Several possibilities exist for increasing the bandwidth while maintain high reflectivity. One possibility is the use of total internal reflection in Brewster angle prism retroreflectors [171]. Cavities using fused silica prisms can provide a finesse of over 100,000 throughout the near-infrared, but such a system has yet to be combined with CE-DFCS. The dispersion of prism cavities is significantly worse than standard optical coatings – except near the zero-dispersion wavelength of the prism material; however, this can be mitigated by dithering the comb (see below). In addition, the choice of prism material is critical for high finesse. Our first attempts to use prism cavity in the near-infrared were limited by water absorption in the prism material. This, along with the difficulty of fabricating prisms from different materials, makes prism cavities challenging to implement in other wavelength regions. Recently, a CaF_2 prism cavity with 99.77% reflectivity at 250 nm and 99.96% reflectivity at 500 nm was demonstrated [172]. For the mid-infrared, BaF_2 would be a good candidate material [171], as could the infrared material KRS-5, which can be low loss [173] (unfortunately, it is challenging to find a manufacturer for KRS-5 prisms). Another interesting possibility, especially in the mid-infrared, are semi-conductor optical coatings, which can have extremely high index contrast and thus very large bandwidth. For example, reflectivities of 99-99.7% have been demonstrated with three layer pairs of EuTe/PbTe or PbEuTe/BaF_2 [174, 175] and even higher reflectivity should be possible (although the losses are currently unknown). Other semiconductor coatings – in this case crystalline GaAs/AlGaAs – have recently been shown to have very high finesse [176] and are promising for low-loss mid-infrared coatings (potentially 10 ppm near 3 μm). These two semiconductor coating technologies could potentially be combined to produce low-loss, extremely broad bandwidth mid-infrared coatings.

In order to maximize the comb-cavity coupling, the comb needs to be spatially mode-matched to the cavity [166, 165]. In addition, both f_{rep} and f_0 of the comb need to be matched to the cavity

FSR and f_0 at the wavelength of interest [45, 46, 47]. Once f_{rep} and f_0 are optimized, these values must also be maintained over an extended period of time. This can be achieved in two different ways: by tightly locking the comb and cavity modes in order to ensure a constant transmission through the cavity, or by modulation of either one of the comb parameters or the cavity FSR so that laser light is periodically coupled into the laser cavity (the swept coupling scheme). Each of these schemes has advantages and limitations as explained below.

3.1.1 Tight locking scheme

In the tight locking scheme the match between the comb modes and cavity resonances is actively maintained with high-bandwidth feedback. The error signal for stabilization can be generated with the Pound-Drever-Hall (PDH) [177] method, the Hänsch-Couillaud method [178], or with a dither lock, where the comb modes are dithered around the cavity modes (or vice-versa) with amplitude smaller or comparable to the full width half maximum (FWHM) cavity linewidth.

One way to achieve a tight lock is to stabilize the two degrees of freedom of the frequency comb to an external frequency reference and to implement a feedback loop that actively controls the cavity FSR to match it to f_{rep}. A difficulty arises from the fact that for different cavity conditions (e.g. when the pressure in the cavity changes) the optimum comb f_0 takes different values, so the locking electronics must be able to follow these changes. Another limitation arises from the fact that the length of linear cavities is often controlled with a large-travel-range PZT. This, combined with the large mass of the cavity mirrors, results in a PZT response bandwidth usually limited to a few hundred Hz, which is not enough to remove fast (acoustic) frequency noise, although in principle this can be addressed by designing a cavity that can accommodate a lower mass mirror.

An alternative scheme is to lock the comb to the resonances of the enhancement cavity by stabilizing the two degrees of freedom of the comb with two servo loops – one for f_{rep} and another for f_0. The error signals for each of the feedback loops are derived from different parts of the cavity reflection spectrum [179]. This can be accomplished by applying a modified PDH detection scheme, using separate photodiodes to detect different parts of the reflected laser spectrum after

diffraction from a grating. A detection scheme using three photodiodes was implemented in [179]: here the PDH error signal from the center of the transmission spectrum was used to control f_{rep} and the difference between two error signals from opposite ends of the transmission bandwidth was used to control f_0. A similar setup using only two error signals based on cavity reflection was used in later experiments in the near-IR near 1550 nm [54, 72] and mid-IR near 3800 nm [55]. In the near-IR, an Er:fiber comb spanning 1510 to 1610 nm was tightly locked to an enhancement cavity with a finesse of 8000 with a transmission bandwidth of 50 nm centered at 1530 nm, limited by the dispersion of the dielectric mirror coatings, which were designed for peak reflectivity at 1600 nm. The limiting effect of cavity dispersion is seen in the mid-IR system, where the simultaneously coupled bandwidth is reduced from 150 nm at 3750 nm (near the center of the 3800 finesse cavity) to around 75 nm at 3900 nm. A single-point lock in the same system provides a bandwidth of around 20 nm. By comparing the single-point lock to the two-point lock, it is also possible to determine the cavity dispersion [55].

The two-point locking scheme enables broadband, tight locking of the comb to the cavity resonances, maximizing the enhancement factor and providing constant, high-power signal in cavity transmission. It can therefore be efficiently combined with Fourier-transform-based detection methods. On the other hand, this scheme requires more complicated locking electronics compared to the swept coupling scheme and also requires higher bandwidth servo actuators in the laser systems. Moreover, residual frequency noise in the laser is translated into amplitude noise (FM-to-AM conversion) by the cavity resonances. This FM-to-AM noise conversion is often the primary source of noise in cavity-enhanced comb spectroscopy, and much effort has gone in to reducing it by frequency modulation [180], balanced detection (see Section 3.3.2), or laser dither as in the swept coupling scheme.

3.1.2 Swept coupling scheme

In addition to noise from FM-to-AM conversion, the walk-off between the comb lines and the cavity modes due to dispersion in the mirror coatings typically limits the spectral bandwidth

that can be achieved for most of CE-DFCS experiments with the tight comb-cavity lock. The bandwidth limitation is more severe when a higher finesse cavity is used, resulting in a compromise between the sensitivity enhancement factor and the simultaneously usable spectral bandwidth. The negative effects caused by cavity dispersion can be reduced by special low-dispersion cavity designs. Alternatively, the swept coupling scheme allows the entire spectral bandwidth of a comb to be transmitted through the cavity [181, 44]. In this case, the comb modes are periodically swept across the cavity modes (or vice versa) with the amplitude of the sweep larger than the FWHM linewidth of the cavity resonance (in contrast to a dither lock), resulting in periodic transmission peaks. By stabilizing the time interval between the transmission peaks (with feedback to either the comb or the cavity), it is possible to eliminate slow drifts between the cavity and comb modes. The dispersion problem is largely avoided as the corresponding mode pairs come into resonance rapidly one after another, thus when averaging over a sweep, the full bandwidth of the source spectrum is transmitted. In addition, the required bandwidth of locking electronics is much lower than in the tight locking scheme, since low-bandwidth feedback is sufficient to stabilize the positions of transmission peaks.

The main disadvantage of this method is a reduction of the useful experimental duty cycle and transmitted power arising from the limited time over which the comb modes are on resonance with the cavity. A more subtle effect is connected with the enhancement factor of the absorption signal. The enhancement of the interaction length is related to the cavity finesse, F, which is proportional to the inverse of the cavity losses. For fast sweeps, the time that the comb lines spend on resonance becomes only a fraction of the cavity lifetime. This results in an enhancement factor that is closer to F/π for rapid sweeps instead of $2F/\pi$ for the tight locking case [44], which decreases the absorption sensitivity assuming the same fractional noise levels. The fact that the enhancement factor is dependent on the sweep parameters implies that a calibration of the effective length enhancement can be necessary for intermediate sweep speeds, although this is not absolutely necessary for higher sweep speeds as the enhancement factor approaches F/π. While the swept coupling scheme can be relatively easily combined with Fourier-transform-based detection methods,

the performance is worse than with a tight lock [182], due to the fact that the amplitude modulation of the transmission signal leads to a disturbance of the detected interference signals.

The swept cavity-comb coupling scheme has been used in a variety of experiments [44, 46], including in the arsine spectroscopy experiment discussed in Section 4.1, and its robustness and reliability has been demonstrated by its application for trace gas detection in the north coast of France [183] and in the Antarctic [184]. Amplitude noise reduction down to the shot-noise level has also been demonstrated [185]; however, the transmitted power is still very low.

3.2 Detection sensitivity

Before we discuss detection methods in more detail, we should first provide a background for comparing systems. The sensitivity of a detection system can be determined from the relative noise, σ, on the baseline of the spectrum. The minimum detectable absorption coefficient can be defined as

$$\alpha_{min}[\mathrm{cm}^{-1}] = \frac{\sigma}{L_{eff}}, \tag{3.2}$$

where L_{eff} is the effective interaction path length with the sample. For a tight comb-cavity lock, L_{eff} is equal to $2FL/\pi$, where L is the physical cavity length (assuming a linear cavity with the entire length used for absorption); in the case of cavity ringdown, L_{eff} is reduced to FL/π. In intermediate cases, i.e., for the swept coupling scheme, L_{eff} takes a value between those two limiting cases [44]. When the system is white noise limited, σ averages down with the square-root of the integration time, so the minimum detectable absorption coefficient normalized to 1 s acquisition time is used for comparison between systems:

$$\alpha_{min}^{1\mathrm{s}}[\mathrm{cm}^{-1}\mathrm{Hz}^{-1/2}] = \frac{\sigma}{L_{eff}}\sqrt{T}, \tag{3.3}$$

where T is the acquisition time of the spectrum. Note that this formula is valid only if the system is white noise limited on the scale of a second or longer. For broadband systems such as DFCS, a figure-of-merit including the number of simultaneously resolved spectral elements, M, can be used

[170, 186]. This absorption sensitivity per spectral element, $\alpha_{min}^{\text{1s, DFCS}}$, is defined as

$$\alpha_{min}^{\text{1s, DFCS}}[\text{cm}^{-1}\text{Hz}^{-1/2}] = \frac{\sigma}{L_{eff}}\sqrt{\frac{T}{M}}. \tag{3.4}$$

This value can be interpreted as the performance in terms of absorption sensitivity that a cw-laser system would need, including scanning time, to match the performance of the broadband system.

The fundamental limit to the sensitivity in an absorption measurement is shot-noise in the laser probe [41]. For a laser power, P, the shot-noise level is given by

$$\sigma = \sqrt{\frac{2eB}{\eta P}}, \tag{3.5}$$

where B is the detection bandwidth, η is the photodiode response, and L_{eff} is the effective path length. Frequently, $B = 1/T$ for a measurement time of T. This gives a shot-noise limited absorption sensitivity of

$$\alpha_{min}^{\text{1s, shot}}[\text{cm}^{-1}\text{Hz}^{-1/2}] = \sqrt{\frac{2e}{\eta P}}\frac{1}{L_{eff}}. \tag{3.6}$$

For shot-noise limited CE-DFCS [54], we substitute $P \approx P/N$, where N is the number of spectral elements in the entire comb spectrum, so P/N is the approximate power per spectral element. Normalizing to the number of spectral elements in the acquired spectrum, M, according to Equation 3.4, we have

$$\alpha_{min}^{\text{1s, shot, DFCS}} = \sqrt{\frac{2eN}{\eta PM}}\frac{\pi}{kFL}, \tag{3.7}$$

where k is a factor ranging from 1-2 depending on the coupling scheme (see Section 3.1), F is the cavity finesse and L is the single-pass absorption length in the cavity.

There are many sources of noise that prevent the shot-noise limit from being reached. As discussed above, FM-to-AM noise conversion will result in amplitude noise significantly above the shot noise in many cases. Another common source of noise in many different experiments is optical etalons. These can occur within, or between, any optical systems and result in fringes in the spectrum. Depending on the source of the etalon fringes, they may be stable over the course of many measurements, in which case they can be removed in post-processing by fitting or filtering, or they may change during a measurement. These etalons are particularly troublesome because

they can contribute significantly to the noise level. There are several ways of tracking down and removing etalons in an experimental setup. Of course, the best option is to not introduce etalons in the first place, which means that optical components should be AR-coated or tilted slightly where possible. In particular, mirror substrates can be a persistent source of etalons, so the back surface should be slightly wedged when possible. The size of an etalon can be deduced from the fringe frequency, and this can be used to guess the origin of the fringes. Another option is to monitor the spectrum while tapping on or moving various optical elements and to look for changes in the etalon phase or frequency. By combining these techniques, etalon effects can be mitigated.

Table 3.1 summarizes the sensitivity of various cavity-enhanced comb systems that have been published. The different detection systems are discussed in more detail in the next section.

Table 3.1: Comparison of cavity-enhanced comb systems.

Ref	Detection system	α_{min} (cm^{-1})	α_{min}^{1s} ($cm^{-1}Hz^{-1/2}$)	α_{min}^{1s} ($cm^{-1}Hz^{-1/2}$) per spec. elem.	Finesse	Resolution (GHz)	Simul. Coverage/ Center Wavelength (nm)/(nm)
[181]	Grating+CCD	8.3×10^{-7} in 40 ms	1.6×10^{-7}	5.9×10^{-9}	420	6	20/860
[187]	Grating+CCD	1×10^{-8}	1×10^{-7}	5×10^{-9}	3000	12	4/420
[188]	Grating+CRDS	6.3×10^{-7}	2.5×10^{-10}	1.3×10^{-11}	4500	25	15/800
[44]	VIPA	8×10^{-10} in 30 s	4.4×10^{-9}	7.4×10^{-11}	28000	0.8	25/1600
[189]	Dual-comb FTS	1.2×10^{-6} in 18 μs	n/a$^{\circ}$	n/a $^{\circ}$	8000	0.4	30/1530
[54]	FTS	1.7×10^{-10} in 400 s	3.4×10^{-9}	3.4×10^{-11}	8000	0.38	30/1530
[72]	FTS	5.4×10^{-9} in 1 s	5.4×10^{-9}	5.4×10^{-11}	3800	0.8	200/3760
[190]	Grating+CCD	8×10^{-10} in 10 s	2.5×10^{-9}	3.3×10^{-10}	18000	110	4/430
[60]	VIPA+VMS	3×10^{-7} in 30 s	1.5×10^{-6}	4×10^{-8}	100	0.03^{+}	10/800
[53]	VIPA	4×10^{-9} in 180 s	4×10^{-8}	9×10^{-10}	30000	0.9	20/1850
[185]	Grating+CCD	3.2×10^{-9} in 18 ms	7×10^{-10}	1.5×10^{-11}	32000	13.5	4/430
[180]	NICE-OFCS	3×10^{-8} in 0.8 s	3.4×10^{-8}	4.3×10^{-10}	2300	2	30/1575
[191]	FTS + swept-coupling	1.5×10^{-7} in 1 h	3×10^{-7}	4.2×10^{-9} †	90000	6	25/1500

$^{+}$ Comb-mode resolved so resolution limited by frequency calibration.

$^{\circ}$ Could not continuously average for 1 s.

† This number is given in the reference as 6×10^{-11}, but they divide by the number of spectral elements, not the square-root.

3.3 Detection techniques

A variety of possible readout systems exist, as illustrated in Figure 3.1. In some cases, the absorbing spectrum is sparse enough that the entire comb can be detected on a single photodiode or dispersed with a grating and measured on a photodiode array, as shown in Figure 3.1(a). The comb modes are then scanned to record the spectrum [192, 193, 120, 194]. This can be combined with comb vernier (where f_{rep} and the cavity FSR are slightly detuned so that only every n-th comb mode is transmitted [195]) or cavity filtering using a high-FSR cavity to obtain comb-mode resolution; however, the number of spectral channels, and thus the bandwidth or resolution, is limited by the size of the photodiode array.

For some transitions, especially vibrational transitions in larger organic molecules in the mid-IR or many visible to UV electronic transitions in molecules, the absorption features to be measured have a width on the order of 0.5 cm^{-1} or more. In this case, a low resolution dispersive spectrometer is suitable, as demonstrated in a comb spectroscopy system for IO, BrO, NO_2 and H_2CO [183]. This technique is very similar to incoherent broad-band cavity enhanced absorption spectroscopy (IBB-CEAS) [196, 197]. For broad spectral features, analysis methods similar to those developed for differential optical absorption spectroscopy can be used [198, 199].

Instead of measuring changes in transmission to detect the presence of absorption lines, it is also possible to measure changes in cavity ring-down time in a technique called cavity ring-down spectroscopy (CRDS) [39]. In cw-CRDS, the laser is tuned to resonance and then the light is rapidly turned off and the temporal decay of light leaking out of the cavity is measured. This technique has the advantage that it is significantly less sensitive to intensity noise because the decay is measured relative to the initial intensity only. It is possible to combine comb spectroscopy with CRDS [188], as illustrated in Figure 3.1(b). Here, a grating is used to disperse the light spectrally in one direction while a rotating mirror is used to provide a time axis. The light is then detected on a 2D camera. While helping to reduce intensity noise, the number of spectral elements is still limited to the size of one dimension of the camera.

For many applications, it is desirable to record spectra simultaneously over a broad bandwidth with high resolution, which means that more spectral elements are required. Two common approaches for this are the VIPA spectrometer or Fourier-transform spectroscopy (Figure 3.1(c) and (d), respectively), which we describe in Sections 3.3.1 and 3.3.2.

3.3.1 VIPA

3.3.1.1 Basic operation

A VIPA, or virtually-imaged phased array [200, 201, 202], is a rectangular etalon plate (sketched in Figure 3.2(a) and pictured in Figure 3.2(b)) with a high reflectivity (HR) coating on the entrance surface (reflectivity $> 99.9\%$) and a partial reflective (PR) coating on the back surface (reflectivity typically about 97%). Additionally, an antireflection-coated (AR coated) entrance stripe is placed at the bottom of the entrance surface to allow light, which is focused in one dimension, to be coupled into the device. In contrast to an ordinary Fabry-Perot etalon, the VIPA etalon is tilted at an angle; because of this and the focusing of the incoming light, it transmits all the incident wavelengths. The basic idea is that the incoming light has a range of k-vectors in one dimension due to the cylindrical lens: each k-vector propagates in the etalon with different path lengths, and thus the etalon resonances are shifted for each k-vector. This results in mapping of frequency to k-vector, i.e., dispersion. The main advantage of a VIPA is the extremely high angular dispersion, up to 30-40 times better than a traditional dispersion grating. The output of the VIPA is a pattern of overlapping mode orders that repeat at the etalon FSR - typically 50 to 100 GHz, depending on the thickness of the plate. To spectrally resolve overlapped orders a cross-dispersion grating with a resolution better than the VIPA FSR is used. After the grating the light is imaged on a two-dimensional camera [51].

An example of the resulting image is shown in Figure 3.2(c). The vertical stripes are single mode orders of the VIPA, which are dispersed in the horizontal direction by the lower-resolution grating. The yellow horizontal lines show the range of one VIPA FSR on the camera, where the

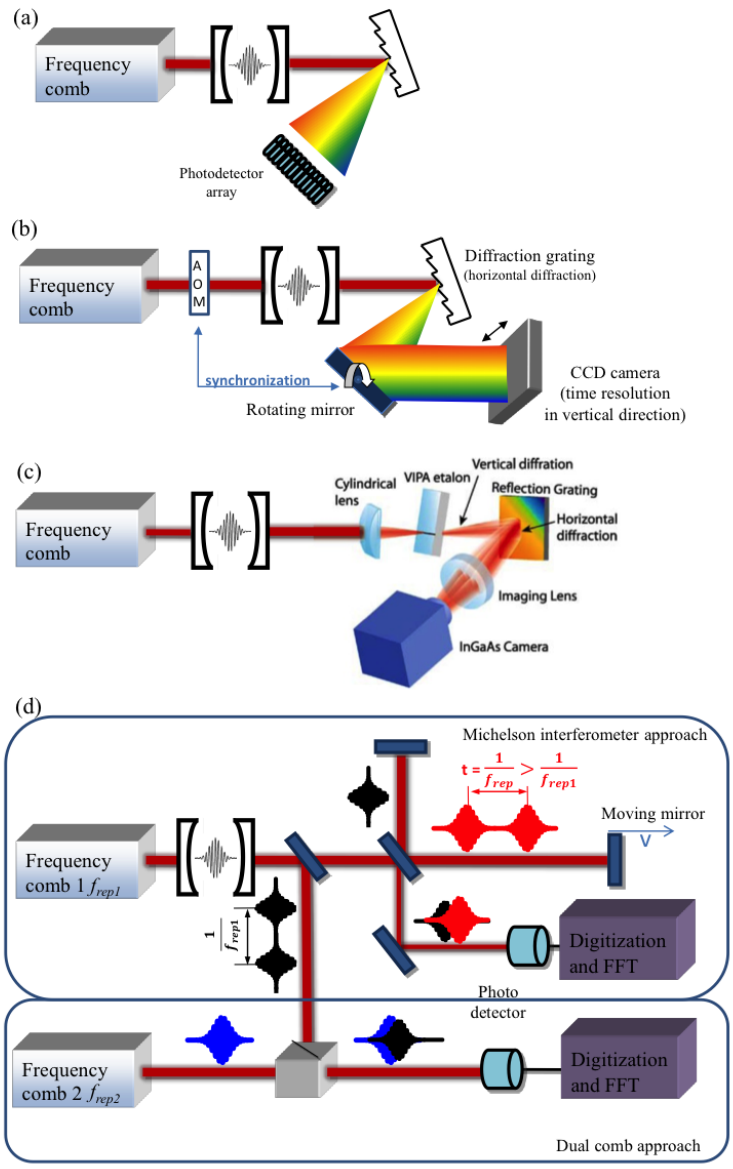

Figure 3.1: Detection schemes for CE-DFCS. (a) A grating spectrometer equipped with a detector array. (b) Broadband cavity ringdown setup. A grating provides spectral dispersion in the horizontal direction and a rotating mirror creates the time scale in the vertical direction for a two-dimensional detector array. An acousto-optic modulator (AOM) is used to turn off the laser beam to initiate the ringdown. (c) A VIPA spectrometer. The cavity output is dispersed vertically with a high-resolution VIPA etalon and is cross-dispersed with a diffraction grating. (d) Femtosecond Fourier-transform spectrometer. In the Michelson interferometer approach, the cavity output is analyzed by an interferometer with a fast scanning mirror in one or both arms. This effectively changes the repetition rate of the frequency comb. The pulses of the combs from the two interferometer arms with different f_{rep} interfere on the detector. In the dual comb approach, the output of the enhancement cavity beats with another frequency comb with $f_{rep,2} \neq f_{rep,1}$ on a photodetector.

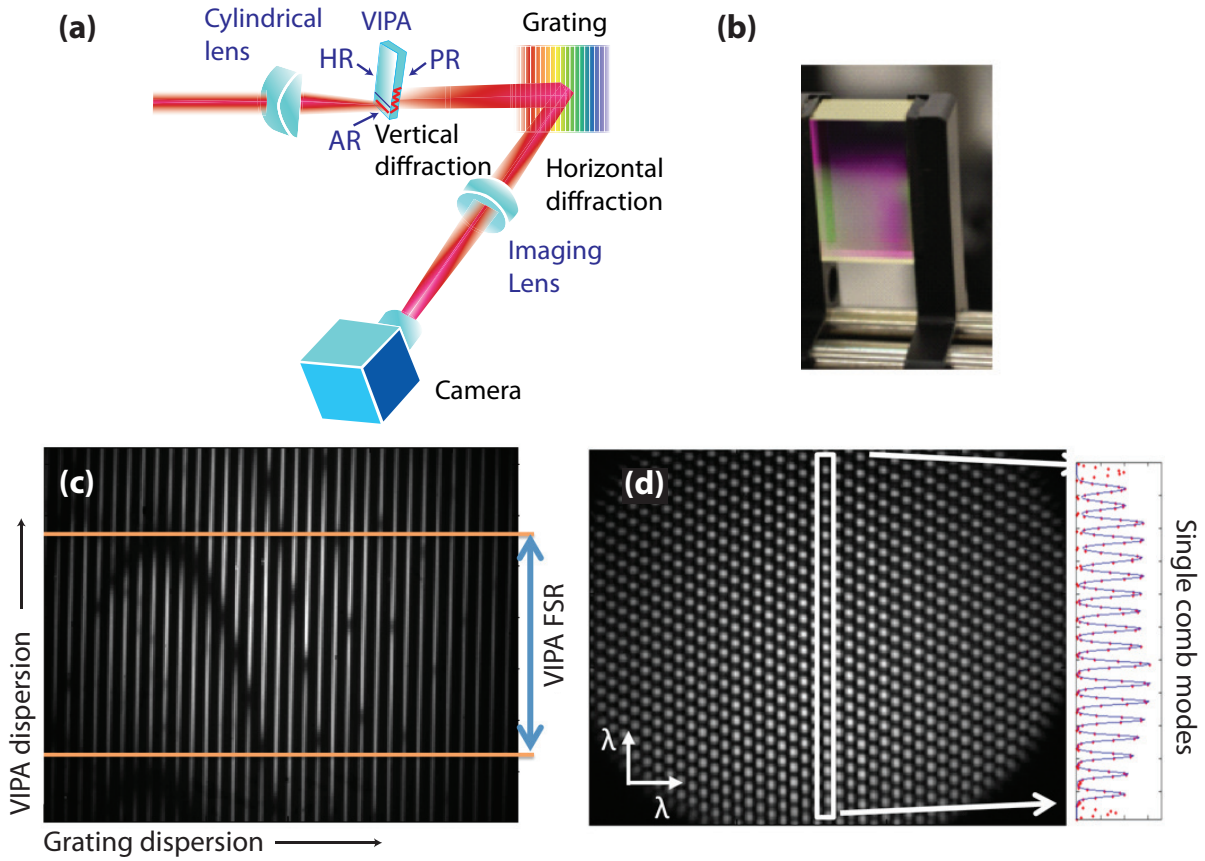

Figure 3.2: VIPA Spectrometer. (a) Sketch of the components. AR, HR, and PR are antireflection, high reflection, and partial reflection. (b) Photo of mid-IR VIPA. (c) Image without comb modes resolved. Dark spots are molecular absorption lines. (d) Image showing single comb-mode resolution.

spectral information is unique. Thus, a single column within this region contains spectral information from one VIPA FSR. By reading the pixels column-by-column a traditional one-dimensional spectrum can be created. The dark spots in the image represent CO_2 absorption signals for individual ro-vibrational transitions around 1800 nm. It is also possible to resolve individual comb modes, as shown in Figure 3.2(c) for a cavity-filtered 2 GHz comb in the mid-infrared.

VIPA spectrometers offer several advantages as a readout system:

(1) The short integration time for a single image, on the order of tens to hundreds of μs, make them an ideal tool for studies of transient events [56].

(2) Spectral information is acquired simultaneously across all of the channels. This helps the S/N and also reduces issues of uncorrelated noise across the spectrum.

(3) The spectrometer does not involve any moving parts and is compact, which makes it particularly attractive for field-deployable devices.

(4) In addition, the approach is compatible with the swept coupling scheme, which reduces the overall complexity of the experimental setup.

On the other hand, there are also several significant disadvantages:

(1) Since the VIPA is an etalon the resulting fringe pattern is sensitive to optical alignment and to mechanical vibrations, which tends to reduce the S/N.

(2) In addition, it is challenging to completely remove FM-AM noise in the tight-locking scheme unless an additional modulation – as in velocity-modulation spectroscopy (Section 3.4) – can be introduced.

(3) Calibration of the frequency axis needs to be carefully checked since the pixel-to-frequency mapping is nonlinear. We typically accomplish by calibrating to known spectra, but this is not always possible. If individual comb modes are resolved, then the absolute frequency at one point is all that is required.

(4) VIPA etalons tend to be relatively expensive and are available only in limited spectral regions.

Number (2) above is particularly troublesome. Unfortunately, it is not currently possible to perform balanced detection with imaging arrays as can be done for single-element detectors. 2D cameras capable of lock-in detection do currently exist, as discussed in Section 3.4.2. The lock-in bandwidth is up to 250 kHz, which is not high enough for frequency-modulation (FM) spectroscopy techniques. However, it should be possible to combine frequency-comb spectroscopy with wavelength-modulation spectroscopy, which has been shown to give similar results to FM spectroscopy at modulation frequencies above the noise bandwidth [203, 204, 205] and has been implemented with cavity enhancement [206]. Currently though, lock-in cameras are only available based on Si detectors (visible to 1 μm), so additional techniques would be needed for other wavelength regions. Active noise cancellation using an AOM is another option for removing amplitude noise, but adds complexity. Because the FM-to-AM noise on neighboring comb teeth is correlated, it should be possible to remove noise by comparing noise on nearby pixels. This only works well though if camera images are captured fast compared to the noise, otherwise residual uncorrelated noise still causes problems. In general, the swept-coupling scheme is used instead of the tight lock with dispersive spectrometers to reduce the effects of FM-to-AM noise conversion.

3.3.1.2 Design considerations

When designing a VIPA spectrometer, there are several parameters that must be optimized to achieve the desired resolution and spectral coverage for a given application. A detailed discussion of VIPA spectrometer design and alignment is given in [207], we only highlight a few additional points here.

The resolution of the VIPA spectrometer is limited by the finesse and FSR of the etalon. The finesse is determined both by the reflectivity of the coatings and by the number of round-trip passages within the tilted etalon. Resolution of 500 MHz has been demonstrated with VIPA FSRs of 25 to 100 GHz. It has proven difficult in practice to achieve higher resolution. One option is

to decrease the FSR for a given finesse; however, this has several disadvantages. First, the grating cross-dispersion must be capable of resolving a single FSR of the VIPA etalon, which is challenging for small FSR as discussed below. In addition, the spectral bandwidth typically decreases for a given camera size with decreasing FSR. Another possibility is to instead increase the finesse of the etalon by increasing the reflectivity of the PR coating. The challenge with this approach is that the number of bounces inside the etalon must also be increased, which means that the etalon needs to be taller while still maintaining a high degree of parallelism (significantly better than $\lambda/2$) between the faces. Since the etalon is thin (on the order of 1-2 mm), this is further complicated by the fact that the etalon will flex a bit when mounted. In an effort to alleviate this, the etalon can have a thick backer plate optically contacted to provide increased rigidity (this can be seen in Figure 3.2(b)); however, distortions of the VIPA lineshape – which appears as a broad pedestal around the main line – have been observed for VIPAs with a design finesse of 1000. These distortions are believed to be caused by surface flatness/parallelism issues and limit the finesse to about 200.

The achievable resolution is sufficient to resolve single modes of high repetition rate combs, as demonstrated with Ti:sapphire combs [51], and used in the velocity modulation experiment in Section 3.4.2 [60, 208]. Another approach to achieve comb mode resolution with lower repetition rate lasers is to use an intermediate filter cavity. This is shown in Figure 3.2(d) for a filtered comb with 2 GHz mode spacing; here, the filter cavity was set to transmit every 15th comb tooth of a femtosecond mid-infrared OPO [52]. The resolution was determined to be around 600 MHz by fitting the individual comb modes.

One note is that the VIPA lineshape – in the ideal case – is a Lorentzian function, not a Gaussian. The broader tails of the Lorentzian lineshape mean that there is the potential for significant cross-talk between VIPA resolution elements, which is made worse by distortions in the lineshape. This must be considered for example for high-precision lineshape studies.

As mentioned above, another important consideration is the resolution of the cross-dispersion system, which is set by the grating dispersion and the focal length, f_i, of the imaging lens. The

separation in the focal plane, Δx, for one VIPA FSR is given by

$$\Delta x = \frac{f_i}{\Lambda \cos\theta_d} \Delta\lambda_{\mathrm{FSR}}, \tag{3.8}$$

where $\Delta\lambda_{\mathrm{FSR}}$ is the wavelength separation for one FSR, Λ is the grating pitch, and $\theta_d = \sin^{-1}(\lambda/\Lambda - \sin\theta_i)$ is the angle of diffraction for an angle of incidence, θ_i. In order for each FSR to be resolved, this must be larger than the diffraction-limited spot size, $\frac{4\lambda f_i}{\pi d}$, for an input beam of size d measured in the grating diffraction plane. An additional consideration is that the maximum resolution of the grating also depends on the number of lines illuminated, N, and the illuminated width, d, by $\Delta\lambda = \lambda/N = \lambda\Lambda/d$. Typically, d is set by the width of the VIPA, which is commonly around 2 mm. For an 1800 line/mm grating, this gives a resolution of around 200 GHz at 800 nm, which would not be enough to resolve mode orders of most VIPAs. Because of this, we sometimes enlarge the output from the VIPA in the direction opposite to the VIPA dispersion direction using a pair of cylindrical lenses.

Finally, we would like the imaging system to be as efficient as possible. There are several places where losses can occur. Of course, the grating needs to be chosen to be as efficient as possible at the angle used. This can be accomplished with a blazed grating operating near the Littrow condition. The losses from the VIPA are typically dominated by clipping of the input and first reflected beam on the HR/AR interface. The ratio of output to input power is [45]

$$P_{out}/P_{in} \approx \left(1 - e^{\frac{(\delta h/2)^2}{w_v^2}}\right)^2 \tag{3.9}$$

where $\delta h = 2t\tan(\theta_v)$ is the height of the first reflection on the input surface, θ_v is the incident angle on the VIPA front surface (obtained using Snell's law from the incident angle outside of the VIPA and the index of refraction of the VIPA), t is the thickness of the VIPA, and w_v is the beam size at the focus of the cylindrical lens. In addition, we would like to concentrate as much power as possible into one order of the VIPA, i.e., we want as much power as possible in the region between the lines indicating one FSR in Figure 3.2. We can approximate this by calculating the size of one FSR in the focal plane,

$$\Delta y_{FSR} \approx \frac{FSR\lambda f_i^2 n^2}{c\bar{y}}, \tag{3.10}$$

where $\bar{y} \approx 1 - 2$ mm is the height by which the interference pattern is shifted out of the VIPA, and also by calculating the size of the image in the focal plane

$$w_y = \frac{\sqrt{2} f_i w_i}{f_c}, \tag{3.11}$$

where f_c is the focal length of the cylindrical lens and w_i is the input beam size. Ideally, $w_y \approx \Delta y_{FSR}$, and Δy_{FSR} is less than the size of the camera. This suggests that the power in one FSR can be increased by increasing the focal length of the cylindrical lens.

VIPA spectrometers can currently cover the visible, near-IR, and mid-IR out to about 4.3 μm. As with high-finesse mirrors, the bandwidth of a single VIPA system is limited by the coatings to typically $\sim 20\%$ of the central wavelength.

3.3.1.3 VIPA alternatives

Another option for achieving high angular dispersion is an echelle grating, which is a coarsely ruled grating that is used in a high diffraction order [209, 210]. The resolving power, $R \equiv \lambda/\Delta\lambda$, is related to the diffraction order (m) and number of grooves illuminated by $R = mN$, which actually only depends on the total illuminated width. The diffraction order sets the free-spectral range of the grating, $F_\lambda = \lambda/m$. This is a useful feature for spectral multiplexing because multiple FSRs can be cross-dispersed as in the VIPA spectrometer. A VIPA has a resolving power of around 300,000, so to match this we need to illuminate a width of around 10 cm in the visible/near-IR; however, this increases to 50-100 cm in the mid-IR, which would be challenging. In addition, the FSR of a standard echelle grating will be significantly different than that of a VIPA. Currently, echelle gratings are readily available with 20 lines/mm and with up to about 75% diffraction efficiency, which gives $m = 2\sin\theta/(\lambda\Lambda) \approx 125$ at 800 nm. This in turn corresponds to $F_\lambda \approx 6$ nm or around 3 THz (100 cm^{-1}), independent of wavelength. In order to resolve 1 GHz, one FSR needs to be recorded using 3000 pixels – a reasonable proposition in the visible/near-IR but currently cost-prohibitive in the mid-IR for anything more than one FSR.

In the mid-IR, an echelle spectrometer has been built with a resolving power of $\sim$30,000 [211].

This spectrometer used a custom echelle grating with 4 lines/mm and a camera with 256×312 pixels. This is still about an order of magnitude lower than that achieved in a VIPA spectrometer. To reach higher resolving power, new gratings etched into Si or Ge prisms (called immersion gratings or grisms) are being developed, aiming at resolving powers above 100,000 [212, 213, 214]. The use of internal diffraction in a high-index material immediately increases the resolving power by up to n^2 compared to a standard grating of equal size [215]. In addition, the FSR is smaller by n for the same grating pitch. Progress has been made on the manufacture of these gratings via wet etching [216, 217, 218]; however, currently these gratings are still custom and will still require large cameras and somewhat large beams for high resolution. Eventually though, this technology may be a viable alternative to VIPAs, even in the mid-IR, and should be able to operate over a wider wavelength region than a comparable VIPA spectrometer.

3.3.2 Fourier-transform spectrometer

A different method for obtaining broad bandwidth spectra is to use an interferometer as the wavelength resolving element: in this approach, a spectrum is obtained by first recording the interference signal as a function of optical delay between the two arms and then taking the Fourier transform of the interferogram. Fourier-transform spectroscopy (FTS) is a common technique in molecular spectroscopy typically using an incoherent light source [6, 7], which can provide extremely broad spectral coverage (from 2 to 50,000 cm^{-1}) and can reach resolutions of about 0.001 cm^{-1} (30 MHz, although resolutions of 1-10 GHz are more typical). The main shortcoming of this method is the long acquisition time – associated with the use of thermal light sources – and the need for long averaging times to obtain high sensitivity. The lack of spatial and spectral coherence of thermal sources makes it very challenging to use a long optical path length (required for high resolution) or to efficiently couple light into an enhancement cavity for high sensitivity. Replacing the thermal source of an existing Fourier-transform spectrometer with an optical frequency comb offers an instantaneous increase in spectral brightness and thus reduces averaging times significantly. The coherent frequency comb also allows an efficient combination of cavity-enhanced spectroscopy and

FTS.

As with dispersive spectrometers, FTS using a scanning interferometer as a readout system for comb spectroscopy has several advantages and disadvantages. The advantages include:

(1) FTS is broad-bandwidth and works with minor changes from the near-IR to beyond 10 μm. FTS can also work in the visible to UV.

(2) The resolving power of FTS is significantly higher than a VIPA spectrometer.

(3) It is possible to employ balanced detection to reduce amplitude noise – for example, from cavity FM-AM conversion – by over a factor of 100, which enables the use of the tight comb-cavity lock.

(4) Broad-bandwidth lock-in detection is possible because the signal is measured using only one detector.

(5) The spectrum is immediately calibrated.

There are also some significant disadvantages:

(1) It is challenging to make the system compact while still maintaing high resolution.

(2) The scanning stage makes FTS more sensitive to vibrations, which would make applications to field deployable systems more challenging.

(3) The acquisition rate and thus temporal resolution is limited by the scanning cart speed and data acquisition card as is typically on the order of seconds.

The use of two combs with detuned repetition rates (called dual-comb spectroscopy, shown in the lower part of Figure 3.1(d)) helps with most of these disadvantages, but requires two comb systems.

We have developed an FTS system for near- and mid-IR comb spectroscopy. The frequency comb light transmitted through a sample cell or cavity is sent into a Michelson interferometer equipped with a fast-scanning delay stage on which two retro-reflectors are mounted. To increase

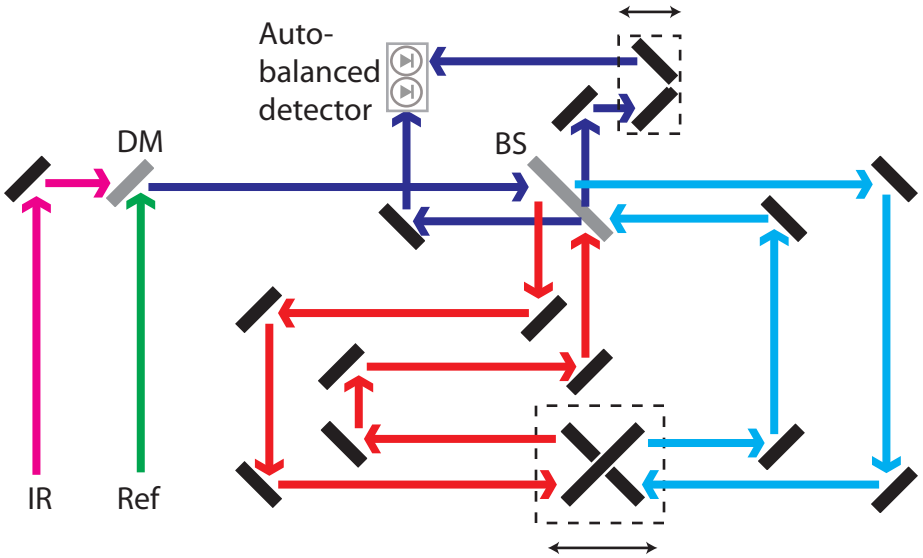

Figure 3.3: Setup of Fourier-transform spectrometer. The comb light (IR) and light from a reference laser (Ref, typically 780 nm or 1064 nm) are co-propogated (offset out of the page) with a half-mirror (HM). The two beams are split by different parts of a quadrant beam-splitter (BS) and then travel through two arms of a Michelson interferometer. The lengths of both arms are scanned simultaneously using two corner-cube retroreflectors mounted on a single state. The two output ports of the interferometer are sent to an auto-balancing detector for the IR. The reference laser is detected separately (not shown).

the optical path difference corresponding to the movement of this stage, the lengths of both interferometer arms are scanned simultaneously but in opposite directions (Figure 3.3). Light from a stable 780 nm (or 1064 nm) cw-laser co-propagates with the comb light in the interferometer and is used as a reference for frequency calibration. To keep the reference and comb beams parallel but easily separable, we use a quadrant beamsplitter in which the first and third quadrants are coated as 50:50 beamsplitters for the comb light and the second and fourth quadrants are coated for the reference light. The two beams are split with the upper two quadrants and are recombined on the lower two quadrants. In addition, we found that the retro-reflectors caused more beam deviation than expected, so the contrast of the interferograms changed by around 50% while scanning across the full range. This can be improved with better retro-reflectors that deviate the beam less.

The comb interferograms at both output ports of the Michelson interferometer are monitored with an auto-balancing detector [219] using either InGaAs photodiodes (for the near-IR) or HgCdZnTe photodiodes (MCZT, from Vigo Systems). The auto-balancing circuit subtracts the photo-currents from the two photodiodes and uses an active feedback to keep the DC currents equal. This subtraction doubles the useful signal compared to a single interferometer output (due to the fact that the two output signals of the interferometer are complementary [6]) while subtracting away the common mode amplitude noise, such as FM-to-AM conversion by the enhancement cavity. Both interferograms (from the comb and reference cw-laser) are digitized by a two-channel analog-to-digital converter at 1 Msample/s with 22-bit amplitude resolution (National Instruments NI 5922). The high data rate allows us to exploit the scanning speed of the FTS; to avoid digitization noise in the analog-to-digital conversion, at least 20-bit resolution is required.

The auto-balancing detector is based on the circuit developed by Hobbs [219]. For the near-IR, the basic auto-balancing circuit works well, but significant modifications were required due to the different behavior of the mid-IR photodetectors. Figure 3.4 shows the schematic for the mid-IR auto-balancing detector. Briefly, the matched transistor pair Q3-A and -B function as a current splitter, with the ratio of currents set by the difference in base-emitter voltages. This basically acts to divide the current from the reference photodiode, with some of the current shunted

to ground via Q3-A. The reduced current from the reference photodiode is subtracted from the current from the signal photodiode and converted to a voltage using the transimpedance amplifier U2. Transistor Q2 is used to reduce the capacitance at the input of the transimpedance to increase the bandwidth. The output signal is compared to reference voltage (near 0 V) and used to servo the splitting ratio of the reference photodiode current to match the current in the two paths at the summing junction. The primary changes to the Hobbs design for the mid-IR detectors is the photodiode reverse-bias control, which was critical to providing the highest common-mode noise cancellation possible. Because the bias voltage is very low for the mid-IR photodiodes (around 0.4 V), small changes in transistor Q2 or Q3 base-emitter voltage can significantly affect the bias voltage and thus the detector response. Such a change will happen as the photocurrent, and thus the current through the transistor, changes. To keep the photocurrent linearly related to laser power, the bias voltage is actively controlled to maintain a constant voltage drop across the diode. The primary challenge is making this feedback very fast – ideally an order of magnitude or more above the signal frequency of around 150 kHz so that oscillations at the signal frequency are highly suppressed. Basically, this feedback works by using a differential instrumentation amplifier, here using two op-amps but a fast three op-amp circuit would be better, to measure the voltage drop across the diode and then using an additional op-amp to close the feedback loop. Many of the capacitor and resistor values were adjusted to optimize the common-mode rejection ratio of the instrumentation amplifier and to reduce parasitic oscillations due to non-linear behavior of the photodiodes. In addition, the photodiodes were chosen to be as well matched as possible. Transistor pairs Q1A-B and Q4A-B are current mirrors, which allow the photocurrent from each diode to be monitored using transimpedance amplifiers U1 and U6. In addition to the lower bias voltage and parasitic oscillations, the mid-IR detectors also have a shunt resistance that is significantly lower than that in visible and near-IR detectors. This low shunt resistance means that voltage noise from op-amps can cause significant noise at the output of a transimpedance amplifier if additional care is not taken. In addition, this shunt resistance could contribute to the oscillations seen in the feedback. The shunt resistance increases at lower temperature, so we are currently using a

detector with an integrated four-stage TE cooler (the manufacturer does not recommend cooling below around 180 K). With these detectors, we measure a constant noise floor (above about 20 μW) and a S/N at ~150 kHz that increases linearly with increasing laser power. The S/N is about a factor of 3 below the shot-noise limit, which indicates that we are detector noise limited. We are not sure if this limit arises from dark current/Johnson noise in the photodiode or from the finite bandwidth of the feedback loop. To improve the performance further, it would be good to remove the feedback loop, which could potentially be accomplished by measuring the photocurrent of each diode with a transimpedance amplifier, and then using a current-to-voltage converter to drive the basic Hobbs circuit. In addition, cooled InSb detectors (for up to 5.5 μm) seem to have slightly better performance – both a higher detectivity (D^*) and higher shunt resistance – than the MCZT detectors. InSb photodetectors do have higher capacitance so will be slower, but are still fast enough. These changes should reduce the detector noise and enable shot-noise limited detection in the mid-IR.

The resolution of the FTS is set by the maximum optical path delay (OPD) between the two interferometer arms, which is limited by the maximum scan range (L) of the cart to $R = 1/OPD = 1/(4L) = 0.0035$ cm^{-1} (105 MHz). This resolution is high enough to resolve individual comb modes using minimal cavity filtering. Once individual comb modes are resolved, the resolution is set by the comb tooth linewidth. Using our mid-IR OPO, we could achieve a resolution of 10 kHz, which would require an OPD of 30 km in a standard FTS!

When FTS is used, the S/N in the spectrum, $(S/N)_f$, is related to the S/N in the time-domain (interferogram), $(S/N)_t$, as

$$(S/N)_f = (S/N)_t \frac{\sqrt{N}}{M}, \tag{3.12}$$

where N is the number of data points in the interferogram and M is the number of resolved spectral elements in the spectrum [220, 54]. To calculate the absorption sensitivity per spectral element, we use Equation 3.4 with $\sigma = (S/N)_f^{-1}$:

$$\alpha_{min}^{\text{1s, DFCS, FTS}}[\text{cm}^{-1}\text{Hz}^{-1/2}] = \frac{\sigma_t}{L_{eff}} \sqrt{M} \sqrt{\frac{T}{N}}. \tag{3.13}$$

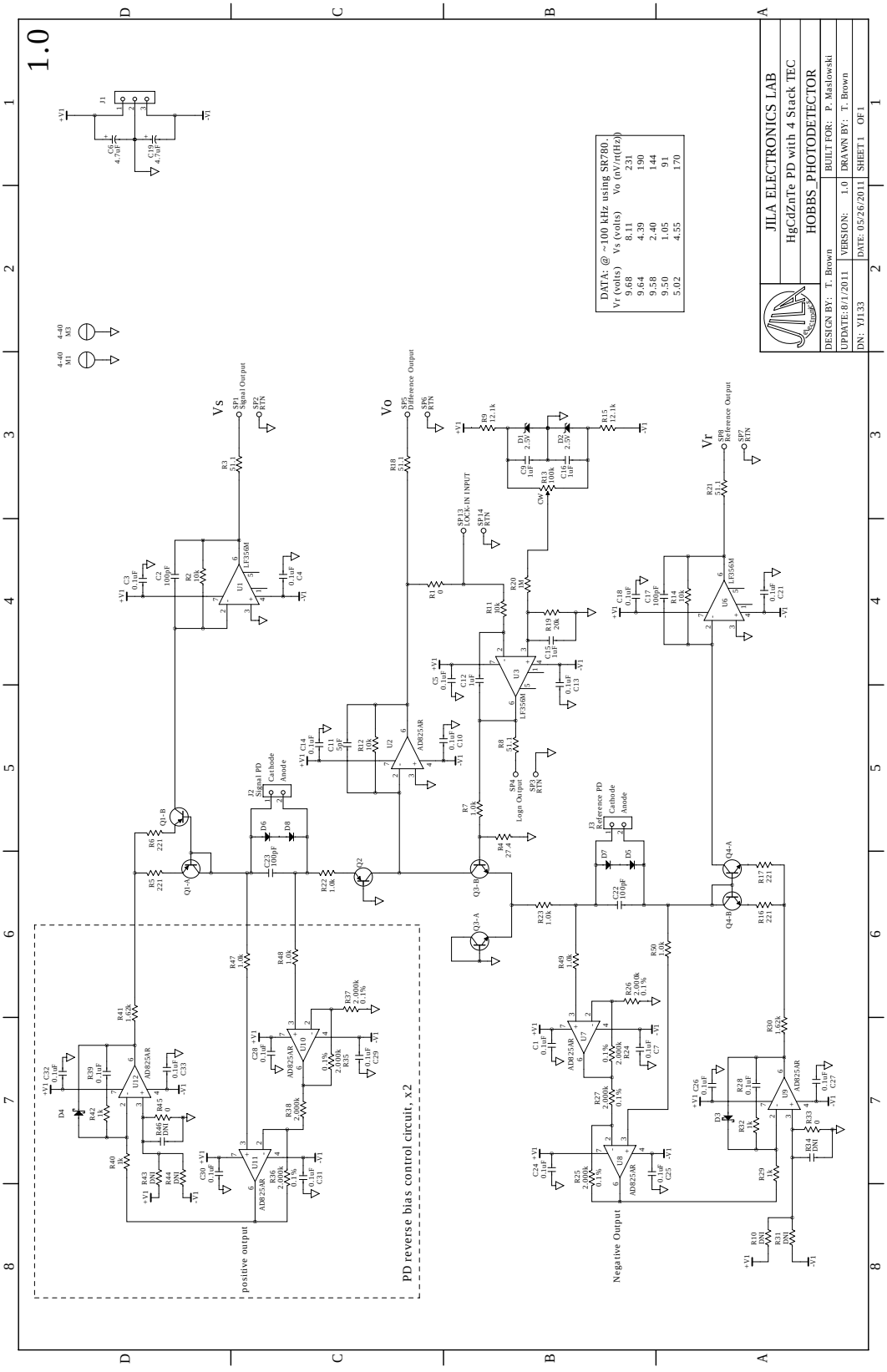

Figure 3.4: Circuit diagram for mid-IR auto-balancing detector. See text for details. Designed by Terry Brown.

The shot-noise limit is given by $\sigma_t^{\text{shot}} = \sqrt{\frac{2eN}{\eta PT}}$, because the effective bandwidth for each point in the time domain is N/T [54]. This results in minimum sensitivity that is a factor of $\sqrt{M}$ worse in FTS than in a spatially multiplexed system for the same total integration time and signal-to-noise.

As discussed earlier, the main limitation of cavity enhanced spectroscopy utilizing a laser continuously locked to a cavity is usually the noise originating from frequency-to-amplitude noise conversion by the narrow cavity modes. Immunity to this type of noise can be obtained by the use of modulation techniques, as is done for cw lasers in noise-immune cavity-enhanced optical heterodyne molecular spectroscopy (NICE-OHMS) [41, 42]. Continuously scanned FTS, as we do here, is a modulation technique as well, since the interferogram appears at an audio frequency – around 160 kHz in our case – limited by the acquisition rate of the data acquisition board. Thus, the signal is detected at a frequency where the noise is significantly lower than at DC. The addition of balanced detection reduced the noise in the near-IR by a factor of 600, which enabled shot-noise limited detection with an optical power of 30 to 100 μW [54]. The deviation from the shot noise limit at powers below 30 μW is due to the decrease of the performance of the auto-balancing detector. At powers above 100 μW the intensity noise starts to dominate over the shot noise. The best shot-noise-limited single element sensitivity obtained for a 6 s acquisition time is 1.4×10^{-9} cm^{-1} at 100 μW, corresponding to 3.4×10^{-11} cm^{-1} per spectral element. At a resolution of 2.3 GHz the measured absorption noise was slightly above that given by the shot noise limit, due to the drift of the residual etalon fringes. Here a single element sensitivity of 7.6×10^{-10} cm^{-1} at 1 s was obtained, which translates to 2×10^{-11} cm^{-1} per spectral element at 1 s. In the mid-IR, a detector-noise limited sensitivity of 5.4×10^{-9} cm^{-1} Hz$^{-1/2}$ was obtained, corresponding to 6.9×10^{-11} cm^{-1} Hz$^{-1/2}$ per spectral element for 6000 resolved elements [55]. Very recently, NICE-OHMS has been combined with frequency comb spectroscopy in a technique termed noise-immune cavity-enhanced optical frequency comb spectroscopy or NICE-OFCS [180]. The achieved sensitivity in the near-IR is close to the shot noise limit.

Instead of a scanning interferometer, two frequency combs with slightly different repetition rates can be used, as shown in the lower part of Figure 3.1(d). This technique, known as multi-

heterodyne spectroscopy or dual comb spectroscopy [221, 222, 223, 189, 224, 225], provides very short acquisition times (tens to hundereds of microseconds) for a single spectrum over a very broad bandwidth. However, as in scanning FTS, the S/N decreases with increasing spectral bandwidth [220]. In addition, the complexity of two independent comb systems makes mid-IR applications of dual comb spectroscopy more challenging [226, 227].

3.4 Velocity-modulation spectroscopy

Broad-bandwidth precision spectroscopy of molecular ions is useful in a wide range of fields including fundamental physics, astrochemistry, and physical chemistry. For the eEDM experiment discussed in Chapter 6, very little data, especially high resolution data, existed for HfF^+ and ThF^+ and the uncertainties in the theoretical calculations of excited states were very large (thousands of wave-numbers), so we needed a technique capable of broad survey spectroscopy to understand and assign the molecular energy level structure. As discussed in Section 6.8 different molecular ions, such as WN^+, could be useful for future versions of the eEDM experiment. Trapped molecular ions may also be useful for measurements of nuclear-spin-dependent parity violation and anapole moments [70, 228]. Sub-millimeter and far-IR spectroscopy of H_3O^+ and deuterated isotopolgues provide high sensitivity to variations of the proton-to-electron mass ratio [68]. Because of it's simplicity, spectroscopy of HD^+ has already been used to test QED calculations [66]; similarly, exact calculations including some QED terms exist for HeH^+ [229], so this system can test the accuracy of multi-electron calculations in molecules. Molecular ions such as SiO^+ [230], AlH^+ [231], and MgH^+ [232] among others are also suitable for direct laser cooling, which will provide more opportunities for tests of fundamental physics. For many future experiments, broad-bandwidth precision spectroscopy of molecular ions will play an important role, either for identifying transitions for follow-up experiments or for providing direct precision measurements.

In astrochemistry, at least 22 ions (both positive and negative) ranging in complexity from H_3^+ to H_2COH^+ and C_8^- and even metal containing species such as $FeCO^+$ [233] have been identified

in interstellar and circumstellar gases [59][1] . Because ion-neutral reactions have very fast rate constants – typically at or near the Langevin limit – and the ion production rate via cosmic ray ionization is typically high, reactions involving molecular ions are central to understanding astrochemistry [58, 234]; nonetheless, some rate constants and branching ratios are still not well known [235]. For example, the pathway for formation of a very simple molecular ion, CH^+, remains elusive [236, 237]. In addition, H_2CO^+ should be observed based on the currently known interstellar species, but so far has not [59]. To aid the searches for new species, laboratory measurements are needed. The development of new microwave and mm-wave observatories – most notably Herschel, ALMA, and SOFIA – has increased the need for accurate measurements of rotational transitions in a variety of molecular ions [238]. While direct laboratory rotational and THz spectroscopy is possible, precise measurements of vibrational and vibronic transitions can also provide indirect measurements of rotational transitions to the accuracy needed [239]; we demonstrate this as well in Chapter 5, where the precision on our rotational constants enable predictions of low-lying rotational transitions to within a few MHz. Another long standing problem in astrochemistry is the identity of the diffuse interstellar bands (DIBs) [240, 241], which are a collection of unidentified bands spanning the visible and near-IR. Identification of these bands currently requires more laboratory measurements of optical transitions to try to match with the observations [236, 235, 242]. The inability to identify the molecules responsible for the DIBs points to a still very incomplete understanding of the processes that govern interstellar chemistry, and it is believed that many more unidentified species such as positively or negatively charged polycyclic aromatic hydrocarbons (PAHs, a possible source of the DIBs) and multiply charged ions are yet to be discovered [235, 243].

On the physical chemistry side, precision spectroscopy of H_3^+ above the barrier to linearity (near 9913 cm^{-1}) provides rigorous tests for *ab initio* theory [244, 245, 246]. Currently, theory can reproduce the spectrum up to the visible with 0.1 cm^{-1} accuracy with the inclusion of non-adiabatic effects. Further improvements in experimental precision will enable further tests of non-adiabatic corrections as well as relativistic corrections. Adding another hydrogen molecule to form

[1] A complete list of molecules is here: `http://www.astro.uni-koeln.de/cdms/molecules`

H_5^+ adds significant further complexity for experiments and theory. The ground state of H_5^+ can be considered as a proton-bound dimer of H_2 and the excited structures are more like H_3^++H_2 so fully understanding the potential energy surface provides information about clusters and about the reaction dynamics [247]. Many carbocations are interesting for both their presence as intermediates in reactions such as combustion as well as the challenges they present to theory; for example, the spectrum of CH_5^+, a highly non-classical carbocation, still remains unassigned due to both its complexity and spectral interference from other contaminant species [248, 249, 250]. Similarly, the ethyl cation ($C_2H_5^+$) is believed to be an intermediate in solution-phase reactions, but its structure is still not well know [251].

3.4.1 Background

One of the primary challenges with performing spectroscopy of molecular ions is separating the ion absorption from neutral species. One option is to create an ion beam, or to use an ion trap, where electric fields can be used to mass-select ion species. Typically though these techniques only produce small numbers of ions and suffer from small absorption path lengths. A new technique of NICE-OHMS in an ion beam has recently been demonstrated and shows considerable promise for high sensitivity ion spectroscopy [252]. High densities of molecular ions can also be created using hollow-cathode lamps and glow discharges; however, in these systems it is hard to separate the ion signal from the competing absorption from neutral species (which are usually present at significantly higher concentrations than the ion species). Our initial efforts of survey spectroscopy of HfF^+ used emission from a hollow-cathode lamp and were not successful because of neutral signal. In fact, even after we identified some HfF^+ transitions using a different technique, we were not able to clearly identify the transitions in the hollow-cathode lamp data [208].

The development of velocity-modulation spectroscopy (VMS) by the Saykally group solved this problem and enabled background-free direct absorption spectroscopy of molecular ions. Velocity-modulation spectroscopy works by modulating the voltage polarity of an AC column discharge (see Figure 3.5). This discharge produces ions with high density and the reversing polarity modulates

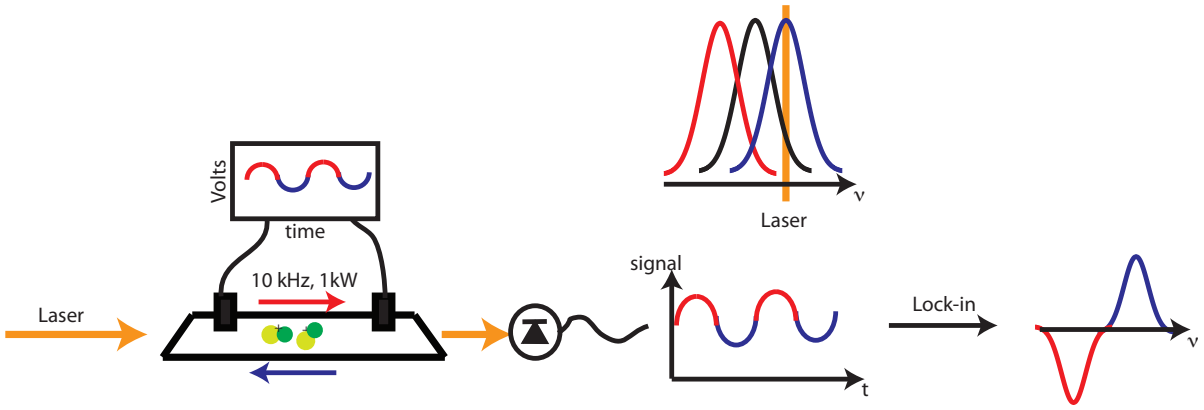

Figure 3.5: Sketch of velocity-modulation spectroscopy (VMS). An alternating voltage is applied to a pair of electrodes, which forms an ac discharge and results in a modulated drift velocity, shown here by red and blue arrows for the positive and negative half-cycles of the drive respectively. A laser propagates on along the discharge and is detected using a photodiode. An absorption line of the ion (black curve in the upper panel) will be Doppler-shifted (red and blue curves) with respect to the laser (orange line). This results in a modulated absorption signal. The final signal after lock-in detection at the modulation frequency is the difference between the two Doppler-shifted peaks.

the drift velocity of the ions. The velocity of neutral species is not influenced by the voltage applied to the plasma. This modulated drift velocity causes a modulated Doppler shift when probed along the axis of the discharge, which is analogous to frequency modulation of the laser. Lock-in detection synchronous with the modulation frequency (i.e., at $1f$) yields an (essentially) background-free absorption signal.

Lock-in detection can be understood as recording a spectrum during each half cycle and then taking the difference between these two signals, as illustrated in Figure 3.5. In the ideal case, the neutral signal in each half cycle is identical and cancels out; on the other hand, the absorption lines in each half cycle are frequency offset and so still yield signal in the difference. It is apparent from this simple analysis that neutral signal may not be completely cancelled if the signals in each half cycle are not identical. This can be caused by asymmetries in the discharge, for example due to pressure/flow gradients or electrode characteristics, so some additional tricks are typically used to improve the neutral suppression.

3.4.2 Comb-vms

While velocity modulation spectroscopy provides high sensitivity for ions, it typically relies on cw lasers and thus is slow to cover a wide spectral bandwidth. Fourier-transform VMS has been demonstrated in emission; however, the sensitivity was low [253, 254]. Instead, we chose to combine VMS with frequency comb spectroscopy. By resolving every comb mode of a femtosecond Ti:sapphire laser (Gigaoptics, 3 GHz repetition rate) simultaneously over a wide spectral bandwidth, we can achieve high resolution and absolute frequency accuracy with over 1500 channels measured at once. Figure 3.6 provides an overview of the experimental setup, more details can be found in [60, 208]. Briefly, we couple light from the Ti:sapphire comb into the 120 MHz free-spectral-range enhancement-cavity that contains an ac discharge cell, with every 25th cavity resonance matched to a comb mode. The comb light transmitted through the cavity is fiber coupled and then spectrally dispersed using a VIPA spectrometer to resolve every comb mode. We then image the light onto a Heliotis C2 “smart pixel” lock-in camera [255, 256], which uses a combination

of CCD and CMOS technology to demodulate and read out each pixel at the discharge modulation frequency. The camera basically has two storage wells per pixel, one for the in-phase signal and one for the quadrature. For the first quarter-cycle of the demodulation period, charge is accumulated in the first well, similarly, charge is stored in the second well for the second quarter-cycle. For the third and fourth quarter-cycles, charge is subtracted from the first and second well, respectively. This process can be repeated for a number of demodulation cycles before a full image (called a frame) is recorded. Up to 320 frames can be stored on the camera in one set.

A co-propogating cw Ti:sapphire laser serves as a frequency reference for stabilizing the comb and provides a marker on the two-dimensional spectral image. The cw laser is locked to its internal reference cavity achieving a linewidth of ∼100 kHz, and feedback to the combs repetition rate locks a single comb tooth to the cw laser. The signal for the feedback originates from a beat note between the comb and cw laser; after frequency division, the beat note frequency is converted to an error signal using a frequency-to-voltage converter. This results in a looser lock than would be possible with a phase detector; however, the lock was significantly more stable to perturbations. Typically, the beat note is stabilized to about 1 MHz.

The repetition rate is controlled by acting on both the comb-laser cavity length (slow feedback via a piezoelectric transducer) and the pump power (fast feedback via an acousto-optic modulator) [257, 258], while the offset frequency of the comb is left free-running. We initially tried to lock f_{rep} to an external rf source and stabilize f_0 using the pump power; however, we could only tune f_0 by about 20 MHz before the comb lost modelock. This is because, in our operating conditions, pump power changes affect f_{rep} more than f_0, probably because non-linear refractive index effects in the crystal can significantly change the cavity length since the crystal is a large fraction of the cavity length in the high repetition rate laser. Since we can only operate the comb in a small range of pump powers around 5.5 W, we do not have the ability to tune the pump power to a region where the feedback to f_0 is optimal [257]. Instead, we opted for the alternative locking scheme above. This scheme has the disadvantage that f_0 noise is written onto f_{rep}, which will make comb teeth farther from the lock point less stable. During a scan, we observe fluctuations of f_{rep} of less than

200 Hz, which will cause at most 300 kHz of noise for a comb tooth 1500 modes (the range of a single acquisition) away from the lock point.

We produce HfF^+ by heating 0.5 g of HfF_4 powder to about 550 °C in a 1 m long home-built discharge cell. Helium buffer gas is flowed through the discharge such that the total pressure is about 3 torr. By recording the emission of the discharge using a low-resolution grating spectrometer, we were able to reliably monitor molecule production. With each loading of the oven we were able to run for about 3 hours. A 2.5 m long bow-tie optical enhancement cavity consisting of two flat, 98% mirrors (input and output couplers) and two 100 cm radius-of-curvature, low-dispersion, 99.9% high reflectors surrounds the discharge cell. The reflectivity of the input and output couplers was chosen to match the losses from the Brewster-angled windows and thus provide efficient input coupling. We use liquid-crystal variable retarders and a polarizing beamsplittler to rapidly (50 ms) switch the direction of propagation through the discharge tube while maintaining the comb-cavity lock. This allows us to subtract out slowly varying noise due to drifts in camera pixel offsets and also to improve the rejection of neutral background absorption. The cavity length is actively stabilized to an integer multiple (25) of the frequency-comb laser cavity length, which ensures that each comb component is coupled to a cavity mode. The error signal was based on a dither lock (later a PDH lock) using the spectrally filtered reflection from the cavity. Our feedback loop provides about 20 kHz of bandwidth by using a high-speed, low-range PZT [169] (oscillation frequency around 50 kHz) and a second long-range PZT. We found it critical to feed forward a 10-kHz compensation voltage onto the lock of the enhancement cavity to compensate for the 10-kHz pickup from the discharge, an effect seen in other cavity-based velocity modulation experiments [259] as well. By using a non-polarizing beam splitter to combine the reflection from the two cavity directions and making sure that the combined reflections are well overlapped, we were able to switch directions without losing lock and without changing the locked spectrum.

About 150 cm^{-1} of spectrum spread over 1500 channels is recoded simultaneously. For each measurement, we average and subtract images for each direction of propagation and also record the power per comb tooth by applying a calibrated amplitude modulation to the laser. In order

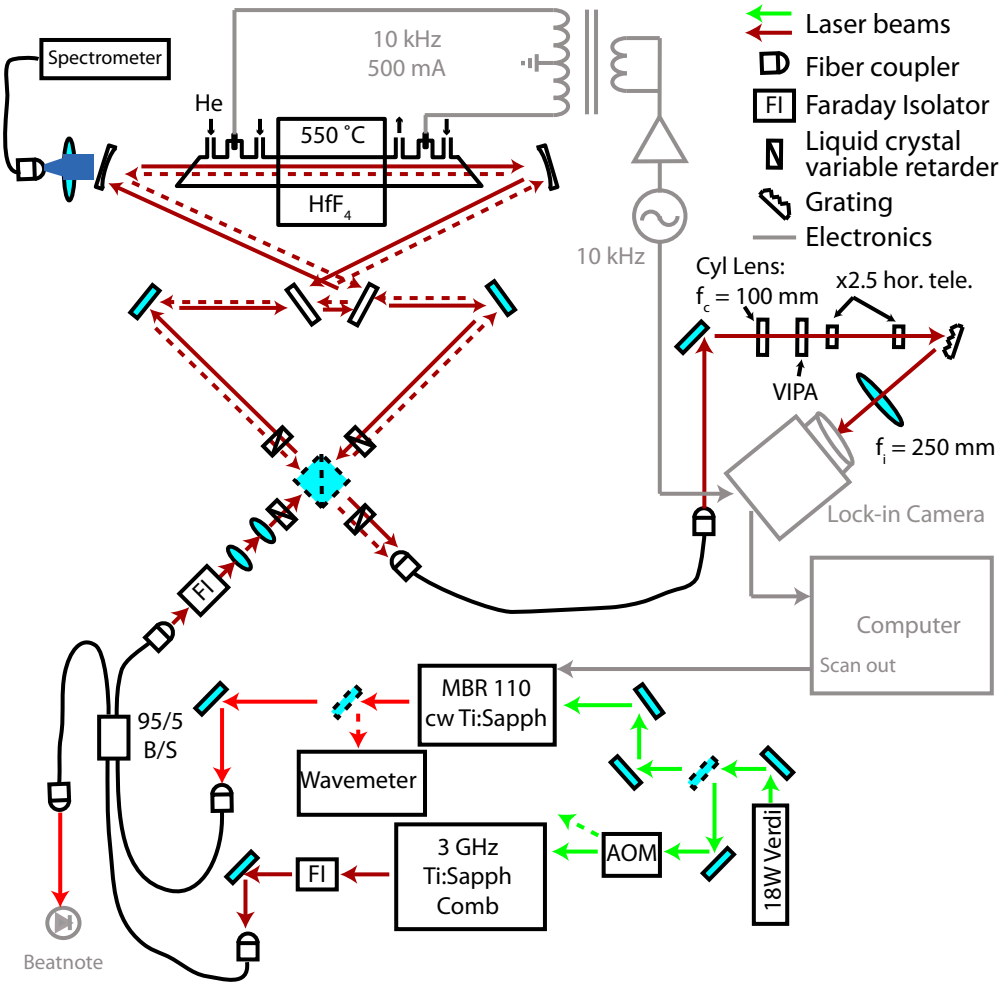

Figure 3.6: Setup for comb-vms. We use a Ti:sapphire comb with a repetition rate of 3 GHz, which is transferred via fiber to the optical cavity. The comb is coupled into one direction of a ring bowtie cavity, which contains an ac-discharge cell with Brewster-angled end windows. The cavity finesse is about 100 and the length is matched to be an integer multiple (25) of the comb cavity. We use liquid crystal variable retarders and a polarizing beamsplitter to alternate the direction of propagation through the cavity. The ac-discharge is driven at 10 kHz with about 500 mA. We flow helium gas through the tube at a pressure of about 3 Torr. HfF^+ ions are created by heating about 0.5 g of HfF_4 powder to 550 °C inside the discharge tube. The cavity transmitted light, which contains the modulated absorption signal, is analyzed using a two-dimensional imaging system and a lock-in camera. A cw Ti:sapphire laser is used to stabilize the comb and serves as a frequency reference in the spectra. A fiber-coupled grating spectrometer is used to monitor the discharge fluorescence.

to fully sample the spectrum, we interleave 30 measurements with the cw laser stepped over 3 GHz. This results in a spectrum that covers 150 cm^{-1} sampled every 100 MHz with an absolute frequency accuracy of 30 MHz (set by a rubidium atomic transition referenced wavemeter). When the wavemeter was not calibrated for a particular measurement, we estimate the uncertainty to be 100 MHz. For strong bands with fully resolved isotope structure, absolute accuracy of the determination of the band origin is limited predominantly not by statistical errors but by the absolute knowledge of the cw Ti:sapphire laser frequency we use as a reference. For our purposes we were satisfied with the 30-100 MHz (0.001 - 0.003 cm^{-1}) absolute accuracy of the wavemeter. This could be readily improved if needed [239]. For analysis purposes we then interpolate the spectrum onto a fixed 0.001 cm^{-1} grid. This allows us to easily average or combine a collection of different scans.

3.4.3 System performance

To track down possible sources of noise, we monitored the intensity noise on a single pixel and across the camera – i.e., by subtracting the first frame from all other frames – as a function of time. One major source of noise was drifting baseline offsets caused by discharge noise coupling to either the laser lock or the cavity. This results in frequency noise, which is converted into amplitude noise at the discharge frequency. The offsets were reduced with a feed-forward by adding a phase-shifted and amplitude-controlled signal from the discharge drive to the cavity lock. Etalon fringes were also a significant source of noise. In particular, we found that one polarizing beam-splitter created fringes and, most significantly, the fiber to the imaging system caused high-contrast etalon fringes until it was replaced with a polarization-maintaining, angle-cleaved fiber. Other sources of laser frequency noise can result in amplitude noise due to FM-to-AM noise conversion by the cavity if the noise bandwidth is high enough to contribute noise at 10 kHz. Several such sources were discovered: in particular, air currents and water flow. Air currents in the comb pump laser beam path can cause significant frequency noise on the comb light. We removed these by carefully enclosing the entire beam path and sealing any small gaps in the enclosure. In addition, we found several issues

related to the cooling water for the comb. The first was vibrations caused by the chiller that were transmitted along the cooling lines. This was improved by including a short section of soft rubber (Tygon) tubing in the cooling lines, which acts as a vibration damper. In addition, turbulent flow presumably near the crystal caused laser frequency noise. We reduced this noise by including a large water reservoir between the chiller and laser to filter pressure fluctuations and by reducing the cooling water flow.

In addition to technical noise, we also care about the readout noise of the camera and the total efficiency of the system. First, we can calibrate the camera to obtain a relationship between counts and intensity by measuring the light from a modulated LED, which is assumed to be shot-noise limited. By comparing the noise as a function of the average number of counts on a pixel, we can determine readout noise as well as the relationship between the number of photons and counts. This calibration gives around 3300 photons/count. When converting to power, it is necessary to include the fact that the in-phase or quadrature signal only comes from half of the integration time and the fact that the first two demodulation cycles (periods) are used for a pixel offset subtraction scheme so the number of cycles of data is reduced by two. The readout noise is about 1 count per cycle (or about 0.15 counts in 50 cycles, which is a more typical operating condition) or equivalently about 15 fW. While the camera noise on a single pixel averages down as expected as a function of time, we found that variations across the camera do not average down at all. We attribute this variation to small pixel-to-pixel offsets, which are removed by subtracting images for the two directions.

For all of the data shown here, we measured the following efficiencies: 30% fiber coupling to cavity, 70% from the fiber output to the cavity, 15% transmitted through cavity, 35% coupling to imaging system, 15% through imaging system, 60% in one VIPA FSR, and ∼30% camera efficiency. This gives an expected power per comb mode of about 20 nW. The fiber coupling efficiencies and cavity transmission (limited by cavity losses) have been improved since. Some of the losses in the imaging system efficiency are due to VIPA coupling efficiency as well as grating losses. We found that the camera efficiency was very dependent on the incident angle due to an angular dependence

of the micro-lens array on the camera; however, we were still never able to increase the efficiency beyond 30%.

Without the discharge running, we measured a fractional technical noise floor of about 1×10^{-5} at 1 s for a single direction. Rapidly taking the difference between two directions reduced this to around 3×10^{-6}. The noise was increased with the discharge running to about 2×10^{-4} for one direction. The combination of switching directions, intensity normalization, and rolling median subtraction (subtracting from every point in the spectrum the median of the surrounding 20 points) reduced the noise to 1×10^{-5} at 1 s. The noise averages down as the square-root of time for up to 100 s before significant deviations are observed.

Recording one full spectrum, consisting of 30 interleaved measurements, takes about 30 minutes and results in a single-pass fractional absorption sensitivity of 3×10^{-7}. Since one scan contains 45000 channels, this equates to a sensitivity of 4×10^{-8} $\mathrm{Hz}^{-1/2}$ per spectral element), which is the sensitivity that a single-frequency laser system would need, in addition to being able to scan 150 cm^{-1} continuously, to match the performance of the comb-vms system. We recorded spectra over a total of spectral bandwidth of 1000 cm^{-1} with both the oven on and off to check for contamination.

3.4.4 Single-frequency vms

In addition, we also scanned some bands using single-frequency velocity-modulation spectroscopy as sketched in Figure 3.7. For these measurements we removed the enhancement cavity and counter-propogated beams from the cw Ti:sapphire laser through the discharge tube. We then subtract these two beams using an auto-balancing photodetector, which is discussed in Section 3.3.2. Due to noise from the discharge, we reached a sensitivity of about 5×10^{-8} $\mathrm{Hz}^{-1/2}$ with 1 mW on the detector; this noise seemed to be related to optical pickup from the discharge emission, which was reduced using irises, and to non-common-mode amplitude noise from acoustical pickup. In particular, we found that we could minimize the acoustical pickup on the cavity mirrors by tuning the discharge frequency slightly to avoid resonances. The use of more rigid mirror mounts also decreased the noise. In order to find bands without scanning the full spectral range, we scanned

several small 1-cm^{-1} sections spaced by 10 cm^{-1}and then move to a new region if no lines were observed. Using this technique we were able to find 15 more bands ranging from 9950 to 14600 cm^{-1}. We can continuously scan about 0.5 cm^{-1} in 4 minutes, which is at least 30 times slower than the comb-vms system.

3.4.4.1 Coherent Subtraction

We have also investigated a novel technique for differential detection that relies on coherent interference between the two counter-propogating laser beams instead of subtraction of photocurrents as discussed previously. This is accomplished by coherently splitting and recombining the two beams using one non-polarizing beamsplitter to form a Sagnac-type interferometer containing the discharge cell and cavity if desired (blue inset to Figure 3.8). The signal is then detected at the destructive interference, or "dark port", of the interferometer. In the regime where laser intensity noise dominates, the signal-to-noise using coherent subtraction increases as the splitting ratio approaches 50:50 between the two beams until detector readout noise or shot noise dominates. Physically, the fractional signal is increasing while the fractional noise level remains constant and dc power are both decreasing. We have tested coherent subtraction versus a single direction of propagation using a photodiode and single-channel lock-in detector with our cw laser and demonstrate a factor of 10 gain in the signal to noise (blue data in Figure 3.8). We expect an improvement in the S/N of about $\frac{T^2-R^2}{R^2+T^2-2RT}$, where T and R are the transmission and reflection of the beamsplitter (assuming no losses). Thus, we would expect roughly a factor of 25 improvement with the 52/48 beamsplitter that was used. The lower than expected enhancement could come from losses in the PBS or alignment differences. We tried to implement a tunable cancellation ratio between the two directions using with Faraday rotator to provide a small polarization rotation, but beam distortion made this challenging.

Coherent subtraction, unlike subtraction of photocurrents, is sensitive to phase as well as amplitude of the light field; thus, the resulting lineshape is dependent on both absorption (approximately first-derivative shaped) and dispersion (approximately second-derivative) and can vary if

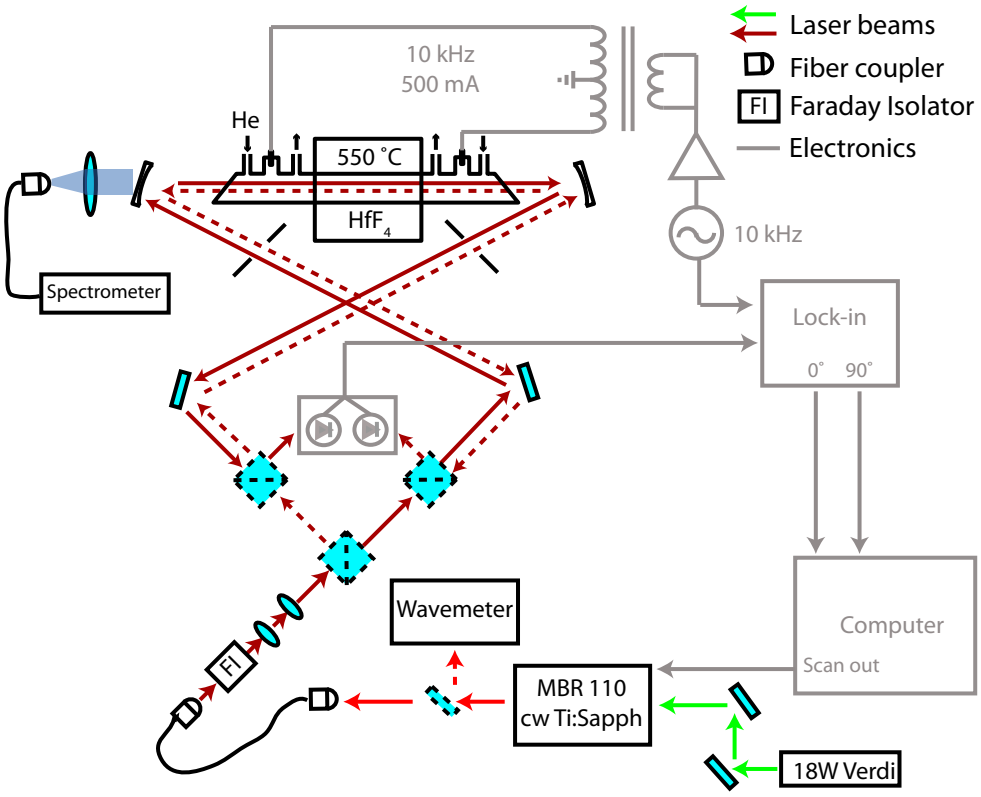

Figure 3.7: Setup for cw-vms. We use a cw Ti:sapphire laser that is tunable from about 9500 - 14800 cm^{-1} (1050 - 675 nm). After fiber coupling between tables, the laser is split with a 50/50 non-polarizing beamsplitter. Each beam goes through an additional 50/50 non-polarizing beamsplitter (to separate the return light) and is then sent in opposite directions through the discharge cell. Half of the returning light in each direction is reflected by the beamsplitters and is differenced using an auto-balancing photodetector [219]. This difference signal is then sent to lock-in detectors to record signal in-phase and 90° out-of-phase with the HfF^+ absorption. We placed irises in the beam paths to reduce the amount of discharge fluorescence observed on the auto-balanced detector; this helped both to reduce noise and primarily to reduce baseline drifts in the spectra.

there are differential phase shifts between the two directions. We performed a simple simulation, shown as dashed lines in Fig. 3.8, that reproduces the lineshape modification. These simulations were done by applying a cosine modulation in time to the center frequency for both the absorption (assumed Gaussian lineshape) and dispersion terms (obtained via Kramers-Kronig) and then selecting the appropriate frequency term from the Fourier cosine transformation. The electric field for the two directions (denoted *cw* and *ccw*) is given by:

$$\begin{aligned} E_{cw}(t) &= T \exp\left[-\alpha(\chi^i_{cw}(t) + i\chi^r_{cw}(t))\right] \exp(i\pi) \exp(i\phi) \\ E_{ccw}(t) &= T \exp\left[-\alpha(\chi^i_{ccw}(t) + i\chi^r_{ccw}(t))\right], \end{aligned} \tag{3.14}$$

where α is the absorption coefficient and $\chi^i(t)$ and $\chi^r(t)$ are the imaginary (Gaussian) and real parts of the polarizability. The time dependance is given by a modulation of the center frequency of the Gaussian absorption lineshape at the discharge modulation frequency, ω_{mod}. The modulation is out-of-phase for the two directions. We then write the detector signal as $I(t) = |E_{cw}(t) + E_{ccw}(t)|^2$ and extract the lock-in signal by $S = \int I(t) \cos(\omega_{mod} t) dt$. Repeating this at a variety of simulated laser frequencies generates the lineshape. The amplitude and linewidth of the single-direction simulation was scaled to the measured value and these values were used for the coherent-subtraction simulation. The constant phase offset (most likely due to the beamsplitter) added to the coherent subtraction simulation was chosen to fit the measured lineshape (about $\pi/20$ radians). In addition to the phase sensitivity, which could be useful for some applications, coherent subtraction has several other advantages. First, the dark port can be used to reduce the optical power seen by the detector thus avoiding saturation while still maintaining a shot-noise limited signal-to-noise ratio. Second, the subtraction is performed prior to the detector and is wavelength independent. This means that coherent subtraction can be used with comb-vms or other dispersive detection systems for increased signal-to-noise. We did not implement coherent subtraction with the comb-vms system here because we were close to camera-noise limited, thus the gains would not have been very significant. It was also not used for the cw scans because the lineshape would change slightly day-to-day, possibly due to alignment variations.

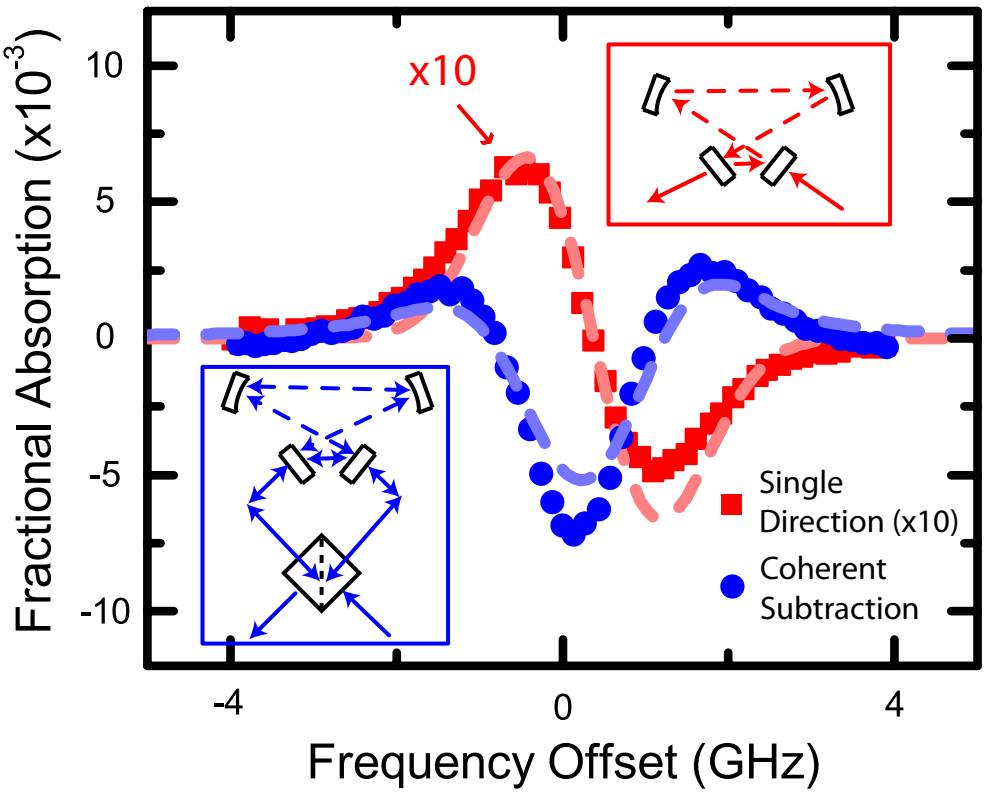

Figure 3.8: Comparison of coherent subtraction and single-direction measurements. The signal to noise for coherent subtraction (using a 52/48 beam splitter) surpasses that of single-direction measurements by a factor of 10 when the noise is primarily technical light intensity noise. Both measurements of a single N_2^+ line were made with the cw laser. The dashed lines are a calculation of the lineshape (see text). The modification in the lineshape for the coherent subtraction is due to a stray differential phase shift of approximately $\pi/20$ between the two counter-propagating beams, which results in a sensitivity to both absorption and dispersion.

3.4.5 Extensions of comb-vms

Frequency comb modulation spectroscopy can be applied to both ionic and neutral molecules by either demodulating at the discharge modulation frequency (ion velocity modulation) or at twice the discharge modulation frequency (neutral-molecule production yield modulation). This technique could also be readily extended to the detection of radicals by concentration modulation [6]. Some ions can also be produced directly in a supersonic-expansion discharge source [260], and can also be detected with concentration modulation. It might also be possible to modulate the discharge direction and perform velocity modulation in the expansion. A high-sensitivity ion-beam VMS system has recently been developed [252], which enables mass-selective spectroscopy of ions with high precision due to kinematic narrowing in the fast ion beam. Such a system should work with any ion production method. In addition to studying the spectra of stable ions, gas-phase ion reactions can be studied using a selected-ion flow tube [235]. Combing comb-vms with these techniques would enable broad bandwidth, high-resolution studies of cold ions and radicals.

For many applications, comb-vms will need to work in a variety of spectral regions. Comb sources also enable efficient non-linear optical generation, which allows for spectral broadening and access to spectral regions ranging from the UV to the mid-IR, as discussed in Chapter 2. Currently, the lock-in camera is only available with Si detectors and thus only works in the visible to near-IR out to 1 μm. It might be possible to use similar technology with other detector materials, such as InGaAs, but this would require significant development work. Some alternatives do exist however. One option is to use only one axis of the camera for spectral information and then use a rotating mirror to provide time information on the second axis of the camera, as was done for comb cavity-ringdown spectroscopy [188] (see Figure 3.1(b)). If timed correctly, every pixel could then record one-quarter of a cycle of the demodulation frequency, which would then be similar to the lock-in detection method. Alternatively, cameras with integration times of under 20 μs are available even in the mid-IR. In this case, the camera could be triggered to only record for one-quarter of a cycle. This would then be repeated for each quarter-cycle, again providing similar information to the

lock-in system. However, both of these techniques will reduce the amount of on-camera averaging and will also require more time for the same amount of data. Another option for the mid-IR is to up-convert the cavity-transmitted light to the near-IR using sum-frequency generation. An upconversion-based VIPA spectrometer for the mid-IR has been demonstrated using a cw Nd:YAG laser [261], but the power was very low. Instead of a dispersive spectrometer, it should be possible to perform comb-vms with FTS. Lock-in detection has been demonstrated with a scanning FTS to enable NICE-OFCS [180], so this should also work with VMS.

Chapter 4

Applications of DFCS

In this chapter, we discuss several implementations of direct frequency comb spectroscopy that highlight new capabilities and explore new spectral regions. First, we look at the application of CE-DFCS to the detection of trace contaminants in arsine gas [53], which is used in the manufacture of many semiconductor devices. This experiment demonstrated for the first time direct frequency comb spectroscopy in a region accessed by supercontinuum generation – in this case, 1.75-1.95 μm (5710-5130 cm^{-1}). This spectral region is mostly unexplored via laser-based spectroscopy owing to the lack of widely tunable lasers operating here. In fact, DFB diode lasers have only recently become available in this spectral region [262], but still with limited tuning range. Two possible broadly tunable sources are optical parametric oscillators [263] or difference frequency generation [264]; however, these cw systems must be carefully scanned to cover the full spectral region. Our CE-DFCS approach provides high sensitivities across more than 2000 detection channels distributed over a broad, simultaneous bandwidth in a robust and compact system. Furthermore, this experiment also demonstrated CE-DFCS for the first time with focus on an industrial application (i.e., trace detection in a strongly absorbing process gas), where the bandwidth is critical for distinguishing impurity signals from background absorption, along with high resolution for making unambiguous identifications.

In the second section, we present our first implementation of direct frequency comb spectroscopy in the mid-infrared [46] using the OPO comb (Section 2.4) and Fourier-transform spectrometer (Section 3.3.2). As discussed in Chapter 1, the mid-infrared is an important spectral

region because of the strong fundamental vibrational bands, which provide both increased sensitivity and access to more molecules than in the near-infrared. This first demonstration achieved part-per-billion detection limits in 30 seconds of integration time for several important molecules for breath analysis and atmospheric chemistry – including methane, ethane, isoprene, and nitrous oxide – across the 2.8-4.8 μm spectral region. We also show how DFCS enables precise concentration measurements even in gas mixtures that exhibit continuous absorption bands and how it allows detection of molecules at levels below the noise floor via simultaneous analysis of multiple spectral features. In addition, the use of a multipass cell – despite the reduced sensitivity – provides access to the full spectral range covered by the source and demonstrates a general system capable of working from the visible to mid-infrared beyond 10 μm. The source and detection system also provided the basis for later applications of mid-infrared CE-DFCS [55, 56].

Finally, we discuss some future prospects of comb spectroscopy and illustrate where the broad bandwidth, high resolution, and high sensitivity of comb spectroscopy could provide an advantage in certain applications. Specifically, we look at continued industrial applications of trace gas detection, prospects for breath analysis, and both laboratory and field applications to the study of atmospheric chemistry.

4.1 Trace detection in Arsine

Arsine (AsH_3) and phosphine (PH_3) are important process gases used in the production of III-V semiconductors via metal organic chemical vapor deposition (MOCVD) [265, 266, 267, 268]. These compounds are used in devices ranging from high-brightness light emitting diodes and high power laser diodes to solar cells. Trace levels of contaminants present in the process gases can result in unintentional doping and lattice defects. The inclusion of these dopants gives rise to additional energy levels in the bandgap of the host semiconductor, leading to undesired changes of its electrical and optical properties. In particular, oxygen incorporation in III-V semiconductors has been shown to form a deep recombination level, resulting in a decrease of photoluminescence efficiency and carrier lifetimes as well as reduced device reliability. A primary source of oxygen

impurities is the presence of traces of water vapor in the precursor gases, which has been shown to negatively impact the semiconductor at the level of 10-100 parts per billion (ppb) [268]. Because of its ubiquity and low vapor pressure, water is extremely difficult for the manufacturer to completely remove. Furthermore, water impurities can be introduced from contamination in the transfer lines at the point of use; therefore, on-line monitoring of water concentrations during semiconductor growth is desirable. In addition to water vapor, many other impurities including carbon dioxide, hydrocarbons (methane and ethane), hydrogen sulfide, silane and germane must be controlled in the process gas [266].

Current systems, employing different techniques, capable of detecting water at the sub-100-ppb level all have significant drawbacks [266]. For example, Fourier transform infrared (FTIR) spectrometers require long acquisition times owing to the low spectral brightness of their thermal light source. In addition, the required sensitivity can only be achieved by using a highly optimized research system with a long pathlength gas cell, a high sensitivity detector, and an ultrahigh purity nitrogen purge system. Another potential technique is negative ion-atmospheric pressure ionization mass spectrometry (APIMS) [269], but these expensive systems are large and complex, not suitable for on-line monitoring and are mainly limited to inert background gases. Current research has focused on laser-based spectroscopy systems such as tunable diode laser spectroscopy (TDLAS) or cavity ring-down spectroscopy (CRDS) [265, 267, 270], which provide highly sensitive measurements with rapid acquisition times; however, these systems typically target one or two absorption lines of the desired impurity species. Thus, multiple contaminants cannot be easily identified and quantified, while unexpected impurities can significantly degrade the reliability of the measurement. In a recent study [268], it was necessary to use gas chromatography with mass spectrometry, atomic emission spectroscopy, and pulsed discharge ionization detection in addition to CRDS, to check for all of the critical impurities in arsine. Many of these impurities could potentially be detected with one system using CE-DFCS. Previous cw-CRDS experiments measuring water in phosphine at 940 nm [270] and 1400 nm [267] were limited by competing background gas absorption and by the line strength of the water transition. The 1.75-1.95 μm (5710-5130 cm^{-1}) region contains

bands of several important impurities, including a water band at 1.85 μm (5400 cm^{-1}) that is stronger than the 1400 nm band by a factor of 2-3, and should be a somewhat transparent region of the arsine absorption spectrum [48]. Therefore, it is a compelling range to explore with CE-DFCS.

4.1.1 Experimental Setup

A sketch of the experimental system is shown in Figure 4.1. We used a home-built mode-locked Erbium-doped fiber ring laser [207] that provides 130 mW average power at a repetition rate of approximately 250 MHz. The laser output was then amplified with a single mode Er:fiber amplifier to produce 81-fs pulses with 400 mW average power. These parameters are readily achievable with commercially available fiber lasers as well. After the amplifier and polarization control optics, all of the light was coupled into 10 cm of standard single mode fiber spliced to a 6 cm long piece of highly nonlinear silica fiber (OFS Specialty Photonics) to provide spectral broadening. The spectrum (covering 1.2-2.1 μm or 8300-4700 cm^{-1}) from this fiber is shown in Figure 4.1(b) and Figure 2.4 as optimized for generation of a frequency comb near 1.85 μm; however, it is easy to change the spectrum by varying the laser polarization and input pulse chirp. The average power after a 40-nm bandwidth filter centered at 1.86 μm was 17 mW. Because the laser and nonlinear spectrum generation were both fiber-based, this entire system was compact and robust – requiring almost no adjustment from day to day. We initially tried Raman shifting fiber to obtain more power, but the coherence of the shifted light was degraded as discussed in Section 2.3.

The optical resonator used for enhancing the absorption detection was a linear Fabry-Perot cavity with one 2-m radius concave mirror and one flat mirror and a peak finesse of 30,000 (mirror reflectivity $\sim$0.9999). In order to obtain accurate absorption values, we characterized the mirror reflectivity via wavelength resolved ringdown measurements, see Figure 4.1(c). For this we recorded ringdown traces of an empty (under vacuum) cavity in 10 nm wavelength increments using a monochromator and a fast extended-InGaAs photodiode. Several measurements for each wavelength were averaged, and the resulting data were fit with an 8th-order polynomial.

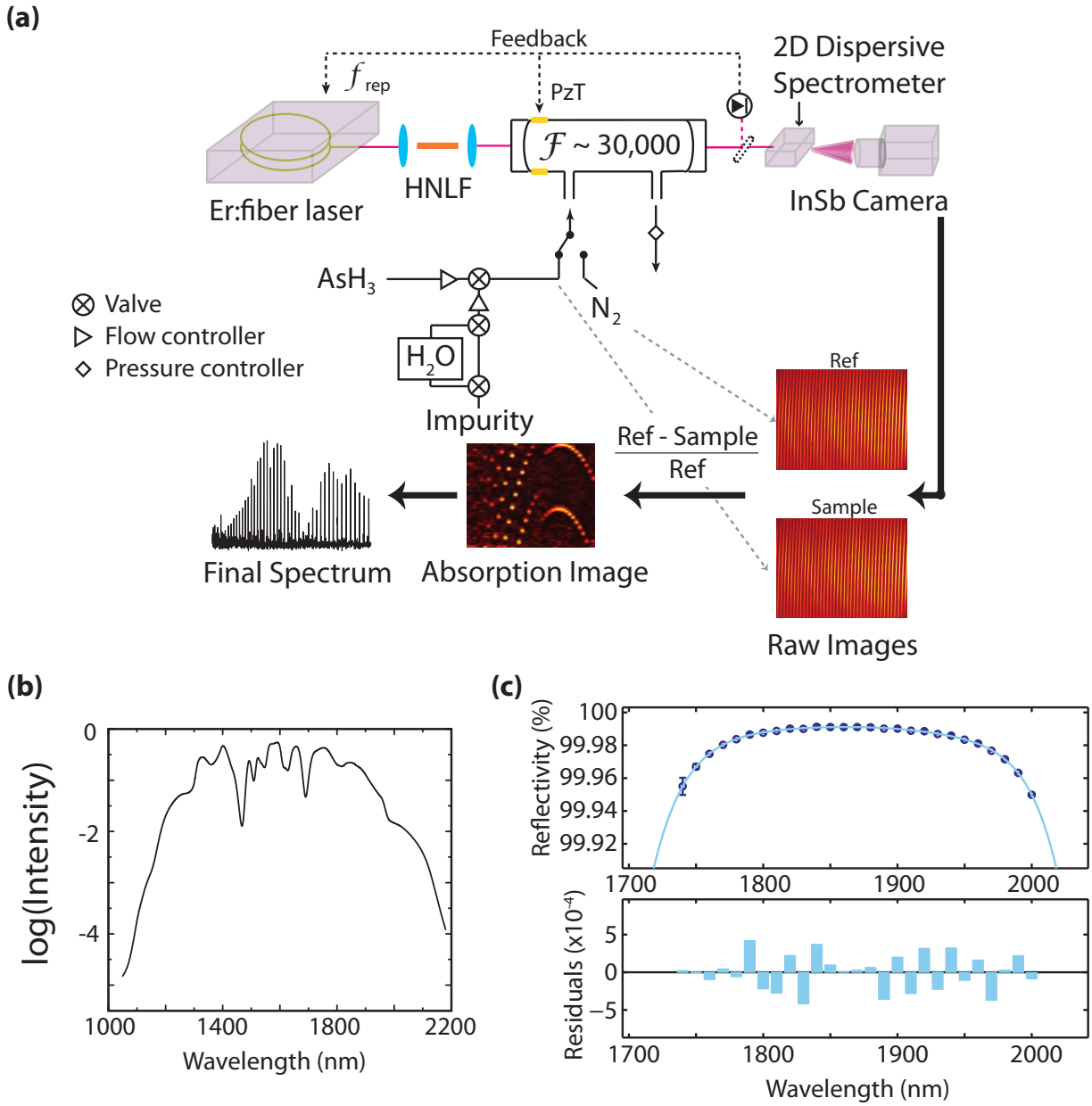

Figure 4.1: Sketch of trace detection in arsine. (a) Outline of experiment. HNLF: highly nonlinear fiber; PzT: piezoelectric transducer; (b) Spectrum after nonlinear fiber. (c) Measured mirror reflectivity and residuals after 8th-order polynomial fit.

The mirrors were first aligned in mirror mounts and then attached to a stainless-steel gas cell using Torr seal, after which the mounts were removed. Prior to the final attachment, it is important to make sure that the input and output laser beam is well centered on the cavity mirrors so that the finesse is not reduced due to clipping. Because arsine gas is extremely toxic, the mirrors were surrounded by a sealed end cap. We also use VCR fittings for the gas line connections because these are more robust than Swagelok. Finally, the entire system was carefully checked for leaks. The temperature of the stainless-steel gas tube was actively controlled using heater tape and could be tuned to adjust the cavity length.

The cavity length (∼60 cm) was adjusted so that the free-spectral range was matched to the comb repetition rate. In addition, the comb f_0 was adjusted via the fiber laser pump power to optimize the transmission of the comb through the enhancement cavity, see Section 3.1. The useful spectral bandwidth of the cavity was about 200 nm (600 cm^{-1}); however, owing to the varying free-spectral range frequency due to cavity dispersion, it is not possible to simultaneously match all comb modes and cavity modes over this bandwidth. To overcome this limitation and to synchronize the cavity and comb during measurements, we use the swept-coupling scheme (Section 3.1.2). In this case, the comb modes were dithered (by changing the laser cavity length and therefore the repetition rate) using a triangle waveform with an amplitude of 150 kHz at a frequency of 7.5 kHz around the cavity modes, and slow feedback to the enhancement cavity length (via a piezo) was used to keep the time gap between the successive transmission peaks constant. Since our integration time per individual record was around 150 ms, we integrated over multiple dither cycles. This dither process effectively allowed us to couple the comb to the cavity over the full spectral bandwidth of the mirrors.

The sample gases flowed through the optical buildup cavity for detection. To measure and quantify impurities in arsine, our gas handling system was designed to add trace contaminants to arsine at well-controlled mixing ratios. For this purpose we obtained a calibrated mixture of 10 parts per million (ppm) each of CO_2, CH_4, and H_2S in a nitrogen gas cylinder. In addition, we added small amounts of water vapor via a diffusion vial (Valco Instruments). Flow controllers were

used to control the relative arsine and impurity gas flow as well as to control the amount of flow across the water diffusion vial. Typically, the total pressure in the sample cell was ∼200 torr and was controlled by a back-pressure controller just after the cell. The gas system was designed to be very flexible for this experiment and to maintain a high degree of safety due to the toxicity of arsine gas (e.g., the pumps and arsine cylinder were located in different rooms); however, it was not optimized for switching speed due to the small diameter of the installed tubing.

The light transmitted from the cavity was analyzed with a VIPA spectrometer (Section 3.3.1). This spectrometer system provides high resolution (900 MHz or 0.031 cm^{-1}) in one dimension, while maintaining broad bandwidth (∼20 nm or 50 cm^{-1}, limited by the size of the cameras imaging sensor) in the orthogonal dimension. Light was coupled into the VIPA etalon (51 GHz free spectral range) with a horizontal, 6-cm focal length cylindrical lens. The etalon was tilted approximately 2° from vertical to provide a high dispersion in the vertical direction. A 1200 lines/mm cross-dispersing grating was used to separate the mode orders in the horizontal direction. Finally, the light was imaged onto the 320x256-pixel InSb focal plane array camera with a 25-cm focal length lens, resulting in images as shown in Figure 4.1.

Images were collected alternating between sample and reference gases, which provides a differential measurement of the change in transmitted power with and without absorber. Typically, we average 20 images (at ∼150 ms integration time per image) with sample gas; then switched to reference gas and averaged another 20 images. We found that 20 images was the maximum number of images between signal and reference before the noise did not continue to average down. This seemed to be caused by drifting etalon fringes and by small changes in the VIPA fringe positions. This sequence was then repeated to average down to the desired sensitivity.

Because we are measuring high-purity arsine gas relative to pure N_2, there was a significant index-of-refraction difference between the sample gas and reference gas. We could not fully compensate for this difference by changing the pressure, so f_{rep} was adjusted slightly for every switch. To completely remove gas switching times, we initially tried to use two separate cavities for the sample and reference; however several technical complications made this challenging to implement.

In particular, we found that the alignment to the VIPA would always change slightly, which caused the fringe patterns to move. This could be removed with a single-mode fiber before the spectrometer. In addition, there was a difference between the finesse of the two cavities, as well as a difference in cavity f_0. Finally, any etalon fringes that differ between the two beam paths will lead to residual fringes in the difference image.

4.1.2 Data Analysis

The two final sets of images, one with sample gas in the cavity and one with nitrogen reference gas, provided a measurement of $\Delta I/I_0$ for each detection channel, i.e., the fractional change in integrated power due to absorption in the cavity. This quantity is equivalent to measuring the fractional change in cavity ringdown time ($\Delta\tau/\tau_0$) because the integrated intensity of an exponential decay is proportional to τ and then the ratio removes the proportionality constant.

The quantity $\Delta\tau/\tau_0$ can be expressed as a function of standard absorption-per-centimeter (α) by using

$$\begin{aligned} \Delta\tau/\tau_0 &= \frac{\tau(\alpha)-\tau_0}{\tau_0} \\ \tau(\alpha) = \frac{2L}{c(1-R^2e^{-2\alpha L})}; \tau_0 &= \frac{2L}{c(1-R^2)}, \end{aligned} \tag{4.1}$$

where L is the cavity length (obtained by counting the laser repetition rate, which is matched to the cavity FSR), and R is the single-mirror reflectivity [19]. This can be solved for α to give

$$\alpha = -\frac{1}{2L}\ln\left[\frac{1}{R^2}\left(1-\frac{1-R^2}{1-\frac{\Delta I}{I_0}}\right)\right], \tag{4.2}$$

where $\Delta I/I_0$ has been substituted for $\Delta\tau/\tau_0$. This equation was used to evaluate the per-channel absorption to give the final spectrum.

We process the images using MATLAB in several steps to generate the final spectrum. First, we use an image flattening algorithm to remove any background between neighboring VIPA fringes so that the minimum between fringes is zero. This background arises from both camera background and the VIPA fringes not being infinitely far from each other. After this, we track each fringe and average over the width of the fringe so that we now have a 2D image that only contains data from

the fringes (i.e., the vertical axis is position in the fringe and the horizontal axis is fringe number). We then take the difference between the sample image and reference image and normalize to the reference image. To account for broad absorption or intensity differences between the images, we flatten the baseline to remove very low frequency structure. In addition we use a high-pass filter to remove pixel-to-pixel noise. The result is shown as the absorption image in Figure 4.1(a). Finally, we identify the region corresponding to 1 FSR on this image and then concatenate each fringe together to form a 1D spectrum. Sometimes, an additional background was removed from this 1D spectrum with a low-order polynomial or median subtraction. We checked to make sure that this processing did not change the intensity of the absorption features.

The wavelength axis was calibrated using known line positions from the HITRAN database [271]. We found that it was necessary to calibrate the wavelength axis using a quadratic fit to at least five know lines. This calibration was necessary every time the grating was rotated to look at a new spectral range or if the different regions of the camera imaged were used. Most likely the non-linear correction arose from the non-linear dispersion of the VIPA and the use of an inaccurate value of the VIPA FSR. We made sure to use calibration lines that were present in the data or that were recorded without changing any part of the optical setup to avoid slight changes in the beam pointing into the VIPA which would change the calibration.

4.1.3 Results

4.1.3.1 Trace gases in N_2

To calibrate our CE-DFCS system, we first recorded the spectrum of the impurity gas cylinder plus 2.5 ppm H_2O in nitrogen (Figure 4.2). The measured absorption spectra are plotted below the axis as inverted peaks in black. For comparison, known spectral lines from HITRAN [271] (for CO_2, H_2O, and CH_4) and PNNL [48] (for H2S) are plotted above the axis. This overall spectrum is a composite of 11 individual spectra, spanning over 700 cm^{-1} (200 nm) spectral bandwidth with a step size of 0.014 cm^{-1}. The total acquisition time was approximately 10 hours; however, this

was severely limited by the switching speed of the gas flow system. By using a gas handling system designed for rapid gas switching (large tube diameter, short lines, high flow rates, etc.) switching times could be significantly reduced, resulting in an estimated acquisition time of ∼15 minutes per individual spectrum (∼2.5 hours for the full bandwidth) to achieve the current sensitivity. In addition, a carefully designed system using two separate cavities (one for sample gas and one for reference gas) can reduce common-mode amplitude noise and would require no gas switching, thus improving sensitivity and further reducing the required acquisition time.

The high resolution of the system can be observed clearly in Figures 4.2(a-c), where three separate regions of the spectrum are expanded, each with a 30-cm^{-1} span. Figure 4.2(a) shows a reference FTIR spectrum (H_2S, in purple, from PNNL), reference line positions for CO_2 (green, from HITRAN), and a spectrum with 1.1 GHz (0.035 cm^{-1}) resolution obtained with broadband CE-DFCS (black line). The current resolution is ideal for the 1-2 GHz wide Doppler and pressure broadened lines observed here. Since 5-10 comb modes sample each absorption feature, lineshape distortion is not an issue and single comb mode resolution is not required; however, if desired, resolutions of below 250 kHz (8×10^{-6} cm^{-1}) are obtainable with modifications to resolve single comb lines. In addition, Figure 4.2 illustrates that the relative frequency accuracy of the spectrum is high; we estimate it to be better than 100 MHz (0.0033 cm^{-1}) across the full 700 cm^{-1} spectral bandwidth by qualitatively comparing measured line positions with HITRAN. Again, by resolving individual comb lines, absolute frequencies with sub-kHz accuracies are possible. Indeed, CE-DFCS can be an effective and accurate tool for future additions and modifications to molecular absorption databases.

Since we are able to observe many absorption lines for each species, the concentration and minimum detectable absorption may be determined with a modification of the Hubaux-Vos regression method [272], which is similar to methods used by the International Union of Pure and Applied Chemistry [273] and Semiconductor Equipment and Materials International [274], using a single measured spectrum at a fixed concentration. All of these methods use a calibration curve of measured absorption versus sample concentration to determine the range of noise at zero concentration.

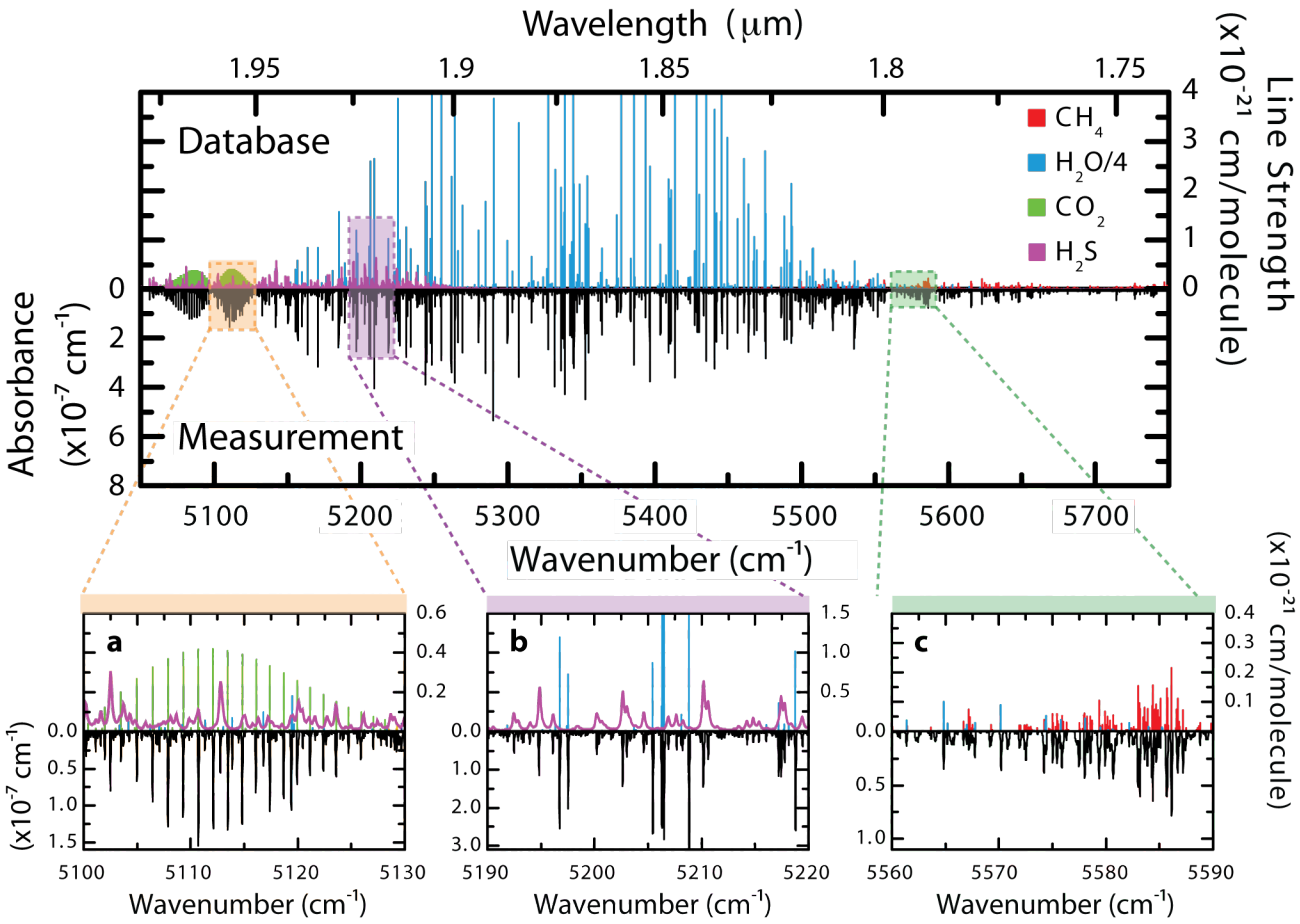

Figure 4.2: The spectrum of 10 ppm methane (CH_4), 10 ppm carbon dioxide (CO_2), 10 ppm hydrogen sulfide (H_2S), and 2.5 ppm water (H_2O) in nitrogen gas. Measured absorption peaks are shown in black below the axis. For comparison, spectral lines for CH_4, CO_2, and H_2O (line strength divided by 10) available from the HITRAN [271] database as well as H_2S lines from the PNNL [48] database are plotted above the central axis. Expanded spectral windows a, b, and c illustrate high-resolution absorption spectra of CO_2 and H_2S, H_2O and H_2S, and H_2O and CH_4, respectively.

Instead of measuring a single absorption feature as a function of sample concentration, we determine the measured absorption as a function of predicted absorption for lines with different strengths. This result allows us to determine both the noise-equivalent absorption and the concentration of the sample. In other words, one spectrum allows us to collect noise statistics over a wide range of signal strengths. To do this, we first predict the spectrum by approximating the concentration and using available HITRAN data with modifications due to pressure broadening, Doppler broadening, spectrometer resolution, and digital filters. We then plot each observed peak height versus the predicted height of the corresponding peak, as shown in Figure 4.3(a) for CO_2 and Figure 4.3(b) for H_2O (note that saturation was observed at higher absorptions, these points were not included in the analysis). The slope of a linear fit to this comparison data gives a correction factor from the approximated concentration to the true concentration and the uncertainty in the slope provides the uncertainty in the true concentration. In addition, the minimum detectable absorption is given by the 3σ standard error of the intercept, which specifies the measured absorption value that can be considered a non-zero true absorption with 99.86% confidence. This is shown graphically in Figure 4.3 by the value of the upper confidence interval when it intersects the y-axis. Since the confidence intervals shown are for the fit, it is not expected that all data should lie within them; the standard error of the fit is much smaller than the standard deviation of each data point due to the large number of points. The error on the intercept is roughly the same as the standard deviation for each data point.

For CO_2 in the nitrogen gas, we measure a concentration of 9.7(2) ppm (3σ uncertainty in slope of fit), consistent with the factory-specified impurity level in the cylinder at 10 ppm $\pm$ 10%. In addition, we obtain a minimum detectable absorption (3σ) of 4.5×10^{-9} cm^{-1}, corresponding to 325 ppb minimum detectable concentration by using the line strength of the strongest measured line. This data was recorded with a total integration time (T) of 180 s (time includes reference and sample images, but not gas switching times), which gives a 1-Hz minimum detectable absorption of 4.2×10^{-8} cm^{-1} $Hz^{-1/2}$. Similarly for H_2O, we measure 2.50(12) ppm, with an absorption sensitivity of 5.5×10^{-9} cm^{-1}or a minimum detectable concentration of 7 ppb. Since this absorption

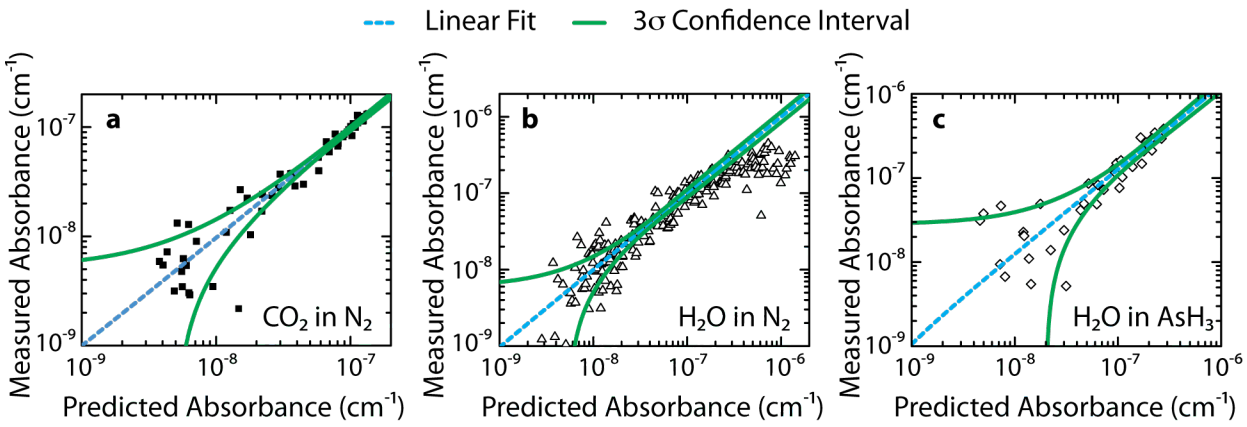

Figure 4.3: Double logarithmic plots of measured peak absorption versus predicted peak absorption from the HITRAN database for 10 ppm CO_2 in N_2 (a), 2.5 ppm H_2O in N_2 (b), and 1 ppm H_2O in arsine (c). Linear fits (dashed) of the data sets were performed up to a measured absorption of 2×10^{-7}, where signal saturation becomes noticeable. The corresponding 3σ (99.87%) confidence intervals (solid lines) are plotted along with the linear fits. Note that these confidence intervals are for the fits to the entire data. The 3σ error on the intercept gives the minimum detectable absorption, the slope of the fit gives a correction factor for the concentration, and the error on the slope gives the uncertainty in the concentration.

sensitivity is uniform across our measured spectral range, we project a minimum detectable concentration of 700 ppb for CH_4 and 370 ppb for H_2S. We also note the advantage of a dramatically increased dynamic range (larger than the single concentration data in Figure 4.3) obtained from simultaneously studying lines with significantly different strengths. Even though strong absorption peaks (above 2×10^{-7} cm^{-1}) provide signals that are saturated at the measured concentration, at lower concentrations they will be in a linear regime while the weak lines will be too small to measure. Additionally, lines that are too weak to measure at the current concentration will be detectable at higher concentrations. By using the range of water line strengths given in HITRAN for this wavelength region, we estimate a measurement range for water concentration from 7 ppb to 100 ppm with this system. The minimum detectable concentrations quoted here are for single lines, fitting many lines simultaneously would give even lower limits as discussed in Section 4.2.3.

4.1.3.2 Impurities in arsine

After calibrating the system, we filled the high finesse optical cavity with arsine interspersed with impurities. The same mixture measured in nitrogen was added to a purified arsine gas in a ratio of 1:8. Figure 4.4 shows the composite spectrum of trace water recorded in the background of arsine gas at ∼160 torr. Again, measured absorption features are plotted as inverted peaks below the axis, with available HITRAN spectral lines on water plotted above the axis. It is apparent that the absorption of arsine continues to increase rapidly towards both ends of the spectral window; past the plotted range, the arsine absorption begins to decrease at ∼1.94 μm, but even at 1.97 μm it was still too strong to collect reliable spectra of trace species. The density of the arsine absorption obscured the other impurity lines, making it only possible to observe water in this experiment. Because of the strongly absorbing background gas, it is clearly a major advantage to have a spectroscopy system based on CE-DFCS providing broad bandwidth and high spectral resolution. Such a system allows us to easily identify and quantify water lines that are isolated from arsine absorption features, as seen by the two zoomed-in bottom panels of Figure 4.4. From this data (see Figure 4.3(c)) we determine a water concentration of 1.27(8) ppm and an absorption

sensitivity of 2.4×10^{-8} cm^{-1} with an integration time of 600 s, which corresponds to a minimum detectable concentration for water in arsine of 31 ppb. Arsine is known to have a weak band centered at 5150 cm^{-1}, which is probably causing the absorption on the red side of the spectrum.

This first demonstration of CE-DFCS for impurity monitoring of industrial process gases has shown an absorption detection sensitivity (3σ) of 3.9×10^{-7} cm^{-1} Hz$^{-1/2}$ for water in arsine around 1.85 μm (5400 cm^{-1}). The 200 nm bandwidth of our system also allowed us to look at absorption regions of other impurities (CH_4, CO_2, and H_2S), which were obscured by densely spaced arsine absorption lines. Furthermore, there is significant room for improvement, which would open open the door for continued industrial applications, as discussed in 4.3. One direction for improvement could be by extending the spectral coverage to the mid-infrared, which we cover next.

4.2 Mid-infrared comb spectroscopy

In this section we discuss our initial demonstrations of frequency-comb FTS based on a high power OPO that operates in the important mid-infrared window from 2100 cm^{-1} to 3700 cm^{-1}. Our system is capable of achieving part-per-billion (ppb)-level sensitivity with an integration time of 30 s or less for a variety of important molecules, such as the greenhouse gases methane, carbon dioxide, and nitrous oxide [275, 276, 277], as well as isoprene and formaldehyde, which are important contributors to pollution [278, 279]. Furthermore, we demonstrate detection of ethane and methanol, which are subjects of interest in human breath analysis [280, 281, 282]. These molecules represent just a small set of trace gasses within the detection range of this new system.

The OPO comb source was discussed in detail in Section 2.4. Idler light from the OPO is coupled into a Herriott multi-pass cell (New Focus 5611) with 0.3 l volume and a total path length of 36.4 m (182 passes), which contains the sample or reference gas. The spatial coherence of the laser source makes the coupling simple and efficient. The multi-pass cell provides a modest path-length enhancement and works over a very broad spectral bandwidth; for higher sensitivity, an enhancement cavity could be used instead, as demonstrated in [55]. We record the spectrum after the multi-pass cell with the scanning Fourier-transform interferometer discussed in Section 3.3.2. To

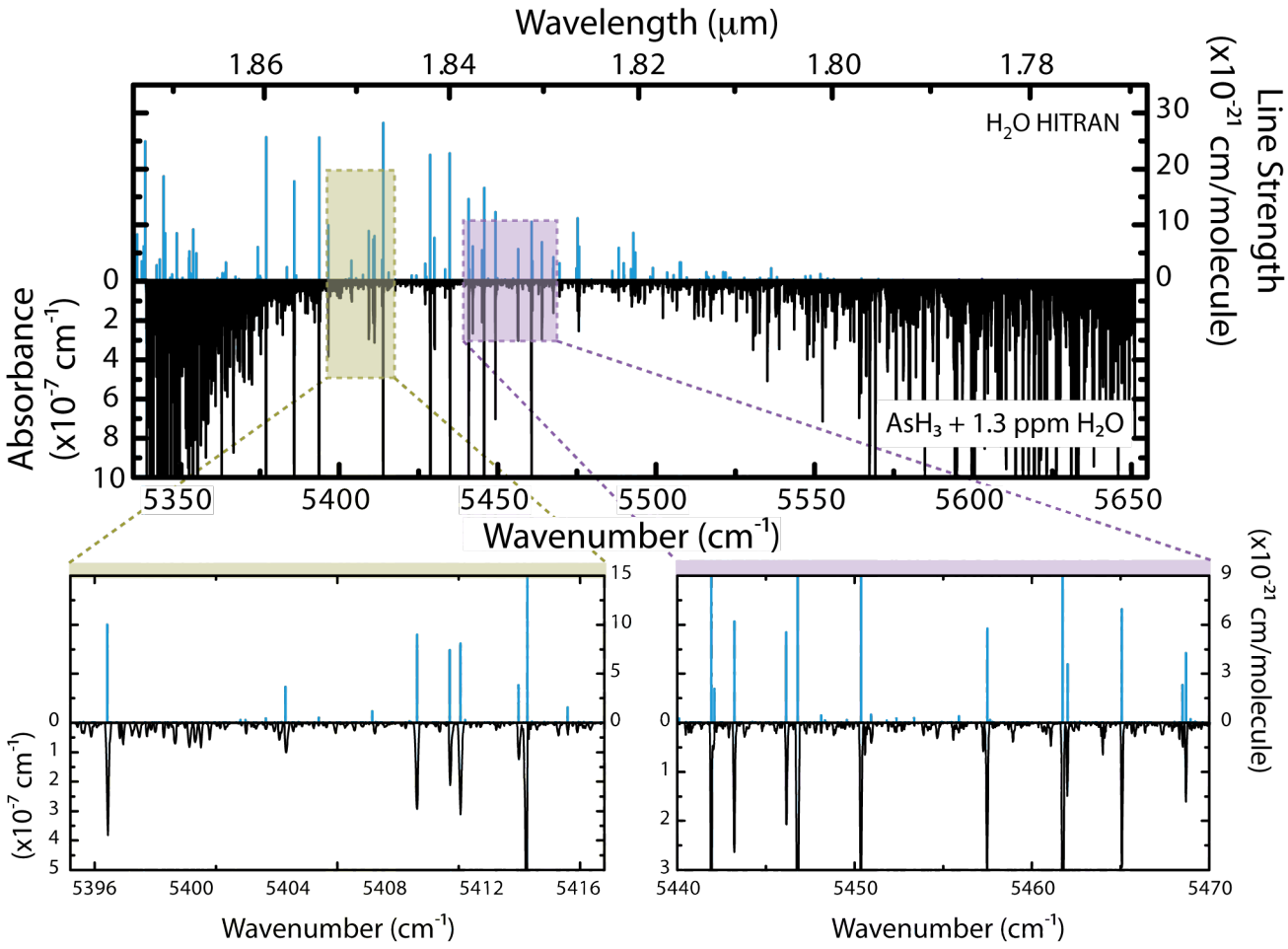

Figure 4.4: Trace water in arsine. The measured spectrum of 1.27 ppm of water vapor in arsine gas is plotted in black below the axis and the HITRAN reference lines for water are shown in blue above the axis. The arsine absorption continues to increase both above 5650 cm^{-1} and below 5350 cm^{-1}, precluding any additional measurements. The two insets show easily resolvable water lines even in a background absorbing gas.

minimize drifts of the spectrum during the measurement, the OPO comb is phase-stabilized to the pump laser, whose repetition rate is locked to a microwave reference for long-term stability. Using a phase-locked OPO comb also ensures low intensity noise compared to non-comb supercontinuum sources.

To extract the absorption spectrum, we measure first the laser spectrum through the sample gas $I_s(\nu)$, then purge the cell, fill it back to the original pressure with N_2, and measure the reference spectrum $I_0(\nu)$. The spectral absorbance $\alpha(\nu)$ is then determined via $\alpha(\nu) = -\frac{\ln[I_s(\nu)/I_0(\nu)]}{L}$, where L is the optical path length inside the multi-pass cell. The gas concentrations are extracted from the data via a numerical fit of a model spectrum calculated with spectral data (line positions, line strengths, pressure broadening and shift coefficients) from HITRAN [271] or reference spectra from the PNNL NWIR database [48] (when HITRAN data was not available) based on a modified Marquardt algorithm [283]. The parameters for the fitted Voigt profile are a concentration value for each sample species, a polynomial baseline, and a frequency correction (to account for misalignment of the beams inside the interferometer, typically on the order of 10^{-3} cm^{-1}). The uncertainty value for the concentration is extracted from the covariance matrix.

4.2.1 Measurement of individual molecular species

To demonstrate the versatility and wide spectral coverage of our spectrometer we recorded spectra of a variety of molecular species (each diluted in pure N_2) in different spectral regions spanning from 2170 cm^{-1} to 3520 cm^{-1}. Figure 4.5 shows measured spectra (black) of nitrous oxide (9.0 ppm in Figure 4.5(a) and 142 ppm in Figure 4.5(f)), 58 ppm formaldehyde (Figure 4.5(b)), 11 ppm ethane (Figure 4.5(c)), 10 ppm methane (Figure 4.5(d)), and 16 ppm isoprene (Figure 4.5(e)). With the exception of the high-resolution spectrum in Figure 4.5(d), all of these spectra were recorded with integration times of 30 s or less. Each plot also shows the fitted spectrum using data from HITRAN or PNNL, as indicated in each graph (plotted in purple and negative for clarity). These measurements show the instruments ability to rapidly cover a wide spectral region with high resolution and extract concentrations regardless of the structure of the

absorption spectrum. For example, isoprene exhibits a continuous absorption band, which makes quantitative measurements susceptible to errors from baseline drifts. Being able to determine the concentration of such a sample is extremely valuable since molecules with continuous bands (e.g., isoprene, methanol, ethanol, acetone, etc.) are highly important for many applications. In additional, removing broad background due to scattering is important for measurements in the atmosphere.

4.2.2 Instrument performance limits

We have made systematic characterizations of the limits of our system in terms of resolution, measurement accuracy, absorption sensitivity, and concentration detection limit. From measurements of the noise floor we obtain an absorption sensitivity of 3.8×10^{-8} cm^{-1} Hz$^{-1/2}$ per spectral element. At a center frequency of 3000 cm^{-1}, we detect ∼45,000 simultaneous channels at maximum resolution. Using the line strength of the molecular transitions as well as the sensitivity and bandwidth of our instrument, we determine the noise equivalent concentration (NEC) at typical measurement settings of 0.014 cm^{-1} unapodized resolution, 600 Torr of N_2 background pressure, and 30 s total integration time (5 averaged scans for reference and sample). The NEC for a small collection of different molecular species within our spectral range is summarized in Table 4.1 (column 3), which shows that ppb-level detection limits are obtained for most molecules in only 30 s. We further confirmed that the noise averages down for at least 6 min, which reduces the NEC by $\sqrt{12}$.

To test the repeatability of our instrument, we take ten independent measurements of a methane mixture certified as 10 ppm (± 5%) in N_2 at a pressure of 600 Torr, 0.014 cm^{-1} resolution, and 30 s integration time and extract the concentration of each dataset from a numerical fit of a HITRAN reference spectrum. We determine the average CH_4 concentration to 10.107(19) ppm, which is in agreement with the specified concentration of the gas mixture and demonstrates that the precision of the entire system (optical and gas handling) is better than 0.2%.

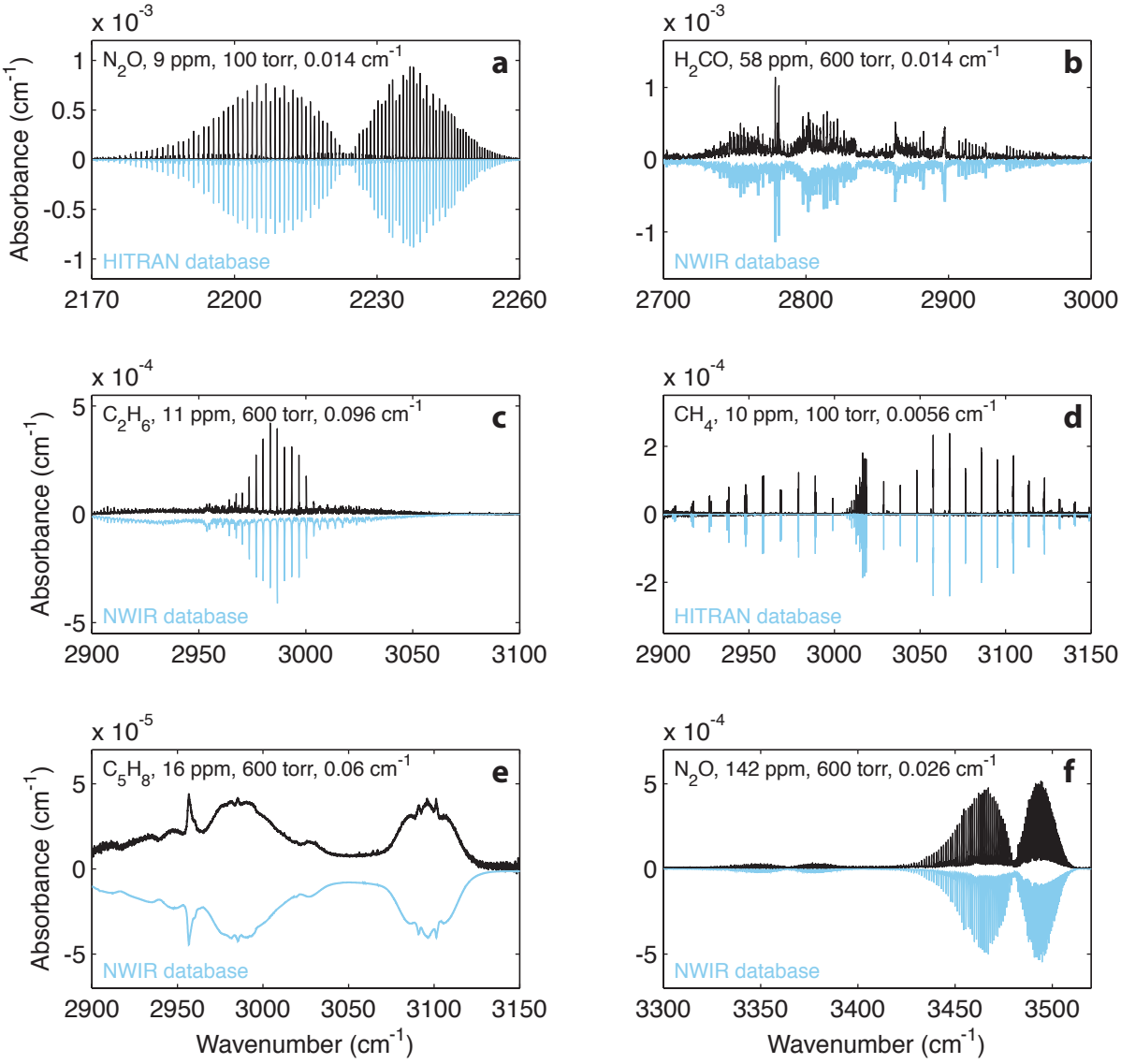

Figure 4.5: Collection of absorption spectra throughout the operating range of our mid-IR frequency comb Fourier transform spectrometer (black) and comparison to HITRAN or PNNL-based fits (purple, plotted negative for clarity). The trace concentration, nitrogen pressure, and spectral resolution are designated in the panels; (a) ν_3 band of nitrous oxide (N_2O) at a concentration of 9 ppm, a pressure of 100 Torr N_2, and a resolution of 0.014 cm^{-1}; (b) formaldehyde (H_2CO), 58 ppm, 600 Torr, 0.014 cm^{-1}; (c) ethane (C_2H_6), 11 ppm, 600 Torr, 0.096 cm^{-1}; (d) methane (CH_4), 10 ppm, 100 Torr, 0.0056 cm^{-1}; (e) isoprene (C_5H_8), 16 ppm, 600 Torr, 0.058 cm^{-1}; (f) $2\nu_2+\nu_3$ and $\nu_1+\nu_3$ band of N_2O, 142 ppm, 600 Torr, 0.026 cm^{-1}. All spectra are obtained with a single wavelength setting of the OPO except (a), which is a combination of two measurements at different central wavelengths.

Table 4.1: Detection limits for a collection of important molecules within the spectral range of our mid-IR FC-FTS. The third column shows the noise equivalent concentration (NEC) results, which are based on the measured absorption sensitivity of 3.8×10^{-8} cm^{-1} $Hz^{-1/2}$ per spectral element under typical experimental conditions of 600 Torr N_2 pressure, 0.014 cm^{-1} unapodized spectral resolution, and 30 s of total integration time (5 averages). The fourth column shows the theoretically estimated multi-line detection limits using the same noise and resolution conditions as those for column three. The fifth column displays the experimentally obtained concentration detection limits from the multi-line fits to measured spectra. The disagreement between the theoretical and experimental values is due to the fact that some spectra were not measured at the best possible noise performance of the system. Note that significantly lower detection limits are achievable with longer integration times (tested to at least 6 min).

Molecule	Band Center (cm^{-1})	NEC (ppb)	Theor. multi-line detection limit (ppb)	Expt. multi-line detection limit (ppb)
CH_4	3020	22	2.0	5
C_2H_6	2990	23	1.8	18
C_5H_8	3000	370	4.3	7
H_2CO	2780	54	2.3	40
CH_3OH	2950	350	3.6	40
N_2O	2220	8	0.5	5
CO_2	2350	2.2	0.2	0.5

4.2.3 Multi-line fitting advantage

An important and already recognized advantage of broadband spectroscopy is that the ability of detecting multiple absorption peaks over a wide region allows one to achieve a lower detectable concentration than with single-peak measurements [284, 285, 286]. In general, the multi-line advantage scales with the integrated area under the absorption curve. To understand this, we derive an equation that allows the estimation of the concentration detection limit obtained with multi-line analysis via the known structure of a molecules absorption spectrum. We assume that $\alpha(\nu)$ is the absorption spectrum measured at k discrete frequencies ν_i with a standard deviation σ_α, which is uniform over the spectrum. The model spectrum $\alpha_M(\nu)$ is calculated for a given sample concentration C at the experimental pressure and temperature. For simplicity we assume that there is no baseline in our spectrum and that the model spectrum has exactly the same frequency axis as the measured spectrum. We would like to find the parameter N (which will be used to estimate the concentration), for which differences between measured and model spectra multiplied by this parameter will be minimized. To do this, we fit the value of parameter N using a linear least-squares method to minimize the function

$$F(N) = \sum_{i=1}^{k} [\alpha(\nu_i) - N\alpha_M(\nu_i)]^2 \tag{4.3}$$

so

$$\frac{dF}{dN} = \sum_{i=1}^{k} 2[\alpha(\nu_i) - N\alpha_M(\nu_i)][-\alpha_M(\nu_i)] = 0. \tag{4.4}$$

Solving this equation gives

$$N = \frac{\sum_{i=1}^{k} \alpha(\nu_i)\alpha_M(\nu_i)}{\sum_{i=1}^{k} \alpha_M^2(\nu_i)}. \tag{4.5}$$

Neglecting error in the model spectra, we can write

$$\sigma_N^2 = \sum_{i=1}^{k} \left[\frac{\partial N}{\partial \alpha(\nu_i)}\right]^2 \sigma_\alpha^2 = \sum_{i=1}^{k} \left[\frac{\alpha_M(\nu_i)}{\sum_{i=1}^{k} \alpha_M^2(\nu_i)}\right] \sigma_\alpha^2 = \frac{\sigma_\alpha^2}{\sum_{i=1}^{k} \alpha_M^2(\nu_i)}. \tag{4.6}$$

This shows that the multi-line analysis improvement of the detection limit depends on the shape of the spectrum and scales with its integrated absorption.

This finding becomes apparent when comparing spectra of methane (Figure 4.5(d)) and isoprene (Figure 4.5(e)), which exhibit clearly different structure. The numbers from Table 4.1 show that the multi-line analysis improves the detection limit by factors of 11 for CH_4 and 93 for C_5H_8 owing to the much larger integrated area of the continuous isoprene absorption spectrum. To confirm this finding, we take the uncertainty of the fitted concentrations of the ten measurements of CH_4, which are extracted by utilizing the entire recorded spectrum, and compare it against the uncertainty when using only one of the strong peaks of the P-branch. The single-peak fits give an uncertainty of 20-30 ppb, which is consistent with the NEC. In contrast, the multi-line fit yields an uncertainty of only 7 ppb, which is significantly lower than the NEC and confirms that analysis of the entire absorption spectrum can indeed decrease the detection threshold below the classical limit given by the single-line S/N ratio. The detection limits obtained from the multi-line fitting procedure for other measured molecules are summarized in the fifth column of Table 4.1. The fourth column in Table 4.1 shows the theoretical estimates for detection limits under the same conditions of noise and resolution used for the third column. The scaling of the detection limit indicated by the theory corresponds well with the experimental numbers: for example, the improvement in detection limit for C_5H_8 is 12 times as high as the one for CH_4 due to the much larger integrated absorption of the continuous spectrum of isoprene. The experimental results shown in the fifth column of the table differ from the theoretical estimates due to the fact that most spectra were not recorded during the best possible noise performance of the system, which depended on day-to-day alignment and was probably limited by etalons or laser noise.

4.2.4 Determination of absolute concentrations of a gas mixture

Most real-world samples measured for atmospheric science, breath analysis, or trace gas monitoring contain more than one species in a particular spectral window. The overlapping absorption features of different molecules make their unambiguous detection nearly impossible if sufficient spectral coverage and resolution are not available. The C-H-stretch region around 3000 cm^{-1}, for instance, contains absorption features of practically any hydrocarbon with sufficient abundance. To

demonstrate the capability of our spectrometer, we measure the absorption spectrum of a mixture of trace amounts of formaldehyde, methanol, and water in nitrogen and determine their absolute concentrations. The spectrum was recorded at a resolution of 0.014 cm^{-1} and an N_2 pressure of 600 Torr under a total integration time of 30 s. Here, methanol – as a molecule without a clear line spectrum – would represent a significant challenge for a cw laser measurement. Figure 4.6(a) shows the measured spectrum of the $H_2CO/CH_3OH/H_2O$-mixture (black curve) in the spectral range from 2900-3050 cm^{-1} and the overall fitted result (gray, plotted negative for clarity). Model spectra created from HITRAN (for H_2CO and H_2O) and PNNL (for CH_3OH) of the individual components at their fitted concentrations are shown in magenta (H_2CO), green (CH_3OH), and blue (H_2O). The overall fit is remarkably accurate, as demonstrated by the fit residuals plotted in Figure 4.6(b). Although the spectrum contains many overlapping features and some of them (from CH_3OH) do not exhibit sharp lines, the broad bandwidth and high spectral resolution of our FC-FTS in combination with the multi-line fitting procedure enable precise determination of the concentrations of all three components. The obtained values are 47.1(1) ppm for H_2CO, 58.30(4) ppm for CH_3OH, and 813(7) ppm for H_2O.

Another important feature of the current system is the large dynamic range in concentration detections. To demonstrate this, we measured a sample of laboratory air, which contains atmospheric methane; however, the high abundance of water vapor, whose absorption lines strongly overlap with the CH_4 band at 3020 cm^{-1}, imposes a particular challenge for trace gas detection. Although the strongest H_2O lines are already close to saturation, the fitting algorithm is able to extract both concentrations, 2.02(1) ppm for CH_4 and 1.03(5)% for H_2O.

4.3 Future applications

In the previous two sections, we highlighted some of the capabilities of frequency-comb spectroscopy systems for trace gas detection. In particular, we saw in the measurement of contaminants in arsine gas how CE-DFCS using a VIPA spectrometer provides high-sensitivity measurements (around 10^{-8} cm^{-1} $Hz^{-1/2}$) with a simultaneous bandwidth of 50 cm^{-1}. This one comb source

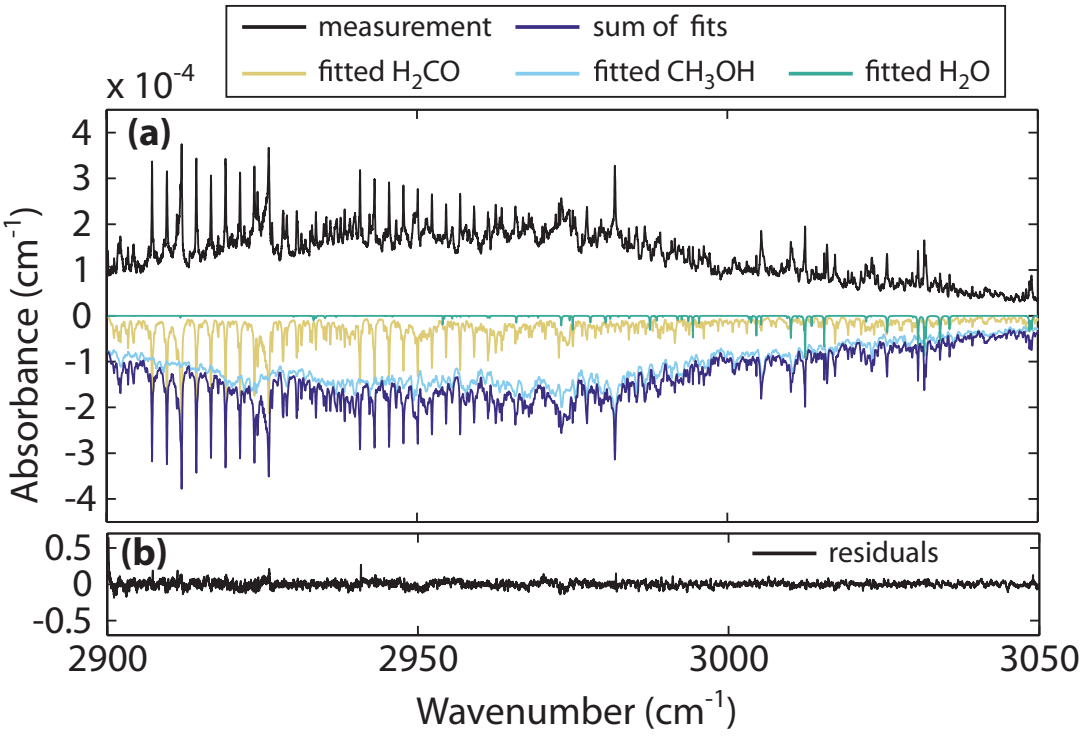

Figure 4.6: Multispecies simultaneous detection. (a) Measured spectrum of a mixture of formaldehyde, methanol, and water at an N_2 pressure of 600 Torr and a resolution of 0.014 cm^{-1} (black), as well as the fitted spectra based on HITRAN and PNNL of the three components (H_2CO, magenta; CH_3OH, green; H_2O, blue) and their sum (gray). The fit gives abundances of 47.1(1) ppm H_2CO, 58.30(4) ppm CH_3OH, and 813(7) ppm H_2O. (b) The residual of the overall fit displays no remaining structure.

can provide spectral coverage across the entire 1-2 μm spectral region. We also saw how the high resolution enables precise measurements of trace species even in the presence of large absorption from other species. The OPO-based spectroscopy measurements demonstrate the application of comb spectroscopy to the mid-IR, which provides access to stronger absorption features for many different species. We showed the ability to achieve low-ppb detection limits for many molecules in 30 s total integration time (including reference and sample spectrum) at an unapodized resolution of 0.014 cm^{-1}. The significant decrease in acquisition time compared to standard FTIR is a direct result of the high spectral brightness and spatial coherence of the frequency comb source. While the absorption sensitivity of this system is lower than a cavity-enhanced system, the concentration detection limits are still very low due to the strong molecular absorptions and the system can operate anywhere from around 3-5 μm (2100-3700 cm^{-1}). In addition, we saw how the broad bandwidth provides better detection limits (or correspondingly higher precision on the measured concentration) as well as the ability to measure mixtures, even when the species in the mixture has continuous absorption features. We now consider some prospective applications of comb spectroscopy and what might be required for these applications. In particular, we consider potential applications to gas purity analysis, breath analysis, atmospheric chemistry, and chemical physics.

The arsine gas purity experiment is one example of the application of comb spectroscopy to process gas analysis. In addition to arsine gas, there are over 30 other gas used in the production of semiconductor devices [266]. Depending on what the gas is used for, there are a wide range of impurities, including water, CH_4, CO_2, CO, and hydrocarbons, that can all have a negative effect on the product. Thus, there is interest in systems capable of detecting multiple contaminants simultaneously in the presence of different process gases. While the first test in arsine was only able to detect one impurity, we showed how this spectral region could detect multiple impurities depending on the gas. Several potential improvements could fully demonstrate the capability of CE-DFCS for process gas measurements. Of course, the gas flow system could be improved to enable rapid switching between sample and reference. In addition, a different readout system that allows reduction of FM-AM noise, such as FC-FTS, could improve the sensitivity (see Table 3.1)

and could enable the use of multiple mirror sets for a wider wavelength coverage. By covering several regions throughout the 1.1-2.2 μm spectral range, it should be possible to detect multiple contaminants. For example, CO_2 has strong bands from 4800-5000 cm^{-1} that might be detectable since we think the arsine absorption that we saw starting at 5350 cm^{-1} is probably due to a weak arsine band centered at 5150 cm^{-1}. Other regions in the near-IR might provide other transparency windows as well, although data on weak arsine bands in the near-IR is limited, so it would be beneficial to scan the arsine absorption first at lower sensitivity. This system could potentially be combined with a single cavity using Brewster angle prisms [171] to cover the full range of the source using a single cavity. Several potential transparency windows also exist in the mid-infrared around 3800, 2500, and 1500 cm^{-1}.

A similar application is monitoring of emissions from industrial applications. For example, greenhouse gases are regulated by the EPA and typically must be monitored. Fluorinated compounds, such as fluorocarbons, NF_3, and SF_6, are major greenhouse gases and are also significant emissions from semiconductor manufacturing [287]. Fluorinated compounds also play a significant role in the removal of ozone at high elevation. A system capable of simultaneously measuring multiple greenhouse gases and fluorinated compounds would potentially have enormous industrial applications. All of these compounds absorb in the 800-1500 cm^{-1} region, which will be within the range of an OPO using OP-GaAs.

The analysis of trace species in breath for disease detection is currently an extremely active field of research [288, 289, 290, 291]. Besides water, oxygen, nitrogen, and carbon dioxide, breath contains hundreds of other compounds in varying quantities. Table 4.2 lists the more abundant ones and typical ranges in human breath. Currently, there are two primary directions for breath research: detection of a single or a few small species and detection of many volatile organic compounds (VOCs) simultaneously. Several FDA approved breath tests already exist based on the first research direction such as measurement of NO for asthma, CO for liver disease (specifically, neonatal jaundice), and methane for various gastrointestinal issues [292]. There are preliminary indications that other species may be useful for testing for diseases or monitoring treatment, although

the evidence is not conclusive: the combination of NO, CO, CO_2, and N_2O has been investigated for chronic obstructive pulmonary disease (COPD) [293]; acetone has been shown to have some correlation with blood glucose and is possibly an indicator for diabetes [294, 295, 296]; ammonia (and possibly methylamines) show correlation with kidney function [297, 298]. In addition to these molecules, breath contains several hundred other VOCs present typically at the 0.1-10 ppb range [299, 300, 301]. Unlike most of the smaller molecules, the physiological origin of many of these is not known, which makes direct links to certain diseases more challenging. It is believed that at least some of the VOCs might be caused by oxidative stress – that is, reactions with oxygen-containing radicals such as OH or O_2^- – which can lead be indicative of various diseases [302, 303, 304]. Because of the unknown origin of most VOCs, studies typically measure many compounds and look for correlations with diseases [305] such as tuberculosis [306], cancer [307, 308, 309, 310, 311], and COPD [312]. Several smaller molecules and VOCs such as CO, H_2O_2, and ethane may also be indicative of oxidative stress [313, 314, 315].

While many of these studies have determined some correlation with a disease – for example, $> 80\%$ sensitivity and specificity have been demonstrated for cancer detection [307] – detecting molecules and identifying a potential correlation are not the primary challenges in breath analysis. In fact, these steps are so easy that they can even be accomplished by dogs [317]! Detection of VOCs is typically performed with gas chromatographymass spectrometry (GC-MS), which has the disadvantage of not being real-time; however, newer techniques such as proton-transfer reaction mass spectrometry (PTR-MS) can selectively detect most VOCs with low-ppt sensitivity and < 100 ms time resolution [318, 319, 320]. These systems are currently commercially available and are moderately portable. The challenges of breath analysis instead are related to the large natural variability present in human breath (as can be seen by the ranges quoted in Table 4.2), confounding variables such as smoking and environmental variations, as well as issues related to breath collection [289, 321, 309, 291]. Looking through many of the references given here, this becomes immediately apparent as many of the studies show results where the mean value of the measured compound is statistically different between the test group and a control group, but the measured range overlaps

Table 4.2: Typical range for the most common trace species in human breath. From [293, 316, 301, 292]

Compound	Concentration
Methane	1-100 ppm
CO	1-3 ppm
Acetone	0.3-3 ppm
N_2O	300-800 ppb
Ammonia	0.2-1 ppm
Methanol	∼500 ppb
Isoprene	10-300 ppb
NO	1-100 ppb
2,3-Butanedione	1-100 ppb
Ethane	2-20 ppb
Other VOCs	0.1-10 ppb

significantly between the two. Because of this, much of the focus is starting to be more towards full clinical studies and less towards small proof-of-principle studies.

So what can frequency comb spectroscopy contribute to breath analysis? In principle, the simultaneous detection of a wide range of VOCs simultaneously would be possible, but this requires very accurate fitting of overlapping, broadband absorption profiles. This is complicated without *a priori* knowledge of all species to include and due to dependences of the absorption profiles with temperature and pressure and various baseline etalon effects. Given the capabilities of PTR-MS, this is probably not the best approach. One potentially beneficial application is to instead demonstrate the ability to detect all of the other compound listed in Table 4.2 simultaneously, or at least in one system, with moderate time resolution. Since the required detection limit would be mostly above 10 ppb, this could be potentially be accomplished with a multipass cell. Such a system would enable multiple breath tests in one system, which would be beneficial for correlating different effects and as a diagnostic tool.

Another field that relies significantly on trace gas analysis is atmospheric chemistry. There are three primary directions for experimental atmospheric chemistry: determination of sources of pollution and tracking pollution through the atmosphere; studying reactivity in the atmosphere; studying reactivity in controlled laboratory settings. Some of the different species studied in field measurements are given in Table 4.3. Many studies focus on understanding several primary atmospheric reaction cycles [199, 322]. The HOx cycle (OH, HO_2, etc.) is responsible for the formation of ozone as well as the oxidation of many VOCs and is initiated by the photolysis or reaction of ozone. This is interconnected with the NOx cycle, which can compete in the oxidation of VOCs [199, 323]. The products or intermediates of the VOC oxidation reactions can further react, resulting in radical recycling and also in the formation of aerosols. Oxygenated halogens (e.g., IO, ClO, and BrO) are also important because they may react with VOCs at low elevation in the atmosphere and also cause tropospheric ozone destruction. In addition, because many of the reactions in these cycles are light-dependent, the dominant cycles and reactions are not only spatially dependent but are also day-night dependent. In order to understand the global tropospheric chemistry, it is thus

important to measure multiple different species from each cycle in different regions and both during the day and night. Despite considerable advances in understanding atmospheric chemistry, there still are many surprises [324, 325, 326, 327] and reactions that are not fully understood [328, 329]. In addition to measurements to understand the chemistry of reactive species, various sources of pollution must be measured so that they can be included into models. These include the halogenated carbons mentioned earlier related to semiconductor processing, various greenhouse gases (such as CH_4, CO_2, SF_6, etc.), as well as VOCs, NOx, and SO_2 from industrial sources [279, 330, 331] and biogenic sources.

Currently, most systems for point detection of trace species rely on incoherent broad-band cavity enhanced absorption spectroscopy (IBB-CEAS), LED-based cavity-enhanced differential optical absorption spectroscopy (LED-CE-DOAS) – both of which are broad bandwidth – or cw-laser spectroscopy. The advantage of comb spectroscopy for atmospheric measurements can be seen from the recent demonstrations of N_2O, IO, BrO, and formaldehyde detection for measurements off the coast of France and Antarctica [185, 184]. If we compare the sensitivity to IBB-CEAS [334, 335] or LED-CE-DOAS [336] systems operating in the same spectral region, the comb system provides one to two orders of magnitude improvement in the sensitivity. In addition to lower detection limits, the improved sensitivity is also critical for high-speed measurements. This capability is important not only for measurements in moving vehicles (e.g., airplanes, cars, ships) where the time resolution is necessary for spatial resolution [330] but also for Eddy covariance flux measurements, which provide information about surface-atmosphere gas exchange [328, 337]. For atmospheric measurements, it is necessary to deal with background losses due – for example – to aerosols [336], which would cause problems for cw-laser systems; however, the bandwidth of the comb enables continuous spectral features to be fit as well and so should mitigate this issue.

Laboratory experiments of reactions seek to provide information about the rates of each reaction [338, 339].[1] For many kinetics studies, it is also desirable to study multiple species

[1] A compilation of currently accepted reaction rates is available at `http://www.iupac-kinetic.ch.cam.ac.uk/`

Table 4.3: Example trace species in the boundary layer (lowest part of the troposphere). If ranges are given, they correspond to the range from remote to polluted environments. If single values are given they correspond to the average value from measurements. From [332, 199, 333, 331].

Compound	Concentration
CH_4	1.7 ppm
N_2O	300 ppb
NO_2	0.01-2000 ppb
NO_3	1-500 ppb
N_2O_5	$<$ 15 ppb
NH_3	0.02-100 ppb
Nitric Acid	0.1-50 ppb
SO_2	0.01-10 ppb
H_2S	0-800 ppt
Isoprene	0.6-2.5 ppb
BrO	0.1-10 ppt
IO	0.1-2 ppt
$CFCl_3$	268 ppt
CF_2Cl_3	533 ppt
CH_3Cl	500 ppt
SF_6	4 ppt
Other halocarbon species	10-100 ppt
CO	200 ppb
HCHO	0.1-60 ppb
Glyoxal (CHOCHO)	0.01-1 ppb
Acetone	0.2-9 ppb
Alkanes	1-300 ppb
Aromatics	0.01-3 ppb
Alkenes/Alkynes	0.01-10 ppb
Terpenes (e.g. α-pinene)	0.03-2 ppb

simultaneously in order to obtain information about branching ratios and rate constants between multiple reaction paths and to identify unexpected paths [323]. It is also ideal to have high time resolution to potentially identify intermediates that may contribute to further reactions. Finally, reactions need to be studied over a range of atmospherically relevant temperatures and pressures [323, 329]. A technique capable of rapid, sensitive detection of many species would thus have wide-ranging applications. We recently demonstrated time-resolved frequency-comb spectroscopy based on a VIPA spectrometer in the mid-IR combined with a reaction flow cell [329] that enabled measurements of the photoproducts of acrylic acid photolysis with a time resolution of 25 μs [56]. In particular, we measured the deuterated-HOCO radical, which is an intermediate in the OH + CO reaction [340]. We also measured several unexpected products that we are still investigating. With increased sensitivity, perhaps by pushing further into the mid-IR [341], this system could enable direct measurement of the Criegee intermediate in the ozonolysis of alkenes [342, 343]. Ozonolysis of alkenes is an important reaction in atmospheric chemistry and the stabilization of Criegee intermediates may help to understand the unexplained OH radical concentrations in the atmosphere [344, 345, 346, 347, 348]. Even without high time resolution, frequency comb systems combined with atmospheric chambers could provide a new method of sensitively measuring stable-product branching ratios [349, 350].

A final application of comb spectroscopy is the measurement of stable isotope ratios, which is useful for breath analysis as well as for atmospheric and geochemistry. For breath analysis, the kinetics of various processes such as metabolism and liver function can be tested by ingesting ^{13}C-labeled substances and monitoring the appearance of, for example, $^{13}CO_2$ [291, 351, 352]. Isotope ratios in CO_2 and CH_4 can also provide information about pollution sources and sinks [353, 354], the history of the atmosphere from ice core samples [355], and the history of other planetary atmospheres [356]. CE-DFCS could in principle provide a significant improvement in the precision of isotope ratio measurements compared to other portable techniques (mass spectrometry techniques are the most precise, but are not portable) because many lines can be measured simultaneously. A proof-of-principle measurement showed the determination of isotope ratios to 4 parts-per-thousand

in breath [44]. Improvements could potentially be made by measuring in different bands – for example, the 2 μm or 4.3 μm bands of CO_2 – to measure less abundant isotopes such as ^{18}O or ^{17}O. To fully demonstrate the capabilities of CE-DFCS for these measurements, more studies of the precision and accuracy – ideally down to the sub-part-per-thousand level [357] – are needed.

4.4 Conclusions

In this chapter, we highlighted some of the real-world applications of comb spectroscopy for sensitive detection of multiple trace species simultaneously. We showed how the bandwidth enables detection of trace impurities in a large absorbing background and measurement of species without highly resolved absorption features, both of which are challenging for cw-laser techniques. We then discussed some future applications of comb spectroscopy including extensions of the semiconductor gas purity analysis, breath analysis, atmospheric measurements, and isotope ratio measurements. In particular, we showed where the broad bandwidth and high sensitivity would provide advantages such as multi-species detection capabilities, rapid measurements, and high precision.

We are also currently developing a cryogenic buffer-gas cooled CE-DFCS system to study the spectra of molecules at 4 K. This will provide significantly narrower absorption lines and will concentrate the absorption strength into a much smaller number of lines, which could be advantageous for trace gas detection and mixture analysis. In addition, such a system has exciting prospects for studying high-resolution spectra of complicated molecules.

Chapter 5

Velocity-modulation spectroscopy of HfF^+

In this chapter, we discuss the survey spectroscopy that we performed on HfF^+ using both frequency comb and cw-laser velocity modulation spectroscopy as detailed in Section 3.4. Trapped HfF^+ is used in the measurement of the electron electric dipole moment (eEDM) discussed in Chapter 6, but for the experiment to be successful we first needed to know more about the electronic structure of HfF^+. In particular, we wanted to learn several things from broad-bandwidth velocity modulation spectroscopy for application to the eEDM experiment:

(1) precise spectroscopic constants for the ground $^1\Sigma^+$ state and metastable $^3\Delta_1$ state, which will be used for the eEDM measurement;

(2) measurement of the parity doubling (Λ-doubling) in $^3\Delta_1$ $J = 1$;

(3) transitions from both states that may be useful for laser-induced fluorescence and state manipulation;

(4) an intermediate state for a Raman transition from the $^1\Sigma^+$ to the $^3\Delta_1$.

Unfortunately, the early theory and experimental results were no where near accurate enough for application to the trapped ion experiments and only were able to provide a rough guide to interpreting the HfF^+ spectra. Here, we provide an introduction to diatomic molecular spectroscopy and then apply this to detailed analysis of the data, aimed at the goals above.

5.1 Results

Figure 5.1(a) shows the spectrum of HfF^+ acquired using the comb-vms system in blue (offset for clarity) as well as all data obtained with single-frequency vms in red. As illustrated in the zoomed region shown in the lower panel of Figure 5.1(b), the spectrum from about 12100-12300 cm^{-1} is extremely congested due to the presence of many bands, each with five isotopes, and the high temperature (500 °C) of our oven, which results in observed J'' values up to about 70. The dynamic range of frequency-comb velocity-modulation spectroscopy is demonstrated by our ability to identify the overlapping $^1\Pi_1 \leftarrow {}^1\Sigma^+$ ($v' = 0$, $v'' = 1$) and $^3\Pi_1 \leftarrow {}^1\Sigma^+$ (3,1) bands despite the difference in linestrengths and an offset in band origin of only $\sim$1 cm^{-1}. Since 150 cm^{-1} sections are acquired simultaneously when using the comb, relative linestrengths within the region are not influenced by variability in oven and discharge conditions, which significantly helps to disentangle bands. The upper panel of Figure 5.1(b) shows predicted line positions from fits to three different bands (the fitting is discussed below), which illustrates our ability to resolve each isotope ($-\circ$, ^{180}Hf; $-\times$, ^{179}Hf; $-*$, ^{178}Hf; $-+$, ^{177}Hf; $-\cdot$, ^{176}Hf) for multiple bands. Figure 5.1(b) also demonstrates excellent overlap between the comb and cw spectra.

5.1.1 Diatomic molecular spectra primer

Before we delve deeper into the analysis of the data, we should take a detour and cover some basics of the spectra of diatomic molecules. More details can be found in numerous books [358, 359, 360, 361]. As we have already seen, molecular spectra can be extremely complicated. Luckily, the spectra of diatomic molecules are frequently not too complicated, but they are significantly more than twice as complicated as atomic spectra. In addition to the usual electronic states, molecules can also vibrate and rotate. So we must consider transitions between combinations of electronic, vibrational, and rotational states. Throughout this chapter, the upper state in a transition is designated with a single prime ($'$) and the lower state with a double prime ($''$). First, we look at the electronic structure of HfF^+, and then briefly cover important aspects of vibration and rotation

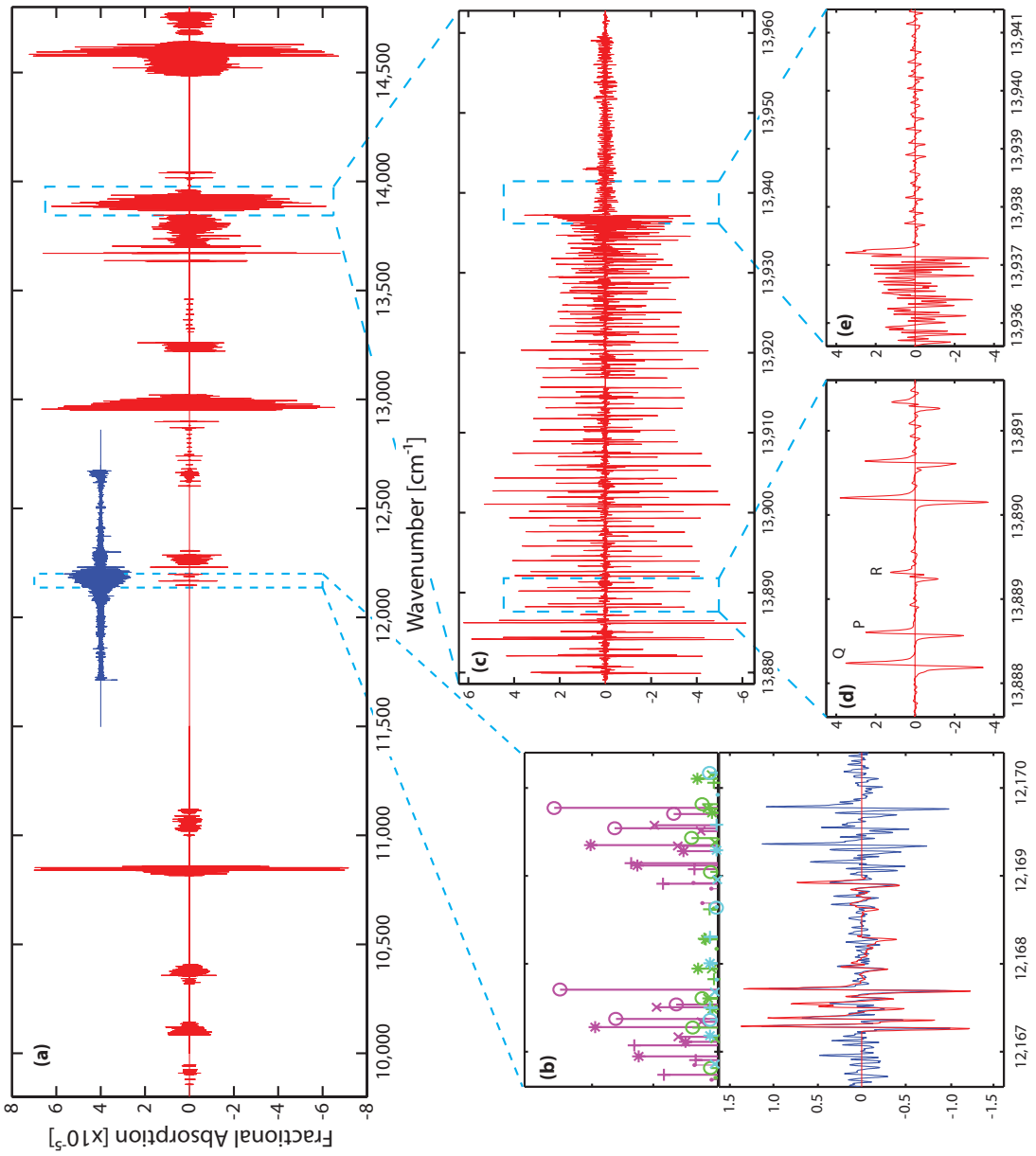

Figure 5.1: All data obtained with cw- and comb-vms (red and blue, respectively). All y-axes are fractional single-pass absorption ($\times 10^{-5}$) and all x-axes are in cm^{-1}. In (a) we show all of the HfF^+ spectra acquired to date. The comb-vms data is vertically offset for clarity. The lower panel of (b) shows a zoomed region of the comb data where some lines were also measured with the cw system. The upper panel of (b) plots predicted line positions from the fits; different colors correspond to different bands (magenta, $^1\Pi_1 \leftarrow {}^1\Sigma^+$ (0,1); green, $^3\Pi_1 \leftarrow {}^1\Sigma^+$ (3, 1); cyan, $^3\Pi_1 \leftarrow {}^1\Sigma^+$ (2, 0)) while different symbols correspond to Hf isotopes: $-\circ$, ^{180}Hf; $-\times$, ^{179}Hf; $-*$, ^{178}Hf; $-+$, ^{177}Hf; $-\cdot$, ^{176}Hf. Inset (c) shows the $^3\Phi_2 \leftarrow {}^3\Delta_1$ (0, 0) band (on the left) and part of the $^3\Sigma^-_{0^+} \leftarrow {}^1\Sigma^+$ (1, 0) on the right. The region in (d) illustrates the cancellation of isotope shifts in $\Delta v = 0$ transitions; the sharpness of P- and Q-branch lines is due to a cancellation between the rotational, vibrational, and electronic contributions to the isotope shift. The splitting in the (higher-J'') R-branch lines that is not observed in the (lower-J'') P- and Q-branch lines is due to Λ-doubling in the $^3\Delta_1$ state. Inset (e) shows a prominent band-head from the $^3\Phi_2 \leftarrow {}^3\Delta_1$ (0, 0) band as well as weaker lines from the $^3\Sigma^-_{0^+} \leftarrow {}^1\Sigma^+$ (1, 0) band.

that will be needed to analyze the data.

We can treat the electronic states of the molecule in the *united atom* picture, where the molecule can be thought of as a single atom (i.e., H_2^+ looks like He^+). Thus every electron exists in a molecular orbital (which can be represented as a linear combination of atomic orbitals) with a well defined value of n and l. In addition, the molecular axis (typically set as the $\hat{z}$ axis) provides a quantization axis for the projection of l, giving values of m_l between $\pm l$. To first order, the energy only depends on $\lambda = |l|$, so we can write state configurations as the values of $(n)l\lambda$ for each electron. The value of λ gives the number of nodal planes that contain the $\hat{z}$ axis, or equivalently, the rotational symmetry about the $\hat{z}$ axis ($\lambda = 0$ is cylindrically symmetric, $\lambda = 1$ is symmetric only with a 360° rotation, $\lambda = 2$ is symmetric with a 180° rotation, etc.). In HfF^+, we only care about the two valence electrons (excitations of core electrons are significantly higher in energy). Table 5.1 gives the possible configurations arising from the two lowest energy terms (s^2 and sd). Because the radial extent of the d orbitals is small compared to the internuclear distance, we expect that the molecular orbitals can be treated approximately as atomic orbitals [362]. Using the $l\lambda$ notation, the d_{xy} and $d_{x^2-y^2}$ atomic orbitals correspond to $d\delta$, d_{xz} and d_{yz} correspond to $d\pi$, and d_{z^2} corresponds to $d\sigma$.

We can get a rough idea of the expected state ordering from (basic) ligand field theory. "What field theory?!," you say. Don't worry, a ligand is the generic term for an atom or molecule bound to a metal. This theory is commonly used to explain octahedral and square-planar complexes with transition metals but can also be applied to diatomics [363, 362]. The general idea is that the orbitals on the metal ion (in this case Hf^{2+}) are perturbed by the electric field of the ligand (in this case F^-), which is treated as a point charge. If we now consider the d orbitals in the presence of this electric field, the orbitals that are closest to the ligand are destabilized the most. This means that the ordering of the d orbitals would be expected to be $d\delta < d\pi < d\sigma$, see Figure 5.2. All of the d orbitals are expected to be destabilized relative to the s orbital, which is much more diffuse and extends beyond the internuclear distance, thus resulting in more coulomb attraction between the metal cation core and the anion ligand [362]. Thus, we would roughly expect the ordering as

given in Table 5.1. This ordering is also seen in the ligand field treatment of LaF [364], which has a similar valence orbital configuration (except that La^+ has an empty f-shell and Hf^{2+} has a full f-shell). In addition to the state ordering, the repulsion of the ligand field causes the orbitals to polarize (i.e., to try to point away from the ion), which distorts the shape of the orbitals. This distortion is equivalent to orbital mixing: the shape of the distortion contains information about which orbitals are mixed and to what extent. Because the $d\sigma$ orbital is repelled the most, it is the most polarized – mostly with $s\sigma$ and $p\sigma$ orbitals in such a way as to try to point mostly away from the ligand. The $d\pi$ orbitals polarize by mixing mostly with $p\pi$ orbitals. The $d\delta$ orbitals however do not polarize and are thus mostly pure atomic d orbitals.

Molecular vibrations are treated as a simple anharmonic oscillator with quantized energy levels $\omega_v = \omega_e(v+1/2) - \omega_e x_e(v+1/2)^2$, where the v subscript indicates the vibrational quantum number and ω_e and $\omega_e x_e$ are the "equilibrium" harmonic vibrational frequency and anharmonicity correction, respectively. As expected from a pair of masses connected by a spring, the harmonic frequency is related to the force constant, k, by $\omega_e = \sqrt{\frac{k}{\mu}}$, where μ is the reduced mass. For different isotopes, k is not expected to change much because it is a function of electronic configuration and bond length, but μ does change; thus, ω_e is different for different isotopes. Rotation is treated as a semi-rigid rotor with energy levels $F(J) = BJ(J+1) - DJ^2(J+1)^2$, with angular momentum quantum number J, rotational constant B, and centrifugal distortion constant D. B is related to the moment of inertia, I, by $B = \frac{\hbar}{4\pi c I} = \frac{\hbar}{4\pi c\mu}\left\langle\frac{1}{R^2}\right\rangle$, where R is the internuclear separation. In an anharmonic oscillator R changes (typically increases) as v increases, so B depends on v. The equilibrium rotational constant, B_e, is the rotational constant at the minimum of the molecular potential curve (at an equilibrium separation of r_e): B_v is related to B_e by $B_v \approx B_e - \alpha_e(v+1/2)$. Because of the reduced mass, B_e also depends on the isotope (r_e is basically constant). The centrifugal distortion constant, D, arises because the molecule stretches as it rotates. We can relate D_e, ω_e, and B_e by $\omega_e = \sqrt{\frac{4B_e^3}{D_e}}$.

Since the electric dipole selection rule for rotation is $\Delta J = 0, \pm 1$, we see three branches for each vibronic transition: P ($J' = J'' - 1$), Q ($J' = J''$), and R ($J' = J'' + 1$). Assuming a rigid

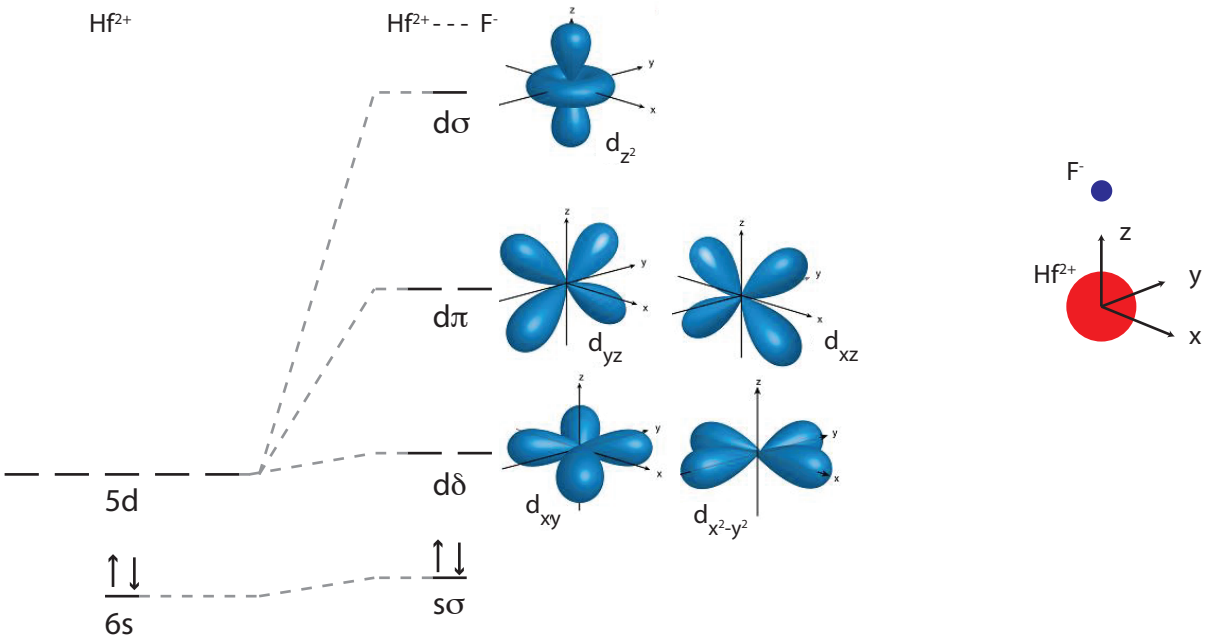

Figure 5.2: Molecular orbital diagram for valence orbitals of HfF^+. The atomic d orbital corresponding to the primary component of each molecular orbital is pictured. Figures are from: `http://en.wikibooks.org/wiki/High_School_Chemistry/Shapes_of_Atomic_Orbitals`.

Table 5.1: Possible states and configurations arising from s^2 and sd electron configurations. Molecular orbitals are denoted in the configuration column by $l\lambda$, where l is the corresponding atomic orbital. Subscripts are used to distinguish orbitals with the same λ but different l. When writing the wavefunction, electron spin is denoted by α or β and the value of m_λ is given by a superscript.

State	Configuration	Λ	Ω	Wavefunction
$X^1\Sigma^+$	$(s\sigma_1)^2$	0	0	$\left[\lvert\sigma_1(\alpha)\sigma_1(\beta)\rangle - \lvert\sigma_1(\beta)\sigma_1(\alpha)\rangle\right]/\sqrt{2}$
$^3\Delta$	$(s\sigma_1)(d\delta)$	2	1	$\left\lvert\sigma_1(\beta)\delta^{2+}(\beta)\right\rangle$
		-2	-1	$\left\lvert\sigma_1(\alpha)\delta^{2-}(\alpha)\right\rangle$
		±2	±2	$\left[\left\lvert\sigma_1(\alpha)\delta^{\pm2}(\beta)\right\rangle + \left\lvert\sigma_1(\beta)\delta^{\pm2}(\alpha)\right\rangle\right]/\sqrt{2}$
$^1\Delta$	$(s\sigma_1)(d\delta)$	2	2	$\left\lvert\sigma_1(\beta)\delta^{2+}(\alpha)\right\rangle$
	$(s\sigma_1)(d\delta)$	-2	-2	$\left\lvert\sigma_1(\beta)\delta^{2-}(\alpha)\right\rangle$
		2	3	$\left\lvert\sigma_1(\alpha)\delta^{2+}(\alpha)\right\rangle$
		-2	-3	$\left\lvert\sigma_1(\beta)\delta^{2+}(\beta)\right\rangle$
$^3\Pi$	$(s\sigma_1)(d\pi)$	±1	±1	$\left[\lvert\sigma_1(\alpha)\pi^{\pm}(\beta)\rangle + \lvert\sigma_1(\beta)\pi^{\pm}(\alpha)\rangle\right]/\sqrt{2}$
		1	0	$\lvert\sigma_1(\beta)\pi^{+}(\beta)\rangle$
		-1	0	$\lvert\sigma_1(\alpha)\pi^{-}(\alpha)\rangle$
$^1\Pi$	$(s\sigma_1)(d\pi)$	±1	±1	$\left[\lvert\sigma_1(\alpha)\pi^{\pm}(\beta)\rangle - \lvert\sigma_1(\beta)\pi^{\pm}(\alpha)\rangle\right]/\sqrt{2}$
$^1\Sigma^+$	$(s\sigma_1)(d\sigma_2)$	0	0	$\left[\lvert\sigma_1(\alpha)\sigma_2(\beta)\rangle - \lvert\sigma_1(\beta)\sigma_2(\alpha)\rangle\right]/\sqrt{2}$
$^3\Sigma^+$	$(s\sigma_1)(d\sigma_2)$	0	1	$\lvert\sigma_1(\alpha)\sigma_2(\alpha)\rangle$
		0	-1	$\lvert\sigma_1(\beta)\sigma_2(\beta)\rangle$
		0	0	$\left[\lvert\sigma_1(\alpha)\sigma_2(\beta)\rangle + \lvert\sigma_1(\beta)\sigma_2(\alpha)\rangle\right]/\sqrt{2}$

rotor, the energies of transitions in each band are given by

$$\begin{aligned} P(J'') &= \nu_0 - (B' + B'')J'' + (B - B'')J''^2 \\ Q(J'') &= \nu_0 + (B' - B'')J'' + (B - B'')J''^2 \\ R(J'') &= \nu_0 + 2B' + (3B' - B'')J'' + (B - B'')J''^2. \end{aligned} \tag{5.1}$$

In general, $B' < B''$ because typically the internuclear spacing is larger in the excited state (due, e.g., to a weaker bond) than in the lower state. In this case there is a place in the R branch where the difference in energy between adjacent J'' values crosses zero and the R branch progression turns around. This is called the band head, and it's position is approximately

$$J'' + 1 = -\frac{B' + B''}{2(B' - B'')} = -\frac{\bar{B}}{\delta B}. \tag{5.2}$$

The parity (defined as the sign with respect to inversion of spatial coordinates) of rotational wavefunctions alternates with J (similar to the parity of atomic orbitals, which alternate with l). The parity operator is equivalent to reflection about a plane containing the internuclear axis, $\hat{\sigma}_v$ in a diatomic [365]. Because of this alternation, we introduce an additional symmetry label of e/f, where e corresponds to states that transform as $\hat{\sigma}_v\psi = +(-1)^J\psi$, i.e., states with + parity for $J = 0$.

One thing to notice is that both B_e and ω_e depend on the reduced mass. This means that they both have an isotope dependence, although the isotope dependence is different for vibration ($\omega_e \sim \sqrt{\frac{1}{\mu}}$) versus rotation ($B_e \sim \frac{1}{\mu}$). Because Hf has five observable isotopes, we were able to use these isotope shifts to gain information about the observed bands. In particular, near the band head the rotational energy is low, so the rotational isotope shift is small at this point (it vanishes at the origin). Thus, we can use shifts in the band head location for different isotopes to roughly measure the difference in vibrational number: for example, $\tilde{\nu}_{180} - \tilde{\nu}_{178} \approx \left(1 - \sqrt{\frac{\mu_{180}}{\mu_{178}}}\right) 750(v' - v'') \approx 0.4$ cm^{-1} for $v' - v'' = 1$, where 750 cm^{-1} is the approximate (average) vibrational constant for the upper and lower states. In this case, the isotopes bands are progressively blue shifted from the ^{180}Hf band (which is the most abundant isotope). In addition, there are small isotope shifts in the electronic energies that arise from finite nuclear size effects as discussed more below. One

interesting point is that the vibrational and electronic isotope shifts are constant across a band while the rotational isotope shifts are not. Thus, the isotope shifts between rotational lines are different depending on where in the progression you look: for a $\Delta v = 0$ transition we do not fully resolve the isotope splitting, so this results in a place where the rotational isotope shift cancels the electronic and (small) vibrational isotope shift, which is observed as the place where the absorption line is narrowest.

The states in Table 5.1 are denoted by $^{2\Sigma+1}\Lambda_\Omega$, where Σ is the total spin angular momentum along the internuclear axis, Λ is the total orbital angular momentum along the internuclear axis, and $\Omega = \Sigma + \Lambda$. In addition to the spin and orbital angular momentum, molecules also have rotational angular moment. There are several primary ways that the angular momentum can couple together, called Hund's cases, as shown in Figure 5.3. This state notation is only technically valid for states in Hund's case (a); a state in case (c) is typically denoted by the value of Ω.

The classification into different cases is determined by the spin-orbit energy (the diagonal elements of the spin-orbit operator) compared to the rotational and electronic energies. The spin-orbit operator is fundamentally a one-electron operator given by $\hat{H}_{SO} = \sum_i \hat{a}_i \vec{l}_i \cdot \vec{s}_i = \sum_i \hat{a}_i \left[l_{z,i} s_{z,i} + \frac{1}{2}(l_{+,i} s_{-,i} + l_{-,i} s_{+,i}) \right]$, where the sum is over open-shell electrons, $\hat{a}_i$ is the spin-orbit operator (different for each orbital), and the z axis is the internuclear axis. We can use the configurations in Table 5.1 to evaluate the diagonal elements of $\hat{H}_{SO}$, for example, $\langle {}^3\Delta_3 | \hat{H}_{SO} | {}^3\Delta_3 \rangle = -\langle {}^3\Delta_1 | \hat{H}_{SO} | {}^3\Delta_1 \rangle = A_{{}^3\Delta}$, where $A_{{}^3\Delta} \equiv \langle d\delta | \hat{a} | d\delta \rangle$. $A_{{}^3\Delta}$ is approximately given by ζ_{5d} – the spin-orbit coefficient of the atomic $5d$ orbital in Hf^{2+}. We can obtain $\zeta_{5d} = \frac{2}{2l+1}(E_{{}^3D_3} - E_{{}^3D_2}) = 1537$ cm^{-1} using the Hf^{2+} energy levels from [366].

States with small spin-orbit energies are typically case (b), thus the $^1\Sigma^+$ state would fall into this category. However, there is no distinction between case (a) and case (b) for $^1\Sigma^+$, so we are free to treat it as case (a). (Note that case (b) states can always be projected to a case (a) basis, see for example [367].) The large spin-orbit interaction technically makes case (c) most appropriate for the states in HfF^+. In general though, we can write the case (c) eigenfunctions as case (a) eigenfunction perturbed by other case (a) functions (see for example [368]) and then denote the

(a) Spin-orbit energy > rotational energy

Good QN: S, Λ, Σ, Ω, J, (F, m_F)

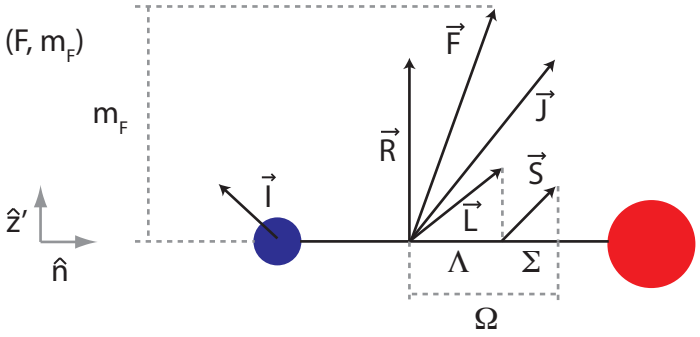

$\vec{L} = \Sigma \vec{\ell}_i$
$\vec{S} = \Sigma \vec{s}_i$
$\vec{R}$ = rotation
$\vec{J} = \vec{L} + \vec{S} + \vec{R}$
$\vec{F} = \vec{J} + \vec{I}$
$\Lambda = \vec{L} \cdot \hat{n}$
$\Sigma = \vec{S} \cdot \hat{n}$
$\Omega = \Lambda + \Sigma$
$m_F = \vec{F} \cdot \hat{z}'$

(b) Small spin-orbit energy

Good QN: S, Λ, N_e, J, (F, m_F)

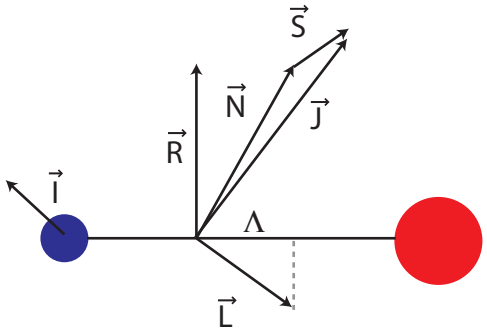

$\vec{N} = \vec{L} + \vec{R}$
$\vec{J} = \vec{N} + \vec{S}$

(c) Spin-orbit energy ~ Electronic energy >> rotational energy

Good QN: Ω, J_e, J, (F, m_F)

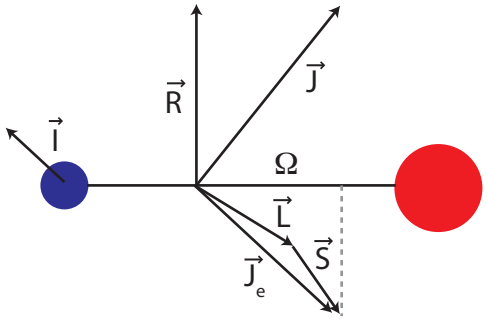

$\vec{J}_e = \vec{L} + \vec{S}$
$\vec{J} = \vec{J}_e + \vec{R}$

Figure 5.3: Angular momentum coupling in diatomic molecules corresponding to Hund's cases (a), (b), and (c). The coupling of the nuclear hyperfine, I, with J to form F is only shown for case (a), although similar coupling is possible in the other cases.

state by its leading case (a) term. The amount of perturbation is small for the low-lying electronic states, but for the higher states it can be significant, leading to allowed transitions that are denoted in the case (a) basis as singlet-triplet transitions.

States with $|\Lambda| \neq 0$ (in Hund's cases (a) and (b)) are in principle doubly-degenerate due to the two projections of Λ onto the internuclear axis (corresponding to two precession directions about the internuclear axis). This degeneracy is lifted due to perturbations and is called Λ-doubling. If we include the coupling with S, then states with $|\Omega| \neq 0$ are degenerate in Hund's cases (a) and (c). The symmetric and antisymmetric combinations of degenerate $|+\Omega\rangle$ and $|-\Omega\rangle$ are states of good parity and have opposite total parity. This degeneracy is removed by a coupling between rotational angular momentum and electronic angular momentum, which directly couples states with $\Delta\Omega = \pm 1$. Thus, the coupling between $\pm\Omega$ is introduced at 2Ω order in perturbation theory. While technically this is Ω-type doubling, it is an extension of Λ-doubling when $S = 0$ and so is typically still called Λ-doubling.

The origin of this Λ-doubling is sometimes referred to as the electron motion changing the moment of inertia; however, Bob Field considers this "nonsense" as it fails to explain the sign or magnitude of the Λ-doubling in general. Instead, the origin of Λ-doubling is perturbations due to Σ states, which shift one parity relative to the other. We can understand this more by considering the rotational Hamiltonian $\hat{H}_{rot} = B(R)\vec{R}^2$, where $B(R)$ is the position-depending rotational constant and $\vec{R}$ is the rotational angular momentum. We can write $\vec{R} = \vec{J} - \vec{L} - \vec{S}$ and, defining z as the internuclear axis, $\vec{R}^2 = R_x^2 + R_y^2 = \frac{1}{2}(R_+R_- + R_-R_+)$, where $R_\pm = J_\pm - L_\pm - S_\pm$. We make use of the commutator relationships

$$\begin{aligned} [J_\pm, J_\mp] &= \pm i\hbar J_z, \\ [J_\pm, V_\mp] &= \pm i\hbar V_z, \\ [V_\pm, V_\mp] &= \pm i\hbar V_z, \\ [L_\pm, S_\mp] &= 0 \end{aligned} \tag{5.3}$$

with $V = L, S$ to write [361]

$$\hat{H}_{rot} = B(R)\vec{R}^2 = \tag{5.4a}$$

$$(J^2 - J_z^2) + (S^2 - S_z^2) + (L^2 - L_z^2) \tag{5.4b}$$

$$+ (J_+L_- + J_-L_+) \tag{5.4c}$$

$$- (J_+S_- + J_-S_+) \tag{5.4d}$$

$$+ (L_+S_- + L_-S_+). \tag{5.4e}$$

Line (b) contains all of the diagonal contributions while lines (b), (c), and (d) are off-diagonal terms called L-uncoupling, S-uncoupling, and rotational-electronic, respectively. These off-diagonal terms can be simply understood if we write $\vec{R} = \vec{J} - \vec{\Omega}$ (we have time averaged $\vec{J}_e$ to give $\vec{\Omega}$: then $\vec{R}^2 = \vec{J}^2 - 2\vec{J}\cdot\vec{\Omega} + \vec{\Omega}^2$. The dot product term leads to the off-diagonal terms above.

For a simple example, we consider the simplest source of Λ-doubling in case (a) $^1\Pi_1$. In this case, we need to connect $|\Lambda = 1, \Omega = 1\rangle$ with $|\Lambda = -1, \Omega = -1\rangle$. This is accomplished with one application of L-uncoupling to a Σ state and then a second L-uncoupling to $|\Lambda = -1, \Omega = -1\rangle$. The magnitude of this perturbation is given by second-order perturbation theory as

$$q \sim \frac{B_e^2 J(J+1)\,\langle \Lambda = -1, \Omega = -1|L_-|\Sigma\rangle\,\langle\Sigma|L_-|\Lambda = 1, \Omega = 1\rangle}{E_\Pi - E_\Sigma}. \tag{5.5}$$

The remaining matrix elements are calculated constants. One simple assumption for calculating these matrix elements is called *pure precession* [369] in which we treat the operator as a single-electron operator and consider the configurations such as given in Table 5.1 as pure configurations: for example $\langle\pi|l_+|\sigma\rangle = \sqrt{l(l+1)}$. From this, we see that the Λ-doubling in $|\Omega|$ states scales roughly as $J^{2\Omega}$. If we consider states with higher multiplicity, in addition to the q term arising from two applications of L-uncoupling we should consider various combinations of L-uncoupling and off-diagnonal terms of H_{SO}, which lead to o and p terms corresponding to H_{SO}^2 and $H_{SO}BL_+$, respectively. More detailed derivations of Λ-doubling in various states can be found in [369] ($^{1,2}\Pi$), [370] ($^{3,4,5}\Pi$), [371] (all Δ states), as well as in [360]. We discuss the Λ-doubling in HfF^+ in more detail in Section 5.1.3.

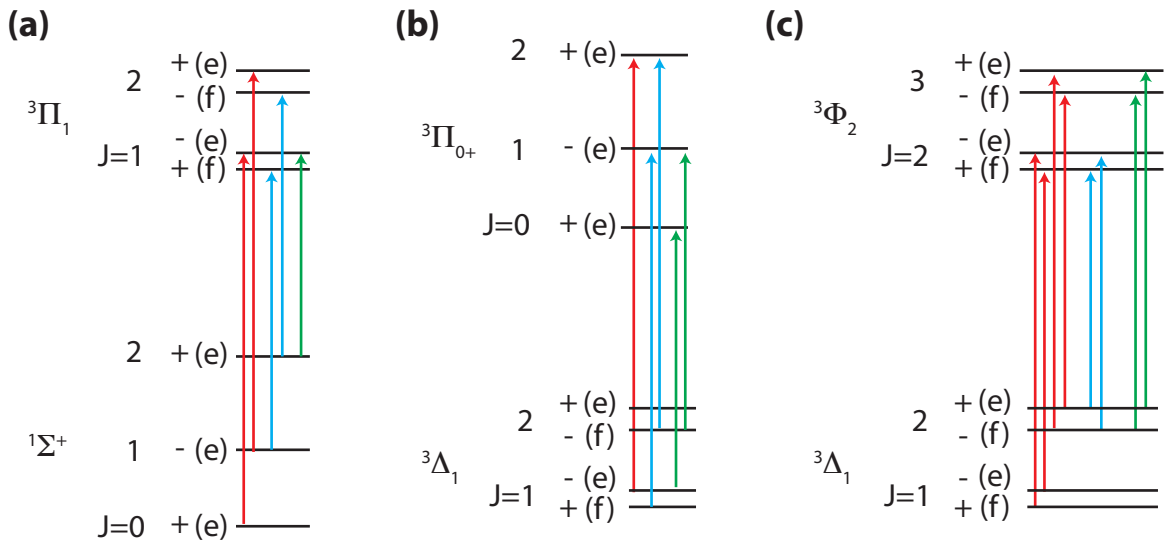

Figure 5.4: Example transitions with Λ-doubling in one or both states. P-, Q-, and R-branch transitions are shown by green, blue, and red arrows, respectively. Total parity as well as e/f is given for each rotational level. (a) $^3\Pi_1 \leftarrow {}^1\Sigma^+$: Λ-doubling in the excited state only results in a difference between an effective B for P/R and Q. (b) $^3\Pi_{0^+} \leftarrow {}^3\Delta_1$: Λ-doubling in the ground state only. This transition enables the sign of the Λ-doubling in the ground state to be determined. (c) $^3\Phi_2 \leftarrow {}^3\Delta_1$: Λ-doubling in both states results in two of each branch.

The consequences of Λ-doubling on rotational bands are shown in Figure 5.4(a-c), which show the possible transitions with Λ-doubling present in the excited state, ground state, or both states. P-, Q-, and R-branch transitions are shown by green, blue, and red arrows, respectively. Remember that electric-dipole selection rules only allow $+ \leftrightarrow -$ transitions, where $+$ and $-$ indicate the overall parity. The corresponding e/f labels are also shown. Notice that the ordering of $+$ and $-$ changes in each J level, but e/f labels do not. When Λ-doubling is present in only one state, the result is a different effective B value for the P/R branches and the Q branch, as can be seen by the fact that the R/P-branch transitions in Figure 5.4(a) always go to the upper doublet state while the Q-branch transitions go to the lower doublet. If Λ-doubling is present in both states, there are instead two sets of P,Q, and R branches, as shown in Figure 5.4(c).

5.1.2 Fitting

The first step in trying to fit any transition is to look for patterns. Typically, there are two patterns that can be identified: a band head and chirped sequences. The band head is pretty straightforward (a particularly obvious one is shown in Figure 5.1(c) and (e)) and gives a rough idea about where the band origin is located. Also, due to isotope splittings, the shape of the band head gives an idea of the difference in vibrational quantum number between the upper and lower states (each isotope band will have a band head in a different spot). Chirped sequences are progressions of lines whose separation (Δ) changes by the same amount each time, i.e., $\delta\Delta$ is a constant. From Equation 5.1, we see that for any branch, $\delta\Delta \approx 2(B' - B'')$. Once a chirped sequence is identified, we can fit it to a quadratic to determine δB and also to determine whether the lines chirp back to the band head (indicating a P/R branch) or to the band origin (indicating a Q branch). In many cases, the Q branch is the easiest to identify first. The distance between the band origin and band head can be used with Equation 5.2 and δB to obtain guesses for B' and B''. From here, an iterative process can be used to fit the bands by simulating the line positions using guessed B values, assigning as many lines as possible, and then re-fitting to obtain better constants.

Another tool for identifying patterns in complex spectra is to use a Loomis-Wood type plot.

The basic idea of this technique is to plot the difference between unidentified line positions and the expected positions of one branch. These expected positions often come from one identified branch using the procedure above, from extrapolation from a partial chirped sequence, or from a guess. For example, we were able to identify and fit the $^3\Pi_1 \leftarrow {}^1\Sigma^+$ (3, 1) band from a collection of unassigned lines in an extremely congested region of the spectrum. To do this, we first tabulated all of the unassigned lines (along with approximate relative intensities) and then plotted the difference with guessed positions of the Q-branch versus m (which corresponds to J). In this case, B'' was already known from a previously fit band and the other parameters were estimated from other fits. We then varied the origin and ΔB and looked for patterns emerging; in particular, a Q branch should appear as a horizontal line and other branches should appear as sloping lines. The result of this is shown in Figure 5.5 after the parameters have been adjusted to place one horizontal line at zero. We immediately see from the Loomis-Wood plot the presence of a second horizontal line located ~ 0.7 cm^{-1} away, which can be attributed to the isotope splitting between ^{178}Hf and ^{180}Hf. In addition, sloped lines corresponding to the P and R branches can also be seen.

Since we were fitting a variety of different transitions with various combinations of Hund's cases, we chose to fit each band with the general expression given in Eq. 5.6

$$\nu(v', v'', J', J'', s', s'') = \nu_0 + F_{v'}(J', s') - F_{v''}(J'', s'') \tag{5.6}$$

where the rotational energies, F_v are

$$F_v(J, s) = (B_v - s\frac{k_v}{2})J(J+1) - (D_v - s\frac{k_{D,v}}{2})J^2(J+1)^2. \tag{5.7}$$

We include rotation (B), centrifugal distortion (D), Λ-doubling proportional to J^2 (k) and J^4 (k_D) for each vibrational level, v; s is an e/f-symmetry term where $s = +1$ for e-symmetry and -1 for f-symmetry. k and k_D are generic constants for the Λ-doubling since we have fit states with several different values of Λ and Ω. In principle, the J dependences of k and k_D are more complicated and depend on the spin and Ω, see for example [369, 370, 371, 360, 361]. In Σ_0 states, only one symmetry term is chosen and k and k_D are both set to 0. ν_0 includes both the electronic and

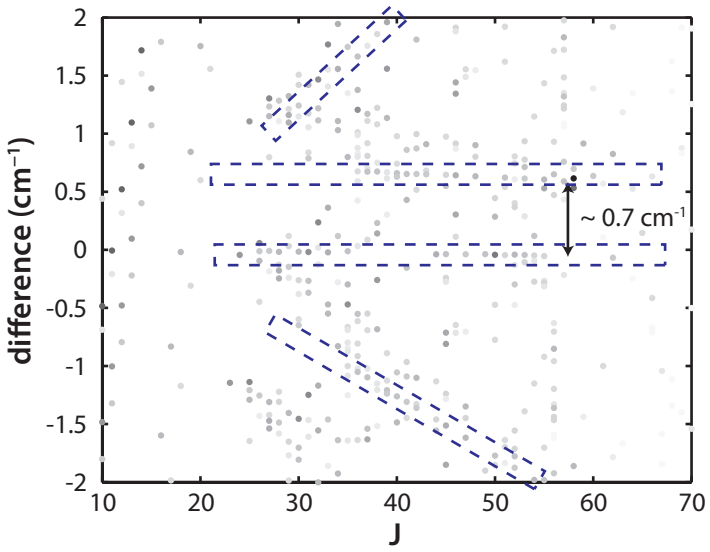

Figure 5.5: Loomis-Wood plot showing branches of the $^3\Pi_1 \leftarrow {}^1\Sigma^+$ (3, 1) transition. Darker points indicate larger relative intensity. Potential branches are indicated by the boxed regions. The isotope splitting between the ^{178}Hf and ^{180}Hf Q-branches is shown by the vertical arrow.

vibrational energies:

$$\nu_0 = T'_e - T''_e + E_{vib}, \tag{5.8}$$

$$E_{vib} \approx (\omega'_e(v' + 1/2) - \omega_e x'_e(v' + 1/2)^2) - (\omega''_e(v'' + 1/2) - \omega_e x''_e(v'' + 1/2)^2). \tag{5.9}$$

Here T_e is defined as the energy difference between the minimum of the potential curve from the minimum of the $X^1\Sigma^+$ curve, and ω_e and $\omega_e x_e$ are the usual vibrational constant and anharmonic correction, respectively.

Due to the congested nature of the spectra, fits were performed to a manually identified list of isolated lines (frequency only) for each band and for each isotope in bands with well resolved isotope structure. Figure 5.7(b) shows the residuals from a representative fit; root-mean-square values for the residuals were typically < 0.005 cm^{-1} with no apparent structure. For most $\Delta v = 0$ transitions the fits were performed to estimated isotope averaged line centers and then the rotational constants were shifted by the reduced mass to the ^{180}Hf values. The $^3\Phi_2 \leftarrow {}^3\Delta_1$ bands exhibited line doubling at high-J due to Λ-doubling (discussed in detail below), for these bands the center of the doublet was used for the fits. Similarly, the $^1\Pi_1 \leftarrow {}^3\Delta_2$ (0, 0) band exhibited doubling of every transition (i.e., 6 branches) due to large Λ-doubling in the $^1\Pi_1$; for this band all six branches were fit simultaneously by assuming the splitting to each transition was $k' \times J'(J' + 1)$. A summary of the fitted constants for each band is given in Table 5.2.

Table 5.2: Fitted constants for observed transitions in $^{180}HfF^+$ in cm^{-1}. Quoted errors are at 95% confidence level, statistical only. For bands recorded with the wavemeter uncalibrated we include an additional 0.006 cm^{-1}uncertainty in ν_0. Internal consistencies in the data suggest that for the $\Delta v = 0$ bands, which typically suffer from partially resolved isotope structure, systematic errors in the fit quantities may exceed the quoted statistical uncertainties in some cases by a factor of two or three. Values without uncertainties were fixed in the fits. All constants are given for the vibrational levels involved in the transition and are not equilibrium values. The Λ-doubling terms, k'', k', and k'_D are generic terms proportional to $J(J+1)$ in the ground and excited states and $J^2(J+1)^2$ in the excited state respectively (see text for more details).

	Assignment	ν_0	B''	B'	D'' $[10^{-7}]$	D' $[10^{-7}]$	k'' $[10^{-4}]$	k' $[10^{-4}]$	k'_D $[10^{-9}]$	δE
1	$^3\Pi_{0^-} \leftarrow {}^3\Delta_1$ (1, 0)	9948.624(6)	0.29891(2)	0.28272(2)	1.85(5)	1.81(4)	-0.123(6)	–	–	?
2	$^3\Pi_1 \leftarrow {}^1\Sigma^+$ (0, 1)	10109.877(6)	0.30333(6)	0.28382(6)	1.9(5)	1.9(5)	–	-3.77(5)	0	0.383
3	$^3\Pi_{0^+} \leftarrow {}^3\Delta_1$ (1, 0)	10137.723(7)	0.29887(5)	0.28277(5)	1.70(20)	1.66(20)	-0.14(2)	–	–	-0.369
4	$^3\Pi_{0^+} \leftarrow {}^1\Sigma^+$ (0, 0)	10401.723(13)$^+$	0.30500(10)	0.28437(11)	2.3(1.2)	2.2(1.2)	–	–	–	-0.035
5	$^1\Pi_1 \leftarrow {}^3\Delta_2$ (0, 0)	10852.757(13)$^+$	0.29915(9)	0.28102(9)	1.7(4)	1.7(4)	0	3.59(3)‡	–	0
6	$^3\Pi_{0^+} \leftarrow {}^1\Sigma^+$ (1, 0)	11114.653(7)	0.30482(4)	0.28281(4)	1.71(14)	1.72(13)	–	–	–	-0.403
7	$^1\Pi_1 \leftarrow {}^1\Sigma^+$ (1, 2)	12136.012(3)	0.30180(5)	0.27973(5)	1.80(14)	1.74(14)	–	2.68(4)	7.4(1.3)	0.412
8	$^3\Pi_1 \leftarrow {}^1\Sigma^+$ (3, 1)$^\circ$	12216.901(10)	0.30335*	0.27958(20)	1.8(3)	1.8(3)	–	-3.8(2)	0	-0.724
9	$^1\Pi_1 \leftarrow {}^1\Sigma^+$ (0, 1)	12217.369(2)	0.30335(2)	0.28115(3)	1.88(8)	1.81(8)	–	3.69(2)	9.7(7)	0.372
10	$^3\Pi_1 \leftarrow {}^1\Sigma^+$ (2, 0)	12304.400(3)	0.30481(5)	0.28096(5)	1.78(12)	1.78(12)	–	-3.82(1)	0	-0.783
11	$^1\Pi_1 \leftarrow {}^1\Sigma^+$ (0, 0)	13002.189(12)$^+$	0.30474(20)	0.28104(20)	1(2)	1(2)	–	3.55(4)	0	-0.04
12	$^3\Sigma^-_{0^+} \leftarrow {}^1\Sigma^+$ (0, 0)	13254.302(7)	0.30478(10)	0.28967(9)	1.7(5)	1.9(5)	–	–	–	-0.084
13	? $\Delta v = 0$	13729.918(17)$^+$	0.29860(60)	0.28680(60)	3(3)	3(3)	0	-0.2(3)	–	0.005
14	? $\Delta v = 0$	13822.270(14)$^+$	0.29980(10)	0.28860(10)	1.9(2)	2.2(2)	0	0	–	-0.035
15	$^3\Phi_2 \leftarrow {}^3\Delta_1$ (0, 0)	13933.340(12)$^+$	0.29900(10)	0.27720(10)	2.2(3)	2.1(3)	†	-0.01(3)	–	-0.05
16	$^3\Sigma^-_{0^+} \leftarrow {}^1\Sigma^+$ (1, 0)	13953.799(6)	0.30483(5)	0.28808(4)	1.78(12)	1.98(13)	–	–	–	0.457
17	$^3\Phi_2 \leftarrow {}^3\Delta_1$ (2, 1)	14534.839(7)	0.29745(8)	0.27488(8)	1.7(4)	1.6(4)	†	0	–	-0.422
18	$^3\Phi_2 \leftarrow {}^3\Delta_1$ (1, 0)	14613.782(7)	0.29888(5)	0.27590(5)	1.71(15)	1.59(15)	†	0	–	-0.434
19	? $\Delta v = 0$	14636.162(13)$^+$	0.29620(30)	0.27600(30)	1.7(1.5)	1.8(1.5)	0	0	–	-0.02

$^\circ$ Values assigned using a manual fit to multiple isotopes due to challenges of determining the line centers of the weaker lines in the dense spectrum.

* Value fixed to the fitted value from the $^1\Pi_1 \leftarrow {}^1\Sigma^+$ (0, 1) transition.

$^+$ Individual isotopes were not fully resolved, thus the fit was done to averaged line positions. We report isotope corrected values with the error due to the uncertainty in the isotope shifts.

† $^3\Phi_2 \leftarrow {}^3\Delta_1$ transitions exhibited line-doubling at high J", but the doublets were not resolved well enough to accurately determine k".

‡ Each transition was a doublet with a splitting given by $k' \times J'(J'+1)$ due to Λ-doubling in $^1\Pi_1$.

Assignments of the observed bands were not particularly straightforward, partially because the presence or absence of low-J lines usually could not be determined due to the high temperature of the ions and complicating isotope structure. In fact, only for the $^1\Pi_1 \leftarrow {}^1\Sigma^+$ (0, 0) band near 13000 cm^{-1} (transition 11) were we able to directly establish that $\Omega' = 1$ and $\Omega'' = 0$ since we observed an R(0) line but no P(1) line. One valuable feature of the isotope structure was the ability to measure isotope shifts for each transition. We define the isotope shift between ^{180}HfF$^+$ and ^{178}HfF$^+$ for a given spectral line as

$$\delta E = E^{180} - E^{178} = (1 - \frac{\mu_{180}}{\mu_{178}})E_{rot} + (1 - \sqrt{\frac{\mu_{180}}{\mu_{178}}})E_{vib} + \delta T'_e - \delta T''_e. \tag{5.10}$$

Here μ_{180} and μ_{178} are the reduced masses, E_{rot} is the rotational energy in ^{180}HfF$^+$ (i.e., offset from the band origin), and E_{vib} is the vibrational energy in ^{180}HfF$^+$. The last column of Table 5.2 gives the isotope shift between ^{180}HfF$^+$ and ^{178}HfF$^+$ measured at the band origin. The isotope shift provides two useful pieces of information for the assignment. First, since the isotope shift is dominated by the vibrational shift, the sign and magnitude of the shift give the value of Δv for the transition. We can also use the isotope shift to group transitions that only differ in vibration: this is done in Figure 5.6 by plotting $\nu_0 + \left(1 - \sqrt{\frac{\mu_{180}}{\mu_{178}}}\right)^{-1} \delta E - 10000$ cm^{-1} versus $\nu_0 - 10000$ cm^{-1} for each transition. Transitions that lie close to the same horizontal line originate from the same electronic states.

We can use Hund's rules to determine a rough ordering of states from the configurations listed in Table 5.1: $^1\Sigma^+$, $^3\Delta_1$, $^3\Delta_2$, $^3\Delta_3$, $^1\Delta_2$, $^3\Pi_0$, $^3\Pi_1$, $^3\Pi_2$, $^1\Pi_1$, $^3\Sigma_0^+$, $^3\Sigma_1$, and $^1\Sigma$. The $^3\Sigma^+$ and $^1\Sigma$ are expected to be very high in energy and are not used in the assignments. These are only states arising from s^2 and sd configurations; in addition, a d^2 configuration is expected to contribute $^3\Sigma^-$, $^3\Phi$, and possibly $^3\Pi$ configurations in the higher energy regions. Several bands with no Q-branch were observed (numbers 4, 6, 12, and 16), which are expected to be $^3\Pi_{0^+} \leftarrow {}^1\Sigma^+$ and $^3\Sigma^-_{0^+} \leftarrow {}^1\Sigma^+$, with the $^3\Pi_{0^+}$ transitions significantly lower in energy. Transitions with $\Delta\Omega = 0$ will give very weak Q-branches that are only visible at low J, which could look like a missing Q-branch.

From Figure 5.6, we can identify transitions 7, 9, and 11 as all originating from the same

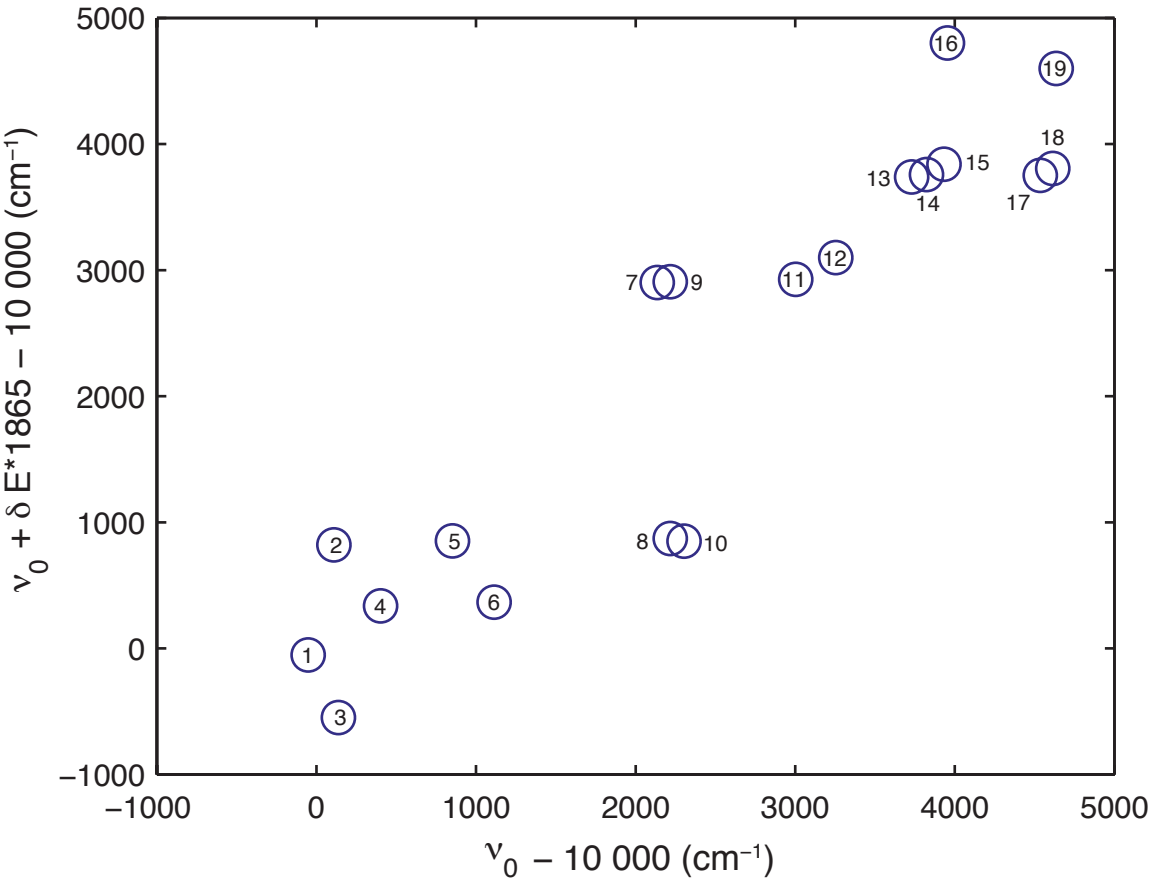

Figure 5.6: Isotope shifts (δE) of each observed transition as numbered in Table 5.2. The isotope shift on the y-axis is scaled to roughly remove the vibrational isotope shifts; the x-axis is the transition energy - 10000 cm^{-1}. Transitions between different vibrational levels but the same upper and lower electronic states should lie on horizontal lines.

electronic states. Since we know that $\Omega' = 1$ and $\Omega'' = 0$, we can assign the ground state to $^1\Sigma^+$ and the excited state to one of $^3\Pi_1$, $^1\Pi_1$ or $^3\Sigma_1$. Furthermore, the splitting between 9 and 11 matches the splitting between $v = 0$ and 1 from [372], so transition 11 gives us the B_0 for $^1\Sigma^+$. This B value also confirms the rough assignment of the no Q-branch transitions in the previous paragraph as being $^3\Pi_{0^+} \leftarrow {}^1\Sigma^+$ (transitions 4 and 6) and $^3\Sigma^-_{0^+} \leftarrow {}^1\Sigma^+$ (transitions 12 and 16), all with the lower state of $^1\Sigma^+$ $J = 0$. We can use the vibrational isotope shifts to assign all of these four transitions now, in particular, transition 6 is $^3\Pi_{0^+} \leftarrow {}^1\Sigma^+$ (1, 0). The splitting between transition 4 and transition 3, which has the same value of B', matches the splitting between $^1\Sigma^+$and $^3\Delta_1$ [372]. This gives us an assignment for transition 3 and a value for B_0 of $^3\Delta_1$.

We now assume that states with different Ω but the same values of S and Λ have similar B values: this is a reasonable assumption because a different value of Ω indicates a different orientation of spin and Λ, which would not be expected to affect the bond strength (and thus length). Since B' for transition 11 is not close to the B' for transition 12 ($^3\Sigma_0$), we can assume that transition 11 (and thus 7 and 9) is to either $^3\Pi_1$ or $^1\Pi_1$. By looking at Figure 5.6 and B'' values, we see that transitions 2, 8, and 10 are another series originating from $^1\Sigma^+$ and going to the same electronic state. Given the transition energy, the excited state could be $^3\Pi_1$, $^1\Pi_1$, or $^3\Pi_2$, but since the value of $|k'|$ is similar to transition 11, we can rule out $^3\Pi_2$ (the doubling for $\Omega = 2$ should be much smaller). Transition 2 and transition 9 both start from the $^1\Sigma^+$ $v'' = 1$ and have similar vibrational isotope shifts (so they both go to the same v') but one must be to $^3\Pi_1$ and one to $^1\Pi_1$: we can use the expected state ordering to assign transition 2 (and 8 and 10) to $^3\Pi_1$ and transition 9 (and 7 and 11) to $^1\Pi_1$.

Transitions 15, 17, and 18 all exhibit line-doubling at very high J and all have similar isotope shifts in Figure 5.6; also, B'' for 15 and 18 is consistent with $^3\Delta_1$ $v'' = 0$ from transition 3. The high-J doublets indicate that both lower and upper states have doubling, and the fact that the doubling is only visible at high-J indicates that $\Omega' > 1$. This implies that the upper state is either $^3\Pi_2$ or $^3\Phi_2$. Since the value of B' is different than B for $^3\Pi_1$, we assign the upper state to $^3\Phi_2$ (additionally, we expect the $^3\Pi_2$ to be a bit closer in energy to the $^3\Pi_1$). Combining all of these

results gives the final assignments in Table 5.2. Transitions 13, 14, and 19 remain unassigned.

From the fitted constants for the 16 assigned bands, we can determine constants for the $X^1\Sigma^+$, $^3\Delta_1$, $^3\Pi_{0^-}$, $^3\Pi_{0^+}$, $^1\Pi_1$, $^3\Pi_1$, $^3\Sigma^-_{0^+}$, and $^3\Phi_2$ states as given in Table 5.4. T_0 and $\Delta G_{1/2}$ are directly obtained from the measurements: T_0 is defined as the energy of the $v = 0$ level of an excited state relative to the $X^1\Sigma^+$ $v = 0$ level, and $\Delta G_{1/2}$ is the energy difference between the $v = 0$ and $v = 1$ levels. All other (equilibrium) constants are extracted from the data. The rotational constant for a given vibrational level is given to first order in v as $B_v = B_e - \alpha_e(v+1/2)$, where B_e is the equilibrium rotational constant. Since we have measured at least two vibrational levels for each state, we can determine $\alpha_e \approx B_v - B_{v+1}$, and then use this to obtain B_e for each state. T_e, ω_e, and $\omega_e x_e$ are determined using Equations 5.8 and 5.9. For the $^3\Pi_1$ state, we were able to calculate ω_e and $\omega_e x_e$ directly; for all other states we assumed a Morse potential so that $\omega_e x_e = \alpha_e^2\omega_e^2/36B_e^3 + \alpha_e\omega_e/3B_e + B_e$ (i.e., the Pekeris relationship).

In addition, we have observed isotope shifts of the state origins, called δT_e in Table 5.4, that we attribute to Hf electronic isotope shifts (due to the finite nuclear charge radius) [373, 374, 375]. For bands with well resolved isotope structure (i.e., $\Delta v \neq 0$), $\delta T'_e - \delta T''_e$ was determined from Equation 5.10 either by fitting both ν_0^{180} and ν_0^{178} or by measuring δE near the origin and then subtracting the vibrational contribution. For $\Delta v = 0$ bands, we found the frequency where the lines were the sharpest, indicating that $\delta E \approx 0$ (as illustrated by the Q- and P-branch lines in Figure 5.1(d)); this location relative to the band origin is used for E_{rot} in Eq. 5.10, which then gave $\delta T'_e - \delta T''_e$. Values of $|\delta T'_e - \delta T''_e|$ were $\lesssim 0.1$ cm^{-1} for all transitions. To obtain the δT_e values given in Table 5.4, we set $\delta T''_e(X^1\Sigma^+) = 0$ and calculated relative shifts of the other states. The simplistic model of Eq. 5.10 neglects vibrational-band-specific perturbations or other more complicated level-dependent effects; however, results were consistent across different transitions, which supports the assignment of the effect to electronic states, not individual bands. Except for the $X^1\Sigma^+$ state the isotope shifts are all fairly similar with an average value of about -0.06 cm^{-1}(-1.7 GHz), which agrees well with the value for the Hf^+ $5d^26s^2 \rightarrow 5d^26s6p$ of -1.8 GHz [375].

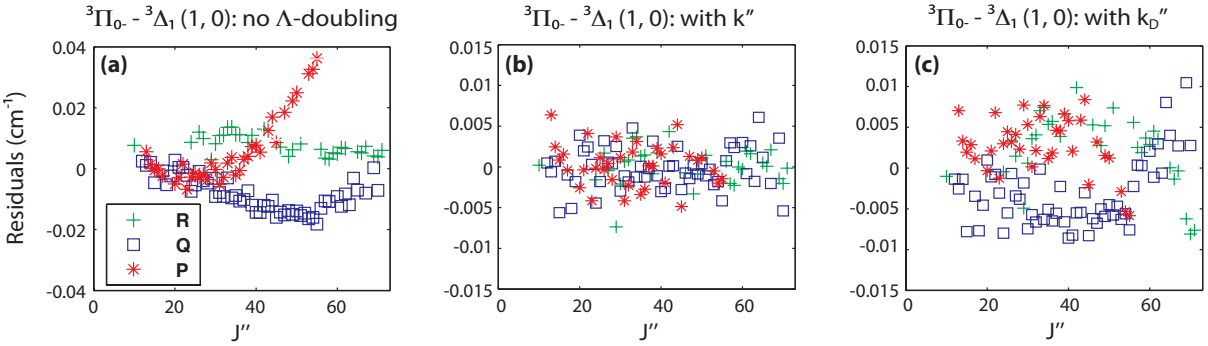

Figure 5.7: Residuals for three fits to the $^3\Pi_{0^-} \leftarrow {}^3\Delta_1$ (1, 0) band. The residuals are only plotted for assigned lines in each branch: R-branch (+), Q-branch(square), and P-branch (*). (a) Fit with no Λ-doubling terms included. Notice the large structure to the residuals. (b) Only k'' included, i.e., only Λ-doubling proportional to J^2 in the lower state. No structure in the residuals; the scatter is primarily due to error in identification of the line center. (c) Only k''_D included, i.e., only Λ-doubling proportional to J^4 in the lower state. There is some slight structure to the residuals, indicating that the primary contribution to the Λ-doubling goes as J^2.

5.1.3 Lambda doubling

Due to our ability to see high-J lines, we were able to measure precise values for the Λ-doubling, parametrized by k and k_D in Equation 5.7, in several different electronic levels. In Hund's case (a), k can be related to the more standard Λ-doubling parameters defined in [370] for Π states (o, p, and q) and to $\tilde{o}_\Delta$ as defined in [371] for $^3\Delta$ states; k was not measurable in Φ states. The values of k and k_D were useful in assigning many transitions and also providing some insight into inter-state perturbations. For the eEDM measurement, the most important Λ-doubling parameter is the splitting of the $J = 1$ levels in the $^3\Delta_1$, as this goes into determining several different potential systematic effects. As discussed in Section 5.1.1, Λ-doubling occurs due to coupling with electronic states that have non-degenerate (single parity) rotational levels – typically Σ states – via off-diagonal spin-orbit and L-uncoupling interactions. The selection rules for these interactions have $\Delta\Lambda = \pm 1, \Delta\Omega = 0$ and $\Delta\Lambda = \pm 1, \Delta\Omega = \pm 1$, respectively. We can now estimate the Λ-doubling terms by using these two interactions to link $\Omega \to -\Omega$.

In a case (a) $^3\Delta_1$ state, the Λ-doubling occurs from two applications of the spin-orbit interaction (which has no J dependence) and two applications of the L-uncoupling interaction ($\sim J$). So, we expect the Λ-doubling splitting to be given by $\pm\tilde{o}_\Delta \times J(J+1)$, where the upper and lower signs refer to the two e/f-symmetry levels and $\tilde{o}$ is given in [371]. We can make a rough estimate of the value of $\tilde{o}_\Delta$ by a simple scaling from that measured in TiO or WC [376]:

$$\tilde{o}_\Delta \approx \frac{\zeta^2(\mathrm{Hf}^{2+})B^2(\mathrm{HfF}^+)}{\zeta^2(\mathrm{WC/TiO})B^2(\mathrm{WC/TiO})} \times \tilde{o}_\Delta(\mathrm{WC/TiO}). \tag{5.11}$$

This scaling relationship arises from the application of two spin-orbit operators, which scale as the atomic spin-orbit, ζ, and two L-uncoupling operators, which scale as the rotational constant B [371, 376]; however, it neglects changes in state order and spacing. Using this and ζ_{5d} from earlier we predict $\tilde{o}_\Delta \approx 50$ kHz.

A more detailed estimate can be made by explicitly writing out the possible perturbations, as in [377]. We only include states in the *sd* manifold given in Table 5.1 because the spin-orbit and L-uncoupling effects are, to a good approximation, just single-electron operators. The Λ-doubling

parameter is given by [371]

$$\tilde{o}_\Delta = \sum_{i,j,k} 4\sqrt{30} \frac{\prod(\text{matrix elements})}{(E_0 - E_i)(E_0 - E_j)(E_0 - E_k)} \begin{Bmatrix} S & S & 2 \\ 1 & 1 & S' \end{Bmatrix} \sqrt{\frac{(2S-2)!}{(2S+3)!}}, \tag{5.12}$$

where i, j, k are the intermediate states, $S = 1$ is the spin multiplicity of $^3\Delta_1$, S' is the other spin multiplicity of the perturbing states, and $\prod$(matrix elements) is the product of matrix elements of either the spin-orbit or L-uncoupling operators. Table 5.3 shows the intermediate state and operator combinations from the states in Table 5.1 that contribute to the Λ-doubling as well as the calculated value of $\tilde{o}_\Delta$ from each combination.

Take, for example, the first line in Table 5.3. We need to evaluate first the spin-orbit matrix element between $^3\Delta_1$ and $^3\Pi_1$, i.e., $\langle ^3\Delta_1 | \hat{H}_{SO} | ^3\Pi_1 \rangle$. Remembering the definition of $\hat{H}_{SO}$ as a sum over single-electron operators from Section 5.1.1 and ignoring the s electron, which does not change, we have that

$$\begin{aligned} \langle ^3\Delta_1 | \hat{H}_{SO} | ^3\Pi_1 \rangle &= \frac{1}{\sqrt{2}} \langle \delta^{2+}(\beta) | \frac{\hat{a}}{2} l_+ \cdot s_- | \pi^+(\alpha) \rangle = \frac{1}{\sqrt{2}} \langle \delta^{2+} | \frac{\hat{a}}{2} l_+ | \pi^+ \rangle \langle \beta | s_- | \alpha \rangle \\ &= \frac{1}{\sqrt{2}} \left(\frac{1}{2} \right) \sqrt{l(l+1) - m_\pi(m_\pi + 1)} \langle \delta | \hat{a}_+ | \delta \rangle = \frac{1}{\sqrt{2}} \zeta_{5d} \left(\frac{1}{2} \right) \sqrt{6-2}. \end{aligned} \tag{5.13}$$

Similarly, $\langle ^3\Pi_1 | \hat{H}_{SO} | ^3\Sigma_1 \rangle = \frac{\sqrt{3}}{2} \langle \pi^+ | \hat{a} | \pi^+ \rangle = \frac{\sqrt{3}}{2} \zeta_{5d}$. For the L-uncoupling operator, we have

$$\langle ^3\Sigma_1 | \hat{L}_+ | ^3\Pi_0 \rangle = \langle \sigma_2(\alpha) | B l_+ | \pi^-(\alpha) \rangle = B\sqrt{6}, \tag{5.14}$$

and $\langle ^3\Pi_0 | \hat{L}_+ | ^3\Delta_{-1} \rangle = 2B$. Finally, we use these matrix elements as well as the energy differences from Table 5.5 in Equation 5.12 to evaluate $\tilde{o}_\Delta$. In this case, we do not involve any singlet states so $S = S' = 1$. Summing all of the contributions gives $\tilde{o}_\Delta \approx 17.6$ kHz.

The Λ-doubling in the $^3\Delta_1$ can be observed at high-J in the $^3\Phi_2 \leftarrow {}^3\Delta_1$ (0, 0) band by comparing neighboring P-, Q-, and R-branch lines, as shown in Figure 5.1(d). Since the R-branch lines have the highest J, there is noticeable doubling in these lines compared to the P- or Q-branch lines, which indicates that this doubling is not due to isotope splitting. In this band, the lines are not sufficiently well resolved to permit an accurate determination of the Λ-doubling constant, but by fitting the $^3\Pi_{0^-} \leftarrow {}^3\Delta_1$ (1, 0) transition, we were able to precisely determine

Table 5.3: Matrix elements for the Λ-doubling in $^3\Delta_1$. Four matrix elements, two applications of spin-orbit (H_{SO}) and two applications of L-uncoupling (H_{L_+}) are required to link $^3\Delta_1$ and $^3\Delta_{-1}$. Each row gives one pathway, with the final value of $\tilde{o}_\Delta$ calculated according to Equation 5.12.

$\Lambda = 2$	$\hat{O}$	$\Lambda = 1$	$\hat{O}$	$\Lambda = 0$	$\hat{O}$	$\Lambda = -1$	$\hat{O}$	$\Lambda = -2$	$\tilde{o}_\Delta$ (kHz)
$^3\Delta_1$	H_{SO}	$^3\Pi_1$	H_{SO}	$^3\Sigma_1$	H_{L_+}	$^3\Pi_0$	H_{L_+}	$^3\Delta_{-1}$	-3.9
$^3\Delta_1$	H_{SO}	$^3\Pi_1$	H_{L_+}	$^3\Sigma_0$	H_{SO}	$^3\Pi_0$	H_{L_+}	$^3\Delta_{-1}$	-4
$^3\Delta_1$	H_{SO}	$^3\Pi_1$	H_{L_+}	$^3\Sigma_0$	H_{L_+}	$^3\Pi_{-1}$	H_{SO}	$^3\Delta_{-1}$	-3.7
$^3\Delta_1$	H_{SO}	$^1\Pi_1$	H_{SO}	$^3\Sigma_1$	H_{L_+}	$^3\Pi_0$	H_{L_+}	$^3\Delta_{-1}$	6.5
$^3\Delta_1$	H_{L_+}	$^3\Pi_0$	H_{SO}	$^3\Sigma_0$	H_{SO}	$^3\Pi_0$	H_{L_+}	$^3\Delta_{-1}$	-4.2
$^3\Delta_1$	H_{L_+}	$^3\Pi_0$	H_{L_+}	$^3\Sigma_{-1}$	H_{SO}	$^3\Pi_{-1}$	H_{SO}	$^3\Delta_{-1}$	-4
$^3\Delta_1$	H_{L_+}	$^3\Pi_0$	H_{L_+}	$^3\Sigma_{-1}$	H_{SO}	$^1\Pi_{-1}$	H_{SO}	$^3\Delta_{-1}$	6.5
$^3\Delta_1$	H_{L_+}	$^3\Pi_0$	H_{SO}	$^3\Sigma_0$	H_{L_+}	$^3\Pi_{-1}$	H_{SO}	$^3\Delta_{-1}$	-3.7
$^3\Delta_1$	H_{SO}	$^1\Pi_1$	H_{L_+}	$^1\Sigma^+$	H_{SO}	$^3\Pi_0$	H_{L_+}	$^3\Delta_{-1}$	6.9
$^3\Delta_1$	H_{SO}	$^1\Pi_1$	H_{L_+}	$^1\Sigma^+$	H_{L_+}	$^1\Pi_{-1}$	H_{SO}	$^3\Delta_{-1}$	5.4
$^3\Delta_1$	H_{L_+}	$^3\Pi_0$	H_{SO}	$^1\Sigma^+$	H_{SO}	$^3\Pi_0$	H_{L_+}	$^3\Delta_{-1}$	8.9
$^3\Delta_1$	H_{L_+}	$^3\Pi_0$	H_{SO}	$^1\Sigma^+$	H_{L_+}	$^1\Pi_{-1}$	H_{SO}	$^3\Delta_{-1}$	6.9

the sign and size of the Λ-doubling. As shown in Figure 5.7, the best fit was obtained with k'' instead of k''_D, implying that the Λ-doubling goes mainly as $J(J+1)$ as expected (adding k''_D to the fit with k'' resulted in no improvement). This fit gives a value of $k'' = -1.23(6) \times 10^{-5}$ cm^{-1}, so $\tilde{o}_\Delta = -k''/2 = 6.2(3) \times 10^{-6}$ cm^{-1} = 185(9) kHz (corresponding to e above f). This is significantly larger than the estimated values above, presumably due to unaccounted for interactions or mixings in the excited state that invalidate the pure configuration approach. The precision on $\tilde{o}_\Delta$ is only about an order of magnitude worse than that obtained for TiO using pure rotational spectroscopy [377], illustrating the ability to obtain high-resolution spectroscopic information from broad-bandwidth ro-vibronic spectra.

Λ-doubling in the $^3\Pi_0$ can arise from interactions with both $^1\Sigma^+$ and $^3\Sigma^+$ states, which result in a splitting of the $\Omega = 0^-$ and 0^+ levels that is independent of J. We measured this splitting to be 189.099(4) cm^{-1} with the 0^+ (e-symmetry) higher in energy than 0^- (f). To the extent that the X$^1\Sigma^+$ state is a pure $(s\sigma)^2$ configuration, we can assume that this splitting is from a higher-lying $^3\Sigma^+$ state with an $(s\sigma d\sigma)$ configuration. The spin-orbit interaction between the $^3\Sigma^+_{0^-}$ (f) and the $^3\Pi_{0^-}$ can be estimated by

$$\frac{(\frac{1}{\sqrt{2}}\langle\sigma_1(\beta)\pi(\beta)|\frac{1}{2}\hat{a}l_+s_-|\sigma_1(\beta)\sigma_2(\alpha)\rangle)^2}{\Delta E} \approx \frac{\frac{3}{4}\zeta^2_{5d}}{\Delta E}. \tag{5.15}$$

We have used $\langle\pi(\beta)|l_+s_-|\sigma_2(\alpha)\rangle \approx \sqrt{6}$ in the pure-precession model [370, 369]. Using the measured splitting and the atomic spin-orbit coefficient, we estimate $\Delta E \approx 11000$ cm^{-1}, which gives an approximate location of the $^3\Sigma^+_{0^-}$ state to be 21200 cm^{-1}. This is close to the predicted position of 21694 cm^{-1} from the new calculations (see Section 5.2). In a Hund's case (a) basis, this splitting corresponds to the more familiar $2(o+p+q)$ [370].

The cause of the Λ-doubling in the $^3\Pi_1$ state is primarily interaction with the $^3\Sigma^+_{0^-}$ state through the $^3\Pi_0$. This type of interaction is characterized by the parameter p in [370]. With e-symmetry above f in $^3\Pi_0$ and $^3\Pi_0$ located below $^3\Pi_1$, we would expect e above f in $^3\Pi_1$, which corresponds to a negative value of k as observed. The magnitude of k is expected to be about

$4Bp/A_\Pi$, where A_Π is the spin-orbit parameter for the $^3\Pi$ manifold and

$$p \approx C\langle {}^3\Pi_1|BL_+|{}^3\Sigma^+_{0^-}\rangle\langle {}^3\Sigma^+_{0^-}|\hat{a}L_-S_+|{}^3\Pi_0\rangle/(E_\Pi - E_\Sigma) \tag{5.16}$$

$$\approx CB\zeta_{5d}\langle\pi^+|l_+|\sigma_2\rangle^2/(E_\Pi - E_\Sigma). \tag{5.17}$$

Here, C is a numerical factor dependent on the spin [370]. Again using the pure-precession model, we estimate $k \approx 8 \times 10^{-4}$ cm^{-1}, in reasonable agreement with experiment.

We attribute most of the Λ-doubling in the $^1\Pi_1$ to interaction with the nearly-degenerate nominal $^3\Sigma^-_{0^+}$ state. It is reasonable that the $^1\Pi$ and $^3\Sigma^-$ are not pure $(s\sigma d\pi)$ and $(d\delta)^2$ configurations, which would lead to increased spin-orbit interaction between $^1\Pi_1$ and $^3\Sigma^-_{0^+}$. Estimating the magnitude of the Λ-doubling in this case is difficult due to uncertainty in the purity of the configurations. Qualitatively though, we would expect the effect of a $^3\Sigma^-$ state above the $^1\Pi_1$ state would be to push e-symmetry below f as observed. In addition we observed Λ-doubling that was strongly vibrational-level dependent (3.69×10^{-4} cm^{-1} for the $v = 0$ compared with 2.68×10^{-4} cm^{-1} for the $v = 1$), which is indicative of nearly-degenerate interacting states. We also measured a Λ-doubling term proportional to J^4 (denoted k_D). This term can be explained by substituting $\Delta E \to \Delta E + (B_\Pi - B_\Sigma)J(J+1)$ in the Λ-doubling denominator; the first two terms in the Taylor expansion give the $J(J+1)$ and the $J^2(J+1)^2$ components. From this we can estimate that $k_D \approx 3k(B_\Pi - B_\Sigma)/(E_\Pi - E_\Sigma)$, which gives $k_D \approx 2 \times 10^{-8}$ cm^{-1}.

5.2 Theory

In earlier theoretical study of HfF^+ [378], the correlation calculations of the spectroscopic constants were performed in two different ways: in the first series 10 electrons from $5d, 6s$ shells of Hf and $2s, 2p$ of F were correlated while in the second series $5s, 5p$ outer core electrons of Hf and $1s$ of F were also correlated. The rest of the $1s - 4d$ inner-core electrons of Hf were excluded from the explicit treatment using the generalized relativistic effective core potential (GRECP) method[1] [379]. While it was shown that the inclusion of the additional electrons in the 20-electrons case

[1] 60-electron core GRECP for Hf is available at www.qchem.pnpi.spb.ru

contributed significantly to the excitation energies, such 20-electron calculations were performed only for one internuclear Hf–F distance in a small space of many-electron basis functions due to computer limitations. This calculation was then applied for other distances as a "core correction". In the present work a new 20-electron relativistic correlation calculation was carried out in order to consider electronic states that were not investigated in [378] as well as to overcome the bottlenecks of the previous studies of HfF^+. Eventually 23 electronic states (with excitation energies up to 22000 cm^{-1}) were considered in the present study instead of ten states in [378].

Some modifications were made in the computational procedure to achieve better accuracy. We used a direct multi-reference configuration-interaction approach accounting for spin-orbit effects (SODCI) [380, 381] as a method to treat both correlation and relativistic effects simultaneously. One-component basis functions (orbitals) are required in this method to construct many-electron spin-adapted functions (SAF's). Instead of the orbitals obtained within the complete active space self-consistent field method (used in [378]), the natural orbitals of a one-electron density matrix averaged over the density matrices of the states of interest were used. The latter density matrices were calculated within the scalar-relativistic coupled-clusters method with single and double cluster amplitudes (CCSD) using the CFOUR code [382]. From numerical investigation [383] it is known that the use of natural orbitals can provide faster convergence in terms of the number of SAF's required to account for a given part of correlation energy.

In the SODCI calculation the same atomic basis sets for Hf and F were used as in our previous study [378], i.e., a generally-contracted basis set for Hf consisting of 6 s-, 5 p-, 5 d-, 3 f- and 1 g- type contracted functions (denoted as {6,5,5,3,1}) and an ANO-I {4,3,2,1} basis set for F [384]. However, a correction on the extension of the basis set was applied additionally in the present work. To evaluate the correction, two scalar-relativistic calculations were performed using the coupled clusters method with single, double and perturbative triple cluster amplitudes: (i) in the same basis set that was used at the SODCI stage, and (ii) with an extended basis set for Hf (produced by uncontracting d- and adding g-, h-, i- type basis functions) and an ANO-L {7,7,4,3} [384] basis for F.

To compute potential curves the described calculations were performed at 14 points in the range of 3.0 – 4.2 a_0. As shown in Table 5.5, the new calculations are in remarkable agreement with all of the experimental results. These improvements should enable more accurate calculations in other species with heavy atoms, where relativistic effects are extremely important.

5.3 Summary

By using a combination of comb-vms and cw-laser vms, we have performed high-resolution survey spectroscopy of HfF^+. We measured 19 transitions (16 identified) and obtained constants for 9 different electronic states. Because of the ability to see high-J lines, many of the constants are fit to high precision, including Λ-doubling terms. This information enabled further development and cross-checks of the theory, which have implications beyond the eEDM measurement: accurate calculations of lanthanides and actinides are important for understanding the bonding and reactivity of species containing these atoms, see for example [385, 386, 387, 388].

In particular, we accomplished the four goals identified in the introduction: we measured precise constants for the $^1\Sigma^+$ and $^3\Delta_1$ states, among others, including the Λ-doubling in $^3\Delta_1$. The splitting in the $J = 1$ is important for the eEDM measurements because it is the opposite parity levels in this state that are mixed in an electric field to polarize the molecule. The necessary electric field for full polarization – i.e., when the Stark effect goes from second order to first order in the electric field – can be found by equating the Stark energy to the energy difference between the two parity states: $\mathcal{E}_{pol} \approx \omega_{ef}/2\pi d_{mf}$ [389], where ω_{ef} is the Λ-doubling splitting (in angular frequency) and d_{mf} is the molecular-frame electric dipole moment of the molecule (4.3 Debye for HfF^+ [62]). We can use our measurement of $\tilde{o}_\Delta$ to estimate that $\omega_{ef} = 2\pi \times 4\tilde{o}_\Delta \approx 2\pi \times 740$ kHz, which is at least an order magnitude larger than previously predicted [62]. Nonetheless, this means that $\mathcal{E}_{pol}$ is still under 1 V/cm, which is important for the eEDM experiment as larger fields tend to lead to more issues with systematic errors. We also identified transitions for laser-induced fluorescence or state manipulation (e.g., $^1\Pi_1$ from $^1\Sigma^+$ and $^3\Phi_2$ from $^3\Delta_1$) as well as an intermediate state for Raman transfer from $^1\Sigma^+$ to $^3\Delta_1$ (the $^3\Pi_{0^+}$). In the next chapter, we use this transition to

selectively transfer population to the $^3\Delta_1$ $J = 1$, see Section 6.3. In addition, Table 5.6 lists the calculated transition dipole moments between the excited states and the three lowest states, which are useful for estimating transition strengths.

We are currently using an improved version of the comb-vms system to characterize ThF^+, which has several advantages over HfF^+ for the eEDM experiment. However for this species, the *ab initio* calculations are even more challenging, leading to larger theoretical uncertainties. The first spectroscopy of ThF^+ using PFI-ZEKE plus some LIF (unassigned) has recently been published [390], but, as was the case with HfF^+, the higher excited states remain uncharacterized. By using highly nonlinear fiber to broaden the comb spectrum (Section 2.3), we have been able to cover the full 700-900 nm range with comb-vms, which corresponds to 3250 cm^{-1} of continuous spectra! This ability to rapidly cover thousands of cm^{-1} with high sensitivity and high resolution will be a powerful new tool for the study of ions and radicals for many applications.

Table 5.4: Derived constants for observed states in $^{180}HfF^+$ in cm^{-1}. Values for T_0 are given to the $\nu = 0$ levels, with the $X^1\Sigma^+$ $\nu = 0$ level set to 0. Values for T_e are to the minimum of the potential curves again with $X^1\Sigma^+$ set to 0. $\Delta G_{1/2}$ is only given for states where we had a direct measurement. All equilibrium values assume a Morse potential unless otherwise noted. Quoted uncertainties are 95% and are statistical, i.e., they do not account for any deviation from the Morse potential. $\delta T_e = T_e^{180} - T_e^{178}$ is an electronic isotope shift relative to $^1\Sigma^+$ for each state as discussed in the text.

	T_0	$\Delta G_{1/2}$	T_e	B_e	ω_e	$\omega_e x_e$	α_e $[10^{-3}]$	δT_e
$^1\Sigma^+$	0	784.820(12)	0	0.30558(3)	790.76(11)	2.97(5)	1.50(2)	0
$^3\Delta_1$	976.930(10)	–	991.83(74)	0.29963(5)	760.9(1.5)	2.78(21)	1.45(8)	-0.049(12)
$^3\Delta_2$	2149.432(18)	–	–	–	–	–	–	-0.055(12)
$^1\Pi_1$	13002.189(12)	–	13046.04(21)	0.28186(5)	702.9(4)	2.70(15)	1.42(6)	-0.071(6)
$^3\Pi_1$	10894.697(14)	–	10933.77(6)$^+$	0.28454(8)	712.382(21)$^+$	2.51(6)$^+$	1.43(4)	-0.054(7)
$^3\Pi_{0^-}$	–	–	10248.34(36)*	0.28517(17)*	–	–	–	-0.033(16)
$^3\Pi_{0^+}$	10401.723(13)	712.930(15)	10437.44(36)	0.28518(13)	719.5(7)	3.3(3)	1.63(11)	-0.047(7)
$^3\Sigma^-_{0^+}$	13254.302(7)	699.497(9)	13296.93(28)	0.29046(14)	705.5(5)	3.0(3)	1.59(10)	-0.106(7)
$^3\Phi_2$	14910.270(16)	680.442(14)	14963.15(33)	0.27778(14)	684.5(7)	2.05(31)	1.16(14)	-0.044(16)

$^+$ Calculated without assuming a Morse potential.

* Assuming ω_e, $\omega_e x_e$, and α_e are the same as for the $^3\Pi_{0+}$.

Table 5.5: Summary of states. Comparison of derived molecular constants from this work and from the experiments of Barker et al. [372] with the old theoretical calculations of Petrov et al. [378] and the improved theory discussed here. The theoretical values of B_e from [378] were computed from the equilibrium bond length. Experimental uncertainties are converted to 95% (2σ).

State (configuration)	Constant	This Work	[372]	[378]	New theory
$^1\Sigma^+$	T_e	0	0	0	0
$(s\sigma_1)^2$	B_e	0.30558(3)	0.304(10)	0.3082	0.309
	ω_e	790.76(11)	791.2(1.0)	751	792
$^3\Delta_1$	T_e	991.83(74)	993(2)	1599	1229
$(s\sigma_1)(d\delta)$	B_e	0.29963(5)	0.301(10)	0.2994	0.301
	ω_e	760.9(1.5)	761.3(2.0)	718	754
$^3\Delta_2$	T_e	2149.432(16)†	2151.7(20)†	2807	2394
$(s\sigma_1)(d\delta)$	B_e	0.29915(9)*	0.300(10)	0.2997	0.302
	ω_e	–	762.3(2.0)	719	766
$^3\Delta_3$	T_e	–	3951(2)	4324	3995
$(s\sigma_1)(d\delta)$	B_e	–	0.308(10)	0.3004	0.301
	ω_e	–	761.5(2.0)$^+$	721	757
$^1\Delta_2$	T_e	–	–	11519	10610
$(s\sigma_1)(d\delta)$	B_e	–	–	0.2981	0.298
	ω_e	–	–	696	747
$^3\Pi_{0^-}$	T_e	10248.34(36)	–	11910	10400
$(s\sigma_1)(d\pi)$	B_e	0.28517(17)	–	0.2848	0.286
	ω_e	–	–	689	716
$^3\Pi_{0^+}$	T_e	10437.44(36)	–	12196	10658
$(s\sigma_1)(d\pi)$	B_e	0.28518(13)	–	0.2854	0.285
	ω_e	719.5(7)	–	699	724
$^3\Pi_1$	T_e	10933.77(6)	–	12686	11058
$(s\sigma_1)(d\pi)$	B_e	0.28454(8)	–	0.2835	0.285
	ω_e	712.382(17)	–	687	712
$^3\Pi_2$	T_e	–	–	14438	13452
$(s\sigma_1)(d\pi)$	B_e	–	–	0.2848	0.287
	ω_e	–	–	703	745

$^+$ $\Delta G_{1/2}$.
† T_0.
* B_0.

Table 5.5: Summary of states. (continued)

State (configuration)	Constant	This Work	[372]	[378]	New theory
$^1\Pi_1$	T_e	13046.3(3)	–	14784	13493
$(s\sigma_1)(d\pi)$	B_e	0.28186(5)	–	0.2805	0.283
	ω_e	702.9(4)	–	679	699
$^3\Sigma^-_{0^+}$	T_e	13296.93(28)	–	–	13773
$(d\delta)^2$	B_e	0.29046(14)	–	–	0.292
	ω_e	705.5(5)	–	–	716
$^3\Sigma^-_1$	T_e	–	–	–	14757
$(d\delta)^2$	B_e	–	–	–	0.292
	ω_e	–	–	–	711
$^3\Phi_2$	T_e	14963.15(33)	–	–	15284
$(d\delta)(d\pi)$	B_e	0.27778(14)	–	–	0.278
	ω_e	684.5(7)	–	–	671
$^3\Phi_3$	T_e	–	–	–	17457
$(d\delta)(d\pi)$	B_e	–	–	–	0.277
	ω_e	–	–	–	658
$^1\Gamma_4$	T_e	–	–	–	18312
$(d\delta)^2$	B_e	–	–	–	0.289
	ω_e	–	–	–	641
$^3\Pi_{0^-}$	T_e	–	–	–	19167
$(d\delta)(d\pi)$	B_e	–	–	–	0.276
	ω_e	–	–	–	691
$^3\Pi_1$	T_e	–	–	–	19332
$(d\delta)(d\pi)$	B_e	–	–	–	0.279
	ω_e	–	–	–	698
$^3\Pi_{0^+}$	T_e	–	–	–	20074
$(d\delta)(d\pi)$	B_e	–	–	–	0.280
	ω_e	–	–	–	748
$^1\Sigma^+$	T_e	–	–	–	20330
$(s\sigma_1)(p\pi)$	B_e	–	–	–	0.288
	ω_e	–	–	–	610
$^3\Pi_2$	T_e	–	–	–	20338
$(s\sigma_1)(p\pi)$	B_e	–	–	–	0.277
	ω_e	–	–	–	665

Table 5.5: Summary of states. (continued)

State	Constant	This Work	[372]	[378]	New theory
$^3\Phi_4$	T_e	–	–	–	20769
	B_e	–	–	–	0.283
	ω_e	–	–	–	740
$^3\Sigma_1^+$	T_e	–	–	–	21415
	B_e	–	–	–	0.276
	ω_e	–	–	–	665
$^3\Sigma_{0^-}^+$	T_e	21200°	–	–	21694
	B_e	–	–	–	0.277
	ω_e	–	–	–	658

° Estimated from Λ-doubling in the $^3\Pi_0$ (see text).

Table 5.6: Calculated molecular-frame dipole moments for $^1\Sigma^+$and $^3\Delta_1$ states as well as transition dipole matrix elements between states in HfF^+ in e a_0. (?) indicates non-zero, but not calculated; (–) indicates < 0.01.

	Dipole (e a_0)		
State	$^1\Sigma^+$	$^3\Delta_1$	$^3\Delta_2$
$^1\Sigma^+$	-1.2		
$^3\Delta_1$	0.02	-1.4	
$^3\Delta_2$	–	0.02	
$^3\Delta_3$	–	–	?
$^1\Delta_2$	–	0.04	0.07
$^3\Pi_{0^-}$	0	0.27	–
$^3\Pi_{0^+}$	0.15	0.27	–
$^3\Pi_1$	0.25	0.03	0.22
$^3\Pi_2$	–	0.03	0.01
$^1\Pi_1$	0.55	0.03	0.18
$^3\Sigma_{0^+}$	0.23	0.08	–
$^3\Sigma_1$	0.03	-0.02	0.07
$^3\Phi_2$	–	0.48	0.10
$^3\Phi_3$	–	–	0.46
$^1\Gamma_4$	–		
$^3\Pi_{0^-}$	–	0.36	–
$^3\Pi_1$	0.06	0.14	0.39
$^3\Pi_{0^+}$	0.12	0.39	–
$^1\Sigma^+$	0.70	0.03	–
$^3\Pi_2$	–	?	0.10
$^3\Phi_4$	–	–	–
$^3\Sigma_1$	0.01	0	0.03
$^3\Sigma_{0^-}$	–	0.17	–

Table 5.7: Franck-Condon factors (vibrational overlap integrals) for $^3\Pi_{0^+}$ - $^3\Delta_1$. The Franck-Condon factors are calculated using the rotational constant for each vibrational level to account for anharmonicity; however, the equilibrium vibrational constant and harmonic oscillator wave functions were used for the calculations.

			v'		
v"	0	1	2	3	4
0	0.68	0.23	0.02	0.00	0.00
1	0.28	0.28	0.33	0.04	0.00
2	0.09	0.32	0.09	0.37	0.07
3	0.03	0.17	0.27	0.02	0.38
4	0.01	0.07	0.21	0.20	0.00

Table 5.8: Franck-Condon factors for $^3\Phi_2$ - $^3\Delta_1$

			v'		
v"	0	1	2	3	4
0	0.41	0.38	0.12	0.01	0.00
1	0.35	0.00	0.29	0.23	0.05
2	0.20	0.15	0.07	0.12	0.28
3	0.10	0.21	0.01	0.15	0.02
4	0.05	0.17	0.10	0.02	0.15

Table 5.9: Franck-Condon factors for $^3\Pi_{0^+}$ - $^1\Sigma^+$

			v'		
v"	0	1	2	3	4
0	0.47	0.35	0.07	0.00	0.00
1	0.35	0.04	0.36	0.16	0.01
2	0.18	0.21	0.01	0.26	0.22
3	0.08	0.22	0.07	0.08	0.15
4	0.04	0.15	0.17	0.01	0.14

Table 5.10: Franck-Condon factors for $^3\Pi_1$ - $^1\Sigma^+$

	v'				
v"	0	1	2	3	4
0	0.45	0.36	0.09	0.01	0.00
1	0.35	0.02	0.34	0.19	0.02
2	0.19	0.19	0.03	0.20	0.26
3	0.09	0.22	0.04	0.12	0.08
4	0.04	0.16	0.14	0.00	0.16

Table 5.11: Franck-Condon factors for $^1\Pi_1$ - $^1\Sigma^+$

	v'				
v"	0	1	2	3	4
0	0.36	0.39	0.14	0.02	0.00
1	0.34	0.00	0.26	0.25	0.05
2	0.22	0.11	0.09	0.09	0.28
3	0.12	0.19	0.00	0.16	0.01
4	0.06	0.18	0.07	0.03	0.14

Table 5.12: Franck-Condon factors for $^3\Sigma_{0^+}$ - $^1\Sigma^+$

	v'				
v"	0	1	2	3	4
0	0.67	0.24	0.02	0.00	0.00
1	0.28	0.25	0.36	0.04	0.00
2	0.10	0.30	0.07	0.41	0.07
3	0.03	0.17	0.23	0.01	0.41
4	0.01	0.08	0.20	0.14	0.00

Chapter 6

Precision spectroscopy of trapped ions

In this chapter, we turn our attention to a different aspect of molecular spectroscopy – tests of fundamental physics with precision spectroscopy of trapped molecular ions. In particular, we discuss an ongoing experiment to constrain the size of the electric dipole moment of the electron (eEDM).

6.1 eEDM Background

As first pointed out by Purcell and Ramsey [391], a permanent electric dipole moment of an elementary particle would be a violation of parity (P) symmetry — that is, an inversion of spatial coordinates ($\vec{r} \rightarrow -\vec{r}$). To show this consider an electron, which has a spin about an axis, much like a spinning top. If we apply a parity transformation, nothing changes — the electron still spins in the same direction. However, if the electron charge distribution is not spherical but is, for example, ovoid as illustrated in Figure 6.1, then this transformation (denoted by the P-transformation arrow in the figure) changes the charge distribution relative to the spin direction. Such an asymmetric charge distribution can be represented as the sum of two displaced charge distributions of opposite charge, which is an electric dipole moment (EDM, with units of electron charge, e, times separation in cm). So we see that under a P-transformation, the dipole moment (red arrow) and the spin vector (blue arrow) reverse direction relative to each other, violating P-reversal symmetry. This assumes that the dipole moment is aligned along the spin vector; however, if this were not the case, then more quantum numbers would be needed to describe the electron, and the Pauli exclusion

principle would not be valid.

In addition to P-symmetry violation, the existence of an electron EDM (eEDM) would be a direct violation of time (T)-reversal symmetry (i.e., $t \rightarrow -t$) [29], as shown with the lower transformation in Figure 6.1. Under T reversal, the direction of the electron spin reverses, but the shape of the charge distribution does not change; so the dipole moment does not change. This again results in the spin vector and dipole moment being antiparallel if they were originally parallel, which is a violation of T-reversal symmetry.

The Standard Model, the current theory explaining fundamental particles and their interactions, has been phenomenally successful and has been tested in many cases to high precision. However, the Standard Model has some potential deficiencies. One primary issue is that the extent of P-symmetry violation (which is linked to T-symmetry violation by the CPT theorem) can not account for the observed ratio between matter and antimatter in the universe by the theory of electroweak baryogenesis (this is one component of the Sakharov criteria) [392, 393, 394]. In addition, the existence of dark matter is not accounted for in the Standard Model. Finally, a significant amount of "fine-tuning" is required to reduce the CP-violating phase θ in quantum chromodynamics to less than 10^{-10} to fit with current measurements of the neutron EDM [395] (the strong-CP problem) and to reduce the energy scale of gravity compared to the electroweak interaction by 10^{34} (the gauge hierarchy problem). Many theories extending the Standard Model, such as the popular supersymmetry (SUSY) [396], have been developed to address difficulties with the Standard Model, but no direct experimental evidence supporting these theories exists. Currently, the experimentally measured instances of P- and T-symmetry violation are explained in the Standard Model; however, the Standard Model does not contain other instances of T-symmetry violation. Thus, if additional cases of T-symmetry violation were discovered, this would provide direct evidence for physics beyond the Standard Model [397, 398, 399, 400].

As discussed more below, measurements of the eEDM are performed currently either in paramagnetic atoms or molecules. In this case, the measured EDM can arise from an eEDM or from an EDM of a proton or neutron appearing as an effective eEDM via electron-nucleon

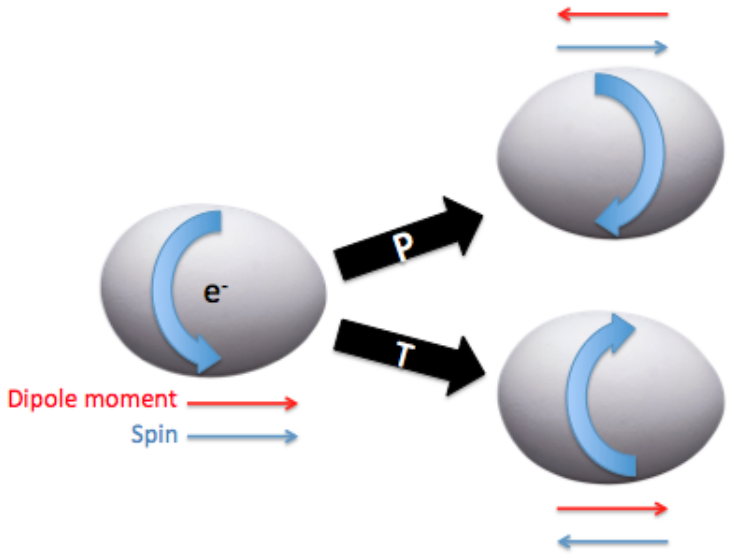

Figure 6.1: An eEDM violates both parity (P) and time (T) reversal symmetry. The solid black arrows show the effect of a P- or T-reversal operation on an electron with both a spin and an electric dipole moment due to a charge distribution asymmetry.

interaction [399, 401, 402, 403]. This second contribution is the dominant term predicted by the Standard Model and is estimated to yield an effective eEDM of around 10^{-38} e cm (although some flexibility exists for increasing it to perhaps 10^{-33} e cm with significant tuning) [402]. The current experimental limit for the sum of these two contributions is $|d_e| < 8.7 \times 10^{-29}$ e cm [31], which means that a non-zero measurement will – at least for a while – be direct evidence of physics beyond the Standard Model. An eEDM arises in new theories because of CP-violating interactions with new particles. As an example, the size of the expected eEDM in SUSY, which arises from a one-loop interaction in the Feynman diagram, is given by [404, 396]

$$d_e \approx e\frac{\alpha}{4\pi}\frac{m_e}{\Lambda^2}\frac{\tan\beta}{4}\sin\phi_{CP} \approx \left(\frac{2.5\text{TeV}}{\Lambda}\right)^2 \tan\beta \sin\phi_{CP} \times 10^{-27} e \text{ cm}, \tag{6.1}$$

where m_e is the mass of the electron (in MeV), Λ is the energy scale for new particles, $\tan\beta$ is the ratio of Higgs boson masses (SUSY assumes a two-Higgs doublet), and $\sin\phi_{CP}$ is a CP-violating phase. This is a fairly generic scaling for many theories that introduce an eEDM with one loop. From here, several assumptions can be made to test different aspects of the theories. First, for simplicity, it is often assumed that the contribution from electron-nucleon interaction is smaller than the eEDM signal, so the current limit represents a limit on d_e. In this case, we can use the current limit with Equation 6.1 to constrain $\Lambda > 8$ TeV, assuming $\tan\beta$ and $\sin\phi_{CP}$ are both $\sim$1. This energy scale is already beyond rough "naturalness" constraints (i.e., not "too-much" fine tuning), which are around 3 TeV, and are close to the upper limit favored by variations of SUSY [396]. Alternatively, we can assume that $\Lambda \sim 1 - 3$ TeV (the range allowed from Large Hadron Collider (LHC) measurements and naturalness), and use the eEDM limit to constrain $\sin\phi_{CP} < 0.01 - 0.1$ for $\tan\beta = 1$. The measured Higgs boson mass[1] is also significantly higher than expected from simple SUSY [406, 396]. This can be partially explained with a larger $\tan\beta$; however, this also makes the eEDM constraints on $\sin\phi_{CP}$ smaller.

Taken together, the LHC results for the Higgs mass, Higgs decay to two-photons, and lack of new particles below 1 TeV combined with the EDM measurements are placing significant constraints

[1] See The Review of Particle Physics [405] at `http://pdg.lbl.gov/`

on many SUSY models. The current eEDM limit is already probing potential two-loop contributions [399, 407] and is competitive with the current neutron EDM limit for probing high energy (e.g., 10-100 TeV) particles in split SUSY [404, 406, 407]. An order of magnitude improvement on the eEDM measurement would start to test string/M-theory predictions, which estimate an eEDM up to about 5×10^{-30} [408]. In addition to these tests, an improvement in the eEDM measurement (as well as the Higgs decay to two-photons) can also constrain models of electroweak baryogenesis [409]. Conversely, the EDM limits can also be used to constrain the ratio of the expected Higgs decay to two-photons relative to the standard model [410]. The eEDM measurement currently limits this ratio to 1 ± 10^{-5}, which will be tested with new measurements at the LHC. All of the eEDM constraints given above have assumed that the electron-nucleon interaction term is negligible. If this term is included in an analysis of all EDM data, the limit is increased to $d_e < 5.4 \times 10^{-27}$ [411]. Of course, the electron-nucleon interaction term also violates CP-reversal symmetry, so it also tests for physics beyond the standard model. Interestingly, in the global analysis, a new eEDM measurement in a different system near the current limit will result in better constraints on both terms separately than would an improved measurement in the same system. The best option then is to make an improved measurement in a new system, which is our goal.

6.1.1 Measurement Basics

Conceptually, measuring an eEDM is simple: an eEDM in an electric field will exhibit an energy difference depending on the orientation of the dipole moment relative to the field. This is analogous to a magnetic dipole moment — for example, a compass needle — placed in a magnetic field. The compass needle aligns with the magnetic field because this is the lowest energy configuration; the configuration with the needle aligned opposite to the field is higher in energy by an amount depending on the strength of the magnetic field and the size of the magnetic dipole. This energy difference increases with the strength of the applied field. To measure an eEDM, one needs to measure the energy difference of the two states of the electron in an electric field using spectroscopy. If the eEDM is assumed to be parallel (or antiparallel) to the electron spin, this is

equivalent to measuring the frequency difference — given by $(2d_eE_{\text{eff}})/h$ where h is the Planck constant and d_e is the magnitude of the eEDM — between states with the electron spin parallel and antiparallel to an applied electric field of magnitude E_{eff}. Since this frequency difference is expected to be small, the two spin states are typically split with a magnetic field first, and then any additional shift due to the electric field can be measured with a Ramsey spectroscopy sequence [412]. Technically most experiments actually use a more general Ramsey-type sequence because the precession frequency is not measured relative to a local oscillator as it would be in Ramsey spectroscopy.

We can measure the splitting between spin up and spin down with the following Ramsey-type procedure:

(1) initially prepare a collection of N_0 electrons all spin up ($|\uparrow\rangle$);

(2) rotate the spins with a $\pi/2$ pulse to $\frac{1}{\sqrt{2}}(|\uparrow\rangle + |\downarrow\rangle)$;

(3) allow the spins to precess for a time τ, after which time $|\uparrow\rangle$ and $|\downarrow\rangle$ have accumulated a phase difference $\phi = (\Delta\omega)\tau$;

(4) rotate the spins again with a $\pi/2$ pulse to $N_\uparrow |\uparrow\rangle + N_\downarrow |\downarrow\rangle)$;

(5) measure $N_\uparrow$ and $N_\downarrow$.

If we include a non-ideal contrast due for example to decoherence, we can write

$$N_{\uparrow(\downarrow)} = \frac{N_0}{2}(1 \mp C\cos\phi), \tag{6.2}$$

where C is the fringe contrast:

$$C = \frac{N_{\max} - N_{\min}}{N_0}, \tag{6.3}$$

with $N_{max(min)}$ being the maximum (minimum) population measured by varying τ. Taking the difference $\frac{N_\uparrow - N_\downarrow}{N_0} = -C\cos\phi$ provides a measurement of the accumulated phase ϕ. The fundamental limit to the precision of such measurement is set by shot noise [413, 395, 400]. The shot-noise-limited

uncertainty can be determined by first taking the derivative with respect to ϕ:

$$\frac{\delta(N_\uparrow - N_\downarrow)}{\delta\phi} = N_0 C \sin\phi. \tag{6.4}$$

Setting $\phi \approx \pi/2$ and using the shot-noise limit $\delta N = \sqrt{N}$, we have

$$\delta\phi = \frac{\delta(N_\uparrow - N_\downarrow)}{N_0 C} \approx \frac{\sqrt{N_0}}{N_0 C}, \tag{6.5}$$

We can relate $\delta\phi$ to an uncertainty in the dipole moment, δd_e since $\phi = (\Delta\omega)\tau$ and $\hbar\Delta\omega = 2d_e\mathcal{E}_{\text{eff}}$:

$$\delta d_e = \frac{\hbar}{2E_{\text{eff}}\tau C\sqrt{N_0 RT}}, \tag{6.6}$$

where T is the total time for repeated measurements at a repetition rate R. In addition to statistical sensitivity, the accuracy of any measurement can also be limited by systematic errors, which are any signals that mimic the splitting due to the eEDM.

A bare electron will rapidly accelerate out of an electric field, making a measurement of the eEDM potentially challenging. While the first attempts to measure the eEDM did do this [414], a more elegant solution was proposed by Sandars [415, 416]. Due to relativistic effects, an unpaired electron in a neutral atom with an applied electric field will experience an effective electric field. Initially, it was expected that this should not be true because $\left\langle \vec{\mathcal{E}} \right\rangle = 0$ for the electron to be stable. This would seem to imply that $\left\langle \vec{d}_e \cdot \vec{\mathcal{E}} \right\rangle = d_e \left\langle \vec{\mathcal{E}} \right\rangle = 0$, so there should be no net effect from the interaction (this is known as Schiff's Theorem). However, relativistic motion leads to length contraction, which means both $\vec{d}_e$ and $\vec{\mathcal{E}}$ are time dependent. So, $\left\langle \vec{d}_e \cdot \vec{\mathcal{E}} \right\rangle \neq \left\langle \vec{d}_e \right\rangle \left\langle \vec{\mathcal{E}} \right\rangle$ and can be non-zero [417]. Even more remarkably, the electric field that the electron experiences in the atom can actually be larger than the applied electric field. Because relativistic effects in general increase for heavier atoms, the magnification also increases with atomic number. Thus, by measuring the energy difference of two spin states in a heavy atom, it is possible to effectively measure the energy difference of an electron oriented in two different directions in an electric field.

This concept has formed the basis of multiple generations of experiments, including one of the most precise measurements to date performed by Regan et al. [418]. The researchers used atomic thallium-205 (Tl) to set a limit on the eEDM of 1.6×10^{-27} e cm. The experiment consisted of four

separate thallium-sodium beams, which each had a different combination of propagation direction (vertically up or down) and applied transverse electric and magnetic fields ($\mathcal{E}$ and B parallel or anti-parallel). Sodium was used as a comagnetometer to measure magnetic-field-related systematic effects. For the measurement, atoms emerged from an oven and were collimated to form a beam. A combination of lasers and a radio-frequency (rf) pulse created a coherent superposition of the $m_F \neq 0$ Zeeman sublevels of the ground $F = 1$ state. After this, the atoms traveled through a 99-cm-long region with a 123 kV/cm transverse electric field and a 0.38 G transverse magnetic field. After the field region, a second rf pulse transferred some population, depending on the exact value of the magnetic and electric fields, back to the $m_F = 0$ level, which was then measured with laser fluorescence. One of the dominant sources of systematic error was due to the motion of the atoms through the electric field combined with stray magnetic fields (termed motional magnetic field effects). While significantly reduced by the use of four atomic beams with different propagation directions, these effects still limited the accuracy of the measurement.

6.1.2 Current Limit

The relativistic enhancement factor for Tl is about 600, meaning that the effective electric field at the electron is 600 times larger than the applied laboratory electric field (the effective electric field in the Regan et al. experiment was about 80 MV/cm). Large enhancement factors are possible using polar molecules with one heavy atom [419, 29]. This is due to the low electric fields necessary to polarize the molecule (a result of the closely spaced levels of opposite parity present in many molecules). This concept eventually resulted in an improved limit on the size of the eEDM over the Tl measurement using ytterbium fluoride (YbF) molecules [30] to reach 1.0×10^{-27} e cm.

The experiment in YbF was conceptually very similar to the Tl experiment; however, only one beam was used instead of the four beams in the Tl experiment and instead the direction of the applied fields were switched. This simplification is partially due to the significantly reduced sensitivity of YbF to motional magnetic field effects. In addition, the required electric field was about 10 kV/cm instead of 100 kV/cm, while the resulting effective electric field was 14.5 GV/cm,

about 200 times larger than that in Tl. The YbF experiment was primarily statistical noise limited but did also have two systematics above 10^{-28} e cm [420]. The first of these is attributed to uncorrected effects from imperfect $\mathcal{E}$ reversal. The second is due to a phase shift that depends on the detuning of the rf pules. An imperfect $\mathcal{E}$ reversal or small bias voltages will result in different Stark shifts and thus rf detunings for different directions of $\mathcal{E}$, which will result in a correlated phase shift. The next generation YbF experiment aims to reduce these systematics by better control over $\mathcal{E}$ reversal.

A recent experiment using ThO has constrained the eEDM to be less than 8.7×10^{-29} e cm [31]. This experiment was again done in a molecular beam, but the choice of molecule provided several crucial advantages over YbF. In particular, the use of a $^3\Delta_1$ electronic state requires a very small polarizing field ($\sim$1 V/cm) due to the closely-spaced Λ-doublet levels (as discussed in Sections 5.1.1 and 5.3) and a has a small magnetic g-factor since $g_F \sim (g_L\Lambda - g_S\Sigma) \sim \alpha/\pi$ [389, 421], where g_F, g_L, and g_S are the magnetic g-factors for each angular momentum component. The Λ-doubling in the $^3\Delta_1$ state can also be used as an internal comagnetometer, which reduces sensitivity to stray magnetic fields and provides the ability to switch $\mathcal{E}$ without reversing any applied fields, an idea initially developed for PbO [422].

The $^3\Delta_1$ internal comagnetometer is illustrated for HfF^+ in the inset of Figure 6.2. In particular, we measure the splitting in both the upper and lower pairs of $m_F = \pm 3/2$ levels (in the $J = 1, F = 3/2$ manifold). These m_F states are split in an applied magnetic and electric field by $3g\mu_B B \pm 2d_e\mathcal{E}_{\text{eff}}$ for the upper and lower pairs, respectively. Here g is the magnetic g-factor for the upper and lower pairs, μ_B is the Bohr magneton, B is the applied magnetic field, d_e is the eEDM (to be measured), and $\mathcal{E}_{\text{eff}}$ is the effective electric field (from theory). By taking the difference of the splitting in the upper and lower states, we can remove all magnetic field dependence — to the extent that the upper and lower pairs of states have the same g-factor.

Another difference in the ThO experiment compared to the YbF experiment is that state preparation and readout were all optical transitions. In particular, preparation of the spin-state superposition was accomplished by preparing a dark state using a depletion laser instead of by

transferring population to a superposition of spin states using an rf pulse. The ThO measurement was also statistical-noise limited, although the systematic error contribution was estimated to be 3×10^{-29} e cm (the systematic error contributions were limited by the precision with which systematic shifts were measured). In addition to possible systematic errors from magnetic field gradients [423] and stray magnetic fields, the largest systematic errors were related to differential Stark shifts of the dark state by the preparation laser that were caused by non-reversing electric fields or by different Rabi rates for the two doublets (due, for example, to interference between E1 and M1 transition amplitudes).

6.1.3 Overview of JILA eEDM measurement

One option for improving the sensitivity of measurements is to increase the free-evolution time or coherence time of the measurement. In addition to an improvement in the shot-noise-limited sensitivity, a longer coherence time also helps to reduce the sensitivity to systematic errors because the Fourier-limited linewidth is smaller. This increase in coherence time can be accomplished by using molecular ions, which can be easily trapped for many seconds. Specifically, we focus on HfF^+ in the initial experiments. A future version of the experiment could use ThF^+ for higher sensitivity, but preliminary spectroscopy work for that molecule is still in progress.

This choice of molecular ion is motivated by several factors. First, the presence of a heavy atom provides a large effective electric field, around 23.3-24 GV/cm in HfF^+ [424, 421, 425] and 38 GV/cm in ThF^+ [426]. Note that this is significantly lower than initially estimated in [421] and is lower than the calculated value for ThO. This is because the ThO bond is more ionic than the ThF^+, which means the s electron experiences a larger field and thus is mixed more with p. Second, these molecules have long-lived, metastable $^3\Delta_1$ electronic states. The small Λ-doubling of this state (740 kHz in HfF^+) results in full polarization with only a 1-V/cm-laboratory electric field, which reduces sensitivity to systematic errors caused by large laboratory electric fields. As can be seen in Figure 6.3, numerical results for $^3\Delta_1$ $J = 1$ hyperfine levels confirm that at 1 V/cm the splitting in the $|m_F| = 3/2$ levels due to eEDM related Stark shift is almost saturated at $2d_e\mathcal{E}_{\text{eff}}$.

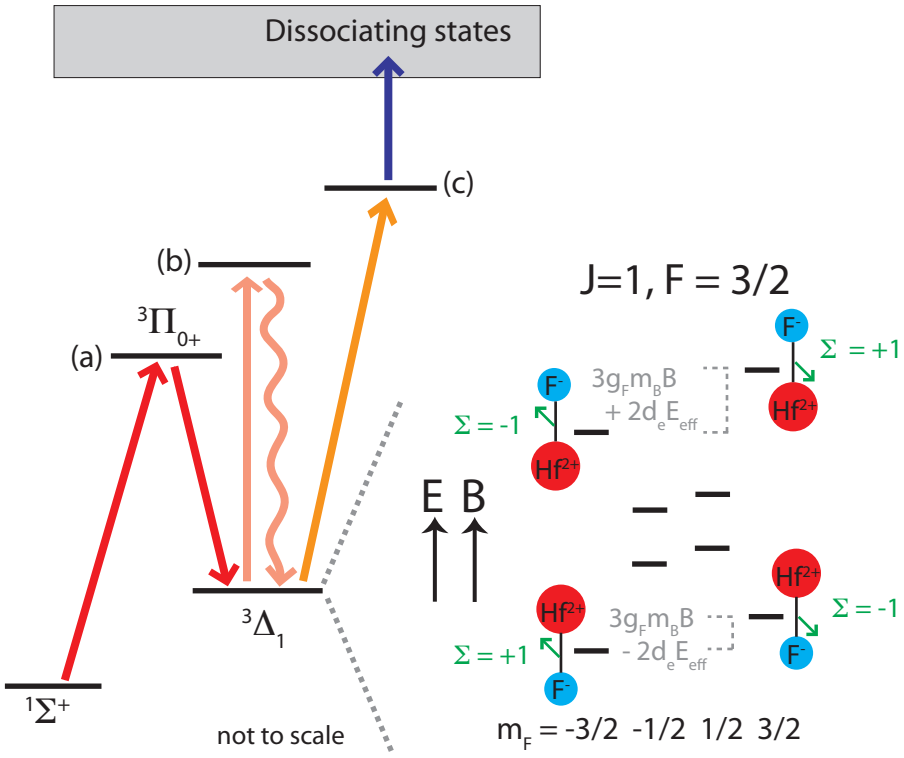

Figure 6.2: Electronic states used in an eEDM measurement in HfF^+. An eEDM is measured by measuring the splitting of the $J = 1, F = 3/2, m_F = \pm 3/2$ sublevels of the low-lying $^3\Delta_1$ excited state, as shown in the inset. The states (a), (b), and (c) are excited states used for: (a) population transfer, (b) state readout via laser-induced fluorescence, and (c) state readout with photodissociation.

This saturation occurs as the molecule becomes fully polarized. These results were obtained as described in [427].

The basic measurement procedure is as follows. First, we state-selectively produce ground state HfF^+ ions using multi-photon photoionization. This process has been shown to produce 30% of the ions in a single quantum state in the ground $^1\Sigma^+$ electronic state [428]. The HfF^+ ions are then trapped using a six-electrode linear Paul trap, see Section 6.2.1. To provide a bias electric field, we apply a sinusoidal potential to each radial trap electrode 60 degrees out-of-phase with the neighboring electrodes. A magnetic field must also be applied parallel or antiparallel to the rotating electric field (Section 6.2.3). After the electric and magnetic fields are applied, population is transferred (Section 6.3) to either the upper or lower pairs of states using a two-photon transition through an intermediate $^3\Pi_{0^+}$ state (Figure 6.2). This transfer scheme results in an incoherent population distribution between the $m_F = \pm 3/2$ levels, so we prepare a pure spin state by depleting one m_F level. The next step in the Ramsey spectroscopy sequence (Section 6.4) is to prepare a coherent superposition of the $m_F = \pm 3/2$ levels via a $\pi/2$ pulse. After this $\pi/2$ pulse, the superposition evolves for a free-evolution period during which the two m_F levels acquire a differential phase shift proportional to their energy difference and the evolution time. A second $\pi/2$ pulse finishes the Ramsey sequence by projecting back to pure spin states. This maps the phase difference to a population difference between the two spin states. We then measure the population in a spin state with depletion followed by resonantly-enhanced multi-photon dissociation (REMPD, Section 6.2.2).

6.2 Experimental Setup

Figure 6.4 shows the basic setup used for the JILA molecular-ion eEDM experiment. Many parts of the experiment have been described in detail elsewhere [64], so we only provide a summary and some added technical details here. We start by producing neutral HfF using laser ablation (532 nm, 10 ns, ∼10 mJ pulses) of a Hf target at the outlet of a pulsed supersonic expansion of 1% SF_6 in Ar (backing pressure of ∼80 psi). Initially, we used a solenoid valve (Parker General Valve), but we

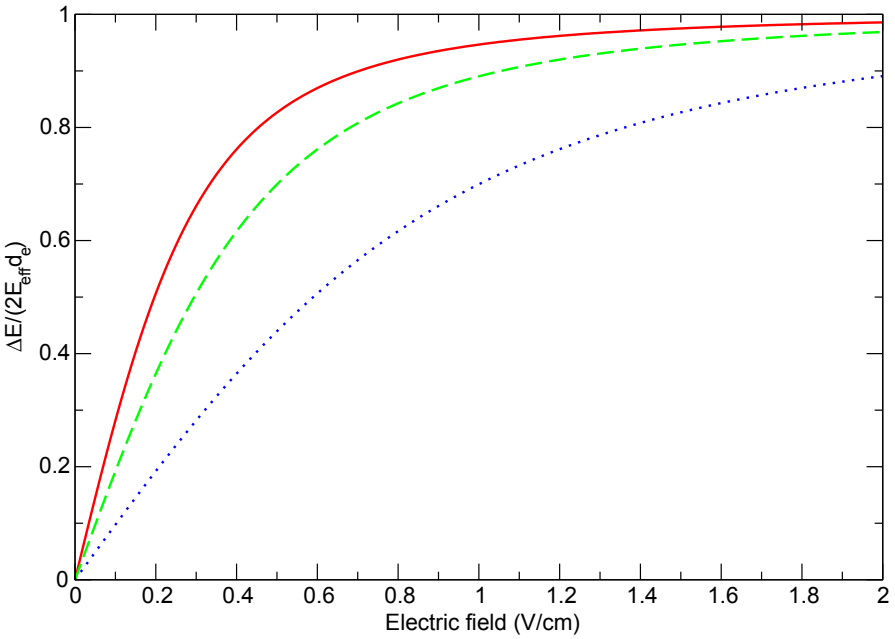

Figure 6.3: The eEDM induced Stark splitting (ΔE) for $J = 1$ hyperfine levels of the $^3\Delta_1$ state of HfF^+: between $F = 3/2$ $m_F = \pm 3/2$ levels (solid line), between $F = 3/2$ $m_F = \pm 1/2$ levels (doted line), and between $F = 1/2$ $m_F = \pm 1/2$ (dashed line).

found overall improved performance with a disk-piezo based valve (Physik Instrumente P-286.23). This valve allowed us to reduce the pulse duration to typically ∼35 μs and simultaneously increased our final ion yield. When installing this valve, the poppet tension was adjusted first so that the valve barely sealed to atmosphere when the chamber was pumped with only a roughing pump and was then tightened about one-half to one turn further. In order to prevent damage to the piezo, the tension should be kept as low as possible. The piezo is biased at 275 Volts to open the valve. The gas exits through a 1-mm diameter nozzle. The ablation target is located just downstream of nozzle and is positioned to be just on the edge of the expanding beam. The timing of the ablation laser is experimentally adjusted to optimize the final trapped HfF^+ yield and is typically ∼110 μs after the start of the gas pulse.

6.2.1 Ion Trap

The supersonic expansion is collimated using a pair of skimmers: the first skimmer (3 mm diameter) is located about 11 mm from the source and the second skimmer (2 mm diameter) is located 9.6 cm farther downstream. This gives an expected transverse translational temperature based on the collimation (i.e., the maximum velocity a molecule can have to barely pass through both skimmers) of 3 K. The first skimmer is also biased at 200 V to remove any ions produced in the ablation. After this, the neutral HfF is ionized using resonant two-photon vibrational auto-ionization through a highly-excited Rydberg level [429]. This process produces HfF^+ only in the $^1\Sigma^+$ $v = 0$ state, with about 35% of the population in the $J = 0$ level. The ions are produced at the center of ion trap and are immediately stopped with a pulsed electric field. The trapping fields are turned on immediately after this.

The trap is a linear Paul trap with a standard rf (50 kHz) radial quadrupole confinement and static dc axial confinement [430, 431, 64]. As shown in Figure 6.4, the trap consists of six radial electrodes. In order to produce the quadrupole radial confinement, we drive some of the electrodes synchronously (e.g., the blue and purple electrodes in Figure 6.4), The motion of a single trapped

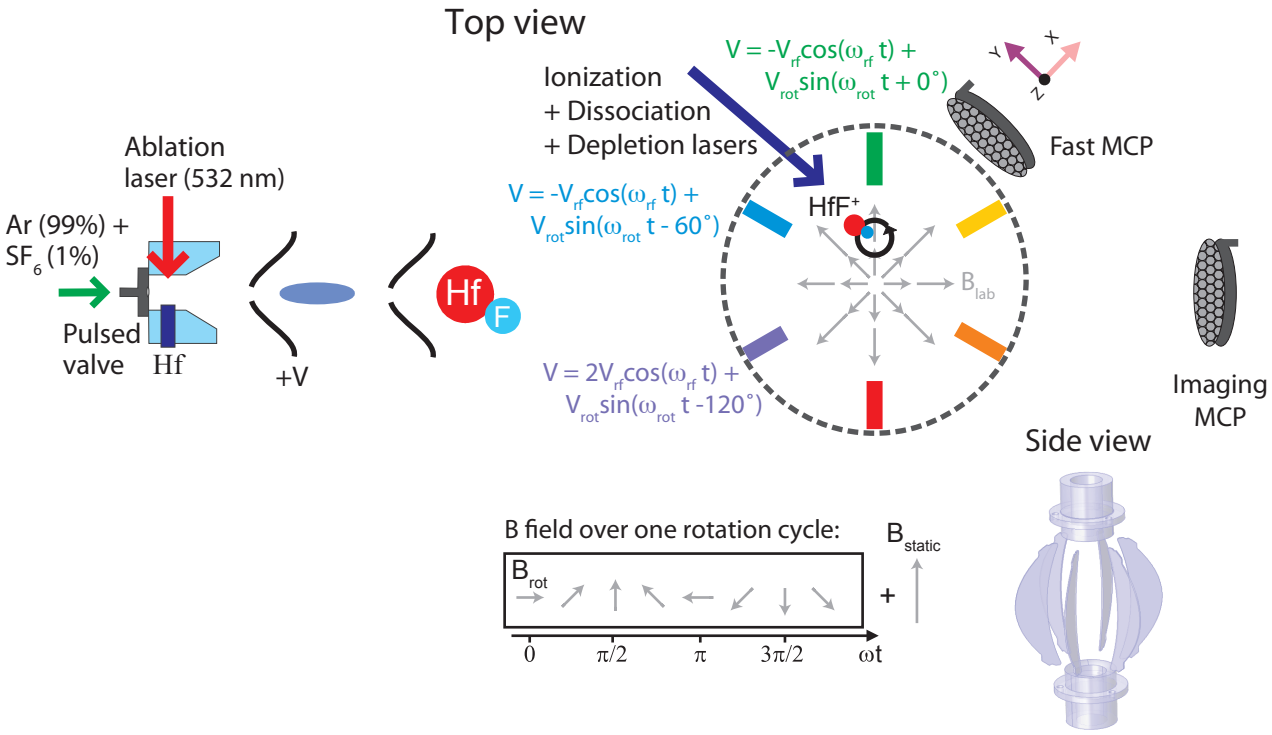

Figure 6.4: Sketch of eEDM experiment. A pulsed beam of neutral HfF is created with a supersonic expansion and ablation of Hf. After a pair of skimmers, we create HfF^+ using photoionization in the center of a six-electrode linear Paul trap (top shown). The radial electrodes provide both a quadrupole rf confinement ($\omega_{rf} = 2\pi \times 50$ kHz) and uniform rotating electric field ($\omega_{rf} \approx 2\pi \times 253$ kHz). A static quadrupole magnetic field gradient leads to a rotating magnetic field due to the circular micromotion from the rotating electric field. Ions can be detected either with a fast micro-channel plate (MCP) aligned along the trap x axis or with an imaging MCP.

ion along the ith direction ($i = x, y, z$) is given approximately by [431]

$$x_j(t) \approx [a_{0j} + a_{1j}\cos(\omega_i t + \phi_i)]\left[1 + \frac{q_i}{2}\cos(\omega_{rf} t)\right], \tag{6.7}$$

where a_{0j} arises from a static dc electric field,

$$a_{0j} = \frac{4e\vec{\mathcal{E}}_{dc}\cdot\hat{x}_j}{m(a_i + \frac{1}{2}q_i^2)\omega_{rf}^2} \tag{6.8}$$

and a_{1j} is the secular motion amplitude with frequency $\omega_i = \frac{1}{2}\omega_{rf}\sqrt{a_j + \frac{1}{2}q_j^2}$. The parameters a_i and q_i are sometimes called the Mathieu parameters and are related to the confinement by

$$\begin{aligned} a_x = a_y = -\frac{1}{2}a_z = -\frac{4e\kappa V_{dc}}{mZ_0^2\omega_{rf}^2} \approx 0.004, \\ q_x = -q_y = \frac{1}{2}a_z = -\frac{2eV_{rf}}{mR^2\omega_{rf}^2} \approx 0.23, \text{ and} \\ q_z = 0 \end{aligned} \tag{6.9}$$

where κ is a geometrical factor and the other parameters are given in Figure 6.4. The kinetic energy averaged over a secular period, assuming $\omega_{rf} >> \omega_i$ and $q >> a$, is

$$E_j = \frac{1}{2}m\left\langle \dot{x}_j^2 \right\rangle = \frac{1}{4}ma_{1j}^2\omega_i^2 + \frac{4}{m}\left(\frac{eq_j\vec{\mathcal{E}}_{dc}\cdot\hat{x}_j}{\omega_{rf}(2a_j + q_j^2)}\right)^2. \tag{6.10}$$

Assuming a thermal distribution, $E_z \approx \frac{1}{2}k_B T_z$ and $E_{x,y} \approx k_B T_{x,y}$ because of the micromotion energy, which is equal to the secular motion energy [431].

We detect ions by turning off the trap and kicking the ions to one of two micro-channel plates (MCP). One MCP is connected to a fast trans-impedance amplifier to provide high temporal resolution; the other MCP provides a two-dimensional image of the ions. The arrangement of these two MCPs is shown in Figure 6.4. The fast MCP is aligned along the x-axis of the trap, while the imaging MCP is 60° off of the x-axis. When used in combination, these two MCPs can provide three-dimensional information about the trap, but first we need to obtain a relationship between the position x_j^d of an ion on the detector along the j^{th} coordinate axis and the position x_j^t and velocity $\dot{x}_j^t$ of the ion in the trap. In particular, we assume that

$$x_j^d = m_{11,j}x_j^t + m_{12,j}\tau_d\dot{x}_j^t \tag{6.11}$$

where τ_d is the time of flight to the detector and $m_{11,j}$ and $m_{12,j}$ are two coefficients that must be measured. Ideally, both of these coefficients would be 1, but by measuring them, we can account for first-order non-uniformity of the kick or stray fields due to patch charges.

In order to measure the two coefficients, we kick the cloud along one axis by pulsing the voltage on the electrodes for a duration of 2 μs (with an approximately triangular waveform). To determine the impulse applied, we measured the kick waveform applied to the electrodes and then integrate the applied voltage: for example, the integrated kick applied to one fin for a programmed 1 V, 2 μs pulse (amplified 25$\times$ in the trap driver electronics) gives 50.5 V μs. The electric field at the center of the cloud is obtained by COMSOL simulation for a 1 V potential applied to one fin:

$$\begin{aligned}
\mathcal{E}_x &= 2\sqrt{3} \times \frac{57.21(1)\,\mathrm{mV/cm}}{1\,\mathrm{V}} \times V_x \equiv k_x V_x; \\
\mathcal{E}_y &= 2 \times \frac{57.21(1)\,\mathrm{mV/cm}}{1\,\mathrm{V}} \times V_y \equiv k_y V_y; \\
\mathcal{E}_z &= 2 \times \frac{8.75(1)\,\mathrm{mV/cm}}{1\,\mathrm{V}} \times V_z \equiv k_z V_z.
\end{aligned} \tag{6.12}$$

The factors of $2\sqrt{3}$ in x and 2 in y and z arise from the electrode geometry. Assuming that the cloud is stationary before receiving a kick along direction j and that the kick is short enough so that it does not affect the position of the ions, the in-trap position and velocity after the kick are

$$\begin{aligned}
x_j^t(t) &= \frac{B_j}{\omega_j} \sin(\omega_j t) \\
\dot{x}_j^t(t) &= B_j \cos(\omega_j t)
\end{aligned} \tag{6.13}$$

where

$$B_j \equiv \frac{e}{m} \int_{-\infty}^{\infty} \mathcal{E}_j(t) dt = \frac{e}{m} k_j \int_{-\infty}^{\infty} V_j(t) dt. \tag{6.14}$$

By scanning the time between the kick and readout, we measure an slosh of the ion cloud on the detector with amplitude A_j^d and phase φ_j:

$$x_j^d(t) = A_j^d \sin(\omega_j t + \varphi_j) = A_j^d \cos(\varphi_j) \sin(\omega_j t) + A_j^d \sin(\varphi_j) \cos(\omega_j t). \tag{6.15}$$

Comparing Equations 6.13 and 6.15, we find that

$$m_{11,j} = \frac{A_j^d \omega_j \cos(\varphi_j)}{B_j} \tag{6.16}$$

$$m_{12,j} = \frac{A_j^d \sin(\varphi_j)}{B_j \tau_d}. \tag{6.17}$$

These measurements can be used to determine the temperature of the ions in the trap. First, we need to find the width of the cloud in the trap from the measured width on the detector:

$$\sigma_{t,j} = \frac{\sigma_j^d}{\sqrt{m_{11,j}^2 + (m_{12,j}\omega_j\tau_d)^2}}. \tag{6.18}$$

Because the imaging detector is not aligned with a primary trap axes, there is some projection of motion along x onto the imaging detector. Taking into account the 30° angle between the imaging detector y' axis and the trap x axis, the observed width $\sigma_{\mathrm{img},y'}$ is a combination of the motion projected along the trap x axis, $\tilde{\sigma}_{\mathrm{img},x}$, and motion along the trap y axis, $\tilde{\sigma}_{\mathrm{img},y}$

$$\sigma_{\mathrm{img},y'} = \frac{1}{2}\sqrt{3\tilde{\sigma}_{\mathrm{img},x}^2 + \tilde{\sigma}_{\mathrm{img},y}^2}. \tag{6.19}$$

The width due to x motion is

$$\tilde{\sigma}_{\mathrm{img},x} = \sigma_{t,x}\sqrt{g_{11,x}^2 + (g_{12,x}\omega_x\tau_{\mathrm{img}})^2}, \tag{6.20}$$

where g_{11} and g_{12} are the coefficients for mapping x motion on the imaging detector. Finally the width observed on the detector due only to y motion is

$$\tilde{\sigma}_{\mathrm{img},y} = \sqrt{4\sigma_{\mathrm{img},y}^2 - 3\left[g_{11,x}^2 + (g_{12,x}\omega_x\tau_{\mathrm{img}})^2\right]\sigma_{t,x}^2}. \tag{6.21}$$

We have measured the transfer functions with several different kicks to obtain the transfer functions given in Table 6.1 for two different configurations, called *relaxed* and *normal*. For these two configurations, the trap is turned on in the given configuration, and then the transfer function coefficients are also measured in that configuration.

Assuming harmonic confinement and neglecting Coulomb repulsion between the ions (i.e., space-charge effects) which distorts the trap profile [432, 433, 434], the trap width along the j-th

Table 6.1: Secular trap frequencies, transfer function coefficients, trap width, and trap temperatures for two different trap configurations. In addition, the secular frequencies, widths, and temperatures are given for an adiabatic ramp starting from the relaxed trap.

Config	Axis	$\omega_j/2\pi$ (kHz)	m_{11} or g_{11}	m_{12} or g_{12}	$\sigma_{t,j}$ (mm)	Temp (K)
Relaxed	x	3.5	0.093(8) μs/mm	0.08(1) μs/mm	1.1	14
	x_{img}	n/a	0.56(9)	0.65(5)	n/a	n/a
	y	4.8	2.7(4)	1.04(16)	1.7	64
	z	1.6	0.75(3)	0.72(6)	3.1	23
Normal	x	4.4	0.079(4) μs/mm	0.08(1) μs/mm	1.2	27
	x_{img}	n/a	0.3(1)	0.60(4)	n/a	n/a
	y	5.6	3.0(1)	0.69(8)	1.8	93
	z	3.7	1.09(7)	0.42(6)	1.9	48
Relaxed +	x	2.8	–	–	1.2	11
ramp	y	4.3	–	–	1.5	44
	z	0.7	–	–	4.2	9

axis is related to the temperature in that direction by

$$\sigma_{t,j}^2 = \frac{k_\mathrm{B} T_j}{m\omega_j^2}, \tag{6.22}$$

Rearranging give the temperature

$$T_j = \frac{m\omega_j^2 \sigma_{t,j}^2}{k_\mathrm{B}}. \tag{6.23}$$

We can use the measured width on the detector and the transfer function coefficients to determine $\sigma_{t,j}$ and use this to determine T_j (Table 6.1). Because of the complication of both x and y appearing on the imaging detector, the y measurements are the least reliable, which is possibly why the temperature seems high. From this, we see that the temperature is lower with a looser initial trap. The x and z temperature are reasonably close to – although higher than – the expected Doppler temperature from the molecular beam collimation. We have also confirmed that the temperature scales approximately with secular frequency during an adiabatic ramp, as expected [435]: it actually seemed that the temperature decreased slightly faster than secular frequency, which could be an indication of space-charge effects. By initializing the trap in the relaxed configuration and then adiabatically ramping to trap frequencies of $(2.8, 4.3, 0.7)$ kHz in (x, y, z), we were able to further decrease the temperature to $(11, 40, 9)$ K. Currently, the trap becomes unstable when we ramp to lower secular frequencies; this is perhaps due to ground loops that introduce noise on the trap electrodes. We have reduced these significantly with optical isolation of digital signals and careful separation of analog power supplies when possible, but there are still residual effects. It is also possible that we need to lower the trap rf frequency in order to further decrease the secular frequencies. We have also tried to reduce the temperature by reducing the size of the ionization laser beams with no effect (if anything, the temperature is lower with larger ionization laser beams).

Of course, to count the highest number of ions possible for the eEDM measurement, we want the absolute detection efficiency of the MCP to be as high as possible. It is often said that ion detection occurs with unit efficiency, but this is not completely correct as the absolute detection efficiency depends on several different factors. As its name implies, an MCP is an array of small glass channels that are fused together to form a plate. The input face of this plate is negatively

biased (typically up to -1.1 kV across one plate) so that positive ions are accelerated toward the surface. When the ion hits inside a channel, several electrons are ejected. These electrons are accelerated towards the output and collide with the wall, which causes a cascade of electrons at the output. These electrodes are detected, either as a current with a fast transimpedance amplifier (for the fast MCP) or a phosphor screen and camera (for the imaging MCP). Typically, multiple plates are stacked together (two for the fast MCP, three for the imaging MCP), which increases the total bias applied and also increases the electron gain. A grounded mesh is located in front of the MCP front surface to shield the trap from the high voltage.

The first limit to the MCP detection efficiency is the transmission of this mesh. Previously, we used a coarse mesh with about 60% transmission, but have now switched to a fine mesh with $\sim$90% transmission. Despite having a large transmission, the pitch of the mesh is small, so we noticed no issues due to worse shielding of the bias voltage. Once an ion is through the mesh, the efficiency of producing secondary electrons depends on the energy (and thus bias, since this accelerates the ions) and mass-to-charge ratio of the impacting ion. As the impact energy is increased, the efficiency has been observed to increase and eventually saturate at $< 100\%$ [436]. This plateau value is close to the open-area-ratio (i.e., the ratio of the total area of the tubes to the area of the plate) of the MCP, typically around 63% for the MCPs that we use. This limit arises because ions that do not enter a tube and just strike the surface emit secondary electrons that are not collected. The efficiency can be increased beyond this by applying an additional return bias fields using another mesh to drive electrons back towards the surface [437]; however, the efficiency improvement seems to only be marginal under most conditions (e.g., 80% instead of 60%) [438]. Coating the MCP with a material to increase the secondary electron yield could push the efficiency up even higher [438]. We measured the counted ion number (for very low total ion number, any peak over a threshold voltage is counted as a single ion) as a function of bias voltage and found that it saturated at about 2.05-2.1 kV, which suggests that we are reaching the limit of the mesh plus open-area-ratio of the MCP. For measuring larger ion numbers, we cannot count peaks because several ions could contribute to a single peak. The large noise in peak heights even for a single ion makes it impossible

to define thresholds for more than one ion, so instead, we integrate to find the total area under the peak. We have determined a calibration based on the average integrated area of single ion peaks and have compared integrated and counted signal at low ion number as a function of bias voltage to be sure that the two methods agree.

Interestingly, we have noticed that using the integrated signal to measure the ion number consistently results in slightly higher noise than using counted ion number. On way of seeing this is to look at the statistics for the number of Hf^+ measured with counting versus integrating and compare this to a Poisson distribution. Histograms of the number of Hf^+ measured using counting and integrating are shown in Figure 6.5. The solid lines are the expected Poisson distribution given the measured mean Hf^+ number. From this, we see that the integrated ion number differs significantly more from a Poisson distribution than the counted ion number. We have also confirmed this by comparing the standard error on Hf^+ measurements to the calculated shot noise. Typically, the noise when using counts is around 20% above shot noise, while the noise using integrated Hf^+ number is around 50% above shot noise.

6.2.2 Photodissociation

Ideally, we would like to be able to measure the population in any desired Zeeman sublevel within the $^1\Sigma^+$ or $^3\Delta_1$ state, but as was pointed out years ago "you can't always get what you want" [439]. In order to get what we need, we can use a combination of techniques. Historically, a common molecular state read-out method is laser-induced fluorescence (LIF) [440], where molecules in the target state are excited by a bound-to-bound transition and the subsequent spontaneously-emitted photons are measured. However, the lack of closed transitions in HfF^+ and the low detection efficiency of photomultiplier tubes at the known LIF transition wavelengths combined to make LIF count rates very low. The low efficiency of photon detection can be circumvented by directly detecting ions instead. In neutral molecules, a common detection technique is resonance-enhanced multiphoton ionization (REMPI) [441, 442], which has been used for efficient measurement of molecular quantum state populations. In molecular ions, the difficulty of efficiently and controllably

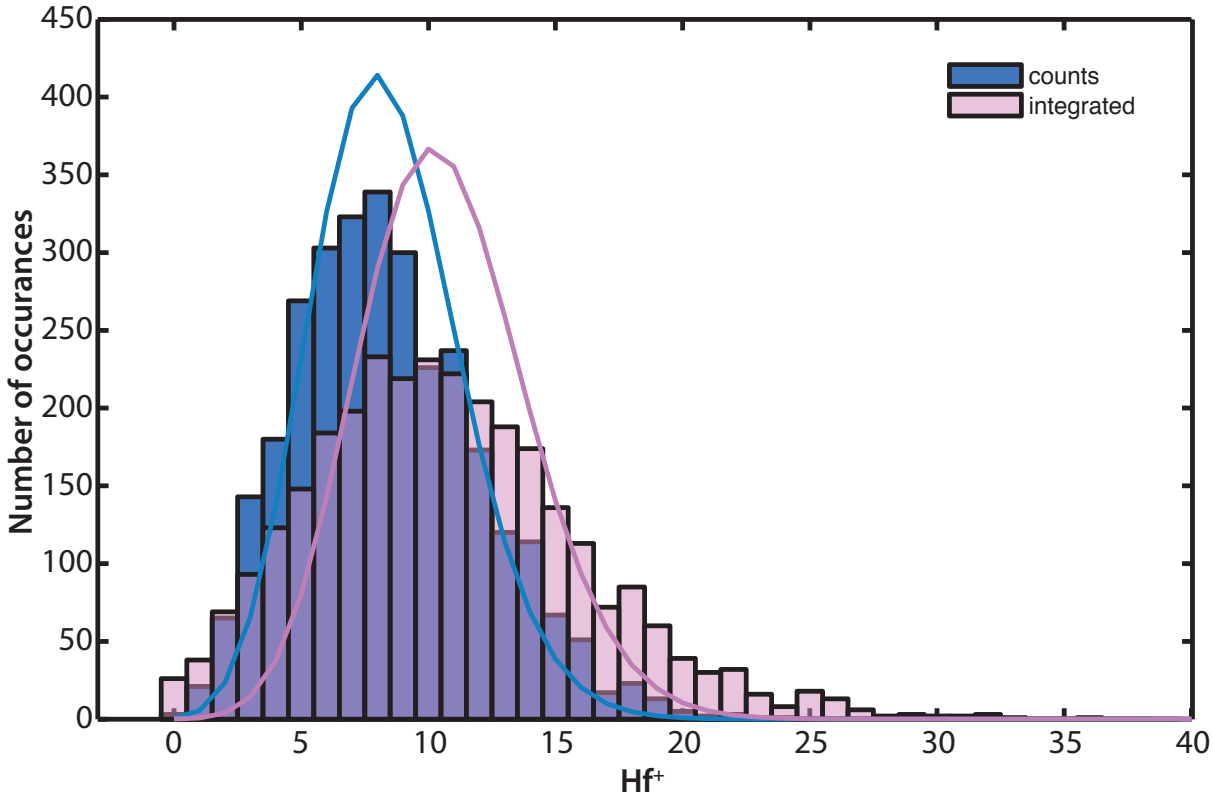

Figure 6.5: Histogram of Hf^+ number measured using counting or integrating. The solid lines are the expected Poisson distribution with the same mean value.

removing the second electron (because of the typically very high second ionization energy) makes REMPI a challenging technique to apply.

An alternative to REMPI is to instead state-selectively dissociate the molecular ion and detect the dissociation products, leading to the development of resonance-enhanced multiphoton photodissociation (REMPD) [443, 444]. Soon after the first demonstrations REMPD was combined with ion trapping to perform spectroscopy on trapped molecular ions [445]. Most applications relied on mass-selectivity to obtain zero-background spectra of excited molecular states, but have not used REMPD to sensitively measure lower state populations. Recent developments have focused on high-senstivity detection of small collections of trapped ions. In Roth et al. [446] and Højbjerre et al. [67], rotational-state-resolved photodissociation was demonstrated with molecular ions in a Coulomb crystal. There, high signal-to-noise images of co-trapped atomic ions showed the photodissociated molecular ions as a loss of dark ions. While providing high quantum efficiency, this technique only works with Coulomb crystals. Rellergert et al. [447] instead used one-photon photodissociation followed by mass-resolved time-of-flight ion detection. This method was sensitive to the distribution of molecular vibrational states but did not provide rotational state selectivity. We demonstrate a combination of these techniques that provides high quantum efficiency, rotational state selectivity for multiple vibronic states, and rapid detection without the need for Coulomb crystals. A similar scheme has recently been demonstrated for rotational-state specific detection of AlH^+ as well [448].

We use $(1{+}1')$ REMPD to break apart HfF^+ into Hf^+ and F and then count the Hf^+ products and remaining HfF^+ ions. The first photon in the $(1{+}1')$ scheme drives a bound-bound transition in HfF^+, making the photodissociation process rotational-state sensitive. Subsequently, the second photon excites HfF^+ from its intermediate state to a repulsive molecular potential, as shown in Fig. 6.6(a). The two ion species are mass-resolved in time-of-flight to the detector. When no photodissociation pulse is applied, we see one large ion peak on the MCP centered 30 μs after the readout kick, which corresponds to the time-of-flight of HfF^+ (Fig. 6.6(b)). If the photodissociation pulses are applied on resonance, a second, smaller number of Hf^+ ions appears at an earlier time. Prior to applying the dissociation lasers, the axial and radial confinement are ramped up to form a

tighter trap ($\sim$ 12 kHz in all three dimensions). This helps to increase the dissociation efficiency, reduce the background counts, and also improve the mass resolution of the time-of-flight detection. We also wait for a "focusing" time after dissociation before kicking the ions toward the MCP [65].

To calibrate the photodissociation detection efficiency, we probe the $X^1\Sigma^+$, $v'' = 0$, $J'' = 0$ ions using the R(0) line of the 35,976 cm^{-1} band shown in Figure 6.7. Note the absence of a Q-branch, which indicates that the intermediate state is also $\Omega = 0$. We observe that the photodissociation yield saturates with a laser fluence of 160(30) μJ/cm^2 for the first photon and approximately 50 mJ/cm^2 for the second photon. The saturation fluence on resonance, F_{sat} is related to the peak transition cross section, σ_0: $F_{sat} = \frac{hc}{\lambda\sigma_0}$, where

$$\sigma_0 = \frac{4\pi^3 g_0 \mu_{21}^2}{3\epsilon_0 h\lambda}\frac{g_2}{g_1}. \tag{6.24}$$

Here $\frac{g_2}{g_1}$ is the ratio of the upper and lower state degeneracy, which we assume to be 1; μ_{21} is the usual transition dipole moment; g_0 is the peak of the normalized line shape function $g(\omega)$. For the 266 nm transition to the dissociating curve, we assume that $g(\omega)$ can be obtained by mapping the harmonic oscillator wave function for the intermediate state onto the dissociating potential, as shown by the dashed gray lines in Figure 6.7(a). The $v = 0$ wave function is a Gaussian with width $\Delta r = \sqrt{\frac{\hbar}{2\pi c\omega_e \mu}}$, where ω_e is the vibrational constant (in cm^{-1}). With $\omega_e \approx 650$ cm^{-1} (estimated from the higher states in Table 5.5), $\Delta r \approx 0.055$ Å. The slope of the dissociating resonance has been estimated to be $k = 80000$ cm^{-1}/Å [63], which gives a width of the photodissociation resonance of $\Delta\tilde{\nu} = k\Delta r = 4400$ cm^{-1}. The peak of an (area) normalized Gaussian with spectral width $\Delta\tilde{\nu}$, $g_0 = \frac{1}{\sqrt{2\pi}2\pi c\Delta\tilde{\nu}}$. If we assume an electronic dipole moment of $\mu_{21} \approx 0.5\ e\mathrm{a}_0$, $\sigma_0 \approx 7.8 \times 10^{-19}$ cm^2. This gives an estimated saturation fluence of ~ 300 mJ/cm^2, which is in reasonable agreement with the experimental result given the large number of assumptions.

From the ratio of total HfF^+ counts on the MCP to the Hf^+ counts that are detected as products of state-sensitive photodissociation, we derive an efficiency of 32(2)%. This includes a dissociation efficiency of 41(2)%, which we measure from the fractional loss of HfF^+ signal when the (1+1′) pulse is applied, and a 78(2)% transport efficiency of the dissociated ions to the detector.

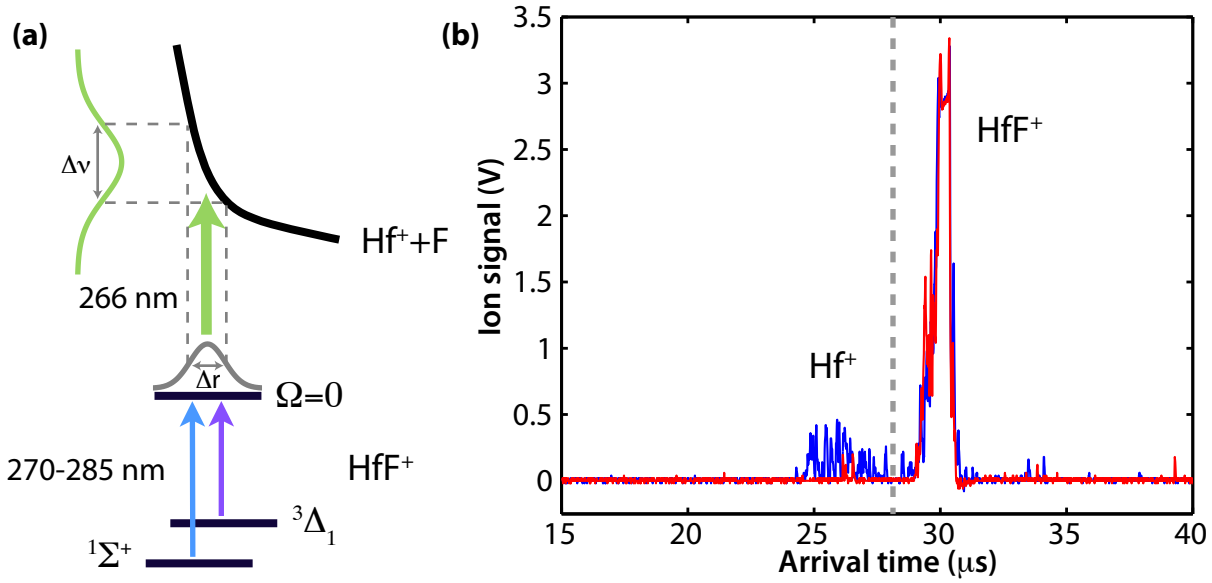

Figure 6.6: (1+1′) resonance-enhanced multiphoton photodissociation (REMPD). (a) Photodissociation pulses consist of two photons of different color. The first photon excites molecules from their initial state (one of $X^1\Sigma^+$ $v'' \in \{0, 1\}$ or $^3\Delta_1$ $v'' = 0$ to an intermediate state, and the second 266 nm photon dissociates the molecules into Hf^+ and F. The spectral width ($\Delta\nu$) of the resonance to the repulsive potential, indicated by the vertical, green Gaussian is related to the radial size (Δr) of the vibrational wavefunction of the intermediate state (gray Gaussian). (b) Mass-resolved time-of-flight ion detection signal, recorded without photodissociation (red) and with photodissociation (blue). The gray dashed line indicates the distinction between Hf^+ (to the left) and HfF^+ (to the right).

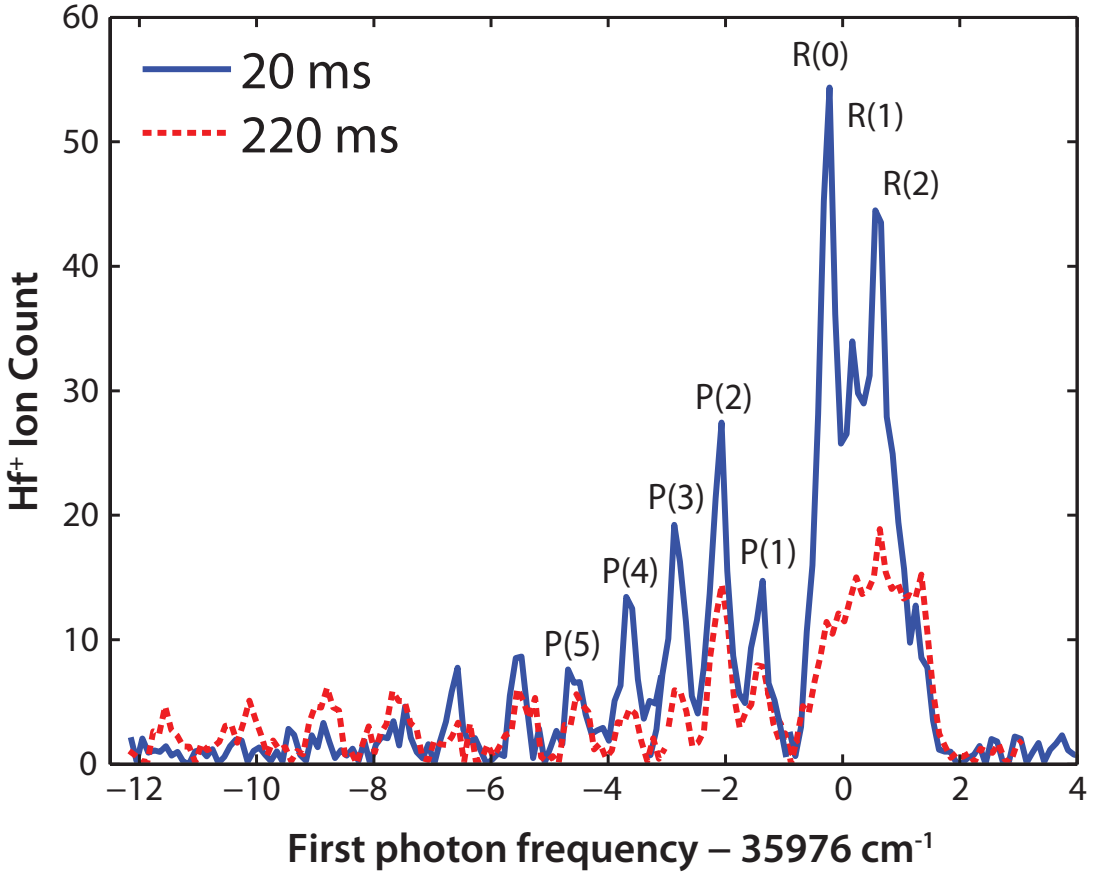

Figure 6.7: Rotational state distribution of trapped ions in $X^1\Sigma^+$ $v'' = 0$ state: 20 ms after trapping (blue) and 220 ms after trapping (red). The first REMPD photon is tuned near 35,976 cm^{-1}. We observed a redistribution towards higher rotational states after 220 ms of wait time.

The detector itself counts 57% (90% throughput from the grounded copper mesh in front of the detector, 63% from the open area of the detector, and 100% quantum efficiency for a given open channel) of the incident ions. Therefore the overall efficiency, including detector loss, is 18(2)%. Compared to LIF detection [428], this is an improvement by a factor of more than 200.

Population in the $^3\Delta_1\, v = 0, J = 1$ can be detected by dissociating through the same intermediate state using the 35,006 cm^{-1} band. The yield on this transition saturates at a fluence of 70(10) $\mu J/cm^2$. We measure a photodissociation efficiency of around 13% (not including detector loss) from $^3\Delta_1$. Currently, we do not understand why the photodissociation efficiency is lower for the $^3\Delta_1$ than for the $^1\Sigma^+$. The dissociation efficiency is lower for the P-branch than for the R-branch, which could indicate that state degeneracies play a role (the ratio of excited state to lower state degeneracy is smaller for the P-branch). To check this (and other effects) we have tried dissociation through other intermediate states but observed no difference in maximum number of dissociated ions.

The dissociation can be increased by applying multiple dissociation pulses (at a 10 Hz rate) and holding the dissociated Hf^+ in the trap between pulses. This is shown for the both $^1\Sigma^+$ and $^3\Delta_1$ in Figure 6.8(a) and (b), respectively. Unfortunately, we find a rapid loss of about 50% of the dissociated Hf^+ within 100 ms (most of the loss was within several ms), which reduces the total efficiency from multiple dissociation pulses. We experimented with different trapping configurations to reduce this loss, thinking that perhaps the trap was too loose during the hold time (we expect the Hf^+ to have about 2000 cm^{-1} of energy, and the trap depth during the hold time was about 2000 cm^{-1}), but increasing the trap depth during the hold time did not help. If we include this loss, we find that we dissociate about 350 HfF^+ from $^1\Sigma^+$ and about 80 from $^3\Delta_1$ out of a total ion number of $\sim$ 3000 HfF^+. This corresponds to about 85% of the expected number in $X^1\Sigma^+\, v = 0,\, J = 0$ and 40% of the $^3\Delta_1\, v = 0, J = 1$ (including the transport efficiency of 78% from the previous paragraph); the reason that the total dissociation is lower for $^3\Delta_1$ is still unknown. We are currently replacing the pulsed YAG laser that pumps a dye laser for the first photodissociation step as well as provides the 266 nm light to have a firing rate of 30 Hz, so we will be able to apply multiple dissociation

pulses faster.

Over the first 200 ms of trapping, we observe a redistribution towards higher rotational states compared to the initial rotational state distribution from the autoionization (see Figure 6.7). We believe this state redistribution is due in part to Langevin collisions of HfF^+ ions with the neutral argon atoms that are injected as the supersonic beam's carrier gas. It could also be caused by collisions with some initially hot ions. Figure 6.9(a) shows rapid initial loss from the $J = 0$ state (due to a relatively high argon pressure) followed by a much smaller loss rate after the argon has been pumped out of the vacuum chamber. The amount of fast loss was reduced by adding an additional turbo pump on the trap chamber and by decreasing the open duration of the pulsed valve (which was possible by switching to the piezo valve instead of the solenoid valve). We observed the fraction of ions initially lost from the $J = 0$ decrease from about 70% to about 40% when the valve duration was lowered from 100 μs to 40 μs. In addition, the timescale (i.e., $1/e$ time) of the loss increased with decreasing pulse duration, which is consistent with a collisional process since the slope is related to the gas density. However, no further improvement was observed with even shorter pulse durations, and below about 35 μs, the initial fraction of ions in $J = 0$ decreased rapidly (presumably due to worse cooling in the supersonic expansion). Currently, we believe that the pump-out speed in the trap center is limited by the mirrors that surround the trap electrodes (which were initially used for fluorescence detection and also serve as the ground plane for the ion trap). Removing these and further increasing the pumping speed may preserve a larger fraction of the ions that occupy the desired rotational state for subsequent experiments; however, we have not yet been able to confirm that this initial heating is currently due to collisions.

6.2.3 Rotating bias fields

For the eEDM measurement, we need to be able to apply parallel (and anti-parallel) electric and magnetic bias fields to our trapped ions. At first glance, this seems impossible, because a static electric field will apply a force to the ions and accelerate them out of the trap, which turns out to be non-ideal for obtaining a long coherence time. We can instead be more creative and

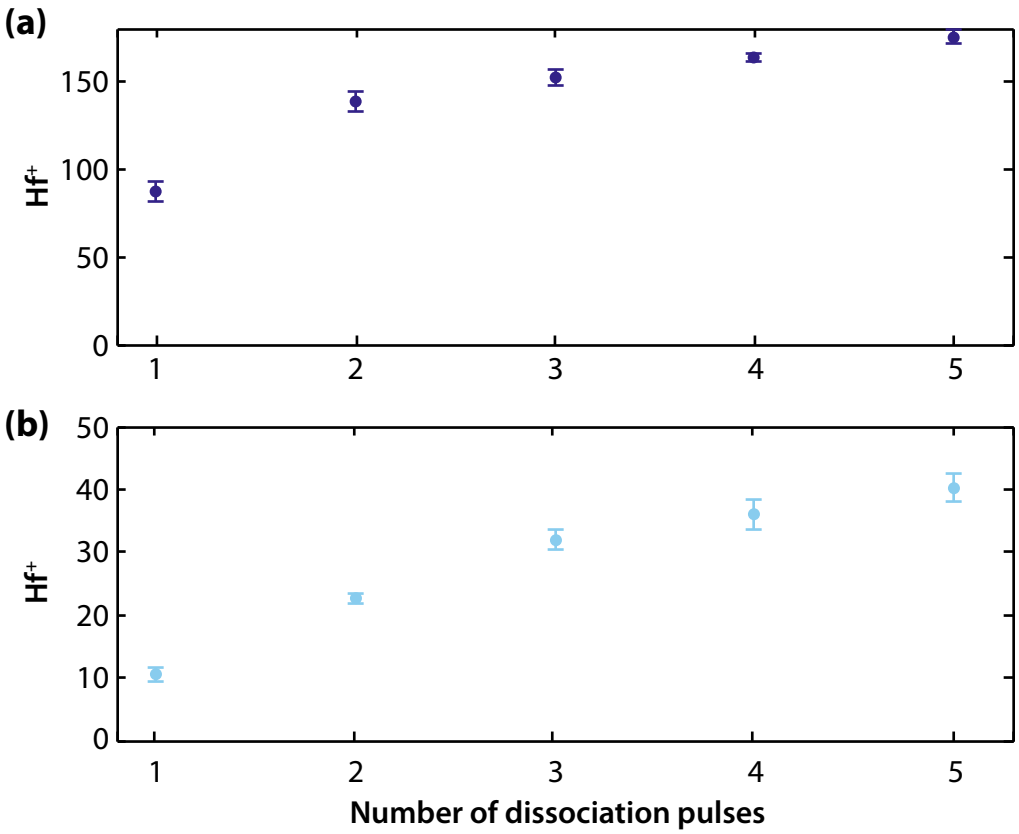

Figure 6.8: Dissociated Hf^+ from the (a) $X^1\Sigma^+ v = 0$, $J = 0$ and (b) $^3\Delta_1 v = 0$, $J = 1$ measured as a function of the number of dissociation pulses. For this measurement, the dissociation shutter was triggered 260 ms after the start of the trap for a variable duration (the dissociation lasers are pulsed at a 10 Hz rate), and the trap duration was fixed to 710.1 ms. The total ion number was about 3000 HfF^+.

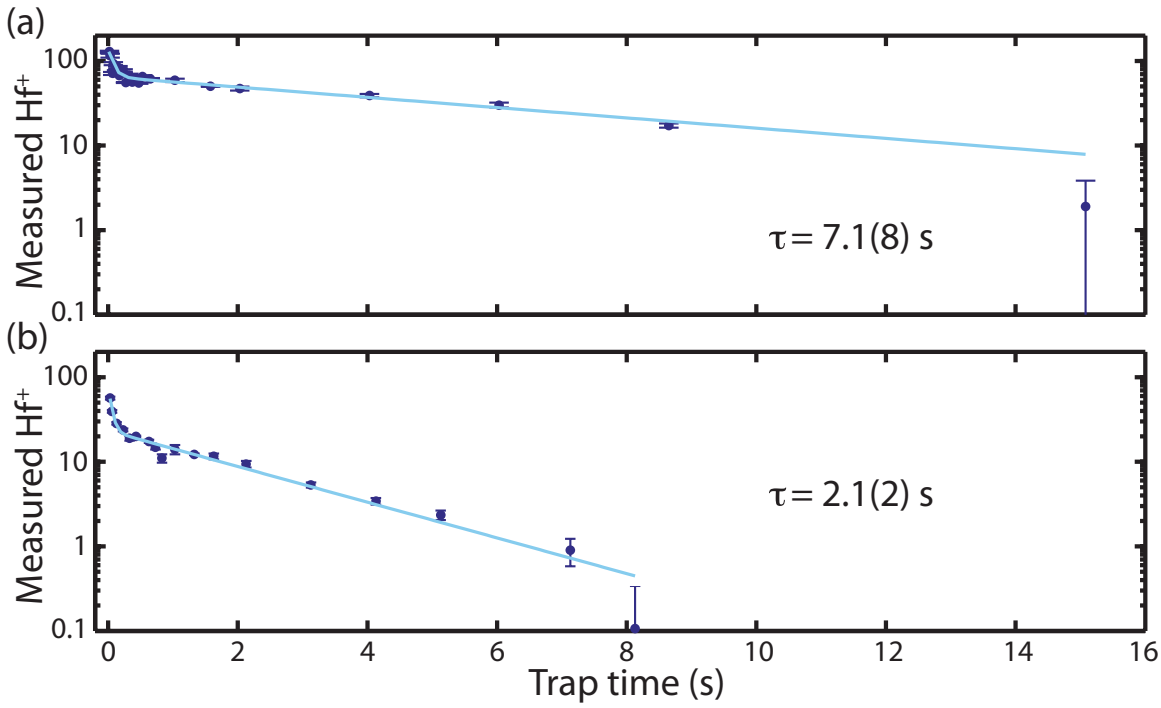

Figure 6.9: Population lifetimes in trapped HfF^+. (a) $X^1\Sigma^+$ $v = 0$, $J = 0$ and (b) $^3\Delta_1$ $v = 0$, $J = 1$. The $X^1\Sigma^+$ lifetime exceeds many seconds after the initial fast decay (100 ms) due to rotational re-distribution as described in Section IV. The $^3\Delta_1$ lifetime is 2.1(2) s.

rapidly rotate the bias electric field. This will cause an additional, rotating micromotion, but if the electric field rotation frequency is significantly higher than the trap rf then the trap motion and rotating micromotion do not influence each other. In addition, the rotation frequency is chosen to be incommensurate with the trap frequency to prevent coherent coupling. One concern, though, is that inevitable non-uniformities in the rotating bias field give rise to a ponderomotive potential [449]. This is the same effect that leads to a net trapping pseudopotential from the rf electric fields in the Paul trap. The ponderomotive potential from a field oscillating with angular frequency ω, $\phi_{\text{pond}} = \frac{e}{4m\omega}\left\langle \mathcal{E}^2 \right\rangle$. This results in a force, $F_{\text{pond}} = -e\nabla\phi_{\text{pond}}$, which can cause several problems. First, the ponderomotive potential adds with the trap pseudopotential and can shift the trap center and add additional confinement or de-confinement. In addition, the ponderomotive force can cause an impulse kick and trap slosh as the field is turned on. To try to avoid these issues, we designed the trap to be as symmetric as possible. We also monitor the voltage applied to each trap electrode and adjust the phase and amplitude of each drive to be as close as possible to the ideal given in Figure 6.4.

The radius of the rotating micromotion at any position in the trap is given by $r_{\text{rot}}(\vec{R}) = \frac{e\mathcal{E}_{\text{rot}}(\vec{R})}{m\omega_{\text{rot}}^2}$, where $\vec{R}$ is the position of the micromotion circle from the center of the trap, $\mathcal{E}_{\text{rot}}(\vec{R})$ is the value of the electric field, and ω_{rot} is the rotation rate. For $\mathcal{E}_{\text{rot}}$ of 20 V/cm and $\omega_{\text{rot}} = 2\pi \times$ 253.7912 kHz, $r_{\text{rot}} \approx 0.4$ mm, corresponding to a tangential velocity of $v_{\text{rot}} = e\mathcal{E}_{\text{rot}}/(m\omega_{\text{rot}}) \approx 620$ m/s.

One option for creating a magnetic field that is parallel to the electric field is to flow current through the trap electrodes when driving them to produce the electric field, but it is difficult to produce a very uniform field with this technique. Instead, we opted to use the rotating micromotion to our advantage and use it to create a rotating bias field from a static field gradient. To do this, we use a pair of anti-Helmholtz coils to produce a radial quadrupole gradient, $\vec{B} = B'(x\hat{x}, y\hat{y}, -2z\hat{z})$. Over one rotating micromotion cycle, we can write the magnetic field experienced by the ion as a sum of a static and a time dependent component, as shown in Figure 6.4: $\vec{B}(t) = \vec{B}_{\text{rot}}(t) + \vec{B}_{static}(\vec{R})$, where $\vec{B}_{\text{rot}}(t) = \nabla_r \vec{B} \cdot \vec{r}_{\text{rot}}(t)$ and $\vec{r}_{\text{rot}}(t)$ is the ion position from the center of the

rotating micromotion circle.

We can understand this by time averaging the instanteous magnetic field projected onto the quantization axis, i.e., $\vec{B}\cdot\vec{\mathcal{E}}/|\vec{\mathcal{E}}|$. The electric field along $\hat{x}$ can be written as a combination of the applied $\mathcal{E}_{\rm rot}$ and the trapping field:

$$\vec{\mathcal{E}} = -\mathcal{E}_{\rm rot}(\cos(\omega_{\rm rot}t)\hat{x}, \sin(\omega_{\rm rot}t)\hat{y}, 0\hat{z}) - \frac{V_{rf}}{R^2}\cos(\omega_{rf}t)(x\hat{x}, -y\hat{y}, 0\hat{z}) - \frac{\kappa V_{dc}}{Z^2}(-x\hat{x}, -y\hat{y}, 2z\hat{z}). \quad (6.25)$$

The position, (x, y, z), is given by Equation 6.7 with the addition of a rotating micromotion term $x_{\rm rot} = r_{\rm rot}\cos\omega_{\rm rot}t$. We can now evaluate $\left\langle \vec{B}\cdot\vec{\mathcal{E}}\right\rangle/|\vec{\mathcal{E}}|$ using Equation 6.7 for (x, y, z) and assuming that $|\vec{\mathcal{E}}| \approx \mathcal{E}_{\rm rot}$ and $\mathcal{E}_{dc} = 0$. We also assume that the trap is symmetric in x, y (i.e., $\omega_x = \omega_y \equiv \omega_r$ and $a_{1x} = a_{1y} \equiv a_{1r}$, which is not exactly correct but should be a good approximation). After time averaging over each motional frequency separately and using Equation 6.9, we find

$$\begin{aligned} B_{\rm rot} &= B'\Big(r_{\rm rot} + \frac{2ma_{1r}^2\omega_r^2}{e\mathcal{E}_{\rm rot}} + \frac{mr_{\rm rot}^2\omega_z^2}{2e\mathcal{E}_{\rm rot}} + \frac{ma_{1z}^2\omega_z^2}{2e\mathcal{E}_{\rm rot}} + \frac{ma_{1r}^2\omega_z^2}{2e\mathcal{E}_{\rm rot}} + \frac{4ma_{1r}^2\omega_z^2\omega_r^2}{e\mathcal{E}_{\rm rot}\omega_{rf}^2}\Big) \\ &\approx B'\Big(r_{\rm rot} + \frac{2(E_x+E_y+E_z)}{e\mathcal{E}_{\rm rot}} + \frac{mr_{\rm rot}^2\omega_z^2}{2e\mathcal{E}_{\rm rot}} + \frac{(E_x+E_y)}{2e\mathcal{E}_{\rm rot}}\frac{\omega_z^2}{\omega_r^2} + \frac{4(E_x+E_y)}{e\mathcal{E}_{\rm rot}}\frac{\omega_z^2}{\omega_{rf}^2}\Big). \end{aligned} \quad (6.26)$$

We chose to use an applied quadrupole magnetic field because the uniformity should be very good. Our anti-Helmholz coils have a radius of 13.6 cm and are separated by 23.6 cm. We can calculate the field expected from this configuration using the results from [450] and estimate the quadratic correction to the gradient to be around $0.1\%/(\text{cm})^2$ in x assuming perfect coil alignment. In addition, we have roughly measured the field from the coils before they were installed on the vacuum system, as shown in Figure 6.10. We see no evidence of inhomogeneity of the magnetic field gradient that is outside of the measurement error. This shows that our assumption about the uniformity of the applied gradient is valid.

6.3 Coherent Transfer

Stimulated Raman adiabatic passage (STIRAP) is a powerful technique for state-selectively transferring population between electronic states in atoms and molecules with high efficiency [451, 452]. By adiabatically eliminating the intermediate state, spontaneous emission can be completely

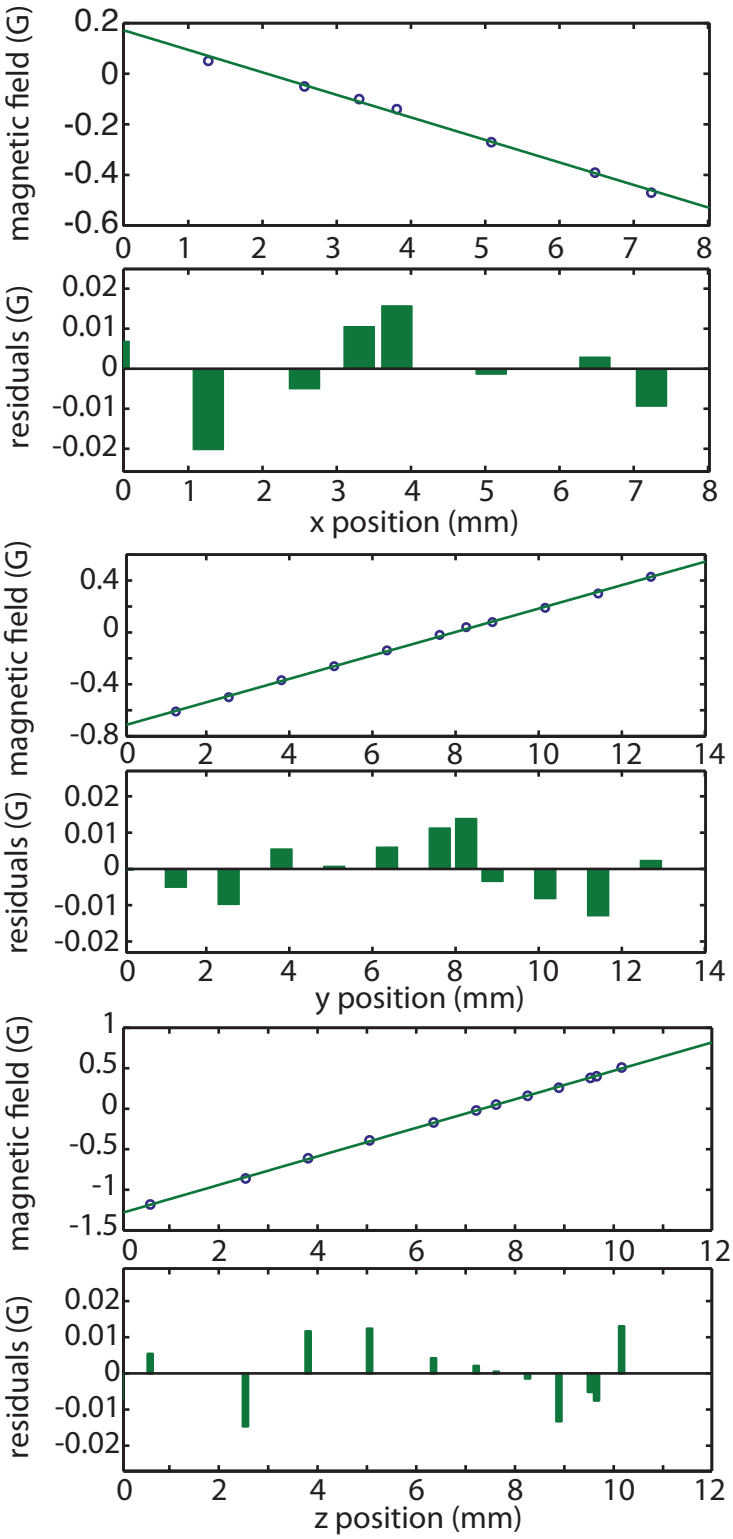

Figure 6.10: Characterization of magnetic field gradient.

removed. While STIRAP can be performed with pulsed lasers, for high spectral resolution (and thus sub-level selectivity) cw-lasers are required. However, in an inhomogenously broadened system – for example, due to Doppler shifts – it is not typically possible to transfer all the population using a standard STIRAP scheme. In the case of trapped ions (in particular, not Coulomb crystallized), oscillating Doppler shifts are present due to harmonic motion in the trap, which makes the use of STIRAP challenging. With our typical trapping conditions, we have a temperature of about 10 K in the axial direction (we want to use the axial direction because of the added micromotion and rotating micromotion in the radial plane), which yields a Doppler linewidth of about 30 MHz for a single-photon transition around 1 μm. For a two-photon transition to the $^3\Delta_1$, we expect the Doppler linewidth to be reduced by a factor of 10, since the difference in energy between $^1\Sigma^+$ and $^3\Delta_1$ is about 970 cm^{-1}. For STIRAP to work over the full 3 MHz of bandwidth, we would want to use pulsed lasers with a duration of below 400 ns. However, the splitting between neighboring Stark manifolds is only around 10 MHz, so we also need pulse durations longer than 100 ns to make sure that we can still resolve the Stark manifolds. This is a challenging pulse duration range to obtain with high power, making STIRAP difficult to apply. Another method, called Stark-induced adiabatic Raman passage (SARP), uses the Stark-shift from a high-power pulsed laser to sweep the two-photon detuning through resonance [453]. Using this method, high transfer efficiency has demonstrated with the need for an off-resonant intermediate state [454], but it will be challenging to achieve the desired resolution.

Instead we developed a different scheme for efficient Raman adiabatic population transfer in an ion trap shown schematically in Figure 6.11. The initial and target states are coupled using two cw lasers detuned by an amount Δ from an intermediate resonance. The oscillating Doppler shifts result in a two-photon detuning δ, which varies as a function of time for each ion. We use this to adiabatically sweep δ for each ion across resonance, which results in some transfer across the avoided crossing (Figure 6.11(c)). In one-half of a period of secular trap oscillation along the axis of the transfer lasers, every ion will cross resonance once and only once, yielding in principle 100% population transfer. However, if the transfer efficiency for one sweep across resonance is not

high enough, this process can be repeated many times, thus equilibrating the population among the initial and target levels.

The two transfer lasers propagate along the z direction so that there is no radial micromotion (or rotating micromotion in the presence of $\mathcal{E}_{\text{rot}}$). Because the transition is a Λ-type, the two lasers co-propagate so the two-photon transition is Doppler free. To maximize the possible transfer efficiency, we ramp the trap in the axial direction to give trap frequencies of around $(12.5, 10, 1)$ kHz in (x, y, z). This ramp allows us to use smaller transfer laser beams to increase the intensity and provides a low temperature and secular frequency along the laser direction, which helps to increase the adiabaticity.

6.3.1 Laser stabilization

For any Raman transfer scheme to be robust, both of the lasers need to be frequency stabilized such that their relative coherence time is longer than the length of the transfer. Also, for ease of use, they should stay on two-photon resonance for a long period of time. One way of achieving these goals is to lock both of the lasers to different teeth of a stabilized frequency comb; however, this adds the additional complexity of another laser system and the locks required to stabilize the comb. Instead, it is possible to use the modes of a stable Fabry-Perot resonator as a "comb" and lock each laser to a different mode. This has the advantage of reducing the complexity, but it has the disadvantage that the absolute frequency of any given cavity mode is not known *a priori*. We can circumvent this problem by using a cavity with a mode spacing (i.e., FSR) large enough so that we can guarantee using a wavemeter that we always lock each laser to the same cavity mode. Another disadvantage is that the cavity modes cannot be actively stabilized to an arbitrary frequency with high feedback bandwidth and the mode frequencies are sensitive to environmental perturbations such as pressure and temperature. For these reasons, it is necessary to build a cavity that is passively stable and to lock each laser with an adjustable frequency detuning from a cavity mode.

The stable cavity consists of two curved mirrors (radius-of-curvature of 50 cm, 0.16% and

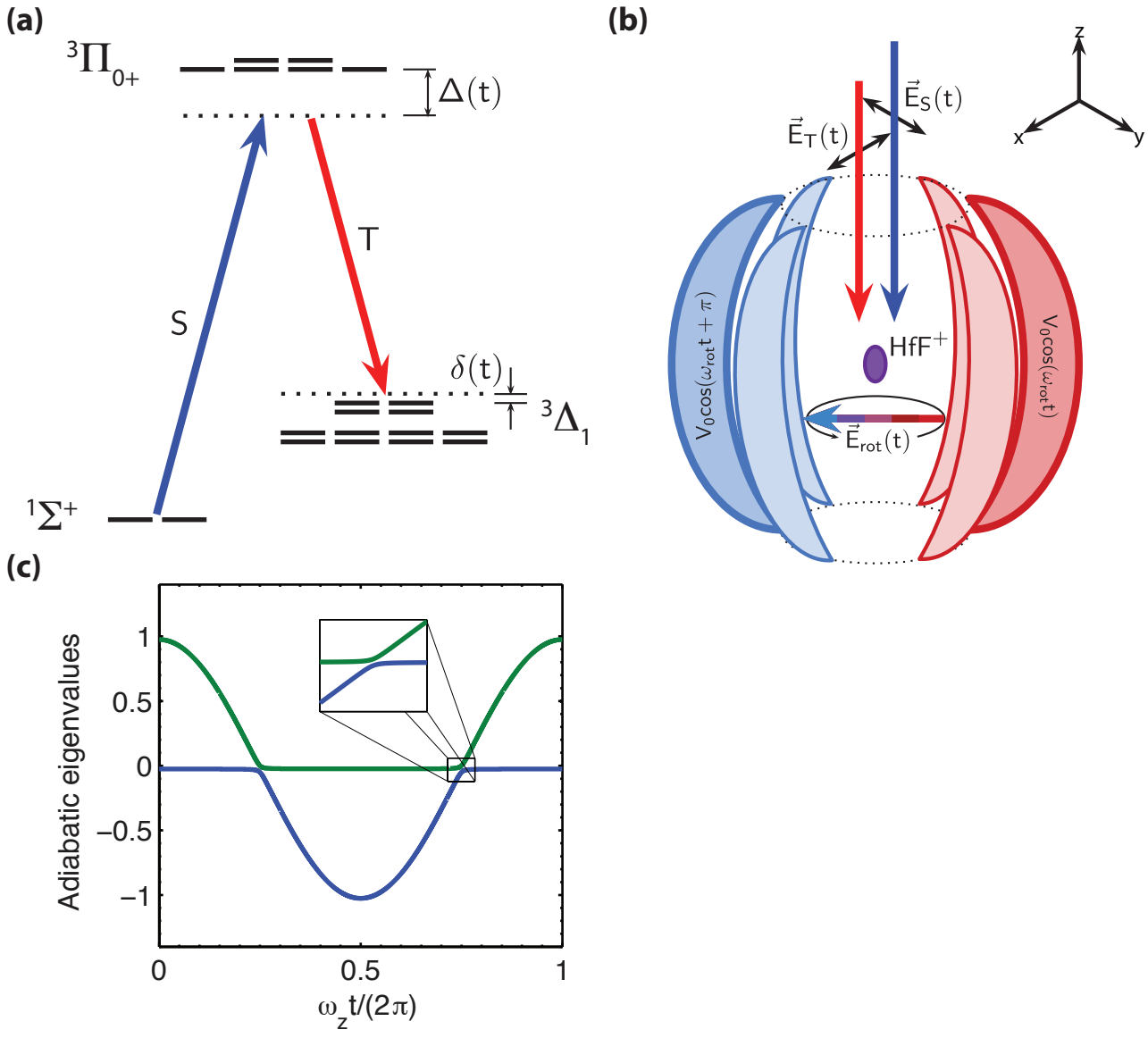

Figure 6.11: Adiabatic transfer from $^1\Sigma^+$ to $^3\Delta_1$. (a) Energy level structure of the three states involved. (b) Laser direction and polarization. (c) Adiabatic eigenvalues of the two-level Hamiltonian (Equation 6.28) over one period of axial trap oscillation, $t = 2\pi/\omega_z$. The inset shows an avoided crossing in the vicinity of $\omega_z t = (n + 1/2)\pi$.

0.12% transmission at 900 and 986 nm) mounted on an ultra-low expansion (ULE) glass spacer. The spacer is about 7.5 cm diameter and 11.5 cm long and has a hole bored out of the center for the laser as well as a perpendicular hole for venting. The mirrors are attached with a thin layer of Crystalbond 509: to do this, a mixture of Crystalbond and acetone (20% by weight) is injected between the mirror and spacer (the mirror can be rotated to get a thin, uniform layer with no bubbles), and the acetone is evaporated under a heat lamp (low heat) for at least 24 hours. After this, the cavity is placed in a temperature-controlled vacuum chamber as shown in Figure 6.12(a). The cavity rests in the center of a 6" Conflat Tee on Viton hemispheres (half of a Viton ball from McMaster-Carr). Viton is used because the extremely low mechanical Q-factor provides good vibrational damping. Two ends of the tee are closed with standard AR-coated windows (Thorlabs, B coating) and the upper part of the tee is connected to a valve (for initial pumping with a turbo) and an ion pump to reach a final pressure of $\sim 2 \times 10^{-7}$ Torr. The entire chamber is supported by clamps isolated from the optical table with sorbothane rubber for additional vibrational isolation.

Several temperature controllers are used to reduce temperature gradients across the chamber. The center portion of the vacuum chamber is wrapped with a Minco flexible heater (resistance of 526 Ω), which is secured with thermally conductive tape. A precision thermistor (Measurement specialties 44008RC, 30 kΩ) is epoxied next to the flange of the tee (away from heater) and is used as the feedback thermister for one control loop. An AD590 temperature sensor is mounted opposite of the thermistor as a temperature monitor. In addition, two small Minco heaters (resistance of 44 Ω each) are mounted in series on each end flange on opposite sides of the window. A thermistor and AD590 are mounted above and below the window, respectively, and are used in two more feedback loops (one for each side). The entire chamber is heated to about 28° C, with the sides slightly warmer than the center. All feedback is done with JILA temperature controllers. Finally, the entire chamber (except for the windows) is wrapped with Thinsulate insulation. The finished chamber is shown in Figure 6.12(b).

Since the cavity has an FSR of ~ 1.3 GHz, an ideal setup would require an offset tuning of 650 MHz so that the laser frequency could be continuously tunable; however, this is technically very

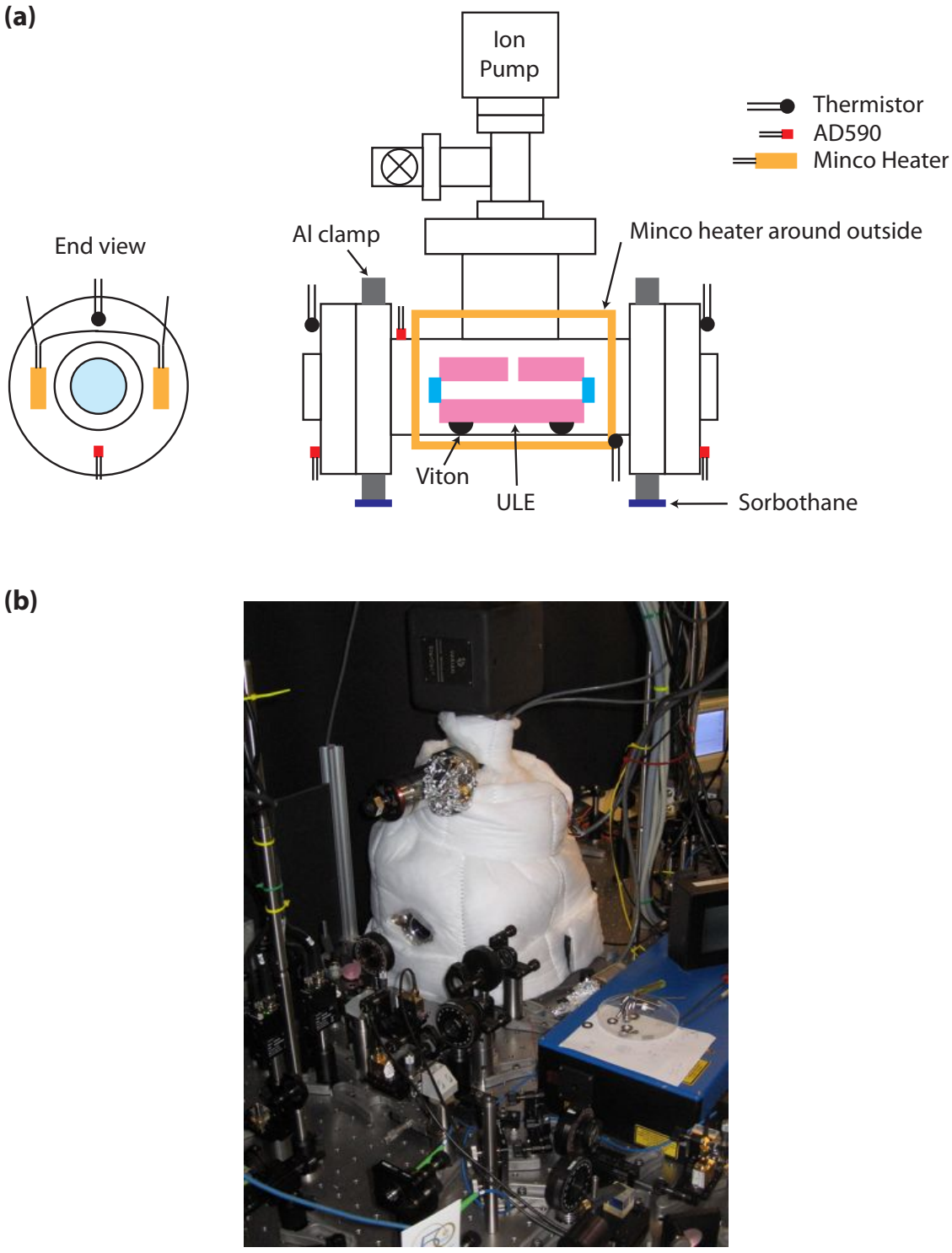

Figure 6.12: Stabilization cavity for Raman transfer lasers. (a) Sketch of vacuum chamber. See text for details. (b) Picture of completed cavity wrapped in thermal insulation (white).

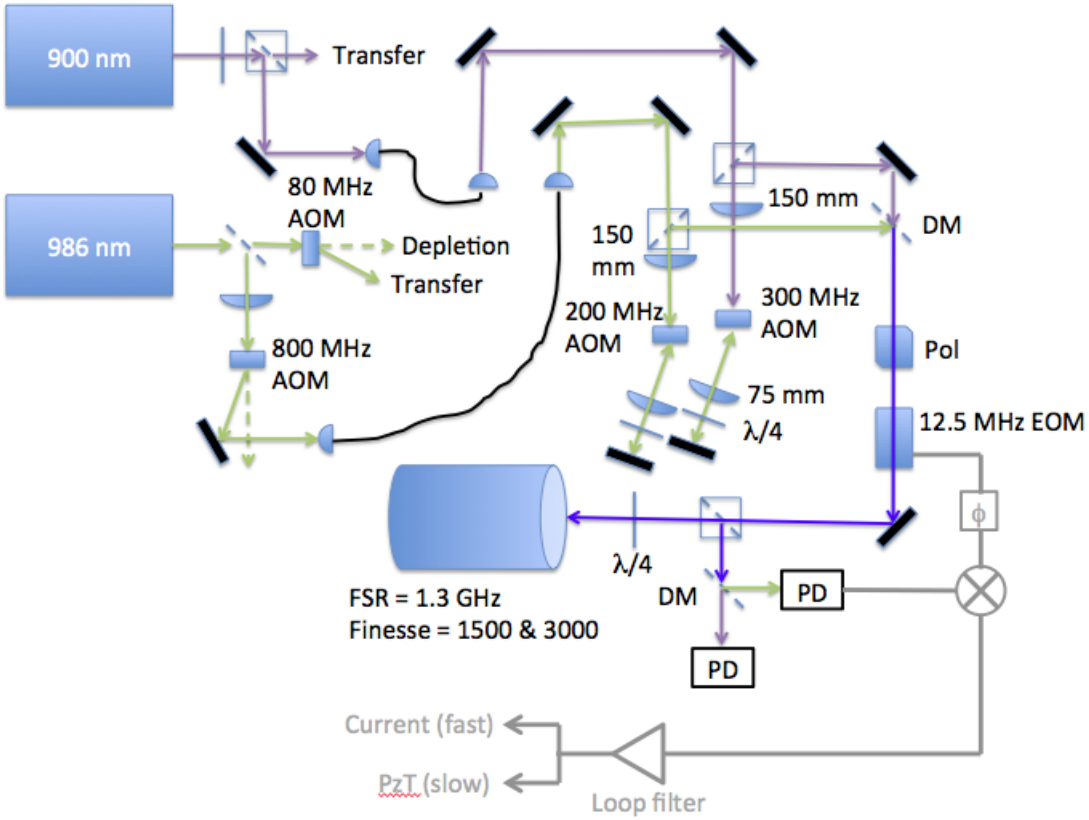

Figure 6.13: Sketch of the laser stabilization setup for the transfer lasers. AOM: acousto-optic modulator; DM: dichroic mirror; Pol: Glan-Thompson polarizer; EOM: electro-optic modulator. The feedback loop is shown in gray. ϕ: phase shifter.

difficult because the low efficiency and alignment sensitivity of high-frequency AOMs makes them hard to double-pass. Since we want to be able to change the two-photon detuning (for example, to measure the hyperfine splitting, etc.), we need to be able to tune one laser continuously by more than 50 MHz without having to adjust the alignment, which is not possible with a single-pass AOM setup because of the changing deflection angle with changing frequency. The final setup was chosen as a compromise between flexibility, tuning range, technical difficulty, and available supplies.

A sketch of the setup used for offset locking the lasers to a cavity mode is shown in Figure 6.13. A small amount of light from each laser is sent to the locking setup via fiber to prevent alignment drifts. For the T laser, an 800 MHz AOM located before the fiber coupling is used to provide coarse frequency tuning (this requires re-alignment for large frequency steps). After the fibers, the light from S and T is sent to a 300 MHz and 200 MHz double-passed AOM, respectively. The AOM frequencies were chosen by first determining the location of the transitions using a wavemeter and then taking the distance to the closest cavity mode. The double-pass setup [455] consists of a PBS, followed by a lens to focus light into the AOM; the focal length (f) of this lens is chosen such that the diffraction-limited beam waist, $w = \frac{4\lambda f}{\pi D}$ for an input beam of diameter D, is comparable to, but a bit smaller than, the active area of the AOM – typically < 300 μm for a 200 MHz AOM. After the AOM, the light is collimated with another lens located one focal length away from AOM ($f_1 = 75$ mm). For good double-pass efficiency, it is important to adjust the position of this lens to nicely collimate the beam. After the lens, the light goes through a quarter-wave plate (fast axis 45° from the polarization axis) and then retro-reflects off of a mirror located a distance f_1 from the second lens. The alignment of this mirror is adjusted until light is observed at the output port of the PBS, although some care needs to be taken to make sure that the beam profile is still nice as a poor exit beam profile can indicate that the light is not diffracting a second time in the AOM.

After the PBS, the light from T and S both pass through half-wave plates before being combined using a dichroic mirror; they then go through a linear (Glan-Thompson) polarizer and finally an EOM (at 12.5 MHz) to create the sidebands used for the Pound-Drever-Hall (PDH) lock. The polarizer sets the polarization to be parallel to the electric field in the EOM crystal to reduce

residual amplitude modulation which can cause noise and offsets in the lock [456]. After the EOM, the light passes through a PBS and quarter-wave plate prior to the cavity. The reflected light from the cavity exits the PBS, is split with another dichroic, and is detected on two PDA8A amplified photodetectors. The cavity transmission is imaged onto a camera to optimize the cavity alignment and lock to the correct mode.

All of the AOMs are driven with a Minicircuits ZHL-1-2W amplifier (max output power 33 dBm). The source for each double-pass AOM is one channel of an Analog Devices AD9959 DDS (clocked externally at 20 MHz with an internal $\times 20$ for a final 400 MHz internal clock). The output of the DDS is amplified and then doubled since the maximum output frequency of the DDS is 200 MHz given the clock frequency and in practice needs to be a bit lower than that because of aliased frequency components at 400 MHz minus the output frequency. The PDH error signal is detected by mixing the rf signal from the photodetector with the monitor output from the EOM drive (after a phase shifter which is adjusted to optimize the error signal magnitude and symmetry). We can characterize the locked laser linewidth by measuring the noise spectrum of the locked error signal compared to amplitude of the PDH error signal [457]. We estimate a linewidth of around 10 kHz.

6.3.2 Transfer theory

If the hyperfine and Stark structure of $^3\Pi_{0^+}$ and $^3\Delta_1$ can be neglected, the transfer problem takes the form of a three-level Λ system. The finite lifetime of the $^3\Pi_{0^+}$ state is modeled by a loss rate γ. For the three-level system, we use the effective single-particle Hamiltonian

$$\mathcal{H}(t) = \hbar \begin{pmatrix} 0 & \Omega_{12}(t)/2 & 0 \\ \Omega_{12}(t)/2 & \Delta(t) - i\gamma & \Omega_{23}(t)/2 \\ 0 & \Omega_{23}(t)/2 & \delta(t) \end{pmatrix}, \tag{6.27}$$

where $\Delta(t) = \Delta_0 + \Delta_1 \cos(\omega_z t + \phi)$, $\delta(t) = \delta_1 \cos(\omega_z t + \phi)$ and $\delta_1 = \frac{\omega_{12} - \omega_{23}}{\omega_{12}} \Delta_1$. Due to the finite size of the transfer laser beams and the radial ion motion, the one-photon Rabi frequencies Ω_{12} and Ω_{23} are also functions of time.

Using the Hamiltonian (6.27), we have numerically simulated the time-evolution of a single particle in a harmonic trap, initially in the state $|\psi(t=0)\rangle = |1\rangle = |^1\Sigma^+\rangle$. We use a time step Δt that is small compared to an axial trapping period, and successively apply the evolution operator $\exp(i\mathcal{H}(t)\Delta t/\hbar)$ to evolve the state forward in time.

If the one-photon detuning Δ_0 is large relative to δ and $\Omega_{12,23}$, we can perform adiabatic elimination by requiring that the population of state $|2\rangle$ does not change in time [64]. In this approximation, we obtain the Hamiltonian

$$\mathcal{H} = -\frac{\hbar}{4\Delta_0}\begin{pmatrix} \Omega_1^2 & \Omega_1\Omega_2 \\ \Omega_1\Omega_2 & \Omega_2^2 - 4\Delta_0\delta(t) \end{pmatrix}. \tag{6.28}$$

The adiabatic eigenvalues of the Hamiltonian (6.28) evolve periodically with the trap frequency ω_z, as shown in Fig. 6.11(c).

6.3.3 Transfer parameters

An intuitive estimation of the transfer efficiency can be obtained by considering the avoided crossing in Figure 6.11(c). In the limit of large initial and final two-photon detuning, the transfer probability for a single sweep (total time T) can be estimated from the Landau-Zener formula [458]

$$P_{LZ}(T) = 1 - \exp\left[-2\pi\frac{\left(\frac{\Omega_{13}}{2}\right)^2}{\dot{\delta}}\right], \tag{6.29}$$

where $\Omega_{13} = \Omega_{12}\Omega_{23}/(2\Delta_0)$ is the two-photon Rabi rate on resonance and $\dot{\delta}$ is the two-photon detuning sweep rate. The factor of 1/2 in Equation 6.29 arises because the Rabi rate is twice the off-diagonal coupling in the Hamiltonian. For trapped ions at a given temperature, the sweep rate can be approximated by assuming a linear sweep from negative to positive Doppler shift in one-half of a trap oscillation period. This gives

$$\dot{\delta} \approx (2\Delta\omega)/T = 4\frac{v_{\mathrm{RMS}}}{c}(\omega_{12} - \omega_{23})\nu_z, \tag{6.30}$$

where $\Delta\omega$ is the maximum Doppler shift (in angular frequency), v_{RMS} is the root-mean square velocity from a Boltzmann distribution, $\omega_{1(2)}$ is the angular frequency of the upward (downward)

laser, and ν_z is the trap secular frequency along the direction of the lasers (defined to be the z-axis). From this, we see that a transfer probability of at least 0.5 can be obtained as long as $\Omega_{12}^2 > (\omega_1 - \omega_2)\nu_i$.

Additional complications arise when considering multiple Landau-Zener transitions. The net transfer probability after two crossings is an oscillating function $P = 4P_{LZ}(1 - P_{LZ})\sin^2\phi_S$, where ϕ_S is the Stückelberg phase [459]. This phase consists of a term acquired during the time between crossings and a term from the non-adiabatic transition. These two terms can cause either constructive or destructive interference for the second crossing, leading to an effect called Landau-Zener-Stückelberg interferometry. For a period series of crossings, the overall behavior is more complicated and is discussed in a variety of papers [459, 460, 461, 462, 463, 464]. In general, the behavior depends on the phase and amplitude of modulation (in this case, the Doppler shift) as well as the two-photon Rabi rate. Since we have a thermal distribution, we have assumed that the interference effects are averaged away and just use the simple Landau-Zener treatment.

In order to figure out the expected transfer efficiency in our system, we need to determine all of the parameters in the Landau-Zener formula. The detuning and trap secular frequencies are well known, and we can estimate the Doppler shift, so all that remains is to determine the one-photon Rabi rates (Ω_{12} and Ω_{23}). We can measure Ω_{12} (i.e., the Rabi rate for the $^3\Pi_0 \leftarrow {}^1\Sigma^+$ transition) by measuring the depletion rate with an on-resonant drive. Because of the oscillating Doppler shifts, this depletion process is treated as a repeated one-photon Landau-Zener transition to the $^3\Pi_0$ from which the population is lost due to spontaneous emission. For a single sweep, the probability of remaining in the ground state is given by Equation 6.29 with Ω_{13} replaced by Ω_{12} and $\dot{\delta}$ given by the first part of Equation 6.30. The probability of remaining in the ground state after N cycles is given by $P_0(N) = 1 - \sum_{n=1}^{N} P(1-P)^{n-1}$, which results in an exponential loss with time constant τ. Thus

$$P_0(T) = \exp(-T/\tau) = \exp\left[-2\pi \frac{\left(\frac{\Omega_{12}}{2}\right)^2}{\frac{2\Delta\omega}{T}}\right], \tag{6.31}$$

which can be solved to give

$$\Omega_{12} = \sqrt{\frac{8\Delta\omega}{\tau}}. \tag{6.32}$$

Measurements of Ω_{12} at different laser intensities are shown in Figure 6.14. For these points, the laser was enlarged (∼15-mm diameter) so that the intensity was uniform across the center. The electric field strength was calculated from the laser power measured over a 9.5-mm-diameter power meter: $\mathcal{E} = \sqrt{\frac{2I}{c\epsilon_0}}$. Since $\Omega_{12} = \mu_{21}\mathcal{E}/\hbar$, a linear fit to the data gives the total dipole moment $\mu_{21} = 0.070(4)\ ea_0$. This is the total dipole moment, which includes angular momentum coupling (S_{21}), statistical weight (g_1), and vibrational wave function overlap: $\mu_{21} = \sqrt{S_{21}/g_1}\,\langle\chi_2|\chi_1\rangle\,\left\langle{}^3\Pi_0|d|{}^1\Sigma^+\right\rangle$. Here S_{21} is referred to as the Hönl-London factor and can be obtained from Clebsch-Gordon coefficients or Wigner 3j symbols. Note that there are some inconstancies among different published versions [358, 365, 465, 466], here we have used an expression for a Case (a) to Case (a) rotational transition:

$$S_{21} = (1 + \delta_{\Omega'0} + \delta_{\Omega''0} - 2\delta_{\Omega''0}\delta_{\Omega'0})(2J'+1)(2J''+1)\begin{pmatrix} J' & 1 & J'' \\ -\Omega' & \Omega' - \Omega'' & \Omega'' \end{pmatrix}. \tag{6.33}$$

For this transition $S_{21} = 2$. Using the Franck-Condon overlap $\langle\chi_2|\chi_1\rangle^2 = 0.38$ and $g_1 = 1$ (ignoring hyperfine), $\left\langle{}^3\Pi_0|d|{}^1\Sigma^+\right\rangle = 0.080(5)\ ea_0$.

We can measure Ω_{23} in a similar fashion, but we do not initially start with population in the ${}^3\Delta_1$. Instead, we can transfer some population into ${}^3\Delta_1$ $J = 1$ and then deplete this population; however, we did not have the ability to shift the laser frequency to be directly on resonance and also follow the same beam path. While it should be possible to measure the depletion at a given detuning, this only works if the lineshape is well known. Given the sidebands and broadening of the one-photon lineshape observed in Figure 6.15, we do not trust this measurement. Instead, we send the on-resonant light in from the radial direction; however, the micromotion in the radial plane (which varies depending on the location in the trap) significantly complicates the interpretation of the depletion time scale. To overcome this, we use the rotating electric field to impose a constant oscillating Doppler shift. We measure a depletion time constant of $\tau = 0.61(8)$ ms

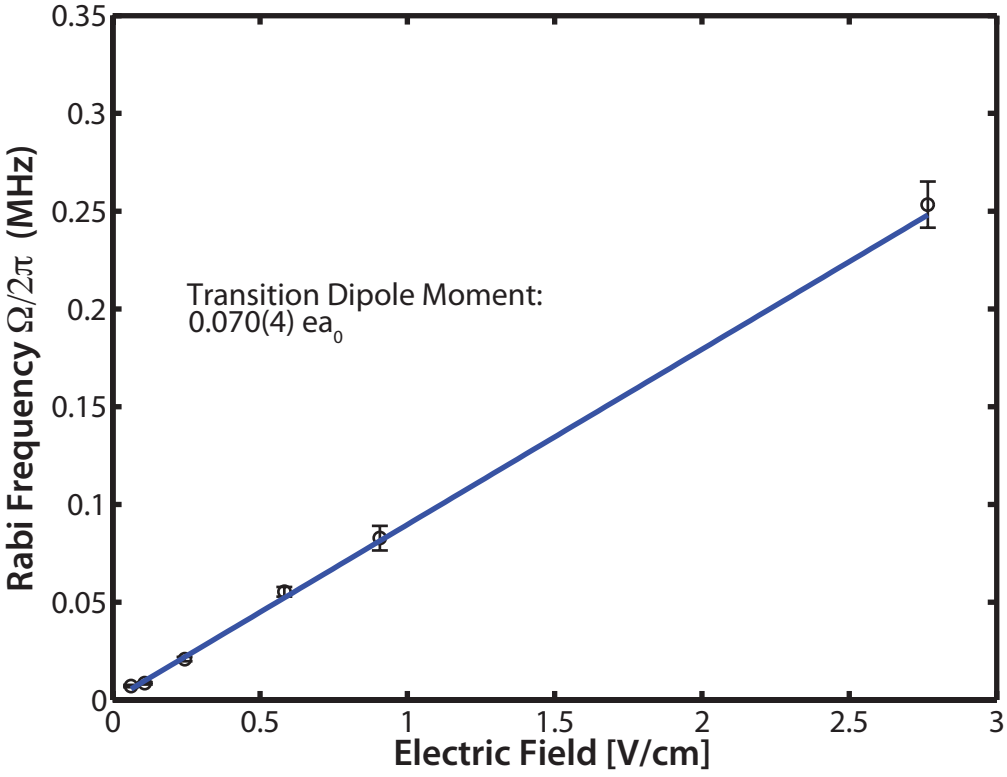

Figure 6.14: Transition dipole moment calibration for the ${}^3\Pi_{0^+} \leftarrow {}^1\Sigma^+$ $(v = 1, J = 1) \leftarrow (v = 0, J = 0)$ transition.

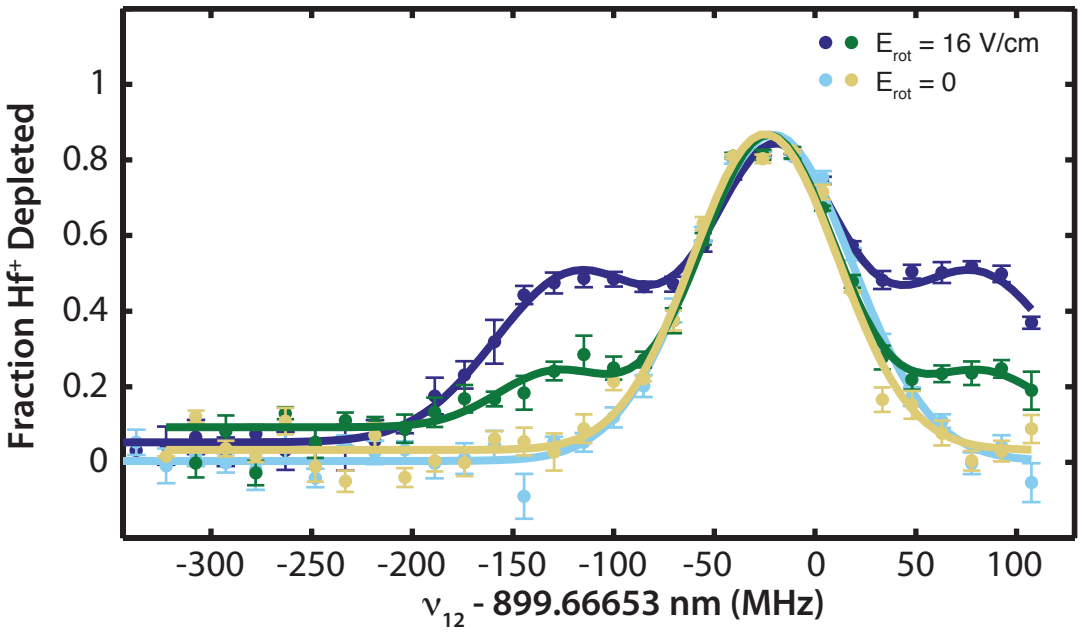

Figure 6.15: One photon lineshape measured by depletion from $^1\Sigma^+$ $J = 0$ (denoted as laser S). The center peak is saturated to show the structure in the sidebands. Dark points are recorded with $\mathcal{E}_{\rm rot} = 16$ V/cm, light points are for 0 V/cm. Blue and green points are for two slightly different alignments of the transfer laser.

with a depletion laser intensity of 25 mW/cm^2 and a rotating field of 16 V/cm. Using Equation 6.32, with $\Delta\omega = v_{\rm rot}/c \times 2\pi c/\lambda$, we find $\Omega_{23} = 2\pi \times 1.03(6)$ MHz, so $\mu_{23} = 0.18(2)\ ea_0$. For this transition, we use the Hönl-London factor $S_{32} = 3/2$, which still ignores hyperfine. Using the Franck-Condon overlap $\langle\chi_2|\chi_1\rangle^2 = 0.31$, we find that $\left\langle {}^3\Pi_0|d|{}^3\Delta_1\right\rangle \approx 0.27(3)\ ea_0$. Compared to the theoretical predictions in Table 5.6, $\left\langle {}^3\Pi_0|d|{}^1\Sigma^+\right\rangle$ is low by about a factor of 2, while $\left\langle {}^3\Pi_0|d|{}^3\Delta_1\right\rangle$ matches the theory.

We initially operated with a total single-photon detuning (Δ) for each laser of 160 MHz. However, we found that the broadened lineshapes shown in Figure 6.15. To reduce the spontaneous emission, the single-photon detuning was increased to ∼1.5 GHz. For the data shown below, we had about 200 mW of S and 350 mW of T just before the trap chamber. This was later increased to 500 and 630 mW, respectively, by removing an AOM and using mechanical shutters instead. To maximize the Rabi rate, we focus the lasers to a beam waist of 1.5 mm at the center of the trap and increase the radial trap confinement to a secular frequency of $(12.5, 10)$ kHz in (x, y). To improve the Landau-Zener probability, we decrease the axial trap frequency to about 1 kHz. Using these parameters and the measured dipole moments gives $\Omega_{12} = 2\pi \times 6$ MHz, $\Omega_{12} = 2\pi \times 19$ MHz, and $\Omega_{13} = 2\pi \times 210$ kHz for the lower laser power. From Equation 6.29, we expect a transition probability for a single crossing of 17% and a transfer time scale from Equation 6.32 of 17 ms.

6.3.4 Transfer efficiency and timescale

We can measure the transfer efficiency by measuring the ${}^1\Sigma^+$ $J = 0$ population while scanning the duration for which the transfer laser shutters are open. An example of such a measurement is shown in Figure 6.16 with both lasers linearly polarized and perpendicular to each other (Figure 6.11(b)). Each time point in this figure is the average of separate measurements alternating between both transfer lasers, only the 899 nm laser, and no transfer lasers to measure the $J = 0$ baseline population. From this data we obtain a transfer efficiency of 63(2)%, with a time constant of 5.8(7) ms; one axial trap period is ∼1 ms. In addition, the loss due to one-photon spontaneous emission is negligible. Because the initial state is $J = 0, F = 1/2$ and **e** parity and the final state

is $J = 1, F = 3/2$, we would expect a transfer of 66.7% after the populations fully equilibrate in the absence of an electric field. In the presence of a bias electric field, the degeneracy between $m_F = \pm 1/2$ and $m_F = \pm 3/2$ is lifted, thus reducing the expected efficiency to 50%. With a rotating bias field of 16 V/cm, we observe an efficiency of 37(2)% and a time constant of 15(2) ms. The transferred fraction at short times and the transfer time scale agree reasonably well with the rough estimates in the previous paragraph. In addition, we observe no transfer with the laser polarizations parallel to each other, which is expected due to selection rules (Section 6.3.5).

The maximum expected efficiency of 50% of course assumes multiple transits through the avoided crossing, with transfer for just one-half cycle (one sweep through the avoided crossing), we should be able to increase this to 100% assuming enough laser power. If we decrease the single-photon detuning to 160 MHz and use the same laser parameters, we should have a Landau-Zener probability of about 99.9%. However, even with the higher laser power, the maximum transfer that we have seen after one-half of a trap cycle is around 40%. Some of this may be due to the opening and closing time of the shutters or due to poor overlap of the trap lasers and ions. We are still investigating this and hope to be able to increase the transfer efficiency to above 50%.

6.3.5 Transfer spectrum

Scanning the second transfer laser (denoted T in Fig. 6.11) through two-photon resonance with each of the hyperfine and Stark levels of $^3\Delta_1$ $J = 1$ yields the transfer spectrum shown in Fig. 6.17(a). Because the single-photon detuning is large compared to the single-photon transition width, we assume that the total rate of transfer W_f into a particular Stark level of $^3\Delta_1$ is proportional to the modulus squared of the two-photon transition dipole moment,

$$W_f \propto \left| \sum_{i,m} \sum_{p_T, p_S} \langle f | T^{(1)}_{p_T} | m \rangle \langle m | S^{(1)}_{p_S} | i \rangle \right|^2 . \tag{6.34}$$

The states $|i\rangle$, $|m\rangle$, and $|f\rangle$ correspond to the various sub-levels of $^1\Sigma^+$, $^3\Pi_{0+}$, and $^3\Delta_1$ respectively.

The rank-1 spherical tensor operators $S^{(1)}$ and $T^{(1)}$ correspond to the first and second transfer lasers, respectively. The spherical tensor components in the molecule-fixed frame $S^{(1)}_{p_S}$ and $T^{(1)}_{p_T}$ are

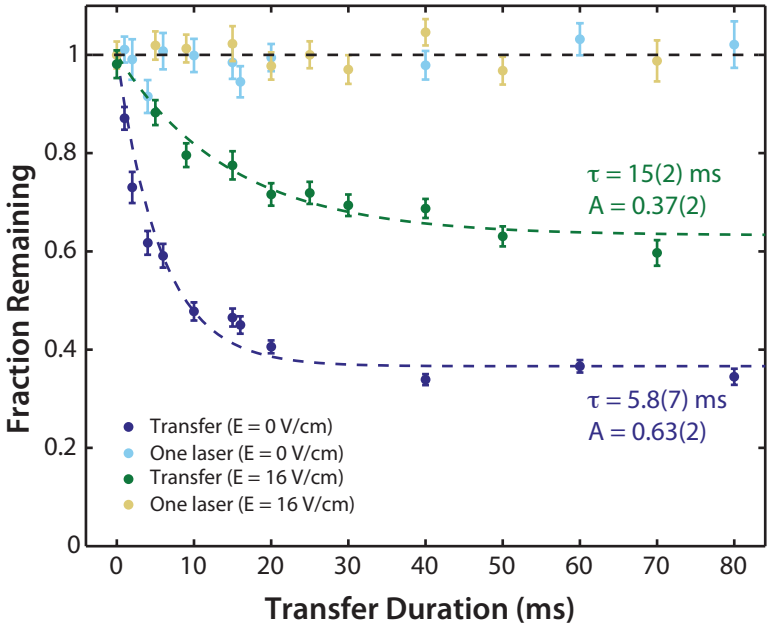

Figure 6.16: Fraction of population remaining in $^1\Sigma^+$ $J = 0$ versus transfer laser on duration. Blue points correspond to $\mathcal{E}_{\rm rot} = 0$ V/cm and green points are for $\mathcal{E}_{\rm rot} = 16.5$ V/cm. In both cases, dark points indicate both transfer lasers and light points indicate only S (the $^3\Pi_{0+} - {}^1\Sigma^+$ laser). The data with both transfer lasers are each fit to a single exponential decay (shown as dashed lines) with a variable time constant (τ) and transfer efficiency (A). In addition, the S-only data show that spontaneous emission losses are negligible.

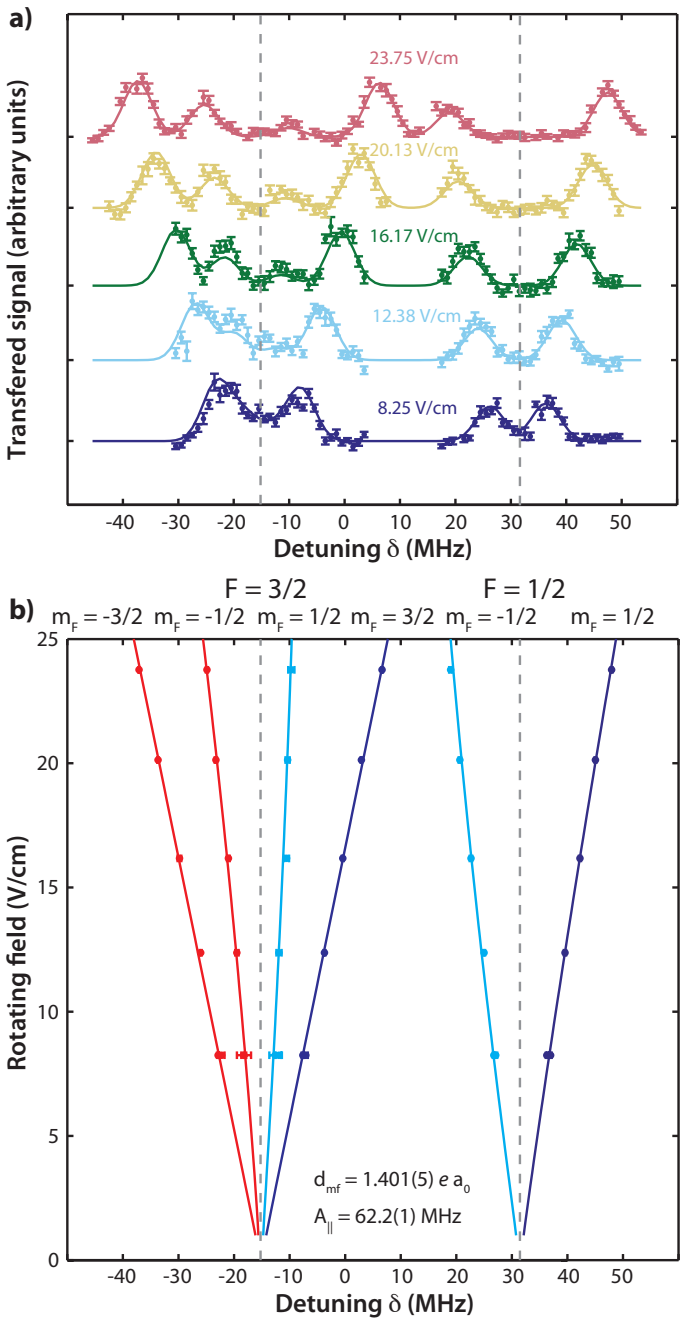

Figure 6.17: Stark spectroscopy of $^3\Delta_1$ $J = 1$. (a) Observed $^3\Delta_1$ $v = 0$, $J = 1$ spectrum using two-photon transfer, for a range of the rotating electric field $\mathcal{E}_{\rm rot}$. The transfer duration was decreased so that the peaks were mostly unsaturated. The solid lines are a fit of the simulated spectrum, discussed in Section 6.3.5, dashed vertical lines indicate positions of the hyperfine peaks for $\mathcal{E}_{\rm rot} = 0$ V/cm. (b) Peak centers for the six Stark manifolds as a function of $\mathcal{E}_{\rm rot}$. The centers are fit to the expected energies (solid lines) to obtain the hyperfine constant, $A_{||}$, and the molecular-frame dipole moment, $d_{\rm mf}$. The lines are color-coded according to the value of m_J in the high-field limit.

related to the lab frame components according to

$$\begin{aligned} S_p^{(1)} &= \sum_{p'} \mathcal{D}^{(1)}_{pp'}(\omega_{\rm rot} t)^* \, S_{p'}^{(1)} \\ T_p^{(1)} &= \sum_{p'} \mathcal{D}^{(1)}_{pp'}(\omega_{\rm rot} t + \theta)^* \, T_{p'}^{(1)} \end{aligned} \tag{6.35}$$

where $\mathcal{D}^{(1)}$ is the $J = 1$ Wigner rotation matrix. In the lab frame, the first and second transfer lasers are linearly polarized with a relative angle of θ. We find that the transfer rate $W_f \simeq \sin^2\theta$ and is independent of $\omega_{\rm rot} t$. This confirms our experimental result that no transfer occurs when $\theta = 0$, and maximum transfer occurs when $\theta = \pi/2$.

Each of the matrix elements $\langle f|T_p^{(1)}|i\rangle$ in Eq. 6.34 can be expanded in terms of the quantum numbers of each state using the Wigner-Eckart theorem. In zero electric field, the states $^1\Sigma^+$, $^3\Pi_{0+}$, and $^3\Delta_1$ can all be written in the Hund's case (c) basis as $|\eta; I; J, \Omega; F, m_F\rangle$, where η are other quantum numbers specific to each state. The dipole matrix elements can be written

$$\begin{aligned} &\langle \eta'; I; J', \Omega'; F', m_F'|T_p^{(1)}|\eta; I; J, \Omega; F, m_F\rangle = \\ &\qquad m_1(F', m_F', p, F, m_F)\, m_2(I, F', J', F, J)\, m_3(J', \Omega', J, \Omega) \end{aligned} \tag{6.36}$$

where

$$\begin{aligned} m_1(F', m_F', p, F, m_F) &= (-1)^{F'-m_F'} \begin{pmatrix} F' & 1 & F \\ -m_F' & p & m_F \end{pmatrix} \\ m_2(I, F', J', F, J) &= (-1)^{F+J'+I+1} \sqrt{(2F'+1)(2F+1)} \begin{Bmatrix} J & F & I \\ F' & J' & 1 \end{Bmatrix} \\ m_3(J', \Omega', J, \Omega) &= \sum_q (-1)^{J'-\Omega'} \sqrt{(2J'+1)(2J+1)} \begin{pmatrix} J' & 1 & J \\ -\Omega' & q & \Omega \end{pmatrix} \langle \eta' || T^{(1)} || \eta \rangle. \end{aligned} \tag{6.37}$$

In a nonzero electric field, the $^3\Delta_1$ sub-levels are Stark states; linear combinations of the states $|\eta; I; J, \Omega; F, m_F\rangle$. The eigenstates and energies are determined by diagonalizing an effective Hamiltonian that includes Stark, hyperfine, and Λ-doubling matrix elements. The hyperfine and Λ-doubling terms are diagonal in the $|\eta; I; J, \Omega; F, m_F\rangle$ states with $\Delta E_{HF} = 45.6(1)$ MHz and

$\Delta E_\Omega = 740(40)$ kHz, and the Stark matrix elements are given by

$$\mathcal{H}_S = -d_{\rm mf}\mathcal{E}_{\rm rot} m_1(F', m'_F, 0, F, m_F)\, m_2(1/2, F', 1, F, 1)\, m_3(1, \Omega', 1, \Omega) \tag{6.38}$$

where $d_{\rm mf}$ is the molecule-frame dipole moment.

The relative energies of the Stark states obtained by diagonalizing the effective Hamiltonian, along with the relative transfer rates given by Eq. (6.34), allow us to simulate the transfer spectrum. Figure 6.17 shows the observed and simulated spectra for a range of $\mathcal{E}_{\rm rot}$, where the hyperfine splitting, Λ-doubling, and molecule-frame dipole moment were fitted parameters. The full width at half max of the lines was fixed at 6 MHz. The simulated spectra recreate the main features of the experimental results: The relative amplitude of each peak is qualitatively correct, with the "stretched" transitions into $|F = 3/2, m_F\Omega = \pm 3/2\rangle$ appearing strongest. In addition, the observation of suppressed transfer into the $|3/2, -1/2\rangle$ and $|1/2, 1/2\rangle$ states is corroborated by the simulated spectra.

We can intuitively understand the amplitude of the transfer peaks by considering the case with no nuclear spin, as shown in Figure 6.18. Since the light polarization is in the plane of the quantization axis, we can only drive π or both $\sigma^\pm$ transitions. From the $^1\Sigma^+$ state, the π transition is forbidden (since $\Delta J = 0$, $\Delta m_J = \pm 1$ only), so we can only drive the blue transitions to $^3\Pi_{0^+}$. From the $^3\Pi_{0^+}$, a second photon with π polarization (opposite of the first photon) can drive transitions to $m_J = \pm 1$ and a σ transition will go to $m_J = 0$; however, the two-σ pathways (all blue lines) cancel because of the signs of the Wigner 3j coefficients, so the transition to $m_J = 0$ is forbidden. This means that we would only expect transitions to $m_J = \pm 1$, and only transition when the laser polarizations are opposite. If we project the $|F, m_F\rangle$ states onto $|J, m_J\rangle$, we find that the relative amplitudes in the transfer spectra in Figure 6.17 correspond to the projection onto $|1, \pm 1\rangle$. In particular, the states that trend toward $m_J = 0$ (light blue in Figure 6.17(b)) decrease in amplitude as $\mathcal{E}_{\rm rot}$ increases, i.e., as the states approach states of good m_J.

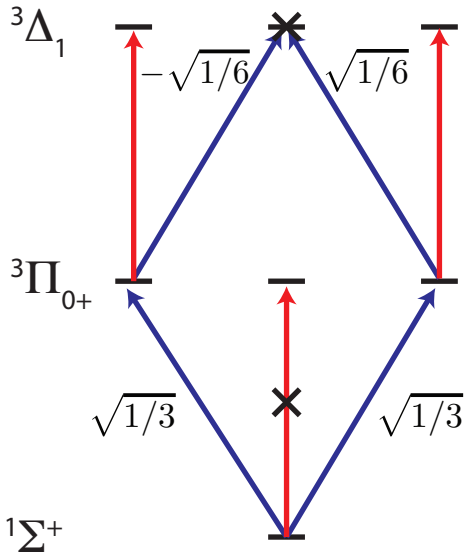

Figure 6.18: Possible two-photon transfer pathways from $^1\Sigma^+$ $J = 0$ through $^3\Pi_{0^+}$ $J = 1$ to $^3\Delta_1$ $J = 1$, ignoring the nuclear spin of fluorine. Red lines indicate π transitions and blue lines indicate σ transitions. The Wigner-3j coefficients for the σ transitions are also given.

6.4 Ramsey Spectroscopy

In the previous sections, we have demonstrated the ability to produce ions with 35% of the population in $^1\Sigma^+$ $J = 0$, trap the produced ions without causing much heating, apply rotating electric and magnetic fields, transfer up to 35% of the population from $J = 0$ to a single Stark doublet in $^3\Delta_1$ $J = 1$, and read out the population in single rotational levels with high efficiency. We now consider how to perform Ramsey spectroscopy between the $m_F = \pm 3/2$ levels in a single doublet, which are the states used in the eEDM measurement as shown in Figure 6.19(a).

One complication arises due to the rotating quantization axis, which results in a coupling between states with $\Delta m_F = \pm 1$ [467, 468, 62, 64]. This coupling can be understood by considering a spin-1/2 system in a rotating magnetic field, which is similar to magnetic resonance [469]. Assume that the the magnetic field is at an angle θ_r from the rotation axis, which defines the lab-fixed $\hat{z}$ axis. The Hamiltonian, $H(t) = -\vec{\mu} \cdot \vec{B}(t)$ can be written in the lab frame as

$$H(t) = \frac{\hbar g \mu_B B}{2} \begin{pmatrix} \cos(\theta_r) & \sin(\theta_r) e^{-i\omega_r t} \\ \sin(\theta_r) e^{i\omega_r t} & -\cos(\theta_r) \end{pmatrix}, \tag{6.39}$$

where the diagonal terms come from the projection onto $\hat{z}$ and the off-diagonal terms are from the rotating $B_\perp$ in the xy plane. We can now apply a unitary transformation into the rotating frame by

$$\begin{aligned} \tilde{H} &= U^\dagger H U - i U^\dagger \frac{\partial U}{\partial t} \\ U &= \begin{pmatrix} e^{-i\omega_r/2 t} & 0 \\ 0 & e^{i\omega_r t/2} \end{pmatrix}. \end{aligned} \tag{6.40}$$

If we assume that the rotation is slow enough that the quantization axis tracks the field, we can also rotate the $\hat{z}$ axis by θ_r to lie along the field direction, defined as the $'$ coordinate system. Then, the Hamiltonian in the field-fixed coordinates is

$$\tilde{H}' = \begin{pmatrix} \frac{\hbar g \mu_B B}{2} + \frac{\omega_r}{2} \cos(\theta_r) & -\frac{\omega_r}{2} \sin(\theta_r) \\ -\frac{\omega_r}{2} \sin(\theta_r) & -\frac{\hbar g \mu_B B}{2} - \frac{\omega_r}{2} \cos(\theta_r) \end{pmatrix}. \tag{6.41}$$

The additional contributions on the diagonal are the standard energy contribution due to a Berry's

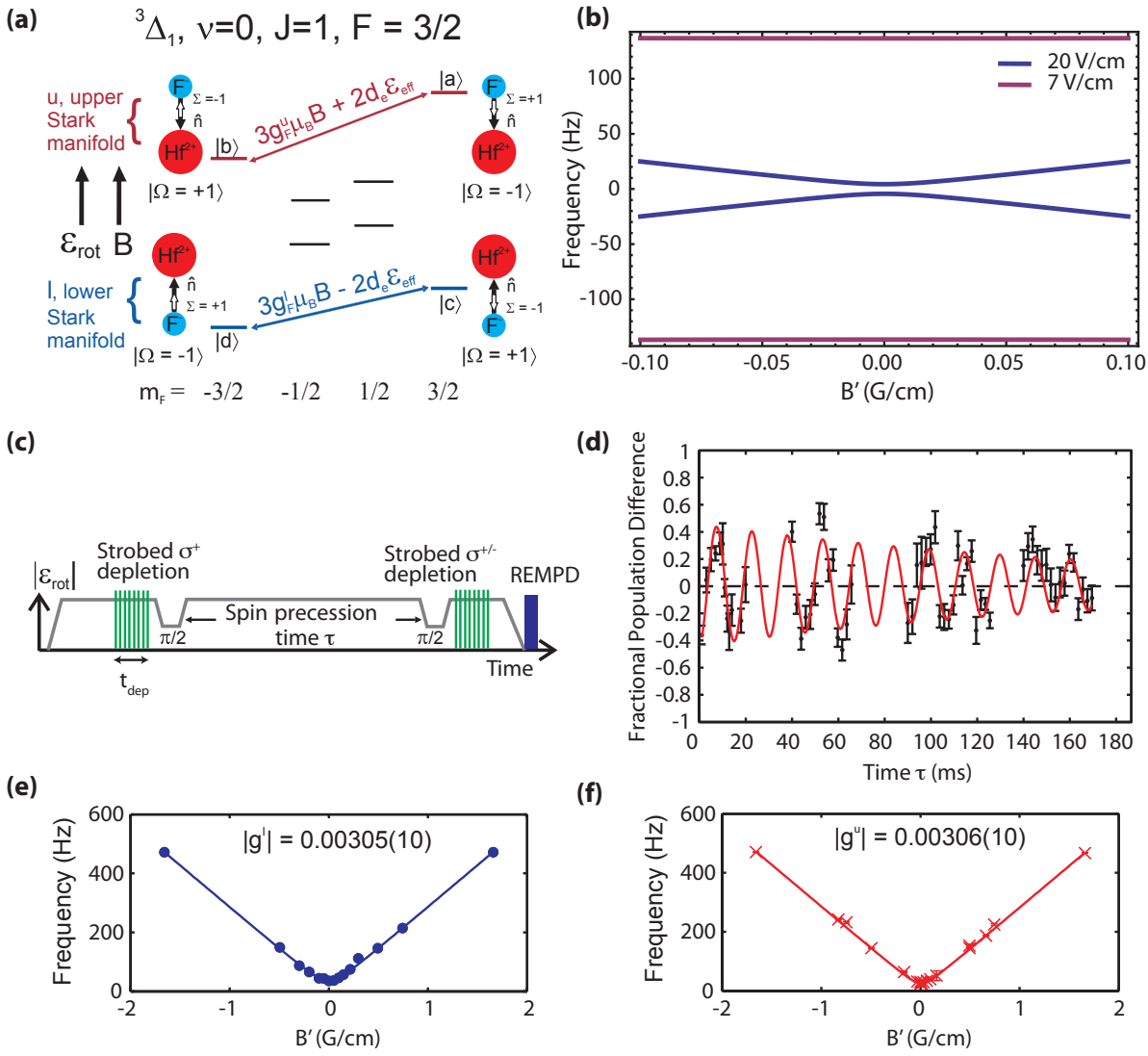

Figure 6.19: Ramsey spectroscopy between $m_F = \pm 3/2$ levels in the $^3\Delta_1$. (a) Level structure of the $^3\Delta_1$ $v = 0, J = 1, F = 3/2$ manifold in electric and magnetic fields. (b) Avoided crossing between $m_F = \pm 3/2$ states due to rotation for two different electric fields with $\omega_{\rm rot} = 2\pi \times 250$ kHz. (c) Ramsey spectroscopy sequence. After the start of the trap, we ramp on $\mathcal{E}_{\rm rot}$ as shown by the gray line. After transfer (not shown), strobed depletion pulses prepare a single spin state. We then reduce $\mathcal{E}_{\rm rot}$ for a period of time for the first $\pi/2$ pulse, wait a precession time τ, and then apply a second $\pi/2$ pulse. After the second pulse, we repeat the strobed depletion process to remove either the $+3/2$ or the $-3/2$ spin state, and finally read out the remaining population with REMPD. (d) Example Ramsey fringe from the initial sets of measurements. (e) and (f) Measurements of the fringe frequency as a function of applied magnetic field gradient allow us to map the avoided crossing and determine the magnitude of g_F for the lower (e) and upper (f) doublets.

phase [470, 471, 472] of $\pm\mathcal{A}/2$, where $\mathcal{A}$ is the solid-angle enclosed by one revolution of the quantization axis. It can be shown that, more generally, the Berry's phase contribution is $m_F\mathcal{A}$ for a state with total angular momentum F and projection m_F [473, 467, 474]. If we set $\theta_r = \pi/2$ – that is, the rotating field is perpendicular to the rotation axis as it is in the ion trap – the diagonal Berry's phase contribution vanishes. We can then re-write the diagonal terms as $\omega_r m_F \sin\alpha \approx \omega_r m_F \alpha$, where α is the tilt angle of the quantization axis from the plane perpendicular to the rotation axis. This tilt could be caused by an axial electric field; however, because the time averaged axial electric field must be zero for the ion to remain trapped, we expect that $\langle\alpha\rangle = 0$ and so there should be no energy shift due to Berry's phase. We discuss other sources of a Berry's phase shift in Section 6.6.

The magnetic-resonance picture also provides an intuitive explanation of what causes the coupling between spin states [475]. A classical dipole $\vec{\mu} = g\vec{J}$ will precess about the static magnetic along $\hat{z}$ at the Larmor frequency, due to the torque $\vec{\mu}\times\vec{B}_{\|}$. If we now transform into a rotating frame, the precession rate appears either faster or slower, which means that the effective magnetic field has changed by an amount ω_r/g. Now, if we include the effect of a rotating field rotating at ω_r, the total magnetic field is tilted away from the $\hat{z}$ axis and has a magnitude $B = \sqrt{B_\perp^2 + \left(B_{\|} - \omega_r/g\right)^2}$. This changes the net project onto the $\hat{z}$ axis, which implies that neighboring m_J values are coupled.

The rotation-induced coupling Hamiltonian, combined with the Λ-doubling Hamiltonian (which connects terms with $\Delta\Omega = \pm 1$), results in a perturbation that couples $|m_F, \Omega\rangle$ with $|-m_F, -\Omega\rangle$. Thus, states in the upper Stark manifold (states $|a\rangle$ and $|b\rangle$ in Figure 6.19(a)) are coupled as are states in the lower Stark manifold ($|c\rangle$ and $|d\rangle$). This results in an avoided crossing between these states, as shown in Figure 6.19(b) as a function of magnetic field.

The first step in the Ramsey sequence shown in Figure 6.19(c) is to start with a pure spin state far outside of the avoided crossing. Since the transfer process creates an incoherent mixture of $m_F = \pm 3/2$ level, we must remove all of the population from a single level. Since we want to address a single spin state and the Zeeman splitting between the two spin states is unresolvable (several hundred Hz at most), we must use a laser with circular polarization and propagation direction along the quantization axis (set by the rotating electric field). This laser drives the ${}^3\Pi_{0^+} \leftarrow {}^3\Delta_1$

$(v = 1, J = 1) \leftarrow (v = 0, J = 1)$ transition and follows the same beam path through the trap as the ionization and dissociation lasers (i.e., it is in the radial plane of the trap). Population excited to the $^3\Pi_{0^+}$ will then spontaneously decay to the $^1\Sigma^+$ or to other vibrational and rotational states in $^3\Delta_1$ and (ideally) will not appear in the measurement. We use light from the second transfer laser (the first order of an AOM, see Figure 6.13) for this depletion light; however, we need to drive the depletion transition on resonance, so we rapidly jump the frequency of laser by stepping the grating position. The jump is adjusted so that the laser frequency changes by 1 FSR and thus we do not lose lock to the cavity. After the AOM and fiber coupling, the depletion laser power is typically about 400 mW. The polarization of the depletion light is set using a combination of a $\lambda/2$ and $\lambda/4$ waveplate to be circular measured before and after the chamber. Typically, we measure a contrast ($\frac{P_{max}-P_{min}}{P_{max}+P_{min}}$) of under 5% when rotating a linear polarizer and measuring the power after the polarizer.

Since the electric field (and thus the quantization axis) is rotating, the depletion light needs to be pulsed on using the AOM only when the electric field is aligned (or anti aligned) with the propagation direction of the depletion laser. We sync the timing of the AOM with the trap frequency and adjust the phase so that we deplete either the $m_F = +3/2$ or the $m_F = -3/2$ depending on the direction of the electric field. As discussed in Section 6.2.3, the rotating micromotion results in a larger micromotion velocity, which in turn results in large Doppler shifts (of about $\pm$600 MHz) for the depletion laser. Thus, the laser is only on resonance for a short time, so the depletion efficiency for a single pulse is low. To alleviate this, we pulse the depletion laser at f_{rot} for about 5 ms with a duty cycle of 10%.

Figure 6.20 shows the fraction of the population removed from $^3\Delta_1$ $J = 1$ after two sets of depletion pulses versus depletion duration (t_{dep}). The light-blue data points show the fraction removed with two sets of depletion pulses of the same polarization (i.e., same phase of $\mathcal{E}_{\text{rot}}$, referred to as *inphase/inphase*) while the dark-blue points correspond to the opposite polarization between the two sets of depletion pulses (*antiphase/inphase*). The difference between these two chops is called the depletion contrast, as shown by the purple data points.

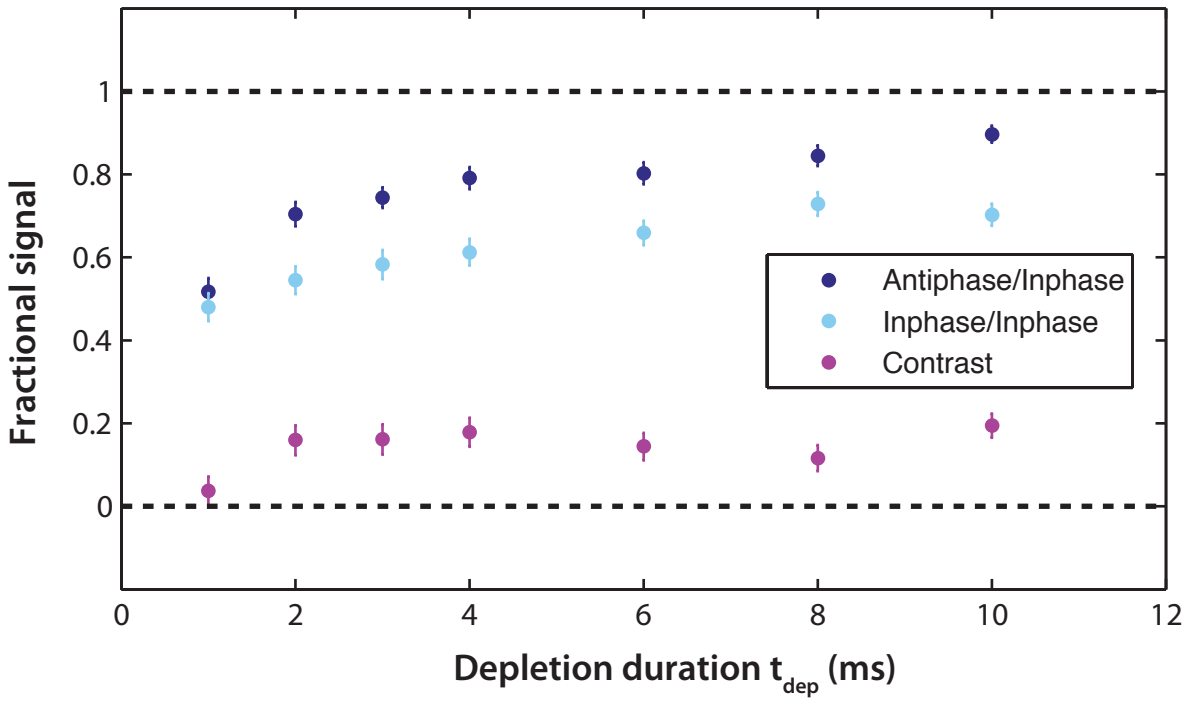

Figure 6.20: Fraction of the population depleted from $^3\Delta_1$ (light- and dark-blue points) and depletion contrast (purple points) as a function of the depletion duration (t_{dep}). The light-blue data points show the fraction removed with two sets of depletion pulses of the same polarization (i.e., same phase of $\mathcal{E}_{\rm rot}$) while the dark-blue points correspond to the opposite polarization between the two sets of depletion pulses. The difference between the two depletion chops is the depletion contrast, shown in purple.

Ideally, for the inphase/inphase chop, we would expect to remove all population from a single m_F level only, resulting in 50% depletion. The antiphase/antiphase chop should remove all population from $^3\Delta_1$, so we should see 100% depletion and 50% contrast. Instead, we see more than 50% depletion for inphase/inphase and less than 100% for antiphase/inphase for $t_{dep} = 4$ ms and a total contrast of 20%.

We have tried to understand this reduced depletion contrast, but so far we have not been able to determine the cause. Interestingly, sometimes the total depletion fraction is more than 90%, but the contrast is not better in these cases. One possible cause of poor depletion contrast is impure circular polarization: we can measure the polarization before and after the chamber but cannot independently measure the polarization at the ions. Stress-induced birefringence in the vacuum windows could lead to the polarization at the ions being different. The linear polarization rotation of a single window outside of vacuum was under 1°, but mounting the window of the chamber and evacuating the chamber will likely result in more birefringence. We have measured the polarization before and after the chamber, and see the same purity of circular polarization. With linear polarization, we observe minimal change of contrast (i.e., minimal added ellipticity) and a rotation of less than 2°. It is possible that the two windows happen to cancel each other; however, the observed rotation is consistent with more careful measurements of a similar window [476]. They noticed significant variability across the window, which we did not consider. Our measurements, combined with theirs, suggest that the window contributes less than 1% to the observed circular polarization impurity, which would not cause the loss of contrast. In addition, we see in Figure 6.20 (as well as in other data sets) that the depletion fraction for inphase/inphase rises rapidly at first and then slowly rises. We attribute this slow rise to polarization ellipticity; comparing the time scale for the fast rise with the slow rise also suggests a 10% ellipticity.

Another explanation for above 50% depletion for inphase/inphase is poor selectivity in transfer. Because of the large, rapidly changing Doppler shifts from the rotating micromotion, any population in all the $m_F = \pm 1/2$ levels will also be depleted. We have used microwave spectroscopy between $J = 1$ and $J = 2$ to attempt to measure population in the other Stark pairs. We

have some indication of population in the closest Stark pair to the target pair, but the poor S/N in the microwave spectroscopy prohibited a quantitative comparison. In addition, while transferring for a shorter duration seemed to decrease the population in the other Stark pair when measured with microwave spectroscopy, it did not seem to improve the contrast, so more work is necessary to understand this. Based on the transfer spectrum in Figure 6.17, the Stark pairs should be well resolved at 16 V/cm, so we do not think that directly populating one of the other Stark pairs could account for the added population. Instead, it is possible that m_F level changing collision could occur when the trap is tight in the radial direction for transfer or there are additional coupling effects that we have neglected.

There are also several possible reasons for the $< 100\%$ total depletion. To address concerns of dark states or other coherent effects, we have measured depletion with the pulse rate $2 \times f_{\mathrm{rot}}$ (i.e., depleting both $+3/2$ and $-3/2$), with linear polarization, and with a pulse rate $f_{\mathrm{rot}}/10$ all with similar results. One possible scenario is that population excited to the $^3\Pi_{0^+}$ is decaying back to $^3\Delta_1$ and not being depleted. Based on the approximate electronic dipole matrix elements, we would expected $\sim$90% of the excited $^3\Pi_{0^+}$ population to decay back to $^3\Delta_1$. This population could decay to various vibrational states, with about 30% (the Franck-Condon factor) going to $v = 0$. Selection rules only allow decay from $^3\Pi_{0^+}$ $J = 1$ to $^3\Delta_1$ $J = 1$ or $J = 2$; ignoring degeneracy, we would expect something like 15% of the depleted population to return to each rotational level. Because most of the population that returns to $J = 1$ should be depleted again (except for population that returns to the opposite $m - F = \pm 3/2$ levels), this should not cause a problem. However, at high dissociation laser power (for the first dissociation step), we lose selectivity between $J = 1$ and $J = 2$ for readout, so population that returns to $J = 2$ may be detected, depending on power. If we are dissociating all of the population in $J = 2$, this would explain the undepleted fraction that we observe, and if the dissociation power is not constant, this could explain why the undepleted fraction seems to drift.

After preparing a single spin state, we pulse $\mathcal{E}_{\mathrm{rot}}$ to preform a $\pi/2$ pulse. Because the avoided crossing splitting (Δ) increases with decreasing $\mathcal{E}_{\mathrm{rot}}$, we can choose a value of $\mathcal{E}_{\mathrm{rot}}^{\pi/2}$ so that the

eigenstates are not the spin states (e.g., $|a\rangle$ and $|b\rangle$) but are instead nearly pure superpositions: $|a'\rangle = \frac{1}{\sqrt{2}}(|a\rangle + |b\rangle)$ and $|b'\rangle = \frac{1}{\sqrt{2}}(|a\rangle - |b\rangle)$. If we start with $|\psi\rangle = |a\rangle$, $|\psi\rangle \rightarrow \frac{1}{\sqrt{2}}(|a'\rangle + |b'\rangle)$ at $\mathcal{E}_{\mathrm{rot}}^{\pi/2}$. After a dwell time of $T_{\pi/2} \approx \frac{1}{4\Delta^{u/l}}$, $|\psi\rangle = \frac{1}{\sqrt{2}}(|a'\rangle + e^{-i\pi/2}|b'\rangle)$. Ramping back to the higher $\mathcal{E}_{\mathrm{rot}}$ gives $|\psi\rangle = e^{i\pi/4}|a\rangle + e^{-i\pi/4}|b\rangle$. We then allow the states $|a\rangle$ and $|b\rangle$ to evolve for a time τ over which they accumulate an additional phase shift, $\phi = \Delta E\tau/\hbar$. After this, we perform a second $\pi/2$ pulse, which maps the phase shift onto a population difference. One thing to note is that our $\pi/2$-pulses are not perfect because the magnetic field results in some detuning from the center of the avoided crossing which results in the eigenstates not being perfect superpositions. This is discussed in more detail in Section 6.6.4.

Finally, we measure the population in either $m_F = \pm 3/2$ after the second $\pi/2$ pulse using a second set of pulsed depletion either inphase or antiphase compared to the initial preparation followed by REMPD. We repeat the entire experimental cycle many times and chop between inphase and antiphase for the second depletion as well as no depletion (to measure the total transferred population in $^3\Delta_1$) and no transfer or depletion (to measure the background). By measuring as a function of time T between, we obtain a Ramsey fringe such as shown in Figure 6.19(d). The fractional population difference plotted on the y-axis is the difference between antiphase depletion and inphase depletion normalized to the difference between transfer and background.

We can measure the fringe frequency as a function of B', as shown in Figure 6.19(e) and (f) for the lower and upper doublet, respectively. These data clearly show the avoided crossing illustrated in Figure 6.19(b). We can extract the values of g_F for both doublets, which are indeed small as expected, as well as measure Δ for both doublets as a function of $\mathcal{E}_{\mathrm{rot}}$ [64, 65].

6.4.1 Sensitivity Estimates

The fringe shown in Figure 6.19(d) forms the basis for the eEDM measurement. We can estimate statistical sensitivity of the first generation of experiments using HfF^+ from Equation 6.6. Relevant parameters are given in Table 6.2 (updated with newer results compared to the fringe in Figure 6.19(d)). From this table, we project a shot-noise limited statistical sensitivity of 1×10^{-27}

e cm/$\sqrt{\text{day}}$ for the first generation measurement. This is of course only a rough estimate. In fact, using measurements in both doublets and for both signs of B should give a $\sqrt{4}$ improvement since each measurement contributes linearly to the eEDM signal (i.e., the total signal is $8d_e\mathcal{E}_{\text{eff}}$) and only increases the noise by $\sqrt{4}$. However, we have also neglected the time that would be necessary for measurements that don't relate directly to the eEDM signal (e.g., the transfer and dissociation background chops, monitoring fringe contrast, initial phase, etc.).

This table provides a good reference for considering how to further optimize the experiment. Many of the key inefficiencies (transfer efficiency, dissociation efficiency, fast loss, and depletion contrast) have been discussed above. A discussion of possible improvements towards a 10^{-29} e cm can be found in Section 6.8, first though, we turn our attention to optimizing τ.

6.5 Coherence Time

The primary motivation for using ions for a precision measurement is the possibility of a long free-evolution time, τ, because of the long possible coherence time. Of course here, like usual in experimental physics, it is not possible to escape Murphy's law. In fact, there are many potential sources of decoherence: in particular the lifetime of the states used in the measurement, collisions, and inhomogeneous fields.

6.5.1 Lifetime

The fundamental limit to the time of any measurement is the lifetime of the state or states used in the measurement, which can be set by several different factors. If both states participating in the Ramsey measurement decay to a third state at the same rate independent of each other and do not decay to each other, then the fringe contrast (normalized to the total number) does not decay; however, the signal-to-noise will decrease due to the loss of population. In the case of the metastable $^3\Delta_1$ $J = 1, v = 0$ state used in the eEDM measurement, the lifetime could be limited by spontaneous electronic decay or blackbody excitation of either rotation or vibration. Since the only electronic state below the $^3\Delta_1$ state electronic state is the $^1\Sigma^+$ state, we can write the decay

Table 6.2: Estimated statistical sensitivity of the first generation measurement using HfF^+

Parameter	Estimate
$\mathcal{E}_{\text{eff}}$	23.3 GV/cm
Total trapped HfF^+	3000
Detector open-area-ratio	63%
Percent in single J, m_J	35%
Fast loss	50%
Transfer efficiency to $^3\Delta_1$	35%
Depletion contrast	20%
Photodissociation detection efficiency	13%
Maximum fringe counts at $\tau = 0$	3
Free-evolution time (τ)	250 ms
Counts per shot (N) after τ	1
Background counts (N_0)	4
Contrast (N/N_0)	0.25
Duty cycle	50%
Rep rate	0.5 Hz
Fourier-limited linewidth ($1/2\pi\tau$)	640 mHz
δd_e (assuming a 10-hour day)	1×10^{-27} e cm/$\sqrt{\text{day}}$

rate of the lowest ro-vibrational state in the $^3\Delta_1$ manifold as [378]:

$$\begin{aligned}\Gamma_{el} = \tau_{el}^{-1} &= \sum_i A_{1i} = \frac{2e^2}{3\epsilon_0 h c^3} \sum_{v_i'} \left(\frac{\Delta E}{\hbar}\right)^3 \left|\langle \psi_{v_i}' | \mathbf{d} | \psi_{v_0} \rangle\right|^2 \\ &\approx \frac{2e^2}{3\epsilon_0 h c^3} \mu_{12}^2 \sum_{v_i'} \left(\frac{\Delta E}{\hbar}\right)^3 \left|\langle \chi_{v_i}' | \chi_{v_0} \rangle\right|^2\end{aligned} \tag{6.42}$$

where the A_{1i} is the Einstein A coefficient for each possible transition, the prime indicates $^1\Sigma^+$ states, ΔE is the energy difference, and $\mathbf{d}$ is the dipole moment operator. In the approximation, μ_{21} is the electronic transition dipole moment and $\left|\langle \chi_{v_i}' | \chi_{v_0} \rangle\right|^2$ is the vibrational wave function overlap (i.e., the Franck-Condon factor). Using the measured energy separation and calculated dipole moments (Table 5.6), we estimate the lifetime of $^3\Delta_1$ $v = 0$ to be about 2 s.

To estimate the blackbody excitation rate, we start with the number of photons-per-mode at a frequency ν for a blackbody spectrum at a temperature T

$$\bar{n} = \frac{1}{e^{\frac{h\nu}{k_B T}} - 1} \approx \frac{k_B T}{h\nu}, \tag{6.43}$$

where the approximation is valid for $h\nu >> k_b T$. For a two-level system, the blackbody excitation rate from the ground to excited state, Γ_{exc}, is related to the spontaneous emission rate from the excited state, Γ_{em}: $\Gamma_{ex} = \bar{n}\Gamma_{em}$. Γ_{em} can be obtained from Equation 6.42 with the sum over $^1\Sigma^+$ states replaced by $^3\Delta_1$ states. For rotational excitation from $J = 1 \rightarrow J = 2$, $\mu_{21} \approx d_{mf} = 1.4\ ea_0$ and the energy difference is $4B = 1.2$ cm^{-1}, so $\bar{n} \approx 174$ at 300 K and $\Gamma_{ex} \approx 0.0025$ s^{-1}. Thus the expected blackbody rotational excitation timescale at 300 K is ~800 s and so can be neglected.

For vibrational excitation from $v = 0 \rightarrow v = 1$, the energy difference is about 760 cm^{-1} so $\bar{n} \approx 0.027$ (here the approximation in Equation 6.43 is not valid). The dipole moment is a bit more complicated to approximate however. The transition dipole moment for a vibrational transition arises from the change in the molecular-frame dipole moment, $d_{mf}(R)$, with internuclear distance R. We can write $d_{mf}(R) \approx d_{mf}(R_0) + d_{mf}'(R_0)R + \cdots$, where R_0 is the internuclear distance at the minimum of the potential. Then $\mu_{12} = \langle \chi_{v_1} | d_{mf}(R) | \chi_{v_0} \rangle \approx d_{mf}'(R_0) \langle \chi_{v_1} | R | \chi_{v_0} \rangle$. The value of $d_{mf}'(R_0)$ can be approximated from [378] to be 1.2 $(ea_0)/a_0$. We can do the integral using harmonic

oscillator wavefunctions and obtain $\langle \chi_{v_1}|R|\chi_{v_0}\rangle = 1/\sqrt{2\alpha} = \sqrt{\frac{\hbar}{2\mu\omega}} \approx 3.6 \times 10^{-12}$ m. This gives a lifetime of $v = 1$ of 280 ms (which matches reasonably well with the previously calculated lifetime of 184 ms from [378]) and a blackbody vibrational excitation timescale of 10.4 s (6.8 ms using the calculated lifetime).

We have used state-resolved photodissociation to measure the $^1\Sigma^+$ $J = 0, v = 0$ lifetime as shown in Figure 6.9(a). The measured lifetime (ignoring the initial, fast collisional loss) of 7.1(8) s is shorter than the trap lifetime (i.e., total ion number decay) and matches well with the estimated blackbody vibrational excitation rate. By using coherent transfer and photodissociation, we can measure the lifetime of the $^3\Delta_1$ $J = 1, v = 0$ state to be 2.1(2) s as shown in Figure 6.9(b). This agrees with the predicted electronic lifetime of 2 s.

6.5.2 Field inhomogeneity

An field inhomogeneity that results in different fringe frequencies for different ions will result in a reduced coherence time. The fringe frequency in the eEDM is set, to first order, by the Zeeman splitting, $3g_F\mu_B B_{\mathrm{rot}}(\vec{R})$. Since $B_{\mathrm{rot}}(\vec{R}) \sim \left(\nabla_r \vec{B}(\vec{R})\right)\left(\mathcal{E}_{\mathrm{rot}}(\vec{R})\right)$, any spatial variability in $\mathcal{E}_{\mathrm{rot}}(\vec{R})$ or in $\nabla_r \vec{B}(\vec{R})$ can potentially lead to decoherence. Since the average position of any ion over the course of one measurement (i.e., many secular trap oscillations) is very close to the trap center, that is $\left\langle \vec{R} \right\rangle = 0$ to high precision, linear gradients in either $\mathcal{E}_{\mathrm{rot}}(\vec{R})$ or in $\nabla_r \vec{B}(\vec{R})$ will be averaged over to give $\langle \mathcal{E}_{\mathrm{rot}} \rangle = \mathcal{E}_{\mathrm{rot}}(0)$ (similarly $\langle \nabla_r B \rangle = \nabla_r B(0)$) for for every ion. Second-order gradients, however, will result in ions that have a larger $\left\langle R^2 \right\rangle$ (e.g., hotter ions) experiencing a different value of $\langle \mathcal{E}_{\mathrm{rot}} \rangle$ or $\langle \nabla_r B \rangle$ than ions that are, on average, closer to the trap center.

The coherence time limited by field inhomogeneity can be approximated as the time necessary for different ions to acquire 1 rad of phase difference. Since the field inhomogeneity results in a fractional frequency difference, the phase difference per period remains the same regardless of frequency, thus, the coherence time should be a fixed number of periods. For a fringe of frequency f, the coherence time can be estimated to be $\tau_{inhom} = \frac{1}{2\pi f \Delta f/f}$, where $\Delta f/f$ is the fractional inhomogeneity. In general, the fringe would not necessarily be expected to decay exponentially,

but instead would have a decay profile obtained from the time-averaged distribution of fringe frequencies. Frequently, this will result in a Gaussian decay profile $\sim e^{-t^2/\tau^2}$ [477]. We tried fitting the decay profile with a Gaussian form, but did not find any noticeable improvement in the quality of fit over a fit with a simple exponential decay. Since the decay constant from an exponential fit versus a Gaussian fit is typically similar [478, 479], we used exponential fits for all presented data.

Figure 6.21 shows several different measurements of the coherence time (from a singe exponential fit) as a function of fringe frequency. All data points are measured with less than 2000 ions and in a loose trap to reduce the effect of collisions. The dashed line shows the $1/f$ scaling due to inhomogeneity; the point at the lowest fringe frequency deviates significantly from the dashed line indicating that the coherence time is at least partially limited by collisions, see Section 6.5.3. The coherence time measured with a fringe frequency of 780 Hz is 48(7) ms, which implies a fractional inhomogeneity of about 0.5% over the size of the cloud.

The applied magnetic field gradient, combined with trapping fields, contributes to a decoherence similar to field inhomogeneity. This can be seen from the expression for B_{rot} from Equation 6.26. The second term in this equation gives the largest contribution to δB_{rot}. To estimate the decoherence, we assume a thermal distribution and replace $E_{x,y,z}$ with $k_B T \approx 10$ K. This gives $\delta B_{\mathrm{rot}}/B_{\mathrm{rot}} \approx 0.006$, which approximately matches the observed decoherence. Decoherence due to this effect can be reduced by decreasing ω_{rot}. This will result in a larger r_{rot}, so we can reduce B' for the same value of B_{rot}.

6.5.3 Collisions

Because of the long-range nature of Coulomb interactions, ion-ion collisions can be a major source of decoherence even in low density ion clouds. The primary concern with ion-ion collisions is the Berry's phase caused by the electric field of one ion tilting the quantization axis of the other ion. In this section we review the basics of ion-ion collisions and use this to obtain estimates for the coherence time.

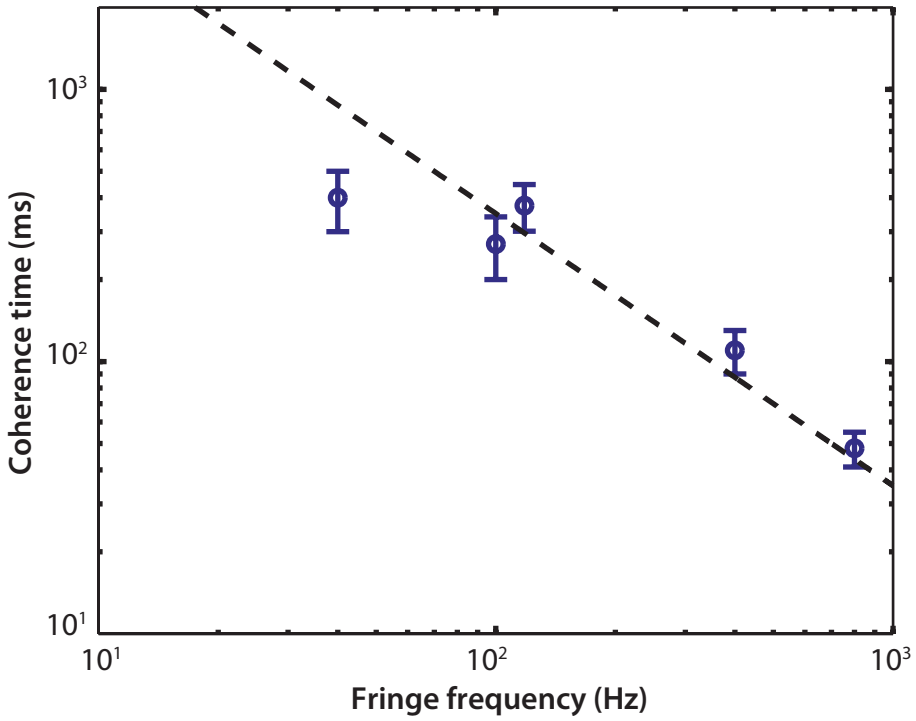

Figure 6.21: Coherence time versus fringe frequency. The dashed line is an approximate fit to a $1/f$ functional form, not including the lowest f point since this point is most likely limited by collisions, see Section 6.5.3.

6.5.4 Collision background

An ion-ion collision, often called a Rutherford collision, is usually treated as a one-body problem in the center-of-mass frame. In this setup, shown generically in Figure 6.22(a), a single particle with mass $\mu = m_1 m_2/(m_1 + m_2)$ is incident on a central Coulomb potential located at the center-of-mass of the two-body collision. The incident particle is offset from the collision axis by a distance b, called the impact parameter. After the collision, the particle is deflected by the Rutherford scattering angle, $\Delta\theta$. We can treat the collision in polar coordinates, (r, θ), and define $\hat{\theta} = 0$ as the direction opposite of the outgoing particle. With this definition, θ runs from $(\Delta\theta, \pi)$.

The incoming particle has angular momentum $L = \mu r^2\dot{\theta} = \mu v b$ and kinetic energy $U_{kin} = \frac{1}{2}\mu v^2 = \frac{L^2}{2\mu b^2}$. The total energy is $E = \frac{1}{2}\mu\dot{r}^2 + \frac{1}{2}\mu r^2\dot{\theta}^2 + V_c(r)$, where $V_c(r) = \frac{e^2}{4\pi\epsilon_0 r}$. We can use conservation of energy and angular momentum to obtain

$$\dot{\theta} = v\frac{b}{r^2} \tag{6.44}$$

and

$$\dot{r} = \pm v\sqrt{1 - \frac{b^2}{r^2} - \frac{V_c(r)}{U_{kin}}} = \pm v\sqrt{1 - \frac{b^2}{r^2} - A}. \tag{6.45}$$

Since $\dot{r}|_{r_{min}} = 0$, we can solve for

$$r_{min} = A + \sqrt{A^2 + b^2}. \tag{6.46}$$

The scattering angle can be related to the impact factor by relating the momentum change in y to the integral of the force:

$$\delta p_y = p_0 \sin(\Delta\theta) = \int_{-\infty}^{\infty} F_y dt = -\int_{\Delta\theta}^{\pi} F \sin\theta \frac{dt}{d\theta} d\theta =$$
$$-\frac{e^2}{4\pi\epsilon_0 r^2}\frac{r^2}{vb}\cos\theta\Big|_{\Delta\theta}^{\pi} = \frac{e^2}{4\pi\epsilon_0 vb}(1 + \cos\Delta\theta).$$

We can solve for b to obtain

$$b = \frac{e^2}{4\pi\epsilon_0 p_0 v}\frac{1 + \cos\Delta\theta}{\sin\Delta\theta} = \frac{A}{\tan\frac{\Delta\theta}{2}}. \tag{6.47}$$

Don't believe the last step? Brush up on your half-angle formulas here[2] since you will need them more later. Equation 6.47 can now be used to determine the differential scattering cross section. As

[2] http://mathworld.wolfram.com/Half-AngleFormulas.html

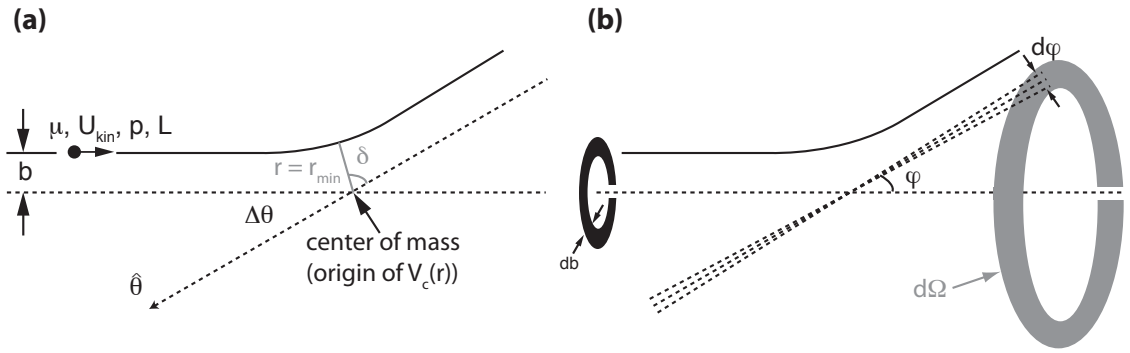

Figure 6.22: (a) Schematic of ion-ion collision treated as a single particle with mass equal to the reduced mass μ incident on a central (Coulomb) potential. The collision coordinates are (r, θ), where $\vec{r}$ is the position vector from the center of mass to the incoming particle and θ is the angle between $\hat{\theta}$ and $\hat{r}$, where $\hat{\theta}$ points opposite of the outgoing particle velocity. (b) Differential solid angle.

shown in Figure 6.22(b), the differential cross section relates the number of particles, dN', exiting in a differential solid angle $d\Omega$ to the total number of incoming particles, N, by

$$\frac{dN'}{d\Omega} = N\frac{d\sigma}{d\Omega}.$$

Since $dN' = N2\pi b db$ and $d\Omega = 2\pi \sin\varphi d\varphi$ we can solve for the differential cross section (using b from Equation 6.47)

$$\frac{d\sigma}{d\varphi} = \frac{b}{\sin\varphi}\left|\frac{db}{d\varphi}\right| = \left(\frac{A}{2}\right)^2 \frac{1}{\sin^4\frac{\varphi}{2}} = \left(\frac{e^2}{4\pi\epsilon_0}\right)^2 \frac{1}{16U_{kin}^2 \sin^4\frac{\varphi}{2}}. \tag{6.48}$$

The trajectory of the particle can be described by a hyperbola

$$r(\theta) = \frac{b^2}{A}\frac{1}{\varepsilon\cos(\theta+\delta)-1}. \tag{6.49}$$

Here $\varepsilon = \sqrt{1+\frac{b^2}{A^2}}$ is the eccentricity and δ is the angle at which $r = r_{min}$.

6.5.5 Coherence time from collisions

Now that we have the basic collision theory under our belts, we can go on to look at how collisions limit the coherence time. As mentioned above, the effect of an ion-ion collision is to introduce an electric field that will add with the rotating electric field and tilt the quantization axis. Over the course of the collision, the electric field vector traces a closed path on the surface of a sphere. For example, the collision trajectory shown in Figure 6.23(a) with $\mathcal{E}_{\text{rot}}$ perpendicular to the collision plane results in the path illustrated in 6.23(b). This trajectory was generated by Equation 6.49 and then the net electric field vector was generated for points along the trajectory by summing $\mathcal{E}_{\text{rot}}$ and the electric field from the ion-ion interaction:

$$\mathcal{E}_{ion-ion} = \frac{e^2}{4\pi\epsilon_0 r_{min}^2}.$$

The solid angle, $\mathcal{A}$, enclosed by this path results in a Berry's phase from the collision of $\Delta\phi_b = \Delta m_F \mathcal{A}$, where $\Delta m_F = 3$ for ions that are in a superposition of $m_F = \pm 3/2$ levels. This phase then leads to decoherence, either from a single collision if the phase is large enough or from phase diffusion after multiple collisions.

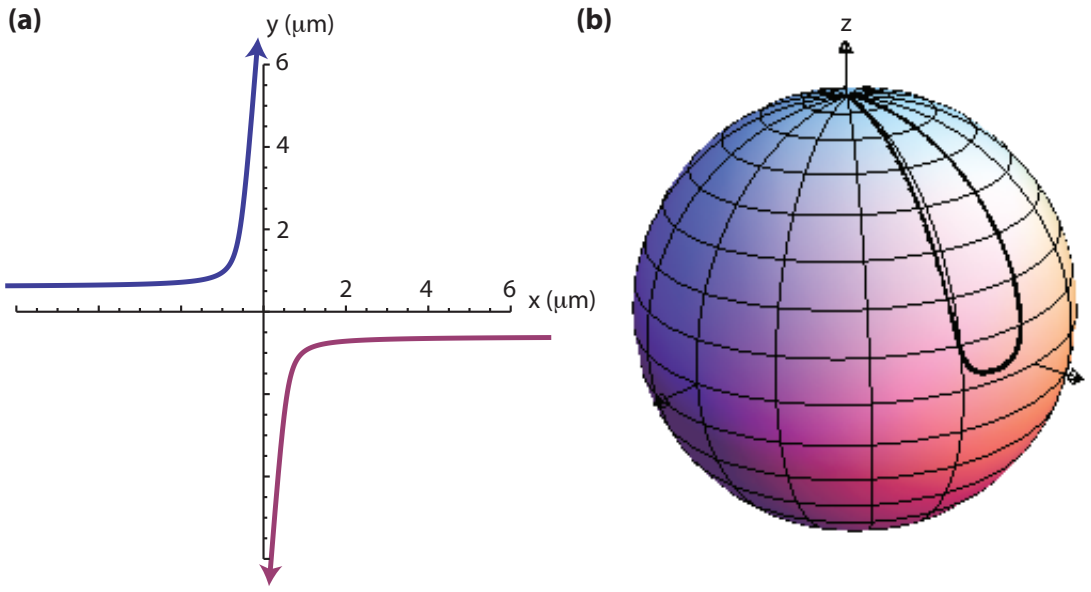

Figure 6.23: (a) Collision trajectory for two particles in the xy plane. (b) The path of $\mathcal{E}_{tot}$ is shown as a dark curve for the collision trajectory shown in (a). $\mathcal{E}_{\rm rot}$ is assumed to point along z. The area of this closed path is the solid angle, $\mathcal{A}$, which leads to a Berry's phase $\Delta\phi_b = \Delta m_F \mathcal{A}$ for this collision.

The rate of collisions, Z, for a collisional process is given by $Z = n\sigma v$, where n is the density, σ is the collision cross section, and v is the velocity. Since σ can be thought of as an area for a hard-sphere collision σv is a volume per unit time that a single particle covers; thus the value of Z gives the number of collisions per unit time. The rate of decoherence, Γ, then is given by Z/N_d, where N_d is the number of collisions required for decoherence. A reasonable assumption would be that decoherence occurs when the total accumulated phase is equal to π, i.e., $N_d = \pi^2/(\Delta\phi_b)^2$ for a random-walk phase diffusion.

We now have all of the tools necessary to numerically estimate the collisionally limited coherence time. Initially we assume that all collisions lie in the plane perpendicular to $\mathcal{E}_{\text{rot}}$ since this should represent the worst case scenario. We first calculate the solid angle for a given scattering angle by numerically integrating to find the area enclosed by the path of the unit electric field vector:

$$\mathcal{A}(\Delta\theta, U_{kin}) = \iint_A \sin\phi d\phi d\theta = \int_{\Delta\theta}^{\pi} \sin\phi(\varphi)\frac{d\phi}{d\varphi}d\varphi \int_{\theta_{min}(\phi)}^{\theta_{max}(\phi)} d\theta, \tag{6.50}$$

where $\phi(\varphi)$ and $\theta(\varphi)$ are the polar angles of $\hat{\mathcal{E}}_{tot}$ as a function of angle during the collision. Figure 6.24 shows plots of $\mathcal{A}(\Delta\theta)$ for different values of U_{kin}. Putting everything together, we have that

$$\Gamma(U_{kin}) = \frac{Z}{N_d} = Z\frac{(\Delta\phi_b)^2}{\pi^2} = n\sigma(\Delta\theta, U_{kin})v(U_{kin})\frac{\Delta\phi_b^2(\Delta\theta, U_{kin})^2}{\pi^2}. \tag{6.51}$$

We can now use the differential cross section from Equation 6.48, substitute $\Delta\phi_b = \Delta m_F \mathcal{A}$, assume that $v = 2\sqrt{k_b T/m}$, and integrate over possible scattering angles to obtain the decoherence rate as a function of collision energy. The coherence time (inverse of Equation 6.51) is shown in Figure 6.25 for 20,000 ions with our measured trap parameters and different values of $\mathcal{E}_{\text{rot}}$.

In addition to the numerical results, it is instructive to obtain some general scaling rules. In particular, the "big paper" [62] has some approximate formulas that appear out of no-where, can we reproduce the scaling in these? First, we will need to find the maximum electric field experienced during the collision, $\mathcal{E}_{ion-ion}\big|_{r=r_{min}}$. After substituting r_{min} from Equation 6.46 and then b from

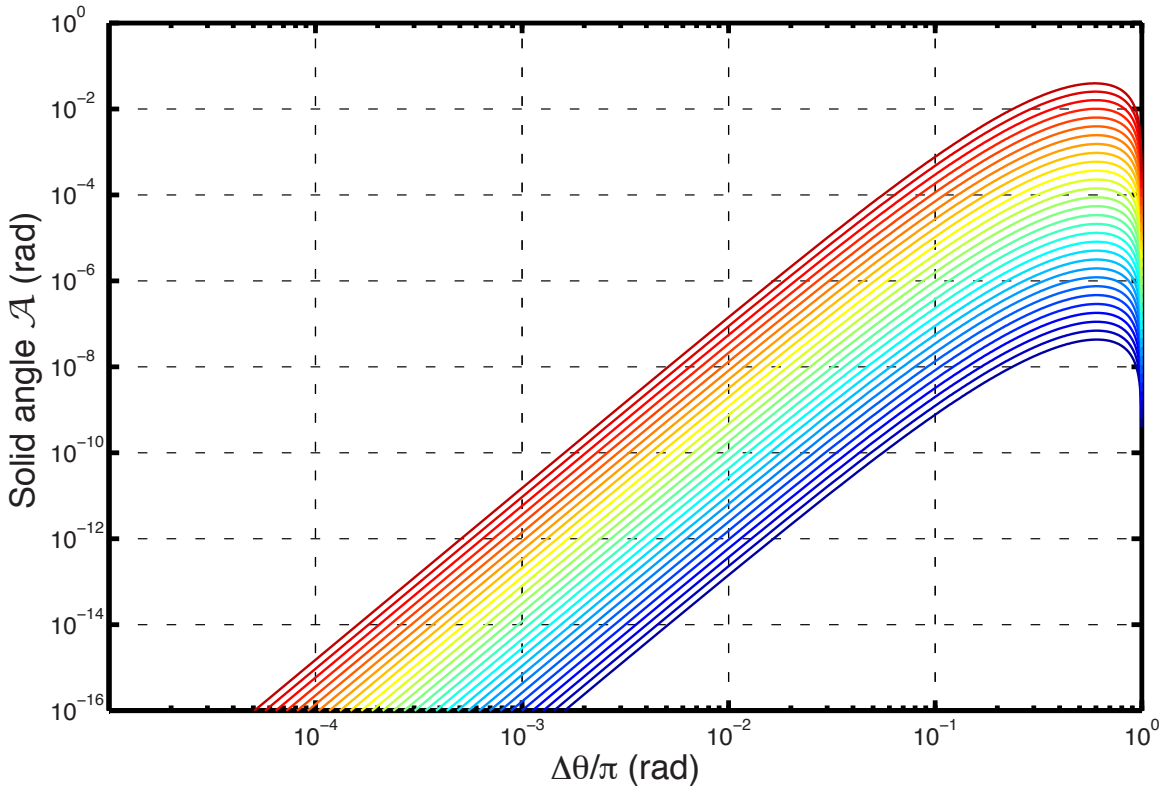

Figure 6.24: Log-log plot of $\mathcal{A}$ as a function of scattering angle for different values of U_{kin}/k_B ranging from 0.3 K to 10 K with $\mathcal{E}_{\rm rot} = 10$ V/cm. For small scatting angles, $\mathcal{A} \sim U_{kin}^4$.

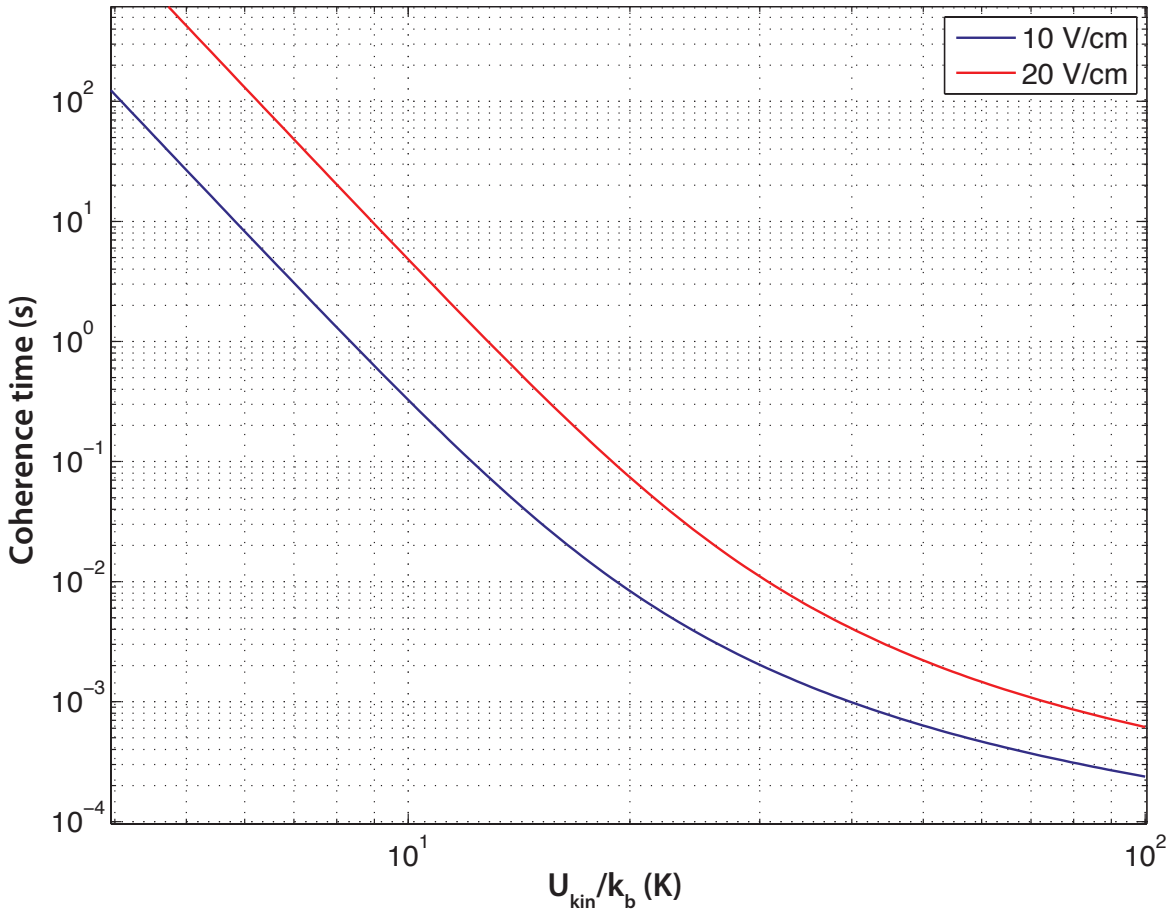

Figure 6.25: Log-log plot of estimated coherence time as a function of collision energy (in temperature units) for $\mathcal{E}_{\rm rot} = 20$ V/cm (red) and 10 V/cm (blue). These calculations are expected to give the worst-case coherence time as discussed in the text. The calculated curves are for 20,000 ions in the normal trap given in Table 6.1.

Equation 6.47 and finally using seemingly random combinations of half-angle formulas we find that

$$\mathcal{E}_{ion-ion}^{max}(\Delta\theta) = \frac{4\pi\epsilon_0}{e^3} 4U_{kin}^2 \left(\frac{\sin\frac{\Delta\theta}{2}}{1+\sin\frac{\Delta\theta}{2}} \right)^2 \sim T^2. \tag{6.52}$$

For small values of $\mathcal{E}_{ion-ion}^{max}$ the solid angle can be approximated by

$$\mathcal{A} \approx \frac{\pi\mathcal{E}_{\perp}^2}{\mathcal{E}_{\text{rot}}^2}, \tag{6.53}$$

where $\mathcal{E}_{\perp}$ is the component of the electric field perpedicular to $\mathcal{E}_{\text{rot}}$. Another approximation that works in more limits is

$$\mathcal{A} \approx \frac{\pi-\Delta\theta}{2}\left(1 - \frac{\mathcal{E}_{\text{rot}}}{\sqrt{\mathcal{E}_{\text{rot}}^2+\mathcal{E}_{ion-ion}^2}}\right) \approx \frac{\pi-\Delta\theta}{2}\frac{\mathcal{E}_{ion-ion}^2}{2\mathcal{E}_{\text{rot}}^2} \sim \frac{T^4}{\mathcal{E}_{\text{rot}}^2}, \tag{6.54}$$

where in the second step we have assumed $\mathcal{E}_{ion-ion} < \mathcal{E}_{\text{rot}}$. From Equation 6.48, we see that the $\frac{d\sigma}{d\varphi} \sim U_{kin}^{-2} \sim T^{-2}$. Since $v \sim T^{1/2}$ we see that

$$\Gamma \sim nT^{-2}\left(\frac{T^4}{\mathcal{E}_{\text{rot}}^2}\right)^2\sqrt{T} \sim nT^{13/2}\mathcal{E}_{\text{rot}}^{-4} \tag{6.55}$$

for low collision energies.

In the high collision energy limit, there is a high probability for a single collision to result in a Berry's phase $\sim \pi$, which would lead to decoherence. For a single collision to result in enough phase shift, we need to have $\mathcal{E}_{ion-ion} \sim \mathcal{E}_{\text{rot}}$. This implies that the distance of closest approach must be

$$r_{min}^2 \approx \frac{e^2}{4\pi\epsilon_0\mathcal{E}_{\text{rot}}}. \tag{6.56}$$

We can use the standard hard-sphere collision rate, $\Gamma = n\sigma v$, with $\sigma = \pi r^2$ and $r^2 = r_{min}^2 \sim \mathcal{E}_{\text{rot}}^{-1}$ to arrive at the high-energy scaling

$$\Gamma \sim n\mathcal{E}_{\text{rot}}^{-1}\sqrt{T}. \tag{6.57}$$

These two limits can be seen in Figure 6.25.

We have measured the coherence time as a function of ion number and as a function of $\mathcal{E}_{\text{rot}}$ as shown in Figure 6.26. Taken together, these measurements provide strong evidence for ion-ion collisions. Figure 6.26(a) shows the measured coherence time as a function of ion number as well

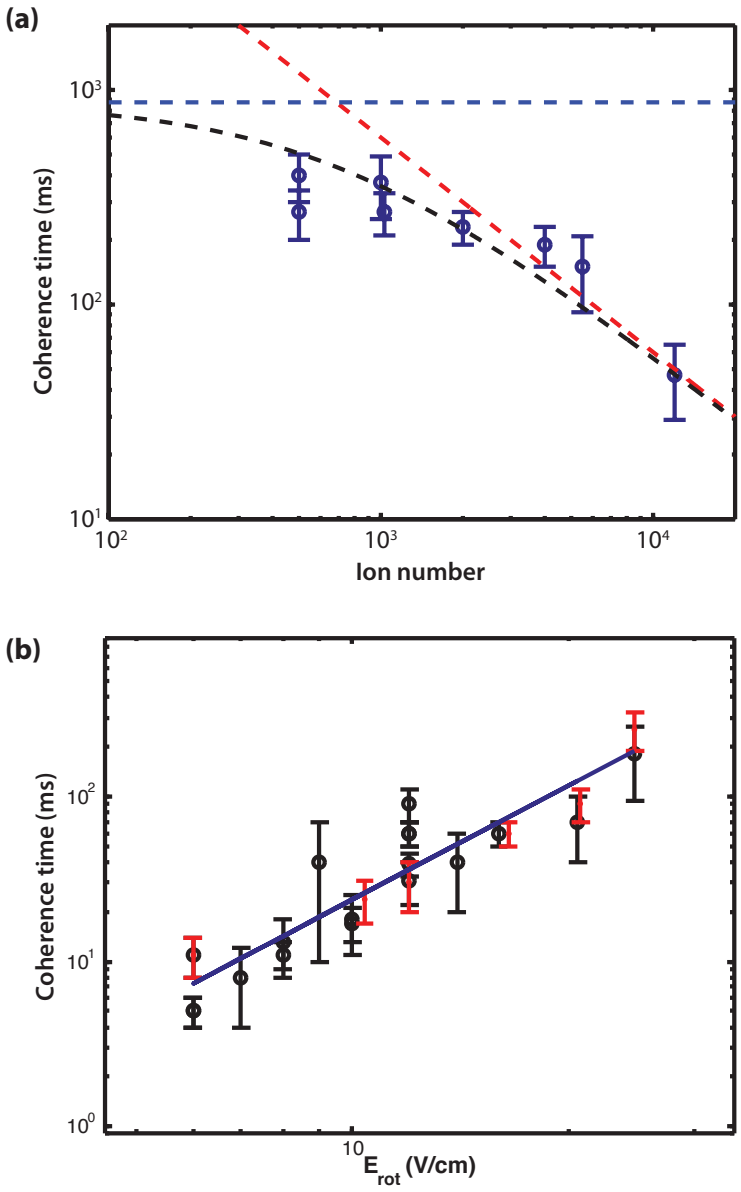

Figure 6.26: Coherence time versus ion number and $\mathcal{E}_{\rm rot}$. (a) Log-log plot of coherence time as a function of total ion number. The red dashed line shows the expected $1/n$ scaling (assuming that the density changes linearly with ion number, i.e., that the trap volume is constant). The blue dashed line is the expected coherence time due to field inhomogeneity for a 40 Hz fringe frequency. The black dashed line is the combined contribution from both sources: $1/\tau = 1/\tau_{coll} + 1/\tau_{inhom}$. (b) Log-log plot of various coherence time measurements as a function of $\mathcal{E}_{\rm rot}$. The coherence time would be expected to scale like $\mathcal{E}_{\rm rot}^{p}$, where p is between 1 and 4 (see Equations 6.56 and 6.57). The blue line is a fit to this scaling, which gives $p = 2.3$.

as the expected $1/n$ dependence (red dashed line), the inhomogeneity limit for a 40 Hz fringe frequency (blue dashed line), as well as the combined limit (black dashed line). The ion number was changed primarily by adjusting the power of the second ionization laser and has been corrected by the open-area ratio of the MCP to reflect the total ion number in the trap. We assume that the density scales linearly with the ion number; that is, we assume that the trap volume does not change when the ion number changes. This assumption is reasonable as long as mean-field effects do not get too large and as long as the ionization laser power do not significantly affect the temperature. The $1/n$ dependence to the coherence time shown by the red dashed line is manually adjusted to the match the highest ion number point.

As the ion number is decreased, the coherence time begins to deviate from the $1/n$ dependence. The measurements with low ion number were all taken at a fringe frequency of 40 Hz, which contributes to the coherence time limit as shown by the blue dashed line. The black dashed line shows the coherence time limit estimated by combining these two sources of decoherence. In general, this combination is done by multiplying the decay from each source of decoherence. If each source is treated as a simple exponential decay (this is not true in general for inhomogeneity but is a good approximation, see Section 6.5.2), the decoherence rates add linearly, so $1/\tau_{tot} = 1/\tau_{coll} + 1/\tau_{inhom}$, if we just consider inhomogeneity and collisional decoherence. This gives the black dashed line in Figure 6.26, which matches well with the data.

Figure 6.26(b) shows the dependence of the coherence time on $\mathcal{E}_{\text{rot}}$. These measurements were taken under a variety of conditions and have been corrected for ion number changes. All of the data are fit to a power lower, $\mathcal{E}_{\text{rot}}^{p}$, yielding $p = 2.3$ (blue line). This is consistent with the expected range of $p = 1 - 4$ from Equations 6.56 and 6.57.

We can compare the numerical results shown in 6.25 with the data in 6.26. With 20,000 ions in the trap, we measure a coherence time of 48(7) ms. Using the normal trap parameters given in Table 6.1, this corresponds to about 1×10^7 ions/cm^3. If we use a trap temperatures of 20 K and $\mathcal{E}_{\text{rot}} = 20$ V/cm, the numerical estimates give a worst-case coherence time of 60 ms and $p \approx 3$. If instead we use the a temperature of 30 K, we would expect a worst-case coherence time of 10 ms

and $p \approx 2.3$. Overall, the numerical estimates are in reasonable agreement with the data. We have also decreased the trap temperature as discussed in Section 6.2.1 ("relaxed + ramp" in Table 6.1) and measured an improved coherence time of 270(80) ms with 20,000 ions and 390(90) ms with 10,000 ions, which is an improvement by a factor of roughly 5.

6.6 Systematic Errors

Of course, you might be wondering,"what about Berry's phase?" or perhaps more generally, "don't you expect some killer systematic error?" Well, let me ease your concerns a bit and let you know that, while crazy, we are not actually crazy enough to do an experiment where we expect a major systematic above the 10^{-28} e cm level. If this is enough to convince you, then you can skip the rest of this section since we will now discuss in detail potential sources of systematic errors.

The first step in determining possible sources of systematic errors is to identify all of the dependences of the measurement signal. The eEDM experiment basically amounts to measuring energy splitting (in our case, actually the unsigned frequency difference) between either the upper or lower pair of $m_F = \pm 3/2$ states. We can write the Hamiltonian for these two states in the upper (u) or lower (l) doublet as

$$H = \hbar \begin{pmatrix} -\frac{3}{2} g_f^{u/l} \mu_B B_{\rm rot} \pm d_e \mathcal{E}_{\rm eff} + \frac{3}{2}\alpha\omega_{\rm rot} & \frac{\Delta^{u/l}}{2} \\ \frac{\Delta^{u/l}}{2} & \frac{3}{2} g_f^{u/l} \mu_B B_{\rm rot} \mp d_e \mathcal{E}_{\rm eff} - \frac{3}{2}\alpha\omega_{\rm rot} \end{pmatrix}. \tag{6.58}$$

The diagonal elements of this matrix contain the Zeeman splitting, eEDM contribution (where the upper (lower) sign refer to the upper (lower) doublet), and the energy shift due to a periodic Berry's phase caused by a tilt of the quantization by an angle α from the horizontal plane. Recall that, because of the way we generate the rotating magnetic field, $B_{\rm rot} \approx B' r_{\rm rot} \approx B' \frac{e\mathcal{E}_{\rm rot}}{m\omega_{\rm rot}^2}$. The off-diagonal components are caused by the coupling in the rotating field, as discussed in Section 6.4. Since Δ is different in the upper and lower doublet, we can define $\Delta^{u/l} = \bar{\Delta} \pm \delta\Delta$ [62, 64]:

$$\begin{aligned} \bar{\Delta} &= \frac{\Delta^u + \Delta^l}{2} \approx 27\omega_{ef} \left(\frac{\hbar\omega_{\rm rot}}{d_{mf}\mathcal{E}_{\rm rot}}\right)^3; \\ \delta\Delta &= \frac{\Delta^u - \Delta^l}{2} \approx \frac{81}{8}\omega_{ef} \left(\frac{\hbar\omega_{\rm rot}}{d_{mf}\mathcal{E}_{\rm rot}}\right)^3 \left(\frac{d_{mf}\mathcal{E}_{\rm rot}}{E_{HF}}\right)^2 \approx \frac{1}{3}\left(\frac{d_{mf}\mathcal{E}_{\rm rot}}{E_{HF}}\right)^2 \bar{\Delta}. \end{aligned} \tag{6.59}$$

To get the frequency difference $f^{u/l}$, we diagonalize the Hamiltonian and take the difference between the eigenvalues, making use of the approximation $\sqrt{a^2+b^2} \approx a + \frac{b^2}{2a}$ for $b << a$:

$$\begin{gathered} 2\pi f^{u/l}(\mathcal{E}_{\rm rot}, B_{\rm rot}, \omega_{\rm rot}, \alpha) = \\ 3g_F^{u/l}\mu_B B_{\rm rot} \pm 2d_e\mathcal{E}_{\rm eff} - 3\alpha\omega_{\rm rot} + \frac{(\Delta^{u/l})^2}{6g_F^{u/l}\mu_B B_{\rm rot}} + \frac{6\alpha\omega_{\rm rot}(\Delta^{u/l})^2}{(6g_F^{u/l}\mu_B B_{\rm rot})^2}, \end{gathered} \tag{6.60}$$

where the Zeeman splitting is assumed to be much larger than any of the other terms. In addition, we assume that trap motion results in $\langle\alpha\rangle \approx 0$. A very rough eEDM measurement could then be made by measuring $\langle f^u(\mathcal{E}, B)\rangle - \langle f^l(\mathcal{E}, -B)\rangle \approx 4d_e\mathcal{E}_{\rm eff}$; however this will be ruined by an imperfect B reversal, as well as other deviations from our initial assumptions. So our goal is to find out how much of an effect deviations have and how we can minimize the impact: in particular, we consider the effects due to non-reversing B (e.g., from stray fields), magnetic fields perpendicular to the quantization axis $B_\perp$, shifts in $\mathcal{E}_{\rm rot}$, and field inhomogeneities. We also briefly discuss any potential systematics arising from state preparation or readout issues. A summary of systematic effects is given in Table 6.3.

6.6.1 Non-reversing magnetic field

A non-reversing magnetic field, B^{nr}, will cause a systematic in the simple B reversal:

$$f^u(\mathcal{E}, B + B^{nr}) - f^u(\mathcal{E}, -B + B^{nr}) \approx 4d_e\mathcal{E}_{\rm eff} + 6g_F^u\mu_B B^{nr}, \tag{6.61}$$

where we have removed the time averaging for simplicity. To reduce this systematic, we can combine a B switch with a doublet switch, which gives

$$f^u(\mathcal{E}, \pm B + B^{nr}) - f^l(\mathcal{E}, \pm B + B^{nr}) \approx \pm 4d_e\mathcal{E}_{\rm eff} + 6\delta g_F\mu_B(B \pm B^{nr}), \tag{6.62}$$

where $\delta g_F = g_F^u - g_F^l$. This final four-way difference

$$f_{\rm edm} = [f^u(B) - f^l(B)] - [f^u(-B) - f^l(-B)] = 8d_e\mathcal{E}_{\rm eff} + 12\delta g_F\mu_B B^{nr}, \tag{6.63}$$

so the effect of B^{nr} is suppressed by the value of $\delta g_F/g_F$. The difference in g_F arises from two contributions [62, 468]:

Table 6.3: Systematic error summary. The first column lists different contributions to the four-way difference, f_{edm}. The next three columns give the sign of the contribution for each of the doublet, applied B', and rotation direction switch. Here + indicates that the contribution does not change sign and − indicates a sign reversal under the switch. Columns 4-6 give the power-law dependence of each effect as a function of the values of $|B'|$, $\omega_{\rm rot}$, and $|\mathcal{E}_{\rm rot}|$. Finally, the final estimated systematic contribution is given in column 7. These assume a fringe frequency ($3g_F\mu_B B_{\rm rot}$)of 40 Hz. See text for more details.

	Switch			Dependence			Est. Contribution
Effect	Doublet	B'	Rot.	$\lvert B'\rvert$	$\omega_{\rm rot}$	$\lvert\mathcal{E}_{\rm rot}\rvert$	to f_{edm}
d_e ($< 3\times10^{-29}$ e cm)	-	-	+	0	0	0	1 mHz
B^{nr} (switch)	+	-	+	0	0	0	0.6 mHz
B^{nr} (leakage)	+	-	-	0	1	1	0.6 mHz
$\frac{\partial\mathcal{E}_{\rm rot}}{\partial z}$	+	-	-	0	1	-1	1 mHz
Motional Fields	+	-	-	0	-3	1	4 μHz
$\delta\Delta$	-	+	+	0	6	-4	$\sim$0
$\delta\frac{\langle B\cdot\mathcal{E}\rangle}{\lvert\mathcal{E}\rvert}$	+	+	+	1	0	-1	40 μHz
$B_\perp$	+	+	-	0	1	-1	2 μHz

(1) mixing of the Stark levels in $J = 1$ with levels in $J = 2$, $\frac{\delta g_{F=3/2}}{g_{F=3/2}} \approx \frac{9 d_{mf} \mathcal{E}_{\rm rot}}{40 hcB_e}$;

(2) rotation-induced mixing of $\Delta m_F = \pm 1$ levels that is different for the upper and lower Stark pair because the separation to the $m_F \Omega = \pm 1/2$ pairs is different, $\frac{\delta g_{F=3/2}}{g_{F=3/2}} \approx \frac{\sqrt{6}\omega_{\rm rot}^2}{\gamma_{F=3/2}^2 d_{mf} \mathcal{E}_{\rm rot} E_{hf}}$.

These two contributions are expected to be (1) 9.1×10^{-4} and (2) 8.6×10^{-4} for a maximum total contribution of 1.8×10^{-3}. These assume that $3 g_F \mu_B B >> \Delta$, if this is not true then $\delta\Delta$ will also contribute to an apparent δg_F. Our current best measurement is $\frac{\delta g_{F=3/2}}{g_{F=3/2}} = 0.003(6)$.

There are several potential sources of B^{nr}, the most obvious of which is poor reversal of the applied B-field gradient. By using current monitors on the anti-Helmholtz coils and/or several magnetometers, we should be able to reverse B' to 1%. This systematic is at most $12 \delta g_F \mu_B B^{nr}$ out of a fringe frequency of $3 g_F \mu_B B_{\rm rot}$, i.e., $\frac{\delta f}{f} \approx 4 \frac{\delta g_F}{g_F} \frac{B^{nr}}{B_{\rm rot}} \approx 1 \times 10^{-4}$. This corresponds to a systematic of 2 mHz for a 20 Hz fringe, which gives an error of 3×10^{-29} e cm. Another source of B^{nr} arises from leakage current in the trap electrodes that oscillates at $\omega_{\rm rot}$. Such a leakage current arises due to capacitance C in the electrodes, which results in an oscillating current $I_{leak}^{max} = \frac{V_{pp}}{2} C \omega_{\rm rot}$ for a peak-peak voltage V_{pp}. We have measured the capacitance of a single electrode plus SHV feedthroughs to be about 40 pF (the electrode itself is estimated to be $\sim$2 pF); if we assume that this capacitance all contributes to a current that flows through the electrode (worst case), this gives a maximum current of 8 mA for $V_{pp} = 250$ V (corresponding to $\mathcal{E}_{\rm rot} = 20$ V/cm) and $\omega_{\rm rot} = 2\pi \times 250$ kHz. The magnetic field at a distance $r = 4$ cm from a wire with current I is $\frac{\mu_0 I}{2\pi r}$, so each electrode produces a peak contribution of 400 μG at the trap center. The total contribution from all electrodes is three times the peak contribution from a single electrode, so $B_{leak}^{nr} < 1.2$ mG, which contributes at most 15 Hz to the Zeeman splitting and a systematic of 0.2 Hz to the four-way difference (Equation 6.63). This contribution assumes that all the electrodes are driven from one direction only and assumes the worst case capacitance. We have switched to driving the electrodes symmetrically from the top and bottom, which suppresses the leakage currents dramatically. A reasonable estimate in this case is that the currents from the top drive balance those from the bottom drive to better than 10%, which reduces the systematic to $<$ 15 mHz or 3×10^{-28} e cm.

This effect will also depend on the value of $\mathcal{E}_{\rm rot}$, so should be detectable. A final contribution to B^{nr} would be a stray magnetic field gradient. This would originate most likely from magnetism in a material, such as the welds in the vacuum chamber or from the optical table: since all material, especially welds, is located a large distance from the trap, stray gradients are expected to be small. If we assume a stray gradient of 2 mG/cm, the resulting systematic is around 12 mHz.

All of the estimates in the previous paragraph assume that we do no active shimming of B^{nr}. A simple potential shim procedure would be to apply a compensation value of B^{nr} to make $f^u(B) - f^u(-B) \approx 6 g_F^u \mu_B B^{nr} = 0$. Then a measurement in the lower doublet would provide a measurement of $4 d_e \mathcal{E}_{\rm eff}$ with a systematic of $6 \delta g_F \mu_B B^{nr}$. A shim of $f^u(B) - f^u(-B) < 100$ mHz would make $B^{nr} < 4$ μG, which then contributes a systematic of 0.6 mHz or 3×10^{-29} e cm. A 100 mHz precision will hopefully only require perhaps 10 minutes of measurement time (assuming that we are at the desired statistical sensitivity of 10^{-29} in a day!), so such a shim would not be too hard to implement. There are several potential issues however with this simple shimming procedure. One concern is a time dependence of B^{nr}; since we can monitor the reversal of the applied B-field gradient at this level (see previous paragraph), the only concern is changes in the leakage current contributions. Other than possible slow temperature-dependent changes, these currents should be static between a shim measurement in one doublet and an eEDM measurement in the other doublet. Another potential issue is a value of B^{nr} that correlates with the doublet. Since the doublet switch is set by a laser detuning, it is hard to come up with a likely source of correlation.

6.6.2 Perpendicular magnetic fields

Because the quantization axis rotates rapidly, static magnetic fields in the xy plane quickly average to zero. However, a magnetic field that is perpendicular to the quantization axis – in this case an axially oriented magnetic field – will not completely average to zero. The effect of such a

$B_\perp$ is to tilt the quantization axis, which will cause a non-zero Berry's phase. The tilt angle,

$$\alpha \approx \frac{\frac{3}{2} g_F^{u/l} \mu_B B_\perp}{\frac{3}{2}\gamma_F d_{mf} \mathcal{E}_{\rm rot} + \frac{3}{2} g_F^{u/l} \mu_B B_{\rm rot}}, \tag{6.64}$$

contributes $3\omega_{\rm rot}\alpha$ to $f^{u/l}(B_{\rm rot})$. A value of $B_\perp = 0.5$ G contributes 130 Hz to a measurement of $f^{u/l}(B_{\rm rot})$. This is mostly removed in a B switch:

$$\begin{aligned} f^{u/l}(B_{\rm rot}) - f^{u/l}(-B_{\rm rot}) &\approx 3\frac{\omega_{\rm rot}}{2\pi}\left[\frac{g_F^{u/l}\mu_B B_\perp}{\gamma_F d_{mf}\mathcal{E}_{\rm rot} + g_F^{u/l}\mu_B B_{\rm rot}} - \frac{g_F^{u/l}\mu_B B_\perp}{\gamma_F d_{mf}\mathcal{E}_{\rm rot} - g_F^{u/l}\mu_B B_{\rm rot}}\right] \\ &\approx 6\frac{\omega_{\rm rot}}{2\pi}\frac{(g_F^{u/l})^2\mu_B^2 B_\perp B_{\rm rot}}{(\gamma_F d_{mf}\mathcal{E}_{\rm rot})^2}. \end{aligned} \tag{6.65}$$

The contribution in the four-way difference is further reduced by the difference in g factors, so

$$f_{\rm edm}^{B_\perp} = 6\frac{\omega_{\rm rot}}{2\pi}\frac{\left[(g_F^u)^2 - (g_F^l)^2\right]\mu_B^2 B_\perp B_{\rm rot}}{(\gamma_F d_{mf}\mathcal{E}_{\rm rot})^2} = 6\frac{\omega_{\rm rot}}{2\pi}\frac{2\bar{g}_F \delta g_F \mu_B^2 B_\perp B_{\rm rot}}{(\gamma_F d_{mf}\mathcal{E}_{\rm rot})^2} \approx 2\mu{\rm Hz}. \tag{6.66}$$

6.6.3 Field inhomogeneity

As mentioned earlier, trap motion results in $\langle\alpha\rangle \approx 0$, where α is the tilt angle of the quantization axis from the plane perpendicular to the rotation axis. This is because the average axial electric field experienced by an ion oscillating in the trap is zero since the ion is assumed to be stably trapped. Thus, the Berry's phase acquired in one-half of an axial cycle (e.g., for $z > 0$) cancels the phase from the other half-cycle ($z < 0$). However, this is not true if there is an axial gradient to $\mathcal{E}_{\rm rot}$ such that $\mathcal{E}_{\rm rot}(z > 0) \neq \mathcal{E}_{\rm rot}(z < 0)$. Since $\alpha \approx \mathcal{E}_z/(\mathcal{E}_{\rm rot} + \delta\mathcal{E}_{\rm rot})$, where $\delta\mathcal{E}_{\rm rot}$ is the (average) added contribution to $\mathcal{E}_{\rm rot}$ for $z > 0$, we can write the energy shift as $m_F\omega_{\rm rot}\frac{\mathcal{E}_z}{\mathcal{E}_{\rm rot}^2}2\delta\mathcal{E}_{\rm rot}$. At a distance $z = 0.5$ cm, $\mathcal{E}_z = \frac{m\omega_z^2 z}{4e} \approx 1$ V/cm. If we assume $\delta\mathcal{E}_{\rm rot}/\mathcal{E}_{\rm rot} \sim 0.5\%$ (the worst case limit from the measured inhomogeneity) and a typical value of $\mathcal{E}_{\rm rot} = 20$ V/cm, the energy shift would be expected to be around $2\pi \times 0.2$ Hz. This almost entirely cancels in a doublet switch, $f^u(B) - f^l(B)$, except for a term that goes as $\frac{(\Delta^u)^2 - (\Delta^l)^2}{(6g_F^{u/l}\mu_B B_{\rm rot})^2} \sim 0.01$, which would give a systematic of 2 mHz or 5×10^{-29} e cm. If we do a B switch first, then the shift does not cancel, and $f^u(B) - f^u(-B) \sim 0.4$ Hz. This would then be shimmed out, leading to a systematic in the four-way difference of $\delta g_F/g_F \times 0.4$ Hz or about 1 mHz (3×10^{-29} e cm). We can change the sign of the Berry's phase contribution by changing the rotation direction. In addition, the Berry's phase

should scale with $\mathcal{E}_{\rm rot}$ as well as $\omega_{\rm rot}$, so should be noticeable. Finally, we could attempt to measure this shift by kicking the ions and looking for a frequency shift.

The magnetic field gradient also causes a shift in $B_{\rm rot}$ according to Equation 6.26. This same effect contributes to decoherence as discussed in Section 6.5.2. All terms in Equation 6.26 depend linearly on B', so the frequency shift will be the same sign for both signs of $B_{\rm rot}$. Therefore, this shift should cancel to a high degree in the B switch. The largest residual effect arises due to the presence of B^{nr}. In particular, if the current in the electrodes causes a B^{nr} that we shim with a deliberately applied B'_{nr}, then this systematic shift will be different for the two signs of $B_{\rm rot}$. We can estimate the leading contribution of this systematic by replacing $E_{x,y,z}$ in Equation 6.26 with $T_{x,y,z}$. Assuming that the temperatures are all about the same, we would expect a contribution of $6g_F^{u/l}\mu_B B'_{nr}\delta B_{\rm rot}$, where $\delta B_{\rm rot} \approx \frac{6k_BT}{e\mathcal{E}_{\rm rot}}$. This is the same sign in the doublet switch, so the contribution to the four-way difference is

$$f_{\rm edm}^{\delta B_{\rm rot}} = 6\delta g_F \mu_B B'_{nr} \frac{6k_BT}{e\mathcal{E}_{\rm rot}} \approx 40\mu{\rm Hz}, \tag{6.67}$$

assuming a temperature of 10 K. Other radial inhomogeneities can be treated in a similar fashion and should also cancel in a B switch.

6.6.4 Other effects

Motion in electric and magnetic fields can lead to induced (relativistic) fields. The largest contribution to the ion velocity comes from the rotating electric field, which yields a micromotion velocity of $\frac{e\mathcal{E}_{\rm rot}}{m\omega_{\rm rot}} \approx 600$ m/s for $\mathcal{E}_{\rm rot}$ of 20 V/cm. This motion in a magnetic field will produce an electric field $\vec{\mathcal{E}}_{\rm motional} = \vec{v} \times \vec{B}$. For a static axial magnetic field, the motional electric field will always be parallel (or antiparallel) to $\mathcal{E}_{\rm rot}$ and so could cause a systematic. The largest axial magnetic field will probably be due to Earth's magnetic field currently (as there is no shielding or cancellation): a 0.5 Gauss axial field will result in a $\delta\mathcal{E}_{\rm rot} = 0.3$ mV/cm, which is suppressed by 10^{-5} from the applied electric field. This electric field will result in a small B^{nr}, which will result

in a contribution to the four-way difference of

$$f_{edm}^{\text{motional}} = 6\delta g_F \mu_B B' \frac{e}{m\omega_{\text{rot}}^2}\left(\frac{e\mathcal{E}_{\text{rot}}}{m\omega_{\text{rot}}}B_\perp\right) \approx 4\mu\text{Hz}. \tag{6.68}$$

Furthermore, $\mathcal{E}_{\text{motional}}$ will change sign with a rotation direction switch. Similarly, motion in an electric field will create a magnetic field: $\vec{B}_{\text{motional}} = \frac{1}{c^2}\vec{v}\times\vec{\mathcal{E}}$. The two dominant electric field contributions are from $\mathcal{E}_{\text{rot}}$ and from trapping fields. With $\mathcal{E}_{\text{rot}} = 20$ V/cm, $B_{\text{motional}} \approx 0.1\mu$G and is oriented axially. Such a small $B_\perp$ will have no effect. Radial trapping fields are smaller than $\mathcal{E}_{\text{rot}}$ and so will generate even smaller magnetic fields. Axial trapping fields will lead to a magnetic field that could contribute to the applied magnetic field; however, even an anomalously large trapping field of 1 V/cm will cause $B_{\text{motional}} < 0.01\mu$G, which is less than 10^{-7} of B_{rot}.

According to Equation 6.59, Δ differs between the upper and lower doublet by $2\delta\Delta$. Because the Zeeman shift is not infinitely large compared to Δ, there will be a difference in the fringe frequency the depends on the doublet. This is difference is expected to be

$$2\pi(f^u(B) - f^l(B)) = \frac{(\Delta^u)^2 - (\Delta^l)^2}{6g_F^{u/l}\mu_B B_{\text{rot}}} = \frac{4\bar{\Delta}\delta\Delta}{6g_F^{u/l}\mu_B B_{\text{rot}}} \approx \frac{\frac{4}{3}\left(\frac{d_{mf}\mathcal{E}_{\text{rot}}}{E_{HF}}\right)^2\bar{\Delta}^2}{6g_F^{u/l}\mu_B B_{\text{rot}}} \approx 0.5\text{Hz} \tag{6.69}$$

for a 40 Hz fringe with $\mathcal{E}_{\text{rot}} = 20$ V/cm. While this initially is concerning, it should be removed in the B switch and so should not cause a problem.

Other potential effects could arise from imperfect state preparation or from phase shifts during the Ramsey sequence. Previous eEDM experiments have observed differential Stark shifts of the upper and lower Stark manifolds from various issues due to state preparation [420, 31], so it is worth considering these effects. We can shutter all lasers during the free evolution period, so Stark shifts due to laser light should not be a problem. In order to look for other effects, we can simulate our Ramsey sequence by numerically integrating the time-dependent Schrödinger equation using the Hamiltonian given in Equation 6.58. The electric field during the Ramsey sequence is shown in Figure 6.27(a). Figure 6.27(b) shows $|\langle +3/2|\psi\rangle|^2$ (blue) and $|\langle -3/2|\psi\rangle|^2$ (red) during the Ramsey sequence. The large population oscillation after the second $\pi/2$ pulse is due to to the proximity to the avoided crossing, which means that the $|\pm 3/2\rangle$ states are not perfect eigenstates.

This oscillation means that the measurement of the phase accumulated during the free-evolution period by measuring population after the second $\pi/2$ pulse will depend on the time the population measurement is done. As long as the time after the second $\pi/2$ pulse is constant, this should not cause a problem, although since our depletion pulses are finite duration we will have to carefully check from potential systematics by measuring with different delay times.

The presence of a finite magnetic field during the $\pi/2$ pulse means that our pulses are actually slightly "off-resonant", i.e., it is equivalent to driving a microwave $\pi/2$ pulse with the microwave frequency detuned from resonance. Assuming a two-level system and that all of the population starts in $|+3/2\rangle = |z\rangle$, we can write the population difference during as the standard Rabi result:

$$P_z = \frac{\epsilon^2 - \Omega_0^2}{\Omega^2} \sin^2(\frac{\Omega t}{2}) + \cos^2(\frac{\Omega t}{2}), \tag{6.70}$$

where $\Omega = \sqrt{\Omega_0^2 + \epsilon^2}$ is the generalized Rabi frequency with on-resonance Rabi frequency Ω_0 and detuning ϵ. In this case, the $\pi/2$-pulse duration is $\sim \pi/(2\Omega)$. For our system, $\Omega_0 = \Delta^{u/l}$ and $\epsilon = 3g_F^{u/l}\mu_B B' \frac{e\mathcal{E}_{\rm rot}^{\pi/2}}{m\omega_{\rm rot}^2}$. From this, we can see that the $\pi/2$-pulse duration will be different for the upper and lower doublets, which we must account for in the experiment. In addition, the off-resonant pulses can lead to small phase shifts. We can use the detailed theory for a Ramsey sequence using off-resonant pulses found in [480] to estimate that potential differential phase shifts should be < 0.01 rad. These phase shifts can also be measured by measuring a fringe at short free-evolution times, so they should not cause a problem.

6.7 eEDM measurement

To perform a basic eEDM measurement, we need to evaluate the four-way difference from Equation 6.63. This can be accomplished by measuring a Ramsey fringe in each combination of doublet and sign of B'. Of course, measuring a full fringe in one configuration (switch state) takes a long time, which increases the susceptibility to experimental drift between fringes. So, a better data taking strategy is needed.

The above method can be immediately improved by alternating between switch configurations

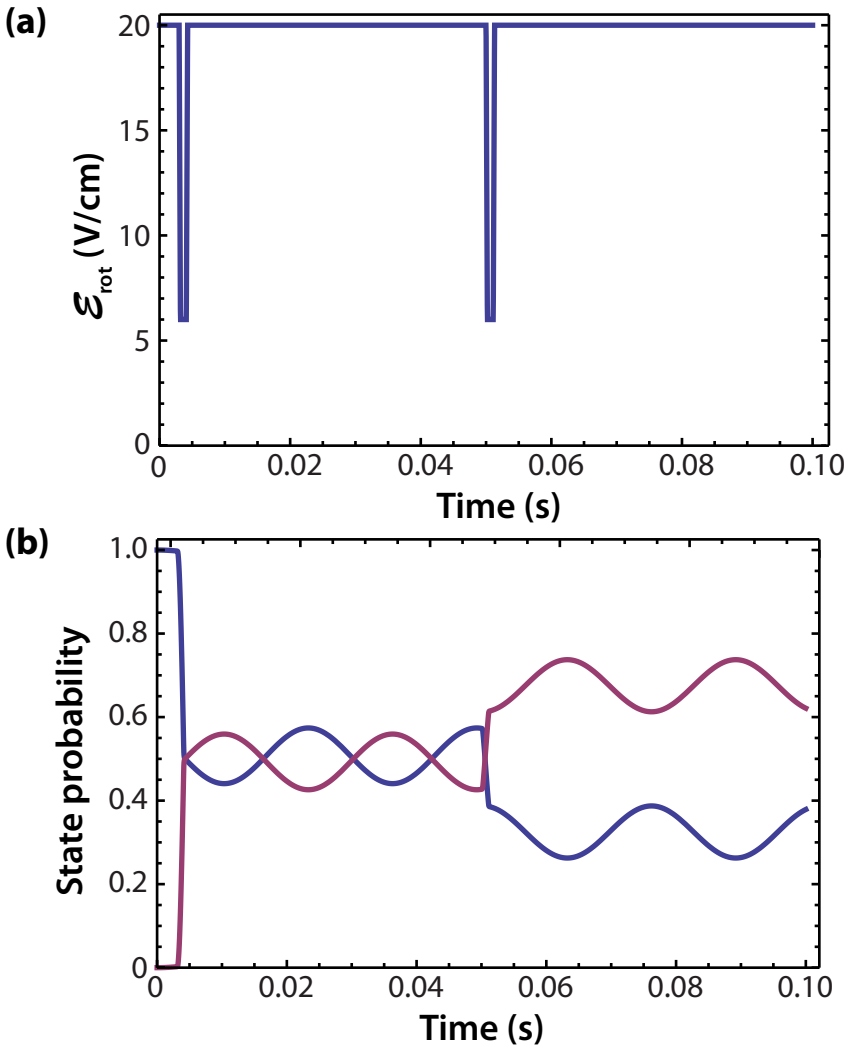

Figure 6.27: Simulation of Ramsey sequence. (a) $\mathcal{E}_{\text{rot}}$ as a function of time (in seconds). (b) Simulation of the population in $|+3/2\rangle$ (red) and $|-3/2\rangle$ (blue) as a function of time during the Ramsey sequence. The delay for the second $\pi/2$ pulse delay is adjusted so that there is a bit of an offset between the average population in $|+3/2\rangle$ and $|-3/2\rangle$.

at one time point in the fringe, thus recording the four fringes simultaneously. An example data set is shown in Figure 6.28, where each column corresponds to the data for one specific switch state. At each time step and in each switch state, we measure Hf^+ in four different chops as shown in the third row: dissociation only (light green); transfer + dissociation (dark green); transfer, σ^+ depletion, wait T, σ^+ depletion, dissociation (light blue); and transfer, σ^+ depletion, wait T, σ^- depletion, dissociation (dark blue). The two depletion chops are converted to a fractional depletion by subtracting the dissociation background and then dividing by the transfer - dissociation, as shown in the second row. Finally, the difference of the two depletion chops gives the Ramsey fringe (fractional population difference) shown in the first row. We fit each fringe to an exponentially decaying sine wave with a decay time fixed to 300 ms. The frequency, amplitude, initial phase, and offset were fit individually for each switch state as shown in Figure 6.28. Taking the four-way difference gives 0.34(33) Hz, so $d_e = 7.5 \pm 7.3 \times 10^{-27}$ e cm. Not bad for the initial test with a few hours of data!

We have now repeated this measurement multiple times, as shown in Figure 6.29. These measurements include one at a 20 Hz fringe frequency as well as with different values of B^{nr} (sometimes removed with a B' shim, sometimes not, see Section 6.6.1). The combined eEDM measurement is now $d_e = -1.5 \pm 3.0 \times 10^{-27}$ e cm, as shown by the solid red line and dashed lines.

For a better measurement, we will want to further improve the data taking efficiency. In principle, we only care about measuring a phase shift after a long wait time, which corresponds to measuring a frequency difference. This phase could be measured by measuring near the zero crossing of the fringe and looking for a change in measured population difference for different switch states. However, to convert a change in the population difference to a phase difference it is necessary to also know the slope of the fringe, which is related to the frequency and the fringe contrast. One option for monitoring the slope is to measure two points at the side of a fringe, one below and one above the zero crossing. This measurement could then be repeated on the opposite slope of the fringe, similar to what is done in the YbF experiment [420]. Such a procedure provides an inherent calibration for the fringe contrast, which is necessary for determining the slope of the fringe and

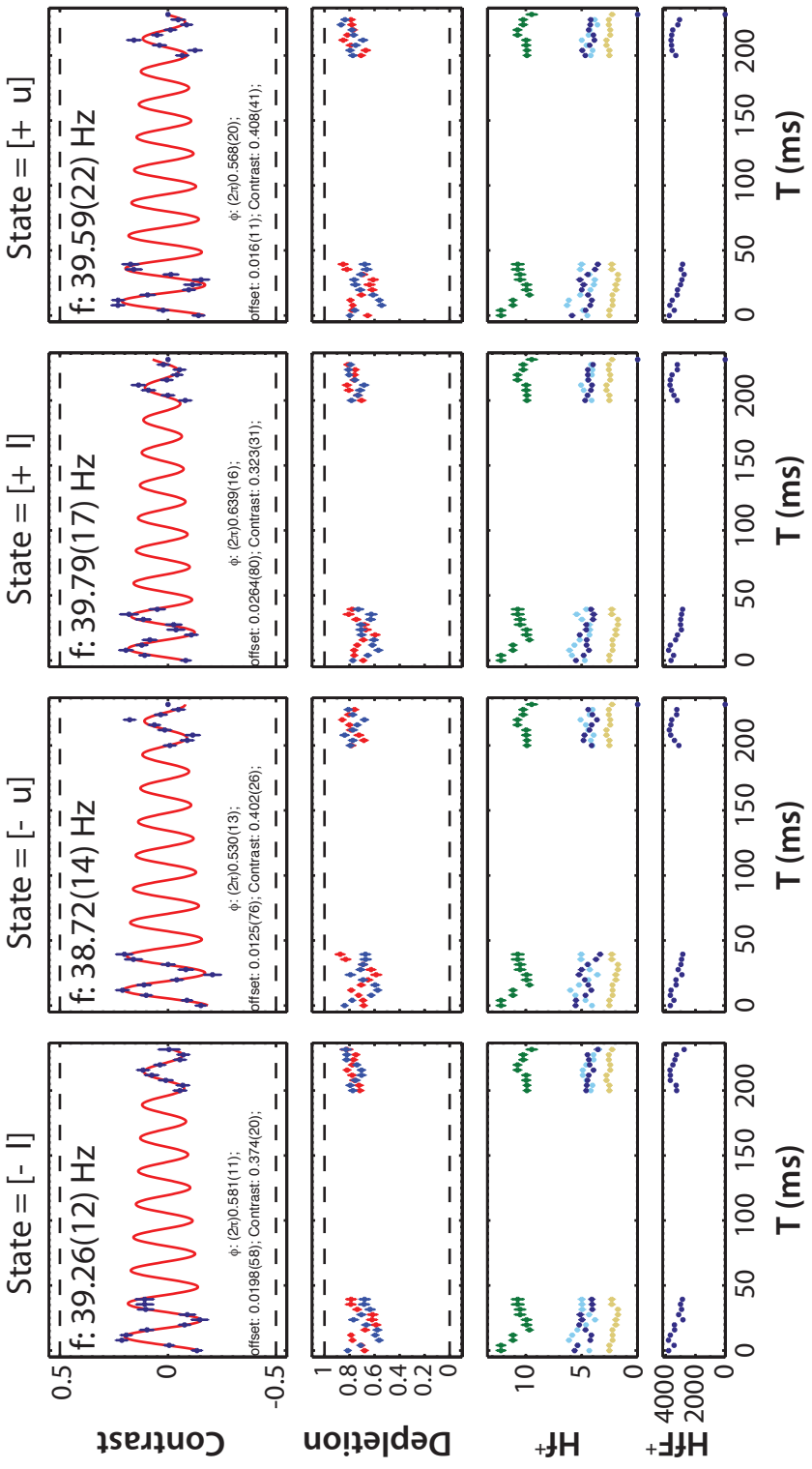

Figure 6.28: Ramsey fringe measured for each switch state [$\pm B'$, u/l doublet].

thus the phase shift. In addition, since we really care about phase shifts that occur at long time due to frequency differences, we need to remove any differences in initial phase. One nice advantage of our experiment is that we can easily measure the phase and contrast at short times by only changing the delay time between $\pi/2$ pulses, as demonstrated in Figure 6.28. This means that we can calibrate the initial phase by alternating between measurements at short time and long time.

6.8 Outlook

The estimates from Table 6.2 give an initial statistical sensitivity of around 1×10^{-27} e cm/$\sqrt{\text{day}}$ with the current parameters. We also have several areas to improve upon these numbers without major upgrades to the experiment. In particular:

(1) by upgrading the photodissociation laser to a higher pulse rate, we should be able to increase the dissociation efficiency by a factor of at least 2;

(2) we should be able to increase the free evolution time to 500 ms by fully understanding the decoherence issues;

(3) we should be able to increase the depletion contrast by a factor of 2.

This would increase N to 4 counts-per-shot (also probably increase the background, N_0, to something like 6) and would increase τ, which would give a statistical sensitivity of around 2×10^{-28} e cm/$\sqrt{\text{day}}$. This sensitivity will enable initial tests of systematic errors at the few 10^{-28} e cm level, which will provide vital information for planning the next generation experiment.

On a longer timescale, we could hope to increase the free evolution time up to perhaps 1 s while increasing the total ion number by lowering the temperature of the ions. This free evolution time is still below the $^3\Delta_1$ lifetime, but we will also need to improve the inhomogeneity limit shown in Figure 6.21 while keeping the fringe frequency significantly larger than Δ. We can accomplish this by decreasing ω_{rot}, which will both increase B_{rot} for a given B' and decrease Δ. Effects due to the ponderomotive potential from the rotating electric field will increase with decreasing ω_{rot}, but

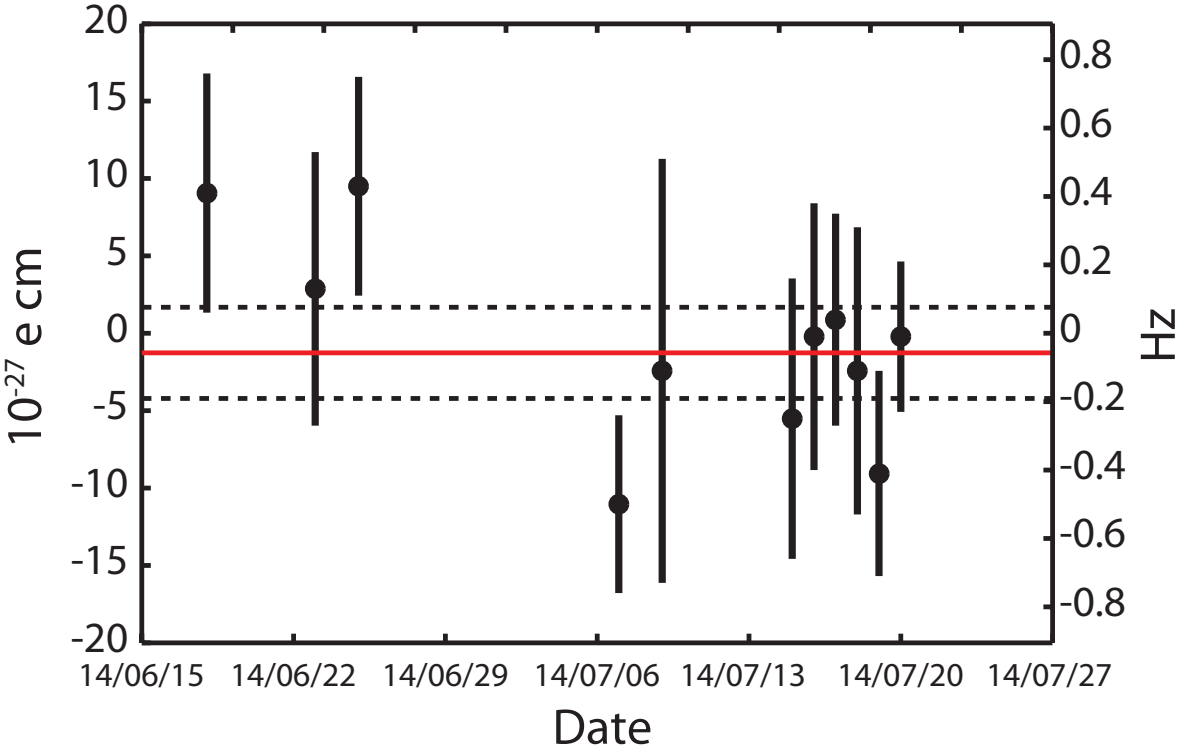

Figure 6.29: All eEDM measurements to date. The red line and dashed line show the mean and standard error, respectively, corresponding to $d_e = -1.5 \pm 3.0 \times 10^{-27}$ e cm.

we should be able to manage this by optimizing the field homogeneity, for example, by increasing the distance between the trap electrodes. In addition to increasing the free-evolution time, a larger trap chamber with a higher pump-out speed (by removing LIF mirrors that limit the conductance to the center of the trap) could also reduce the fast initial loss caused by collisional heating with background Ar. Several further possibilities exist for improving the signal-to-noise:

(1) It might be possible to increase the fraction of population in $^1\Sigma^+$ $J = 0$ by a factor of 2. This could be accomplished by using microwave/laser STIRAP to excite the neutral precursor to a non-core penetrating (high angular momentum) Rydberg state. Because the electron in a non-core penetrating state does not interact with the ion core, it can then be removed without influencing the quantum state of the ion core. We could also consider implementing a sympathetic cooling scheme using an atomic magneto-optical trap [447].

(2) Based on the transfer time scales that we have observed, we should be able to transfer more population in a half-trap cycle if we can increase the transfer laser power and decrease the one-photon detuning. This should be possible without causing significant spontaneous emission by eliminating scattered light, which causes the sidebands observed in the one-photon linewidth shown in Figure 6.15. Removing the LIF mirrors and possibly following the "paint it black" philosophy should significantly reduce the scattered light. This could provide another factor of 2-3.

(3) By reducing the Hf^+ loss between photodissociation shots and increasing the MCP efficiency with a combination of a return bias voltage and coating with CsI or similar material, we could increase the REMPD detection efficiency by a factor of 2.

With these improvements, we should be able to reach 1×10^{-29} e cm/$\sqrt{\text{day}}$.

Instead of a trapped ion cloud, it is intriguing to consider the use of a single trapped ion as in optical clocks using atomic ions [481, 482, 483]. Quantum-logic spectroscopy [484] is used in atomic ion clocks for state detection with extremely high fidelity, so the noise is limited by quantum-projection noise (i.e., shot noise on one count). Typically, quantum-logic spectroscopy

relies on the ability to perform clean π-pulses between motional states, which can be challenging with molecules without cycling transitions; however, several options exist for extending quantum-logic spectroscopy to molecules [485, 486, 487]. One of motivations for considering a single trapped ion is the potential for a very long coherence time, since ion-ion collisions are eliminated and field inhomogeneity is significantly reduced. With HfF^+, our free-evolution time will be limited by the $^3\Delta_1$ lifetime to 2 s. However, ThF^+ should have a significantly longer lifetime, currently estimated to be greater than 30 s, so this would not be a limit. Other possible ions include TaO^+ and WN^+, which both might be expected to have $^3\Delta_1$ ground states. WN^+ has been proposed for an eEDM measurement in a storage ring due to it's expected $^3\Delta_1$ ground state [488]. This can be explained by ligand-field theory (what, you don't remember this?, see Section 5.1.1): typically more ionic bonds due to the O^{2-} or N^{3-} ligands will stabilize an *sd* configuration to below the s^2 configuration, see for example ScF vs TiO [489]. In addition, WC – which is isoelectronic with WN^+ – has a $^3\Delta_1$ ground state [490]. Assuming then that state lifetime is not a problem, how long of a coherence time can we expect? A coherence time of around 5 s has been demonstrated between hyperfine states in trapped $^{43}Ca^+$ [491], so a coherence time of perhaps 10 s seems reasonable. Because we use states which are first-order Zeeman sensitive, a coherence time of of 10 s requires better than 0.25% magnetic and electric field stability given the current Zeeman splitting. At this point, we would also have to worry about the coherence time due to blackbody radiation, which is around 7 s for HfF^+ at room temperature. Assuming we reach 10 s, this would result in a sensitivity of around 1×10^{-29} e cm/$\sqrt{\text{day}}$, which is comparable to the projected sensitivity of the current experimental design. However, many systematic errors will be very different using a single ion confined to a well defined location. For example, Berry's phase due to axial motion should be suppressed. On the other hand, stray electric and magnetic field gradients would not be averaged over and would have to be shimmed away. Depending on what systematics are discovered in the current experiment, it may be worthwhile considering a single-ion experiment, but, for statistical sensitivity, there is not much of a gain.

It is worth noting that ground state $^3\Delta_1$ could be very beneficial for pushing below the 10^{-29} e cm level with a trapped ion cloud. Efficient ionization combined with optical pumping and possibly sympathetic cooling could produce perhaps 25% of the ions in a single m_F level, which is 1000 ions at a modest ion number of 4000! In addition, precision spectroscopy of molecular ions is currently in an infancy, so the techniques that we have developed and will continue to develop should be beneficial for other experiments as well.

6.9 Useful numbers

In this section, we provide several tables of useful numbers.

Table 6.4: Useful numbers

Parameter	Symbol	Estimate
Rotating electric field	$\mathcal{E}_{\mathrm{rot}}$	20 V/cm
Electric field rotation angular frequency	ω_{rot}	$2\pi \times 253.7912$ kHz
Trap rf	ω_{rf}	$2\pi \times 50$ kHz
Magnetic field gradient	B'	0.08 G/cm
Molecular frame dipole moment	d_{mf}	1.401(5) e $\mathrm{a}_0 \approx 2\pi \times 1.8$ MHz/(V/cm)
Stark energy	$d_{mf}\mathcal{E}_{\mathrm{rot}}/h$	36.6 MHz
Electric field coupling factor	γ_F	1/3 for $F = 3/2$, 2/3 for $F = 1/2$
Stark shift of $m_F = \pm 3/2$	$\gamma_F m_F d_{mf}\mathcal{E}_{\mathrm{rot}}/h$	18.3 MHz
Magnetic g-factor in $^3\Delta_1$	g_F	0.00305(10)
Difference in g-factor	$\delta g_F/g_F$	0.003(6) measured; < 0.002 theory
Radius of micromotion	r_{rot}	0.4 mm
Rotating micromotion velocity	v_{rot}	620 m/s
Zeeman splitting between $\pm 3/2$	$3g_F\mu_B B$	$2\pi \times 40$ Hz
Ω-doublet splitting	ω_{ef}	$2\pi \times 740(40)$ kHz
Hyperfine splitting	E_{hf}	$h \times 45.6(1)$ MHz

Table 6.5: $\bar{\Delta}$, $\delta\Delta$, and Stark shift for different values of $\mathcal{E}_{\rm rot}$, from theory

$\mathcal{E}_{\rm rot}$	$\gamma_F m_F d_{mf} \mathcal{E}_{\rm rot}/h$	$\bar{\Delta}$	$\delta\Delta$
5	4.6 MHz	434.5 Hz	31.4 Hz
6	5.5	251.4 Hz	21.8 Hz
7	6.4	158.3 Hz	16.0 Hz
8	7.3	106.1 Hz	12.3 Hz
10	9.1	54.3 Hz	7.8 Hz
12	11.0	31.4 Hz	5.4 Hz
16	14.6	13.3 Hz	3.1 Hz
20	18.3	6.8 Hz	2.0 Hz
25	22.8	3.5 Hz†	1.3 Hz†
30	27.4	2 Hz†	0.9 Hz†

† Due to a level crossing between the upper Stark manifold and the $F = 1/2$, $m_F = \pm 1/2$ levels, this might deviate from the theory.

Chapter 7

Conclusion

In this thesis, we have presented a variety of experiments covering a range of techniques and applications of molecular spectroscopy. Direct frequency comb spectroscopy – with or without cavity enhancement – provides a unique combination of bandwidth, resolution, and sensitivity that is not easily available in other systems. We have shown how this combination can be beneficial for trace species detection by enabling simultaneous, multi-species detection even with competing background absorption or Rayleigh scattering. Spectroscopy systems using the demonstrated technology or extensions farther into the mid-infrared have many potential applications including industrial gas purity monitoring, pollution control, breath analysis, and atmospheric chemistry. In addition, the newly-developed technique of time-resolved frequency-comb spectroscopy has exciting prospects for the study of chemical reactions including characterization of reaction intermediates and precise measurements of branching ratios to different products. Frequency comb velocity modulation spectroscopy extends this combination of bandwidth, resolution, and sensitivity for the first time to the study of molecular ions with applications to astrochemistry, chemical physics, as well as fundamental physics. Precision spectroscopy of molecular ions is an exciting direction for tests of fundamental physics because of the long coherence times and thus narrow linewidths that can be obtained. Currently, we have achieved a Fourier-limited linewidth of 400 mHz in trapped HfF^+ and used this to perform a preliminary measurement of the electron electric dipole moment. By further increasing the signal and coherence time, this system will be competitive with the current best measurement of the eEDM.

Bibliography

[1] J. C. D. Brand, Lines Of Light: The Sources Of Dispersive Spectroscopy, 1800-1930. CRC Press, 1995.

[2] R. W. Wood, Researches in physical optics, with special reference to the radiation of electroncs, Part I. New York: Columbia University Press, 1913.

[3] R. W. Wood, Researches in physical optics, Resonance Radiation and Resonance Spectra, Part II. New York: Columbia University Press, 1919.

[4] R. S. Mulliken, "Nobel Lecture: Spectroscopy, Molecular Orbitals, and Chemical Bonding," in Nobel Lectures, Chemistry 1963-1970, Amsterdam: Elsevier, 1972.

[5] G. Herzberg, "Nobel Lecture: Spectroscopic Studies of Molecular Structure," in Nobel Lectures, Chemistry 1971-1980 (T. Frangsmyr and S. Forson, eds.), Singapore: World Scientific, 1993.

[6] S. P. Davis, M. C. Abrams, and J. W. Brault, Fourier Transform Spectrometry. Academic Press, 2001.

[7] P. R. Griffiths and J. A. D. Haseth, Fourier Transform Infrared Spectroscopy. New Jersey: Wiley-Interscience, 2007.

[8] P. Bernath, "Atmospheric chemistry experiment (ACE): Analytical chemistry from orbit," TrAC Trends in Analytical Chemistry, vol. 25, pp. 647–654, July 2006.

[9] N. de Oliveira, M. Roudjane, D. Joyeux, D. Phalippou, J.-c. Rodier, and L. Nahon, "High-resolution broad-bandwidth Fourier-transform absorption spectroscopy in the VUV range down to 40 nm," Nature Photonics, vol. 5, pp. 149–153, 2011.

[10] W. Demtröder, Laser Spectroscopy: Basic Concepts and Instrumentation. Springer Science & Business Media, 2003.

[11] J. L. Hall, "Sub-Doppler Spectroscopy, Methane Hyperfine Spectroscopy, and the Ultimate Resolution Limits," Methodes de spectroscopie sans largeur Doppler de niveaux excites de systemes moleculaires simples, vol. 217, 1974.

[12] J. Hall, "Nobel Lecture: Defining and measuring optical frequencies," Reviews of Modern Physics, vol. 78, pp. 1279–1295, Nov. 2006.

[13] T. Hänsch, "Nobel Lecture: Passion for precision," Reviews of Modern Physics, vol. 78, pp. 1297–1309, Nov. 2006.

[14] S. Cundiff and J. Ye, "Colloquium: Femtosecond optical frequency combs," Reviews of Modern Physics, vol. 75, pp. 325–342, Mar. 2003.

[15] S. A. Diddams, "The evolving optical frequency comb," Journal of the Optical Society of America B, vol. 27, no. 11, pp. B51–B62, 2010.

[16] B. Bobin, C. J. Bordé, J. Bordé, and C. Bréant, "Vibration-rotation molecular constants for the ground and ($\nu 3 = 1$) states of 32SF6 from saturated absorption spectroscopy," Journal of Molecular Spectroscopy, vol. 121, pp. 91–127, Jan. 1987.

[17] D. W. Pratt, "High resolution spectroscopy in the gas phase: even large molecules have well-defined shapes.," Annual Review of Physical Chemistryhysical chemistry, vol. 49, pp. 481–530, Jan. 1998.

[18] B. E. Brumfield, J. T. Stewart, and B. J. McCall, "Extending the Limits of Rotationally Resolved Absorption Spectroscopy: Pyrene," The Journal of Physical Chemistry Letters, vol. 3, pp. 1985–1988, Aug. 2012.

[19] F. Dong, S. Davis, and D. J. Nesbitt, "Slit discharge IR spectroscopy of a jet-cooled cyclopropyl radical: structure and intramolecular tunneling dynamics.," The Journal of Physical Chemistry A, vol. 110, pp. 3059–70, Mar. 2006.

[20] L. Dong, B. K. Thomas, and L. Fu, "Highly nonlinear silica suspended core fibers.," Optics Express, vol. 16, pp. 16423–30, Oct. 2008.

[21] C. Duan and D. Luckhaus, "High resolution IR-diode laser jet spectroscopy of malonaldehyde," Chemical Physics Letters, vol. 391, pp. 129–133, June 2004.

[22] O. Birer and M. Havenith, "High-resolution infrared spectroscopy of the formic acid dimer.," Annual Review of Physical Chemistry, vol. 60, pp. 263–75, Jan. 2009.

[23] K. Evenson, J. Wells, F. Petersen, B. Danielson, G. Day, R. Barger, and J. Hall, "Speed of Light from Direct Frequency and Wavelength Measurements of the Methane-Stabilized Laser," Physical Review Letters, vol. 29, pp. 1346–1349, Nov. 1972.

[24] M. Quack, "Molecular Spectra, Reaction Dynamics, Symmetries and Life," CHIMIA International Journal for Chemistry, vol. 57, pp. 147–160, Apr. 2003.

[25] S. K. Tokunaga, C. Stoeffler, F. Auguste, A. Shelkovnikov, C. Daussy, A. Amy-Klein, C. Chardonnet, and B. Darquié, "Probing weak force-induced parity violation by high-resolution mid-infrared molecular spectroscopy," Molecular Physics, vol. 111, pp. 2363–2373, Aug. 2013.

[26] C. Lemarchand, M. Triki, B. Darquié, C. J. Bordé, C. Chardonnet, and C. Daussy, "Progress towards an accurate determination of the Boltzmann constant by Doppler spectroscopy," New Journal of Physics, vol. 13, p. 073028, July 2011.

[27] D. DeMille, S. Sainis, J. Sage, T. Bergeman, S. Kotochigova, and E. Tiesinga, "Enhanced Sensitivity to Variation of me/mp in Molecular Spectra," Physical Review Letters, vol. 100, p. 043202, Jan. 2008.

[28] D. Hils and J. Hall, "Improved Kennedy-Thorndike experiment to test special relativity," Physical Review Letters, vol. 64, pp. 1697–1700, Apr. 1990.

[29] E. A. Hinds, "Testing time reversal symmetry using molecules," Physica Scripta, vol. T70, pp. 34–41, Jan. 1997.

[30] J. J. Hudson, D. M. Kara, I. J. Smallman, B. E. Sauer, M. R. Tarbutt, and E. A. Hinds, "Improved measurement of the shape of the electron.," Nature, vol. 473, pp. 493–6, May 2011.

[31] J. Baron, W. C. Campbell, D. DeMille, J. M. Doyle, G. Gabrielse, Y. V. Gurevich, P. W. Hess, N. R. Hutzler, E. Kirilov, I. Kozyryev, B. R. O'Leary, C. D. Panda, M. F. Parsons, E. S. Petrik, B. Spaun, A. C. Vutha, and A. D. West, "Order of magnitude smaller limit on the electric dipole moment of the electron.," Science, vol. 343, pp. 269–72, Jan. 2014.

[32] E. Hudson, H. Lewandowski, B. Sawyer, and J. Ye, "Cold Molecule Spectroscopy for Constraining the Evolution of the Fine Structure Constant," Physical Review Letters, vol. 96, p. 143004, Apr. 2006.

[33] A. Shelkovnikov, R. Butcher, C. Chardonnet, and A. Amy-Klein, "Stability of the Proton-to-Electron Mass Ratio," Physical Review Letters, vol. 100, p. 150801, Apr. 2008.

[34] S. Truppe, R. J. Hendricks, S. K. Tokunaga, H. J. Lewandowski, M. G. Kozlov, C. Henkel, E. A. Hinds, and M. R. Tarbutt, "A search for varying fundamental constants using hertz-level frequency measurements of cold CH molecules.," Nature Communications, vol. 4, p. 2600, Jan. 2013.

[35] G. C. Bjorklund, "Frequency-modulation spectroscopy: a new method for measuring weak absorptions and dispersions," Optics Letters, vol. 5, p. 15, Jan. 1980.

[36] M. Gehrtz, G. C. Bjorklund, and E. A. Whittaker, "Quantum-limited laser frequency-modulation spectroscopy," Journal of the Optical Society of America B, vol. 2, p. 1510, Sept. 1985.

[37] J. A. Silver, "Frequency-modulation spectroscopy for trace species detection: theory and comparison among experimental methods.," Applied optics, vol. 31, pp. 707–17, Feb. 1992.

[38] T. Hänsch, A. Schawlow, and P. Toschek, "Ultrasensitive response of a CW dye laser to selective extinction," IEEE Journal of Quantum Electronics, vol. 8, pp. 802–804, Oct. 1972.

[39] A. O'Keefe and D. A. Deacon, "Cavity ring-down optical spectrometer for absorptoin measurements using pulsed laser sources," Review of Scientific Instruments, vol. 59, no. 12, pp. 2544–2551, 1988.

[40] G. Gagliardi and H.-P. Loock, eds., Cavity-Enhanced Spectroscopy and Sensing. Springer Berlin Heidelberg, 2013.

[41] J. Ye and J. L. Hall, "Ultrasensitive detections in atomic and molecular physics : demonstration in molecular overtone spectroscopy," Journal of the Optical Society of America B, vol. 15, no. 1, pp. 6–15, 1998.

[42] A. Foltynowicz, F. Schmidt, W. Ma, and O. Axner, "Noise-immune cavity-enhanced optical heterodyne molecular spectroscopy: Current status and future potential," Applied Physics B, vol. 92, pp. 313–326, Aug. 2008.

[43] I. Galli, S. Bartalini, S. Borri, P. Cancio, D. Mazzotti, P. De Natale, and G. Giusfredi, "Molecular Gas Sensing Below Parts Per Trillion: Radiocarbon-Dioxide Optical Detection," Physical Review Letters, vol. 107, pp. 1–4, Dec. 2011.

[44] M. J. Thorpe and J. Ye, "Cavity-enhanced direct frequency comb spectroscopy," Applied Physics B: Lasers and Optics, vol. 91, pp. 397–414, May 2008.

[45] M. J. Thorpe, Cavity-enhanced direct frequency comb spectroscopy. PhD thesis, University of Colorado - Boulder, 2009.

[46] F. Adler, M. J. Thorpe, K. C. Cossel, and J. Ye, "Cavity-enhanced direct frequency comb spectroscopy: technology and applications.," Annual Review of Analytical Chemistry, vol. 3, pp. 175–205, Jan. 2010.

[47] P. Maslowski, K. C. Cossel, A. Foltynowicz, and J. Ye, "Cavity-Enhanced Direct Frequency Comb Spectroscopy," in Cavity-Enhanced Spectroscopy and Sensing (G. Gagliardi and H.-P. Loock, eds.), vol. 179 of Springer Series in Optical Sciences, Berlin, Heidelberg: Springer Berlin Heidelberg, 2014.

[48] S. W. Sharpe, T. J. Johnson, R. L. Sams, P. M. Chu, G. C. Rhoderick, and P. A. Johnson, "Gas-Phase Databases for Quantitative Infrared Spectroscopy," Appl. Spectrosc., vol. 58, pp. 1452–1461, 2004.

[49] A. Ruehl, M. Martin, K. Cossel, L. Chen, H. McKay, B. Thomas, C. Benko, L. Dong, J. Dudley, M. Fermann, I. Hartl, and J. Ye, "Ultrabroadband coherent supercontinuum frequency comb," Physical Review A, vol. 84, p. 011806(R), July 2011.

[50] F. Adler, K. C. Cossel, M. J. Thorpe, I. Hartl, M. E. Fermann, and J. Ye, "Phase-stabilized, 1.5 W frequency comb at 2.8 um," Optics Letters, vol. 34, no. 9, pp. 1330–1332, 2009.

[51] S. A. Diddams, L. Hollberg, and V. Mbele, "Molecular fingerprinting with the resolved modes of a femtosecond laser frequency comb.," Nature, vol. 445, pp. 627–30, Feb. 2007.

[52] L. Nugent-Glandorf, T. Neely, F. Adler, A. J. Fleisher, K. C. Cossel, B. Bjork, T. Dinneen, J. Ye, and S. A. Diddams, "Mid-infrared virtually imaged phased array spectrometer for rapid and broadband trace gas detection," Optics Letters, vol. 37, pp. 3285–3287, Aug. 2012.

[53] K. C. Cossel, F. Adler, K. A. Bertness, M. J. Thorpe, J. Feng, M. W. Raynor, and J. Ye, "Analysis of trace impurities in semiconductor gas via cavity-enhanced direct frequency comb spectroscopy," Applied Physics B, vol. 100, pp. 917–924, July 2010.

[54] A. Foltynowicz, T. Ban, P. Maslowski, F. Adler, and J. Ye, "Quantum-Noise-Limited Optical Frequency Comb Spectroscopy," Physical Review Letters, vol. 107, p. 233002, Nov. 2011.

[55] A. Foltynowicz, P. Maslowski, A. J. Fleisher, B. J. Bjork, and J. Ye, "Cavity-enhanced optical frequency comb spectroscopy in the mid-infrared application to trace detection of hydrogen peroxide," Applied Physics B, vol. 110, pp. 163–175, May 2012.

[56] A. J. Fleisher, B. J. Bjork, T. Q. Bui, K. C. Cossel, M. Okumura, and J. Ye, "Mid-Infrared Time-Resolved Frequency Comb Spectroscopy of Transient Free Radicals," The Journal of Physical Chemistry Letters, vol. 5, pp. 2241–2246, July 2014.

[57] E. E. Ferguson and F. Arnold, "Ion chemistry of the stratosphere," Accounts of Chemical Research, vol. 14, pp. 327–334, Nov. 1981.

[58] E. Herbst, "The chemistry of interstellar space," Chemical Society Reviews, vol. 30, pp. 168–176, Jan. 2001.

[59] W. Klemperer, "Astronomical Chemistry," Annual Review of Physical Chemistry, vol. 62, pp. 173–184, 2011.

[60] L. C. Sinclair, K. C. Cossel, T. Coffey, J. Ye, and E. A. Cornell, "Frequency Comb Velocity-Modulation Spectroscopy," Physical Review Letters, vol. 107, p. 093002, Aug. 2011.

[61] K. C. Cossel, D. N. Gresh, L. C. Sinclair, T. Coffey, L. V. Skripnikov, A. N. Petrov, N. S. Mosyagin, A. V. Titov, R. W. Field, E. R. Meyer, E. A. Cornell, and J. Ye, "Broadband velocity modulation spectroscopy of HfF+: Towards a measurement of the electron electric dipole moment," Chemical Physics Letters, vol. 546, pp. 1–11, Sept. 2012.

[62] A. E. Leanhardt, J. L. Bohn, H. Loh, P. Maletinsky, E. R. Meyer, L. C. Sinclair, R. P. Stutz, and E. A. Cornell, "High-resolution spectroscopy on trapped molecular ions in rotating electric fields: A new approach for measuring the electron electric dipole moment," J. Mol. Spectrosc., vol. 270, p. 1, 2011.

[63] R. P. Stutz, Towards measuring the electron electric dipole moment using trapped molecular ions. PhD thesis, University of Colorado - Boulder, 2010.

[64] H. Loh, Search for an electron electric dipole moment with trapped molecular ions. PhD thesis, University of Colorado - Boulder, 2013.

[65] H. Loh, K. C. Cossel, M. C. Grau, K.-K. Ni, E. R. Meyer, J. L. Bohn, J. Ye, and E. A. Cornell, "Precision spectroscopy of polarized molecules in an ion trap.," Science, vol. 342, pp. 1220–2, Dec. 2013.

[66] J. Koelemeij, B. Roth, A. Wicht, I. Ernsting, and S. Schiller, "Vibrational Spectroscopy of HD+ with 2-ppb Accuracy," Physical Review Letters, vol. 98, p. 173002, Apr. 2007.

[67] K. Hø jbjerre, A. K. Hansen, P. S. Skyt, P. F. Staanum, and M. Drewsen, "Rotational state resolved photodissociation spectroscopy of translationally and vibrationally cold MgH + ions: toward rotational cooling of molecular ions," New Journal of Physics, vol. 11, p. 055026, May 2009.

[68] M. G. Kozlov and S. A. Levshakov, "Senstivity of the H3O+ inversion-rotational spectrum to changes in the electron-to-proton mass ratio," The Astrophysical Journal, vol. 726, p. 65, Jan. 2011.

[69] K. Beloy, M. Kozlov, A. Borschevsky, A. Hauser, V. Flambaum, and P. Schwerdtfeger, "Rotational spectrum of the molecular ion NHˆ{+} as a probe for α and m_{e}/m_{p} variation," Physical Review A, vol. 83, p. 062514, June 2011.

[70] A. Borschevsky, M. Iliaš, V. A. Dzuba, K. Beloy, V. V. Flambaum, and P. Schwerdtfeger, "Nuclear-spin-dependent parity violation in diatomic molecular ions," Physical Review A, vol. 86, p. 050501, Nov. 2012.

[71] J. Ye and S. T. Cundiff, eds., Femtosecond Optical Frequency Comb Technology: Principle, Operation and Application. Springer: New York, 2004.

[72] A. Foltynowicz, P. Maslowski, T. Ban, F. Adler, K. C. Cossel, T. C. Briles, and J. Ye, "Optical frequency comb spectroscopy," Faraday Discussions, vol. 150, pp. 23–31, 2011.

[73] G. Rieker, F. R. Giorgetta, W. C. Swann, I. Coddington, L. C. Sinclair, C. L. Cromer, E. Baumann, A. Zolot, and N. R. Newbury, "Open-Path Dual-Comb Spectroscopy of Greenhouse Gases," in CLEO: 2013, (Washington, D.C.), p. CTh5C.9, OSA, 2013.

[74] D. J. Jones, "Carrier-Envelope Phase Control of Femtosecond Mode-Locked Lasers and Direct Optical Frequency Synthesis," Science, vol. 288, pp. 635–639, Apr. 2000.

[75] M. E. Fermann, A. Galvanauskas, and G. Sucha, eds., Ultrafast Lasers: Technology and Applications. CRC Press, 2002.

[76] U. Keller, "Recent developments in compact ultrafast lasers.," Nature, vol. 424, pp. 831–8, Aug. 2003.

[77] J.-C. Diels and W. Rudolph, Ultrashort Laser Pulse Phenomena. Academic Press, 2nd ed., 2006.

[78] D. Kuizenga and A. Siegman, "FM and AM mode locking of the homogeneous laser - Part I: Theory," IEEE Journal of Quantum Electronics, vol. 6, pp. 694–708, Nov. 1970.

[79] U. Keller, K. Weingarten, F. Kartner, D. Kopf, B. Braun, I. Jung, R. Fluck, C. Honninger, N. Matuschek, and J. Aus der Au, "Semiconductor saturable absorber mirrors (SESAM's) for femtosecond to nanosecond pulse generation in solid-state lasers," IEEE Journal of Selected Topics in Quantum Electronics, vol. 2, no. 3, pp. 435–453, 1996.

[80] C.-C. Lee, T. R. Schibli, G. Acosta, and J. S. Bunch, "Ultra-short Optical Pulse Generation with Single-layer Graphene," Journal of Nonlinear Optical Physics & Materials, vol. 19, p. 767, 2010.

[81] H.-J. Kim, H.-J. Choi, S.-M. Nam, and Y.-W. Song, "High-performance laser mode-locker with glass-hosted SWNTs realized by room-temperature aerosol deposition.," Optics Express, vol. 19, pp. 4762–7, Feb. 2011.

[82] A. Schmidt, P. Koopmann, G. Huber, P. Fuhrberg, S. Young, D.-i. Yeom, F. Rotermund, V. Petrov, and U. Griebner, "175 fs Tm:Lu2O3 laser at 2.07 m mode-locked using single-walled carbon nanotubes," Optics Express, vol. 20, no. 5, pp. 5313–5318, 2012.

[83] R. W. Boyd, Nonlinear Optics. Academic Press, third edit ed., 2008.

[84] D. E. Spence, P. N. Kean, and W. Sibbett, "60-fsec pulse generation from a self-mode-locked Ti:sapphire laser," Optics Letters, vol. 16, p. 42, Jan. 1991.

[85] U. Keller, G. W. tHooft, W. H. Knox, and J. E. Cunningham, "Femtosecond pulses from a continuously self-starting passively mode-locked Ti:sapphire laser," Optics Letters, vol. 16, p. 1022, July 1991.

[86] I. T. Sorokina and K. L. Vodopyanov, eds., Solid-State Mid-Infrared Laser Sources, vol. 89 of Topics in Applied Physics. Berlin, Heidelberg: Springer Berlin Heidelberg, June 2003.

[87] M. Ebrahim-Zadeh and I. T. Sorokina, eds., Mid-Infrared Coherent Sources and Applications. NATO Science for Peace and Security Series B: Physics and Biophysics, Dordrecht: Springer Netherlands, 2008.

[88] M. N. Cizmeciyan, H. Cankaya, A. Kurt, and A. Sennaroglu, "Kerr-lens mode-locked femtosecond Cr2+: ZnSe laser at 2420 nm," Optics Letters, vol. 34, no. 20, pp. 3056–3058, 2009.

[89] F. Salin, J. Squier, and M. Piché, "Mode locking of Ti:AI2O3 lasers and self-focusing: a Gaussian approximation," Optics Letters, vol. 16, p. 1674, Nov. 1991.

[90] H. Haus, E. Ippen, and K. Tamura, "Additive-pulse modelocking in fiber lasers," IEEE Journal of Quantum Electronics, vol. 30, no. 1, pp. 200–208, 1994.

[91] L. C. Sinclair, I. Coddington, W. C. Swann, G. B. Rieker, A. Hati, K. Iwakuni, and N. R. Newbury, "Operation of an optically coherent frequency comb outside the metrology lab.," Optics Express, vol. 22, pp. 6996–7006, Mar. 2014.

[92] R. A. Kaindl, F. Eickemeyer, M. Woerner, and T. Elsaesser, "Broadband phase-matched difference frequency mixing of femtosecond pulses in GaSe: Experiment and theory," Applied Physics Letters, vol. 75, p. 1060, Aug. 1999.

[93] S. M. Foreman, D. J. Jones, and J. Ye, "Flexible and rapidly configurable femtosecond pulse generation in the mid-IR.," Optics Letters, vol. 28, pp. 370–2, Mar. 2003.

[94] C. Erny, K. Moutzouris, J. Biegert, D. Kühlke, F. Adler, A. Leitenstorfer, and U. Keller, "Mid-infrared difference-frequency generation of ultrashort pulses tunable between 3.2 and 4.8 μm from a compact fiber source," Optics Letters, vol. 32, p. 1138, May 2007.

[95] A. Gambetta, R. Ramponi, and M. Marangoni, "Mid-infrared optical combs from a compact amplified Er-doped fiber oscillator.," Optics Letters, vol. 33, pp. 2671–3, Nov. 2008.

[96] T. W. Neely, T. A. Johnson, and S. A. Diddams, "High-power broadband laser source tunable from 3.0 μm to 4.4 μm based on a femtosecond Yb:fiber oscillator.," Optics Letters, vol. 36, pp. 4020–2, Oct. 2011.

[97] J. H. Sun, B. J. S. Gale, and D. T. Reid, "Composite frequency comb spanning 0.4-2.4 μm from a phase-controlled femtosecond Ti :sapphire laser and synchronously pumped optical parametric oscillator," Optics Letters, vol. 32, no. 11, pp. 1414–1416, 2007.

[98] D. T. Reid, B. J. S. Gale, and J. Sun, "Frequency comb generation and carrier-envelope phase control in femtosecond optical parametric oscillators," Laser Physics, vol. 18, pp. 87–103, Feb. 2011.

[99] S. T. Wong, K. L. Vodopyanov, and R. L. Byer, "Self-phase-locked divide-by-2 optical parametric oscillator as a broadband frequency comb source," Journal of the Optical Society of America B, vol. 27, no. 5, pp. 876–882, 2010.

[100] N. Leindecker, A. Marandi, R. L. Byer, and K. L. Vodopyanov, "Broadband degenerate OPO for mid-infrared frequency comb generation," Optics Express, vol. 19, pp. 6296–302, Mar. 2011.

[101] S. Marzenell, R. Beigang, and R. Wallenstein, "Synchronously pumped femtosecond optical parametric oscillator based on AgGaSe 2 tunable from 2 μm to 8 μm," Applied Physics B: Lasers and Optics, vol. 69, pp. 423–428, Dec. 1999.

[102] N. Leindecker, A. Marandi, R. L. Byer, K. L. Vodopyanov, J. Jiang, I. Hartl, M. Fermann, and P. G. Schunemann, "Octave-spanning ultrafast OPO with 2.6-6.1 μm instantaneous bandwidth pumped by femtosecond Tm-fiber laser," Optics Express, vol. 20, p. 7046, Mar. 2012.

[103] G. Agrawal, Nonlinear Fiber Optics. Academic Press, 4th ed., 2006.

[104] G. Genty, S. Coen, and J. M. Dudley, "Fiber supercontinuum sources," Journal of the Optical Society of America B, vol. 24, no. 8, p. 1771, 2007.

[105] P. Russell, "Photonic crystal fibers.," Science, vol. 299, pp. 358–62, Jan. 2003.

[106] J. C. Knight, "Photonic crystal fibres.," Nature, vol. 424, pp. 847–51, Aug. 2003.

[107] L. Fu, B. K. Thomas, and L. Dong, "Efficient supercontinuum generations in silica suspended core fibers.," Optics Express, vol. 16, pp. 19629–42, Nov. 2008.

[108] T. Okuno, M. Onishi, T. Kashiwada, S. Ishikawa, and M. Nishimura, "Silica-based functional fibers with enhanced nonlinearity and their applications," IEEE Journal of Selected Topics in Quantum Electronics, vol. 5, no. 5, pp. 1385–1391, 1999.

[109] K. Moutzouris, E. Adler, F. Sotier, D. Träutlein, and a. Leitenstorfer, "Multimilliwatt ultrashort pulses continuously tunable in the visible from a compact fiber source.," Optics Letters, vol. 31, pp. 1148–50, Apr. 2006.

[110] G. Imeshev and M. Fermann, "230-kW peak power femtosecond pulses from a high power tunable source based on amplification in Tm-doped fiber," Optics Express, vol. 13, pp. 7424–31, Sept. 2005.

[111] F. Adler and S. A. Diddams, "High-power, hybrid Er:fiber/Tm:fiber frequency comb source in the 2 μm wavelength region.," Optics letters, vol. 37, pp. 1400–2, May 2012.

[112] G. Imeshev, M. E. Fermann, K. L. Vodopyanov, M. M. Fejer, X. Yu, J. S. Harris, D. Bliss, and C. Lynch, "High-power source of THz radiation based on orientation-patterned GaAs pumped by a fiber laser.," Optics Express, vol. 14, pp. 4439–44, May 2006.

[113] P. Domachuk, N. A. Wolchover, M. Cronin-Golomb, A. Wang, A. K. George, C. M. B. Cordeiro, J. C. Knight, and F. G. Omenetto, "Over 4000 nm bandwidth of mid-IR supercontinuum generation in sub-centimeter segments of highly nonlinear tellurite PCFs.," Optics Express, vol. 16, pp. 7161–8, May 2008.

[114] J. S. Sanghera, L. Brandon Shaw, and I. D. Aggarwal, "Chalcogenide Glass-Fiber-Based Mid-IR Sources and Applications," IEEE Journal of Selected Topics in Quantum Electronics, vol. 15, pp. 114–119, Jan. 2009.

[115] R. Cherif, A. Ben Salem, M. Zghal, P. Besnard, T. Chartier, L. Brilland, and J. Troles, "Highly nonlinear As2Se3-based chalcogenide photonic crystal fiber for midinfrared supercontinuum generation," Optical Engineering, vol. 49, no. 9, p. 095002, 2010.

[116] W. Q. Zhang, H. Ebendorff-Heidepriem, T. M. Monro, and S. Afshar V, "Fabrication and supercontinuum generation in dispersion flattened bismuth microstructured optical fiber.," Optics Express, vol. 19, pp. 21135–44, Oct. 2011.

[117] R. J. Jones, K. Moll, M. Thorpe, and J. Ye, "Phase-Coherent Frequency Combs in the Vacuum Ultraviolet via High-Harmonic Generation inside a Femtosecond Enhancement Cavity," Physical Review Letters, vol. 94, p. 193201, May 2005.

[118] C. Gohle, T. Udem, M. Herrmann, J. Rauschenberger, R. Holzwarth, H. A. Schuessler, F. Krausz, and T. W. Hänsch, "A frequency comb in the extreme ultraviolet.," Nature, vol. 436, pp. 234–7, July 2005.

[119] A. K. Mills, T. J. Hammond, M. H. C. Lam, and D. J. Jones, "XUV frequency combs via femtosecond enhancement cavities," Journal of Physics B: Atomic, Molecular and Optical Physics, vol. 45, p. 142001, July 2012.

[120] A. Cingoz, D. C. Yost, T. K. Allison, A. Ruehl, M. E. Fermann, I. Hartl, and J. Ye, "Direct frequency comb spectroscopy in the extreme ultraviolet," Nature, vol. 482, no. 2 February, pp. 68–71, 2012.

[121] T. Suzuki, M. Hirai, and M. Katsuragawa, "Octave-Spanning Raman Comb with Carrier Envelope Offset Control," Physical Review Letters, vol. 101, pp. 2–5, Dec. 2008.

[122] P. Del'Haye, O. Arcizet, A. Schliesser, R. Holzwarth, and T. Kippenberg, "Full Stabilization of a Microresonator-Based Optical Frequency Comb," Physical Review Letters, vol. 101, pp. 1–4, July 2008.

[123] P. Del'Haye, T. Herr, E. Gavartin, M. Gorodetsky, R. Holzwarth, and T. Kippenberg, "Octave Spanning Tunable Frequency Comb from a Microresonator," Physical Review Letters, vol. 107, pp. 1–4, Aug. 2011.

[124] T. J. Kippenberg, R. Holzwarth, and S. a. Diddams, "Microresonator-based optical frequency combs.," Science, vol. 332, pp. 555–9, Apr. 2011.

[125] S. B. Papp and S. A. Diddams, "Spectral and temporal characterization of a fused-quartz-microresonator optical frequency comb," Physical Review A, vol. 84, Nov. 2011.

[126] T. Herr, K. Hartinger, J. Riemesnberger, C. Y. Wang, E. Gavartin, R. Holzwarth, M. L. Gorodetsky, and T. J. Kippenberg, "Universal foration dynamics and noise of Kerr-frequency combs in microresonators," Nature Photonics, vol. 6, no. July, pp. 480–487, 2012.

[127] L. Matos, D. Kleppner, O. Kuzucu, T. R. Schibli, J. Kim, E. P. Ippen, and F. X. Kaertner, "Direct frequency comb generation from an octave-spanning, prismless Ti:sapphire laser," Optics Letters, vol. 29, p. 1683, July 2004.

[128] T. M. Fortier, A. Bartels, and S. A. Diddams, "Octave-spanning Ti:sapphire laser with a repetition rate ¿1 GHz for optical frequency measurements and comparisons," Optics Letters, vol. 31, p. 1011, Apr. 2006.

[129] A. Bartels, D. Heinecke, and S. A. Diddams, "Passively mode-locked 10 GHz femtosecond Ti:sapphire laser," Optics Letters, vol. 33, p. 1905, Aug. 2008.

[130] R. Grilli, G. Méjean, S. Kassi, I. Ventrillard, C. Abd-Alrahman, E. Fasci, and D. Romanini, "Trace measurement of BrO at the ppt level by a transportable mode-locked frequency-doubled cavity-enhanced spectrometer," Applied Physics B, Nov. 2011.

[131] A. Ruehl, A. Marcinkevicius, M. E. Fermann, and I. Hartl, "80 W, 120 fs Yb-fiber frequency comb.," Optics Letters, vol. 35, pp. 3015–7, Sept. 2010.

[132] J. Rauschenberger, T. Fortier, D. Jones, J. Ye, and S. Cundiff, "Control of the frequency comb from a modelocked Erbium-doped fiber laser," Optics Express, vol. 10, pp. 1404–1410, Dec. 2002.

[133] B. R. Washburn, S. A. Diddams, N. R. Newbury, J. W. Nicholson, M. F. Yan, and C. G. Jrgensen, "Phase-locked, erbium-fiber-laser-based frequency comb in the near infrared," Optics Letters, vol. 29, p. 250, Feb. 2004.

[134] B. Walton, H. Margolis, V. Tsatourian, and P. Gill, "Transportable optical frequency comb based on a mode-locked fibre laser," IET Optoelectronics, vol. 2, no. 5, p. 182, 2008.

[135] S. Herrmann, A. Resch, H. Müntinga, and C. Laemmerzahl, "Atom optical experiments in the drop tower: a pathfinder for space based precision measurements," 38th COSPAR Scientific Assembly. Held 18-15 July 2010, 2010.

[136] D. Chao, M. Sander, G. Chang, J. Morse, J. Cox, G. Petrich, L. Kolodziejski, F. Kaertner, and E. Ippen, "Self-referenced Erbium Fiber Laser Frequency Comb at a GHz Repetition Rate - OSA Technical Digest," in Optical Fiber Communication Conference, p. OW1C.2, Optical Society of America, Mar. 2012.

[137] J. Jiang, C. Mohr, J. Bethge, M. Fermann, and I. Hartl, "Fully Stabilized, Self-Referenced Thulium Fiber Frequency Comb - OSA Technical Digest (CD)," in CLEO/Europe and EQEC 2011 Conference Digest, p. PDB_1, Optical Society of America, May 2011.

[138] M. N. Cizmeciyan, H. Cankaya, a. Kurt, and a. Sennaroglu, "Operation of femtosecond Kerr-lens mode-locked Cr:ZnSe lasers with different dispersion compensation methods," Applied Physics B, vol. 106, pp. 887–892, Jan. 2012.

[139] A. V. Husakou and J. Herrmann, "Supercontinuum generation, four-wave mixing, and fission of higher-order solitons in photonic-crystal fibers," Journal of the Optical Society of America B, vol. 19, no. 9, pp. 2171–2182, 2002.

[140] J. Herrmann, U. Griebner, N. Zhavoronkov, A. Husakou, D. Nickel, J. C. Knight, W. J. Wadsworth, P. S. J. Russell, and G. Korn, "Experimental Evidence for Supercontinuum Generation by Fission of Higher-Order Solitons in Photonic Fibers," Physical Review Letters, vol. 88, p. 173901, Apr. 2002.

[141] J. Dudley and S. Coen, "Numerical simulations and coherence properties of supercontinuum generation in photonic crystal and tapered optical fibers," IEEE Journal of Selected Topics in Quantum Electronics, vol. 8, pp. 651–659, May 2002.

[142] J. M. Dudley and S. Coen, "Supercontinuum generation in photonic crystal fiber," Reviews of Modern Physics, vol. 78, pp. 1135–1184, Oct. 2006.

[143] J. M. Dudley and J. R. Taylor, eds., Supercontinuum Generation in Optical Fibers. 2010.

[144] K. Blow and D. Wood, "Theoretical description of transient stimulated Raman scattering in optical fibers," IEEE Journal of Quantum Electronics, vol. 25, no. 12, pp. 2665–2673, 1989.

[145] G. P. Agrawal, Applications of Nonlinear Fiber Optics. Academic Press, 2008.

[146] Q. Lin and G. P. Agrawal, "Raman response function for silica fibers.," Optics Letters, vol. 31, pp. 3086–8, Nov. 2006.

[147] I. Cristiani, R. Tediosi, L. Tartara, and V. Degiorgio, "Dispersive wave generation by solitons in microstructured optical fibers," Optics Express, vol. 12, no. 1, p. 124, 2004.

[148] T. Hori, N. Nishizawa, T. Goto, and M. Yoshida, "Experimental and numerical analysis of widely broadened supercontinuum generation in highly nonlinear dispersion-shifted fiber with a femtosecond pulse," Journal of the Optical Society of America B, vol. 21, no. 11, pp. 1969–1980, 2004.

[149] I. Hartl, G. Imeshev, L. Dong, G. C. Cho, and M. E. Fermann, "Ultra-compact dispersion compensated femtosecond fiber oscillators and amplifiers," in Conference on Lasers and Electro-Optics, 2005, vol. 3, pp. 1641–1643, IEEE, 2006.

[150] N. R. Newbury and W. C. Swann, "Low-noise fiber-laser frequency combs," JOSA B, vol. 24, no. 8, pp. 1756–1770, 2007.

[151] J. M. Dudley and S. Coen, "Numerical simulations and coherence properties of supercontinuum generation in photonic crystal and tapered optical fibers," IEEE Journal of Selected Topics in Quantum Electronics, vol. 8, no. 3, pp. 651–659, 2002.

[152] M. Nakazawa, K. Tamura, H. Kubota, and E. Yoshida, "Coherence degradation in the process of supercontinuum generation in an optical fiber," Optical Fiber Technology, vol. 4, no. 2, pp. 215–223, 1998.

[153] T. R. Schibli, I. Hartl, D. C. Yost, M. J. Martin, A. Marcinkevicius, M. E. Fermann, and J. Ye, "Optical frequency comb with submillihertz linewidth and more than 10 W average power," Nature Photonics, vol. 2, no. 6, pp. 355–359, 2008.

[154] A. Ruehl, A. Marcinkevicius, M. E. Fermann, and I. Hartl, "80 W, 120 fs Yb-fiber frequency comb," Optics Letters, vol. 35, no. 18, pp. 3015–3017, 2010.

[155] H. P. Yuen and V. W. S. Chan, "Noise in homodyne and heterodyne detection," Optics Letters, vol. 8, no. 3, pp. 177–179, 1983.

[156] K. L. Corwin, N. R. Newbury, J. M. Dudley, S. Coen, S. A. Diddams, K. Weber, and R. S. Windeler, "Fundamental noise limitations to supercontinuum generation in microstructure fiber," Physical Review Letters, vol. 90, no. 11, p. 113904, 2003.

[157] R. Paschotta, "Noise of mode-locked lasers (Part I): numerical model," Applied Physics B: Lasers and Optics, vol. 79, no. 2, pp. 153–162, 2004.

[158] M. Bellini and T. W. Haensch, "Phase-locked white-light continuum pulses: toward a universal optical frequency-comb synthesizer," Optics Letters, vol. 25, no. 14, pp. 1049–1051, 2000.

[159] M. J. Martin, S. M. Foreman, T. R. Schibli, and J. Ye, "Testing ultrafast mode-locking at microhertz relative optical linewidth," Optics Express, vol. 17, no. 2, pp. 558–568, 2009.

[160] A. Demircan and U. Bandelow, "Analysis of the interplay between soliton fission and modulation instability in supercontinuum generation," Applied Physics B: Lasers and Optics, vol. 86, no. 1, pp. 31–39, 2007.

[161] G. D. Boyd, "Parametric Interaction of Focused Gaussian Light Beams," Journal of Applied Physics, vol. 39, p. 3597, Nov. 1968.

[162] G. I. Stegeman and R. A. Stegeman, Nonlinear Optics: Phenomena, Materials and Devices. John Wiley & Sons, 2012.

[163] M. J. McCarthy and D. C. Hanna, "All-solid-state synchronously pumped optical parametric oscillator," Journal of the Optical Society of America B, vol. 10, p. 2180, Nov. 1993.

[164] T. Graf, G. McConnell, A. I. Ferguson, E. Bente, D. Burns, and M. D. Dawson, "Synchronously Pumped Optical Parametric Oscillation in Periodically Poled Lithium Niobate with 1-W Average Output Power," Applied Optics, vol. 38, p. 3324, May 1999.

[165] W. Nagourney, Quantum Electronics for Atomic Physics. Oxford University Press, 2014.

[166] A. E. Siegman, Lasers. University Science Books, 1986.

[167] D. E. Zelmon, D. L. Small, and D. Jundt, "Infrared corrected Sellmeier coefficients for congruently grown lithium niobate and 5 mol.% magnesium oxide doped lithium niobate," Journal of the Optical Society of America B, vol. 14, p. 3319, Dec. 1997.

[168] L. Myers and W. Bosenberg, "Periodically poled lithium niobate and quasi-phase-matched optical parametric oscillators," IEEE Journal of Quantum Electronics, vol. 33, no. 10, pp. 1663–1672, 1997.

[169] T. C. Briles, D. C. Yost, A. Cingöz, J. Ye, and T. R. Schibli, "Simple piezoelectric-actuated mirror with 180 kHz servo bandwidth.," Optics Express, vol. 18, pp. 9739–46, May 2010.

[170] F. Adler, P. Maslowski, A. Foltynowicz, K. C. Cossel, T. C. Briles, I. Hartl, and J. Ye, "Mid-infrared Fourier transform spectroscopy with a broadband frequency comb.," Optics Express, vol. 18, pp. 21861–72, Oct. 2010.

[171] K. K. Lehmann, P. S. Johnston, and P. Rabinowitz, "Brewster angle prism retroreflectors for cavity enhanced spectroscopy," Applied Optics, vol. 48, pp. 2966–2978, 2009.

[172] B. Lee, K. Lehmann, J. Taylor, and A. Yalin, "A high-finesse broadband optical cavity using calcium fluoride prism retroreflectors.," Optics Express, vol. 22, pp. 11583–91, May 2014.

[173] A. P. Belousov, E. M. Dianov, I. S. Lisitski, T. M. Nesterova, V. G. Plotnichenko, and V. K. Sysoev, "Single crystals of thallium halides with optical losses below 10dB/km," Soviet Journal of Quantum Electronics, vol. 12, pp. 496–497, Apr. 1982.

[174] E. W. Baumgartner, T. Schwarzl, G. Springholz, and W. Heiss, "Highly efficient epitaxial Bragg mirrors with broad omnidirectional reflectance bands in the midinfrared," Applied Physics Letters, vol. 89, p. 051110, Aug. 2006.

[175] T. Schwarzl, M. Eibelhuber, W. Heiss, E. Kaufmann, G. Springholz, A. Winter, and H. Pascher, "Mid-infrared high finesse microcavities and vertical-cavity lasers based on IVVI semiconductor/BaF2 broadband Bragg mirrors," Journal of Applied Physics, vol. 101, p. 093102, May 2007.

[176] G. D. Cole, W. Zhang, M. J. Martin, J. Ye, and M. Aspelmeyer, "Tenfold reduction of Brownian noise in high-reflectivity optical coatings," Nature Photonics, vol. 7, pp. 644–650, July 2013.

[177] E. D. Black, "An introduction to PoundDreverHall laser frequency stabilization," American Journal of Physics, vol. 69, p. 79, Jan. 2001.

[178] T. Hänsch and B. Couillaud, "Laser frequency stabilization by polarization spectroscopy of a reflecting reference cavity," Optics Communications, vol. 35, pp. 441–444, Dec. 1980.

[179] R. J. Jones, I. Thomann, and J. Ye, "Precision stabilization of femtosecond lasers to high-finesse optical cavities," Physical Review A, vol. 69, p. 051803, May 2004.

[180] A. Khodabakhsh, C. Abd Alrahman, and A. Foltynowicz, "Noise-immune cavity-enhanced optical frequency comb spectroscopy.," Optics Letters, vol. In Press, 2014.

[181] T. Gherman and D. Romanini, "Modelocked Cavity–Enhanced Absorption Spectroscopy," Optics Express, vol. 10, p. 1033, Sept. 2002.

[182] S. Kassi, K. Didriche, C. Lauzin, X. d. G. d'Elseghem Vaernewijckb, A. Rizopoulos, and M. Herman, "Demonstration of cavity enhanced FTIR spectroscopy using a femtosecond laser absorption source.," Spectrochimica Acta Part A: Molecular and Biomolecular Spectroscopy, vol. 75, pp. 142–5, Jan. 2010.

[183] R. Grilli, G. Méjean, S. Kassi, I. Ventrillard, C. Abd-Alrahman, and D. Romanini, "Frequency Comb Based Spectrometer for in Situ and Real Time Measurements of IO, BrO, NO(2), and H(2)CO at pptv and ppqv Levels.," Environmental Science & Technology, vol. 46, pp. 10704–10, Oct. 2012.

[184] R. Grilli, M. Legrand, A. Kukui, G. Méjean, S. Preunkert, and D. Romanini, "First investigations of IO, BrO, and NO 2 summer atmospheric levels at a coastal East Antarctic site using mode-locked cavity enhanced absorption spectroscopy," Geophysical Research Letters, vol. 40, pp. 791–796, Feb. 2013.

[185] R. Grilli, G. Méjean, C. Abd Alrahman, I. Ventrillard, S. Kassi, and D. Romanini, "Cavity-enhanced multiplexed comb spectroscopy down to the photon shot noise," Physical Review A, vol. 85, pp. 1–5, May 2012.

[186] J. Mandon, G. Guelachvili, and N. Picqué, "Fourier transform spectroscopy with a laser frequency comb," Nature Photonics, vol. 3, no. February, pp. 99–102, 2009.

[187] T. Gherman, S. Kassi, A. Campargue, and D. Romanini, "Overtone spectroscopy in the blue region by cavity-enhanced absorption spectroscopy with a mode-locked femtosecond laser: application to acetylene," Chemical Physics Letters, vol. 383, pp. 353–358, Jan. 2004.

[188] M. J. Thorpe, K. D. Moll, R. J. Jones, B. Safdi, and J. Ye, "Broadband cavity ringdown spectroscopy for sensitive and rapid molecular detection.," Science, vol. 311, pp. 1595–9, Mar. 2006.

[189] B. Bernhardt, A. Ozawa, P. Jacquet, M. Jacquey, Y. Kobayashi, T. Udem, R. Holzwarth, G. Guelachvili, T. W. Hänsch, and N. Picqué, "Cavity-enhanced dual-comb spectroscopy," Nature Photonics, vol. 4, pp. 55–57, 2010.

[190] G. Méjean, S. Kassi, and D. Romanini, "Measurement of reactive atmospheric species by ultraviolet cavity-enhanced spectroscopy with a mode-locked femtosecond laser," Optics Letters, vol. 33, p. 1231, May 2008.

[191] M. Villa, L. Fusina, G. Di Lonardo, X. De Ghellinck d'Elseghem Vaernewijck, and M. Herman, "Femto-FT-CEAS investigation of rare acetylene isotopologues (H 12 C 13 CD, D 12 C 13 CH and D 12 C 13 CD)," Molecular Physics, vol. 111, pp. 1972–1976, Aug. 2013.

[192] A. Marian, M. C. Stowe, J. R. Lawall, D. Felinto, and J. Ye, "United time-frequency spectroscopy for dynamics and global structure.," Science, vol. 306, pp. 2063–8, Dec. 2004.

[193] D. Felinto and C. López, "Theory for direct frequency-comb spectroscopy," Physical Review A, vol. 80, p. 013419, July 2009.

[194] E. Peters, D. C. Yost, A. Matveev, T. W. Hänsch, and T. Udem, "Frequency-comb spectroscopy of the hydrogen 1S-3S and 1S-3D transitions," Annalen der Physik, vol. 525, pp. L29–L34, July 2013.

[195] C. Gohle, B. Stein, A. Schliesser, T. Udem, and T. Hänsch, "Frequency Comb Vernier Spectroscopy for Broadband, High-Resolution, High-Sensitivity Absorption and Dispersion Spectra," Physical Review Letters, vol. 99, p. 263902, Dec. 2007.

[196] S. E. Fiedler, A. Hese, and A. A. Ruth, "Incoherent broad-band cavity-enhanced absorption spectroscopy," Chemical Physics Letters, vol. 371, pp. 284–294, Apr. 2003.

[197] S. M. Ball, J. M. Langridge, and R. L. Jones, "Broadband cavity enhanced absorption spectroscopy using light emitting diodes," Chemical Physics Letters, vol. 398, pp. 68–74, Nov. 2004.

[198] S. M. Ball and R. L. Jones, "Broad-band cavity ring-down spectroscopy.," Chemical Reviews, vol. 103, pp. 5239–62, Dec. 2003.

[199] U. Platt and J. Stutz, Differential Optical Absorption Spectroscopy. Physics of Earth and Space Environments, Berlin, Heidelberg: Springer Berlin Heidelberg, 2008.

[200] M. Shirasaki, "Large angular dispersion by a virtually imaged phased array and its application to a wavelength demultiplexer," Optics Letters, vol. 21, pp. 366–369, 1996.

[201] S. Xiao and A. M. Weiner, "2-D wavelength demultiplexer with potential for 1000 channels in the C-band," Optics Express, vol. 12, pp. 2895–2902, 2004.

[202] S. X. Wang, S. Xiao, and A. M. Weiner, "Broadband, high spectral resolution 2-D wavelength-parallel polarimeter for Dense WDM systems," Optics Express, vol. 13, pp. 9374–9380, 2005.

[203] J. A. Silver, "Frequency-modulation spectroscopy for trace species detection: theory and comparison among experimental methods: errata.," Applied Optics, vol. 31, p. 4927, Aug. 1992.

[204] D. S. Bomse, A. C. Stanton, and J. A. Silver, "Frequency modulation and wavelength modulation spectroscopies: comparison of experimental methods using a lead-salt diode laser.," Applied Optics, vol. 31, pp. 718–31, Feb. 1992.

[205] G. B. Rieker, J. B. Jeffries, and R. K. Hanson, "Calibration-free wavelength-modulation spectroscopy for measurements of gas temperature and concentration in harsh environments.," Applied Optics, vol. 48, pp. 5546–60, Oct. 2009.

[206] A. Zybin, Y. Kuritsyn, V. Mironenko, and K. Niemax, "Cavity enhanced wavelength modulation spectrometry for application in chemical analysis," Applied Physics B: Lasers and Optics, vol. 78, pp. 103–109, Jan. 2004.

[207] M. J. Thorpe, F. Adler, K. C. Cossel, M. H. de Miranda, and J. Ye, "Tomography of a supersonically cooled molecular jet using cavity-enhanced direct frequency comb spectroscopy," Chemical Physics Letters, vol. 468, pp. 1–8, Jan. 2009.

[208] L. C. Sinclair, Development of Frequency Comb Velocity-Modulation Spectroscopy, Spectroscopy of HfF+ and the JILA eEDM Experiment. PhD thesis, University of Colorado - Boulder, 2012.

[209] G. R. HARRISON, "The Production of Diffraction Gratings: II The Design of Echelle Gratings and Spectrographs," Journal of the Optical Society of America, vol. 39, p. 522, July 1949.

[210] D. J. Schroeder, "An echelle spectrometer-spectrograph for astronomical use.," Applied Optics, vol. 6, pp. 1976–80, Nov. 1967.

[211] D. Nevejans, E. Neefs, E. Van Ransbeeck, S. Berkenbosch, R. Clairquin, L. De Vos, W. Moelans, S. Glorieux, A. Baeke, O. Korablev, I. Vinogradov, Y. Kalinnikov, B. Bach, J.-P. Dubois, and E. Villard, "Compact high-resolution spaceborne echelle grating spectrometer with acousto-optical tunable filter based order sorting for the infrared domain from 2.2 to 4.3 μm," Applied Optics, vol. 45, no. 21, p. 5191, 2006.

[212] D. L. McDavitt, J. Ge, S. Miller, and J. Wang, "Silicon Immersion Gratings for Very High Resolution Infrared Spectroscopy," in Astronomical Telescopes and Instrumentation (E. Atad-Ettedgui and P. Dierickx, eds.), pp. 536–544, International Society for Optics and Photonics, Sept. 2004.

[213] N. Ebizuka, K. Oka, A. Yamada, M. Kashiwagi, K. Kodate, K. S. Kawabata, M. Uehara, C. Nagashima, K. Ichiyama, T. Ichikawa, T. Shimizu, S. Morita, Y. Yamagata, H. Omori, H. Tokoro, Y. Hirahara, S. Sato, and M. Iye, "Novel immersion grating, VPH

grating, and quasi-Bragg grating," in Optomechanical Technologies for Astronomy. Edited by Atad-Ettedgui (E. Atad-Ettedgui, J. Antebi, and D. Lemke, eds.), vol. 6273, pp. 62732G–62732G–8, June 2006.

[214] D. J. Mar, J. P. Marsh, C. P. Deen, H. Ling, H. Choo, and D. T. Jaffe, "Micromachined silicon grisms for infrared optics," Applied Optics, vol. 48, p. 1016, Feb. 2009.

[215] J. Ge, J. L. Bernecker, D. L. McDavitt, and S. Miller, "Silicon anamorphic gratings for IR high-resolution spectroscopy with future giant telescopes," in Astronomical Telescopes and Instrumentation (J. R. P. Angel and R. Gilmozzi, eds.), pp. 624–633, International Society for Optics and Photonics, Jan. 2003.

[216] J. P. Marsh, D. J. Mar, and D. T. Jaffe, "Production and evaluation of silicon immersion gratings for infrared astronomy.," Applied Optics, vol. 46, pp. 3400–16, June 2007.

[217] M. Gully-Santiago, W. Wang, C. Deen, and D. Jaffe, "Near-infrared metrology of high-performance silicon immersion gratings," in Modern Technologies in Space- and Ground-based Telescopes and Instrumentation II. Proceedings of the SPIE (R. Navarro, C. R. Cunningham, and E. Prieto, eds.), vol. 8450, p. 84502S, Sept. 2012.

[218] J. Ge, B. Zhao, S. Powell, A. Fletcher, X. Wan, L. Chang, H. Jakeman, D. Koukis, D. B. Tanner, D. Ebbets, J. Weinberg, S. Lipscy, R. Nyquist, and J. Bally, "Silicon immersion gratings and their spectroscopic applications," in SPIE Astronomical Telescopes + Instrumentation (R. Navarro, C. R. Cunningham, and E. Prieto, eds.), p. 84502U, International Society for Optics and Photonics, Sept. 2012.

[219] P. C. Hobbs, "Ultrasensitive laser measurements without tears.," Applied Optics, vol. 36, pp. 903–20, Feb. 1997.

[220] N. R. Newbury, I. Coddington, and W. Swann, "Sensitivity of coherent dual-comb spectroscopy.," Optics Express, vol. 18, pp. 7929–45, Apr. 2010.

[221] S. Schiller, "Spectrometry with frequency combs," Optics Letters, vol. 27, p. 766, May 2002.

[222] A. Schliesser, M. Brehm, F. Keilmann, and D. W. van der Weide, "Frequency-comb infrared spectrometer for rapid, remote chemical sensing.," Optics Express, vol. 13, pp. 9029–38, Oct. 2005.

[223] I. Coddington, W. C. Swan, and N. R. Newbury, "Coherent Multiheterodyne Spectroscopy Using Stabilized Optical Frequency Combs," Physical Review Letters, vol. 100, p. 13902, 2008.

[224] A. M. Zolot, F. R. Giorgetta, E. Baumann, J. W. Nicholson, W. C. Swann, I. Coddington, and N. R. Newbury, "Direct-comb molecular spectroscopy with accurate, resolved comb teeth over 43 THz.," Optics Letters, vol. 37, pp. 638–40, Feb. 2012.

[225] T. Ideguchi, A. Poisson, G. Guelachvili, N. Picqué, and T. W. Hänsch, "Adaptive real-time dual-comb spectroscopy.," Nature Communications, vol. 5, p. 3375, Jan. 2014.

[226] Z. Zhang, T. Gardiner, and D. T. Reid, "Mid-infrared dual-comb spectroscopy with an optical parametric oscillator.," Optics letters, vol. 38, pp. 3148–50, Aug. 2013.

[227] Y. Jin, S. M. Cristescu, F. J. M. Harren, and J. Mandon, "Two-crystal mid-infrared optical parametric oscillator for absorption and dispersion dual-comb spectroscopy.," Optics letters, vol. 39, pp. 3270–3, June 2014.

[228] A. Borschevsky, M. Iliaš, V. A. Dzuba, V. V. Flambaum, and P. Schwerdtfeger, "Relativistic study of nuclear-anapole-moment effects in diatomic molecules," Physical Review A, vol. 88, p. 022125, Aug. 2013.

[229] K. Pachucki and J. Komasa, "Rovibrational levels of helium hydride ion.," The Journal of Chemical Physics, vol. 137, p. 204314, Nov. 2012.

[230] J. H. V. Nguyen and B. Odom, "Prospects for Doppler cooling of three-electronic-level molecules," Physical Review A, vol. 83, p. 053404, May 2011.

[231] J. H. V. Nguyen, C. R. Viteri, E. G. Hohenstein, C. D. Sherrill, K. R. Brown, and B. Odom, "Challenges of laser-cooling molecular ions," New Journal of Physics, vol. 13, p. 063023, June 2011.

[232] P. F. Staanum, K. Hø jbjerre, P. S. Skyt, A. K. Hansen, and M. Drewsen, "Rotational laser cooling of vibrationally and translationally cold molecular ions," Nature Physics, vol. 6, pp. 271–274, Mar. 2010.

[233] D. T. Halfen and L. M. Ziurys, "Laboratory Detection of FeCO + (X 4 Σ -) by Millimeter/Submillimeter Velocity Modulation Spectroscopy," The Astrophysical Journal, vol. 657, pp. L61–L64, Mar. 2007.

[234] N. Indriolo and B. J. McCall, "Cosmic-ray astrochemistry.," Chemical Society reviews, vol. 42, pp. 7763–73, Oct. 2013.

[235] T. P. Snow and V. M. Bierbaum, "Ion chemistry in the interstellar medium.," Annual Review of Analytical Chemistry, vol. 1, pp. 229–59, Jan. 2008.

[236] T. P. Snow and B. J. McCall, "Diffuse Atomic and Molecular Clouds," Annual Review of Astronomy and Astrophysics, vol. 44, pp. 367–414, Sept. 2006.

[237] N. Indriolo, T. Oka, T. R. Geballe, and B. J. McCall, "Constraining the Environment of CH+ Formation With CH3+ Observations," The Astrophysical Journal, vol. 711, pp. 1338–1342, Mar. 2010.

[238] G. Cazzoli, L. Cludi, G. Buffa, and C. Puzzarini, "PRECISE THz MEASUREMENTS OF HCO+ , N2H+ , AND CF+ FOR ASTROPHYSICAL OBSERVATIONS," The Astrophysical Journal Supplement Series, vol. 203, p. 11, Nov. 2012.

[239] B. M. Siller, J. N. Hodges, A. J. Perry, and B. J. McCall, "Indirect rotational spectroscopy of HCO+.," The journal of physical chemistry. A, vol. 117, pp. 10034–40, Oct. 2013.

[240] P. J. Sarre, "The diffuse interstellar bands: A major problem in astronomical spectroscopy," Journal of Molecular Spectroscopy, vol. 238, pp. 1–10, July 2006.

[241] T. Oka and B. J. McCall, "Astronomy. Disclosing identities in diffuse interstellar bands.," Science (New York, N.Y.), vol. 331, pp. 293–4, Jan. 2011.

[242] J. P. Maier, G. A. H. Walker, D. A. Bohlender, F. J. Mazzotti, R. Raghunandan, J. Fulara, I. Garkusha, and A. Nagy, "Identification of H2CCC as a Diffuse Interstellar Band Carrier," The Astrophysical Journal, vol. 726, p. 41, Jan. 2011.

[243] E. Herbst and E. F. van Dishoeck, "Complex Organic Interstellar Molecules," Annual Review of Astronomy and Astrophysics, vol. 47, pp. 427–480, Sept. 2009.

[244] J. L. Gottfried, B. J. McCall, and T. Oka, "Near-infrared spectroscopy of H3+ above the barrier to linearity," The Journal of Chemical Physics, vol. 118, no. 24, p. 10890, 2003.

[245] C. P. Morong, J. L. Gottfried, and T. Oka, "H3+ as the benchmark for rigorous ab initio theory," Journal of Molecular Spectroscopy, vol. 255, pp. 13–23, May 2009.

[246] M. Pavanello, L. Adamowicz, A. Alijah, N. Zobov, I. Mizus, O. L. Polyansky, J. Tennyson, T. Szidarovszky, A. G. Császár, M. Berg, A. Petrignani, and A. Wolf, "Precision Measurements and Computations of Transition Energies in Rotationally Cold Triatomic Hydrogen Ions up to the Midvisible Spectral Range," Physical Review Letters, vol. 108, p. 023002, Jan. 2012.

[247] T. C. Cheng, L. Jiang, K. R. Asmis, Y. Wang, J. M. Bowman, A. M. Ricks, and M. A. Duncan, "Mid- and Far-IR Spectra of H 5 + and D 5 + Compared to the Predictions of Anharmonic Theory," The Journal of Physical Chemistry Letters, vol. 3, pp. 3160–3166, Nov. 2012.

[248] E. T. White, "CH5+: The Infrared Spectrum Observed," Science, vol. 284, pp. 135–137, Apr. 1999.

[249] O. Asvany, P. K. P, B. Redlich, I. Hegemann, S. Schlemmer, and D. Marx, "Understanding the infrared spectrum of bare CH5+.," Science, vol. 309, pp. 1219–22, Aug. 2005.

[250] X. Huang, A. B. McCoy, J. M. Bowman, L. M. Johnson, C. Savage, F. Dong, and D. J. Nesbitt, "Quantum deconstruction of the infrared spectrum of CH5+.," Science, vol. 311, pp. 60–3, Jan. 2006.

[251] H.-S. Andrei, N. Solcà, and O. Dopfer, "IR spectrum of the ethyl cation: evidence for the nonclassical structure.," Angewandte Chemie (International ed. in English), vol. 47, pp. 395–7, Jan. 2008.

[252] A. A. Mills, B. M. Siller, M. W. Porambo, M. Perera, H. Kreckel, and B. J. McCall, "Ultrasensitive high-precision spectroscopy of a fast molecular ion beam.," The Journal of Chemical Physics, vol. 135, p. 224201, Dec. 2011.

[253] P. Martin and G. Guelachvili, "Velocity-Modulation Fourier-Transform Spectroscopy of Molecular Ions," Physical Review Letters, vol. 65, no. 20, pp. 2535–2538, 1990.

[254] N. Picque and G. Guelachvili, "High-resolution multimodulation Fourier-transform spectroscopy," Applied Optics, vol. 38, no. 7, pp. 1224–1230, 1999.

[255] T. Spirig, M. Marley, and P. Seitz, "The Multitap Lock-In CCD with Offset Subtraction," IEEE Transactions on Electron Devices, vol. 44, no. 10, pp. 1643–1647, 1997.

[256] S. Beer and P. Seitz, "A smart pixel array with massively parallel signal processing for real-time optical coherence tomography performing close to the physical limits," Research in Microelectronics and Electronics, 2005 PhD, vol. 2, pp. 135–138, 2005.

[257] K. Holman, R. Jones, A. Marian, and S. Cundiff, "Detailed studies and control of intensity-related dynamics of femtosecond frequency combs from mode-locked Ti:sapphire lasers," IEEE Journal of Selected Topics in Quantum Electronics, vol. 9, pp. 1018–1024, July 2003.

[258] D. Heinecke, a. Bartels, T. Fortier, D. Braje, L. Hollberg, and S. Diddams, "Optical frequency stabilization of a 10 GHz Ti:sapphire frequency comb by saturated absorption spectroscopy in ˆ{87}rubidium," Physical Review A, vol. 80, pp. 1–7, Nov. 2009.

[259] B. M. Siller, A. A. Mills, and B. J. McCall, "Cavity-enhanced velocity modulation spectroscopy.," Optics Letters, vol. 35, pp. 1266–8, Apr. 2010.

[260] D. T. Anderson, S. Davis, T. S. Zwier, and D. J. Nesbitt, "An intense slit discharge source of jet-cooled molecular ions and radicals (Trot ¡ 30 K)," Chemical Physics Letters, vol. 4, no. August, pp. 1–6, 1996.

[261] T. A. Johnson and S. A. Diddams, "Mid-infrared upconversion spectroscopy based on a Yb:fiber femtosecond laser," Applied Physics B, vol. 107, pp. 31–39, Oct. 2011.

[262] R. Wehr, S. Kassi, D. Romanini, and L. Gianfrani, "Optical feedback cavity-enhanced absorption spectroscopy for in situ measurements of the ratio 13C:12C in CO2," Applied Physics B: Lasers and Optics, vol. 92, pp. 459–465, 2008.

[263] M. H. Dunn and M. Ebrahimzadeh, "Parametric Generation of Tunable Light from Continuous-Wave to Femtosecond Pulses," Science, vol. 286, pp. 1513–1517, 1999.

[264] M. L. Hamilton, R. Peverall, G. A. D. Ritchie, L. J. Thornton, J. H. van Helden, and J. H. Helden, "Wavelength modulation and cavity enhanced absorption spectroscopy using ˜1.9 um radiation produced by difference frequency generation with a MgO doped PPLN crystal," Applied Physics B: Lasers and Optics, vol. 97, pp. 715–722, July 2009.

[265] S. K. Lehman, K. A. Bertness, and J. T. Hodges, "Detection of trace water in phosphine with cavity ring-down spectroscopy," Journal of Crystal Growth, vol. 250, pp. 262–268, 2003.

[266] H. H. Funke, B. L. Grissom, C. E. McGrew, and M. W. Raynor, "Techniques for the measurement of trace moisture in high-purity electronic specialty gases," Review of Scientific Instruments, vol. 74, p. 3909, Sept. 2003.

[267] H. H. Funke, M. W. Raynor, K. A. Bertness, and Y. Chen, "Detection of Trace Water Vapor in High-Purity Phosphine Using Cavity Ring-down Spectroscopy," Applied Spectroscopy, vol. 61, pp. 419–423, 2007.

[268] J. Feng, R. Clement, and M. Raynor, "Characterization of high-purity arsine and gallium arsenide epilayers grown by MOCVD," Journal of Crystal Growth, vol. 310, pp. 4780–4785, Nov. 2008.

[269] K. Siefering, H. Berger, and W. Whitlock, "Quantitative analysis of contaminants in ultrapure gases at the parts-per-trillion level using atmospheric-pressure ionization mass spectroscopy," Journal of Vacuum Science and Technology, vol. 11, pp. 1593–1597, 1993.

[270] S. Y. Lehman, K. A. Bertness, and J. T. Hodges, "Optimal spectral region for real-time monitoring of sub-ppm levels of water in phosphine by cavity ring-down spectroscopy," Journal of Crystal Growth, vol. 261, pp. 225–230, 2004.

[271] L. S. Rothman, I. E. Gordon, A. Barbe, D. C. Benner, P. E. Bernath, M. Birk, V. Boudon, L. R. Brown, A. Campargue, J. P. Champion, K. Chance, L. H. Coudert, V. Dana, V. M. Devi, S. Fally, J. M. Flaud, R. R. Gamache, A. Goldman, D. Jacquemart, I. Kleiner, N. Lacome, W. J. Lafferty, J. Y. Mandin, S. T. Massie, S. N. Mikhailenko, C. E. Miller, N. Moazzen-Ahmadi, O. V. Naumenko, A. V. Nikitin, J. Orphal, V. I. Perevalov, A. Perrin, A. Predoi-Cross, C. P. Rinsland, M. Rotger, M. Simeckova, M. A. H. Smith, K. Sung, S. A. Tashkun, J. Tennyson, R. A. Toth, A. C. Vandaele, and J. Vander Auwera, "The HITRAN 2008 molecular spectroscopic database," Journal of Quantitative Spectroscopy and Radiative Transfer, vol. 110, no. 9-10, Sp. Iss. SI, pp. 533–572, 2009.

[272] A. Hubaux and G. Vos, "Decision and Detection Limits for Linear Calibration Curves," Analytical Chemistry, vol. 42, pp. 849–855, 1970.

[273] G. L. Long and J. D. Winefordner, "Limit of Detection A Closer Look at the IUPAC Definition," Analytical Chemistry, vol. 55, pp. 712A–724A, 1983.

[274] SEMI, "C10-1109, Guide for Determination of Method Detection Limits."

[275] M. B. Esler, D. W. T. Griffith, S. R. Wilson, and L. P. Steele, "Precision Trace Gas Analysis by FT-IR Spectroscopy. 1. Simultaneous Analysis of CO 2 , CH 4 , N 2 O, and CO in Air," Analytical Chemistry, vol. 72, pp. 206–215, Jan. 2000.

[276] E. D. Schulze, S. Luyssaert, P. Ciais, A. Freibauer, I. A. Janssens et al., J. F. Soussana, P. Smith, J. Grace, I. Levin, B. Thiruchittampalam, M. Heimann, A. J. Dolman, R. Valentini, P. Bousquet, P. Peylin, W. Peters, C. Rödenbeck, G. Etiope, N. Vuichard, M. Wattenbach, G. J. Nabuurs, Z. Poussi, J. Nieschulze, and J. H. Gash, "Importance of methane and nitrous oxide for Europe's terrestrial greenhouse-gas balance," Nature Geoscience, vol. 2, pp. 842–850, Nov. 2009.

[277] A. R. Ravishankara, J. S. Daniel, and R. W. Portmann, "Nitrous oxide (N2O): the dominant ozone-depleting substance emitted in the 21st century.," Science, vol. 326, pp. 123–5, Oct. 2009.

[278] T. N. Rosenstiel, M. J. Potosnak, K. L. Griffin, R. Fall, and R. K. Monson, "Increased CO2 uncouples growth from isoprene emission in an agriforest ecosystem.," Nature, vol. 421, pp. 256–9, Jan. 2003.

[279] W. Lei, M. Zavala, B. de Foy, R. Volkamer, M. J. Molina, and L. T. Molina, "Impact of primary formaldehyde on air pollution in the Mexico City Metropolitan Area," Atmospheric Chemistry and Physics, vol. 9, pp. 2607–2618, Apr. 2009.

[280] W. Miekisch, J. K. Schubert, and G. F. E. Noeldge-Schomburg, "Diagnostic potential of breath analysis–focus on volatile organic compounds.," Clinica Chimica Acta, vol. 347, pp. 25–39, Sept. 2004.

[281] K. D. Skeldon, L. C. McMillan, C. A. Wyse, S. D. Monk, G. Gibson, C. Patterson, T. France, C. Longbottom, and M. J. Padgett, "Application of laser spectroscopy for measurement of

exhaled ethane in patients with lung cancer.," Respiratory medicine, vol. 100, pp. 300–6, Feb. 2006.

[282] M. R. McCurdy, Y. Bakhirkin, G. Wysocki, R. Lewicki, and F. K. Tittel, "Recent advances of laser-spectroscopy-based techniques for applications in breath analysis.," Journal of breath research, vol. 1, p. 014001, Sept. 2007.

[283] D. W. Marquardt, "An Algorithm for Least-Squares Estimation of Nonlinear Parameters," Journal of the Society for Industrial and Applied Mathematics, vol. 11, pp. 431–441, June 1963.

[284] D. Benner, C. P. Rinsland, V. Devi, M. A. H. Smith, and D. Atkins, "A multispectrum nonlinear least squares fitting technique," Journal of Quantitative Spectroscopy and Radiative Transfer, vol. 53, pp. 705–721, June 1995.

[285] Y. Qu, Z.-H. Kang, Y. Jiang, and J.-Y. Gao, "Multiline absorption spectroscopy for methane gas detection.," Applied optics, vol. 45, pp. 8537–40, Nov. 2006.

[286] A. Karpf and G. N. Rao, "Enhanced sensitivity for the detection of trace gases using multiple line integrated absorption spectroscopy.," Applied optics, vol. 48, pp. 5061–6, Sept. 2009.

[287] EPA, "Protocol for Measuring Destruction or Removal Efficiency (DRE) of Fluorinated Greenhouse Gas Abatement Equipment in Electronics Manufacturing," 2010.

[288] A. Amann and D. Smith, Breath Analysis for Clinical Diagnosis and Therapeutic Monitoring. World Scientific Publishing Company, Incorporated, 2005.

[289] T. Risby and S. Solga, "Current status of clinical breath analysis," Applied Physics B, vol. 85, pp. 421–426, May 2006.

[290] B. Buszewski, M. Kesy, T. Ligor, and A. Amann, "Human exhaled air analytics: biomarkers of diseases.," Biomedical Chromatography, vol. 21, pp. 553–66, June 2007.

[291] A. Amann, W. Miekisch, J. Schubert, B. Buszewski, T. Ligor, T. Jezierski, J. Pleil, and T. Risby, "Analysis of Exhaled Breath for Disease Detection," Annual Review of Analytical Chemistry, vol. 7, pp. 455–482, July 2014.

[292] B. P. J. de Lacy Costello, M. Ledochowski, and N. M. Ratcliffe, "The importance of methane breath testing: a review.," Journal of breath research, vol. 7, p. 024001, June 2013.

[293] J. H. Shorter, D. D. Nelson, J. B. McManus, M. S. Zahniser, S. R. Sama, and D. K. Milton, "Clinical study of multiple breath biomarkers of asthma and COPD (NO, CO(2), CO and N(2)O) by infrared laser spectroscopy.," Journal of breath research, vol. 5, p. 037108, Sept. 2011.

[294] M. Sulway and J. Malins, "ACETONE IN DIABETIC KETOACIDOSIS," The Lancet, vol. 296, pp. 736–740, Oct. 1970.

[295] C. Deng, J. Zhang, X. Yu, W. Zhang, and X. Zhang, "Determination of acetone in human breath by gas chromatography-mass spectrometry and solid-phase microextraction with on-fiber derivatization.," Journal of Chromatography B, vol. 810, pp. 269–75, Oct. 2004.

[296] C. Turner, C. Walton, S. Hoashi, and M. Evans, "Breath acetone concentration decreases with blood glucose concentration in type I diabetes mellitus patients during hypoglycaemic clamps," Journal of Breath Research, vol. 3, p. 046004, Dec. 2009.

[297] L. R. Narasimhan, W. Goodman, and C. K. Patel, "Correlation of breath ammonia with blood urea nitrogen and creatinine during hemodialysis.," Proceedings of the National Academy of Sciences of the United States of America, vol. 98, pp. 4617–21, Apr. 2001.

[298] C. Popa, D. C. A. Dutu, R. Cernat, C. Matei, A. M. Bratu, S. Banita, and D. C. Dumitras, "Ethylene and ammonia traces measurements from the patients breath with renal failure via LPAS method," Applied Physics B, vol. 105, pp. 669–674, Sept. 2011.

[299] M. Phillips, "Method for the collection and assay of volatile organic compounds in breath.," Analytical Biochemistry, vol. 247, pp. 272–8, May 1997.

[300] M. Phillips, J. Herrera, S. Krishnan, M. Zain, J. Greenberg, and R. N. Cataneo, "Variation in volatile organic compounds in the breath of normal humans," Journal of Chromatography B: Biomedical Sciences and Applications, vol. 729, pp. 75–88, June 1999.

[301] P. Mochalski, J. King, M. Klieber, K. Unterkofler, H. Hinterhuber, M. Baumann, and A. Amann, "Blood and breath levels of selected volatile organic compounds in healthy volunteers.," The Analyst, vol. 138, pp. 2134–45, Apr. 2013.

[302] T. H. Risby and S. S. Sehnert, "Clinical Application of Breath Biomarkers of Oxidative Stress Status," Free Radical Biology & Medicine, vol. 27, no. 99, pp. 1182–1192, 1999.

[303] H. P. Chan, C. Lewis, and P. S. Thomas, "Oxidative Stress and Exhaled Breath Analysis: A Promising Tool for Detection of Lung Cancer," Cancers, vol. 2, pp. 32–42, Feb. 2010.

[304] M. Hakim, Y. Y. Broza, O. Barash, N. Peled, M. Phillips, A. Amann, and H. Haick, "Volatile organic compounds of lung cancer and possible biochemical pathways.," Chemical Reviews, vol. 112, pp. 5949–66, Nov. 2012.

[305] K. D. G. van de Kant, L. J. T. M. van der Sande, Q. Jöbsis, O. C. P. van Schayck, and E. Dompeling, "Clinical use of exhaled volatile organic compounds in pulmonary diseases: a systematic review.," Respiratory research, vol. 13, p. 117, Jan. 2012.

[306] M. Phillips, R. N. Cataneo, R. Condos, G. a. Ring Erickson, J. Greenberg, V. La Bombardi, M. I. Munawar, and O. Tietje, "Volatile biomarkers of pulmonary tuberculosis in the breath.," Tuberculosis (Edinburgh, Scotland), vol. 87, pp. 44–52, Jan. 2007.

[307] M. Phillips, N. Altorki, J. H. M. Austin, R. B. Cameron, R. N. Cataneo, R. Kloss, R. a. Maxfield, M. I. Munawar, H. I. Pass, A. Rashid, W. N. Rom, P. Schmitt, and J. Wai, "Detection of lung cancer using weighted digital analysis of breath biomarkers.," Clinica Chimica Acta, vol. 393, pp. 76–84, July 2008.

[308] P. J. Mazzone, "Analysis of volatile organic compounds in the exhaled breath for the diagnosis of lung cancer.," Journal of Thoracic Oncology, vol. 3, pp. 774–80, July 2008.

[309] S. Kischkel, W. Miekisch, A. Sawacki, E. M. Straker, P. Trefz, A. Amann, and J. K. Schubert, "Breath biomarkers for lung cancer detection and assessment of smoking related effects - confounding variables, influence of normalization and statistical algorithms.," Clinica Chimica Acta, vol. 411, pp. 1637–1644, June 2010.

[310] M. Phillips, R. N. Cataneo, C. Saunders, P. Hope, P. Schmitt, and J. Wai, "Volatile biomarkers in the breath of women with breast cancer.," Journal of Breath Research, vol. 4, p. 026003, June 2010.

[311] P. Fuchs, C. Loeseken, J. K. Schubert, and W. Miekisch, "Breath gas aldehydes as biomarkers of lung cancer.," International Journal of Cancer, vol. 126, pp. 2663–70, June 2010.

[312] M. Corradi, I. Rubinstein, R. Andreoli, P. Manini, A. Caglieri, D. Poli, R. Alinovi, and A. Mutti, "Aldehydes in exhaled breath condensate of patients with chronic obstructive pulmonary disease.," American Journal of Respiratory and Critical Care Medicine, vol. 167, pp. 1380–6, May 2003.

[313] J. E. Repine, J. W. Eaton, M. W. Anders, J. R. Hoidal, and R. B. Fox, "Generation of hydroxyl radical by enzymes, chemicals, and human phagocytes in vitro. Detection with the anti-inflammatory agent, dimethyl sulfoxide.," The Journal of clinical investigation, vol. 64, pp. 1642–51, Dec. 1979.

[314] P. Paredi, S. A. Kharitonov, D. Leak, S. Ward, D. Cramer, and P. J. Barnes, "Exhaled ethane, a marker of lipid peroxidation, is elevated in chronic obstructive pulmonary disease.," American journal of respiratory and critical care medicine, vol. 162, pp. 369–73, Aug. 2000.

[315] R. Stolarek, P. Bialasiewicz, M. Krol, and D. Nowak, "Breath analysis of hydrogen peroxide as a diagnostic tool.," Clinica Chimica Acta, vol. 411, pp. 1849–61, Dec. 2010.

[316] K. Schwarz, a. Pizzini, B. Arendacká, K. Zerlauth, W. Filipiak, a. Schmid, a. Dzien, S. Neuner, M. Lechleitner, S. Scholl-Bürgi, W. Miekisch, J. Schubert, K. Unterkofler, V. Witkovský, G. Gastl, and a. Amann, "Breath acetoneaspects of normal physiology related to age and gender as determined in a PTR-MS study," Journal of Breath Research, vol. 3, p. 027003, June 2009.

[317] B. Buszewski, T. Ligor, T. Jezierski, A. Wenda-Piesik, M. Walczak, and J. Rudnicka, "Identification of volatile lung cancer markers by gas chromatography-mass spectrometry: comparison with discrimination by canines.," Analytical and Bioanalytical Chemistry, vol. 404, pp. 141–6, July 2012.

[318] J. de Gouw and C. Warneke, "Measurements of volatile organic compounds in the earth's atmosphere using proton-transfer-reaction mass spectrometry.," Mass Spectrometry Reviews, vol. 26, no. 2, pp. 223–57, 2007.

[319] R. S. Blake, P. S. Monks, and A. M. Ellis, "Proton-transfer reaction mass spectrometry.," Chemical reviews, vol. 109, pp. 861–96, Mar. 2009.

[320] P. Trefz, M. Schmidt, P. Oertel, J. Obermeier, B. Brock, S. Kamysek, J. Dunkl, R. Zimmermann, J. K. Schubert, and W. Miekisch, "Continuous real time breath gas monitoring in the clinical environment by proton-transfer-reaction-time-of-flight-mass spectrometry.," Analytical Chemistry, vol. 85, pp. 10321–9, Nov. 2013.

[321] T. H. Risby, "Critical issues for breath analysis," Journal of Breath Research, vol. 2, p. 030302, Sept. 2008.

[322] B. J. Finlayson-Pitts, "Tropospheric Air Pollution: Ozone, Airborne Toxics, Polycyclic Aromatic Hydrocarbons, and Particles," Science, vol. 276, pp. 1045–1051, May 1997.

[323] P. W. Seakins and M. A. Blitz, "Developments in laboratory studies of gas-phase reactions for atmospheric chemistry with applications to isoprene oxidation and carbonyl chemistry.," Annual Review of Physical Chemistry, vol. 62, pp. 351–73, Jan. 2011.

[324] J. Lelieveld, T. M. Butler, J. N. Crowley, T. J. Dillon, H. Fischer, L. Ganzeveld, H. Harder, M. G. Lawrence, M. Martinez, D. Taraborrelli, and J. Williams, "Atmospheric oxidation capacity sustained by a tropical forest.," Nature, vol. 452, pp. 737–40, Apr. 2008.

[325] R. Sinreich, S. Coburn, B. Dix, and R. Volkamer, "Ship-based detection of glyoxal over the remote tropical Pacific Ocean," Atmospheric Chemistry and Physics, vol. 10, pp. 11359–11371, Dec. 2010.

[326] B. Dix, S. Baidar, J. F. Bresch, S. R. Hall, K. S. Schmidt, S. Wang, and R. Volkamer, "Detection of iodine monoxide in the tropical free troposphere.," Proceedings of the National Academy of Sciences of the United States of America, vol. 110, pp. 2035–40, Feb. 2013.

[327] S. S. Brown, J. A. Thornton, W. C. Keene, A. A. P. Pszenny, B. C. Sive, W. P. Dubé, N. L. Wagner, C. J. Young, T. P. Riedel, J. M. Roberts, T. C. VandenBoer, R. Bahreini, F. Öztürk, A. M. Middlebrook, S. Kim, G. Hübler, and D. E. Wolfe, "Nitrogen, Aerosol Composition, and Halogens on a Tall Tower (NACHTT): Overview of a wintertime air chemistry field study in the front range urban corridor of Colorado," Journal of Geophysical Research: Atmospheres, vol. 118, pp. 8067–8085, July 2013.

[328] B. H. Lee, E. C. Wood, M. S. Zahniser, J. B. McManus, D. D. Nelson, S. C. Herndon, G. W. Santoni, S. C. Wofsy, and J. W. Munger, "Simultaneous measurements of atmospheric HONO and NO2 viaabsorption spectroscopy using tunable mid-infrared continuous-wave quantum cascade lasers," Applied Physics B, Oct. 2010.

[329] A. K. Mollner, S. Valluvadasan, L. Feng, M. K. Sprague, M. Okumura, D. B. Milligan, W. J. Bloss, S. P. Sander, P. T. Martien, R. a. Harley, A. B. McCoy, and W. P. L. Carter, "Rate of gas phase association of hydroxyl radical and nitrogen dioxide.," Science, vol. 330, pp. 646–9, Oct. 2010.

[330] R. A. Washenfelder, M. Trainer, G. J. Frost, T. B. Ryerson, E. L. Atlas, J. A. de Gouw, F. M. Flocke, A. Fried, J. S. Holloway, D. D. Parrish, J. Peischl, D. Richter, S. M. Schauffler, J. G. Walega, C. Warneke, P. Weibring, and W. Zheng, "Characterization of NO x , SO 2 , ethene, and propene from industrial emission sources in Houston, Texas," Journal of Geophysical Research, vol. 115, p. D16311, Aug. 2010.

[331] J. B. Gilman, B. M. Lerner, W. C. Kuster, and J. A. de Gouw, "Source signature of volatile organic compounds from oil and natural gas operations in northeastern Colorado.," Environmental science & technology, vol. 47, pp. 1297–305, Feb. 2013.

[332] B. J. Finlayson-Pitts, J. N. Pitts, and Jr., Chemistry of the Upper and Lower Atmosphere: Theory, Experiments, and Applications. Academic Press, 1999.

[333] J. H. Seinfeld and S. N. Pandis, Atmospheric Chemistry and Physics: From Air Pollution to Climate Change. John Wiley & Sons, 2012.

[334] S. Vaughan, T. Gherman, A. A. Ruth, and J. Orphal, "Incoherent broad-band cavity-enhanced absorption spectroscopy of the marine boundary layer species I2, IO and OIO.," Physical Chemistry Chemical Physics, vol. 10, pp. 4471–7, Aug. 2008.

[335] R. A. Washenfelder, A. O. Langford, H. Fuchs, and S. S. Brown, "Measurement of glyoxal using an incoherent broadband cavity enhanced absorption spectrometer," Atmospheric Chemistry and Physics, vol. 8, pp. 7779–7793, Dec. 2008.

[336] R. Thalman and R. Volkamer, "Inherent calibration of a blue LED-CE-DOAS instrument to measure iodine oxide, glyoxal, methyl glyoxal, nitrogen dioxide, water vapour and aerosol extinction in open cavity mode," Atmospheric Measurement Techniques, vol. 3, pp. 1797–1814, Dec. 2010.

[337] S. Coburn, I. Ortega, R. Thalman, B. Blomquist, C. W. Fairall, and R. Volkamer, "Measurements of diurnal variations and Eddy Covariance (EC) fluxes of glyoxal in the tropical marine boundary layer: description of the Fast LED-CE-DOAS instrument," Atmospheric Measurement Techniques Discussions, vol. 7, pp. 6245–6285, June 2014.

[338] R. Atkinson, D. L. Baulch, R. A. Cox, J. N. Crowley, R. F. Hampson, R. G. Hynes, M. E. Jenkin, M. J. Rossi, and J. Troe, "Evaluated kinetic and photochemical data for atmospheric chemistry: Volume I - gas phase reactions of Ox, HOx, NOx and SOx species," Atmospheric Chemistry and Physics, vol. 4, pp. 1461–1738, Sept. 2004.

[339] R. Atkinson, D. L. Baulch, R. A. Cox, J. N. Crowley, R. F. Hampson, R. G. Hynes, M. E. Jenkin, M. J. Rossi, and J. Troe, "Evaluated kinetic and photochemical data for atmospheric chemistry: Volume II gas phase reactions of organic species," Atmospheric Chemistry and Physics, vol. 6, pp. 3625–4055, Sept. 2006.

[340] J. S. Francisco, J. T. Muckerman, and H.-G. Yu, "HOCO radical chemistry.," Accounts of Chemical Research, vol. 43, pp. 1519–26, Dec. 2010.

[341] Y.-T. Su, Y.-H. Huang, H. A. Witek, and Y.-P. Lee, "Infrared Absorption Spectrum of the Simplest Criegee Intermediate CH2OO," Science, vol. 340, pp. 174–176, Apr. 2013.

[342] W. H. Bunnelle, "Preparation, Properties, and Reactions of Carbonyl Oxides," Chemical Reviews, vol. 91, pp. 335–362, 1991.

[343] M. D. Hoops and B. S. Ault, "Matrix isolation study of the early intermediates in the ozonolysis of cyclopentene and cyclopentadiene: observation of two Criegee intermediates.," Journal of the American Chemical Society, vol. 131, pp. 2853–63, Mar. 2009.

[344] N. M. Donahue, G. T. Drozd, S. a. Epstein, A. a. Presto, and J. H. Kroll, "Adventures in ozoneland: down the rabbit-hole.," Physical Chemistry Chemical Physics, vol. 13, pp. 10848–57, June 2011.

[345] R. L. Mauldin, T. Berndt, M. Sipilä, P. Paasonen, T. Petäjä, S. Kim, T. Kurtén, F. Stratmann, V.-M. Kerminen, and M. Kulmala, "A new atmospherically relevant oxidant of sulphur dioxide.," Nature, vol. 488, pp. 193–6, Aug. 2012.

[346] C. J. Percival, O. Welz, A. J. Eskola, J. D. Savee, D. L. Osborn, D. O. Topping, D. Lowe, S. R. Utembe, A. Bacak, G. McFiggans, M. C. Cooke, P. Xiao, A. T. Archibald, M. E. Jenkin, R. G. Derwent, I. Riipinen, D. W. K. Mok, E. P. F. Lee, J. M. Dyke, C. A. Taatjes, and D. E. Shallcross, "Regional and global impacts of Criegee intermediates on atmospheric sulphuric acid concentrations and first steps of aerosol formation," Faraday Discussions, vol. 165, p. 45, Dec. 2013.

[347] Y. Sakamoto, S. Inomata, and J. Hirokawa, "Oligomerization reaction of the criegee intermediate leads to secondary organic aerosol formation in ethylene ozonolysis.," The journal of physical chemistry. A, vol. 117, pp. 12912–21, Dec. 2013.

[348] Y.-T. Su, H.-Y. Lin, R. Putikam, H. Matsui, M. C. Lin, and Y.-P. Lee, "Extremely rapid self-reaction of the simplest Criegee intermediate CH2OO and its implications in atmospheric chemistry.," Nature chemistry, vol. 6, pp. 477–83, June 2014.

[349] M. M. Galloway, A. J. Huisman, L. D. Yee, a. W. H. Chan, C. L. Loza, J. H. Seinfeld, and F. N. Keutsch, "Yields of oxidized volatile organic compounds during the OH radical initiated oxidation of isoprene, methyl vinyl ketone, and methacrolein under high-NOx conditions," Atmospheric Chemistry and Physics, vol. 11, pp. 10779–10790, Nov. 2011.

[350] A. S. Hasson, G. S. Tyndall, J. J. Orlando, S. Singh, S. Q. Hernandez, S. Campbell, and Y. Ibarra, "Branching ratios for the reaction of selected carbonyl-containing peroxy radicals with hydroperoxy radicals.," The Journal of Physical Chemistry A, vol. 116, pp. 6264–81, June 2012.

[351] T. Rubin, T. von Haimberger, a. Helmke, and K. Heyne, "Quantitative determination of metabolization dynamics by a real-time 13CO2 breath test.," Journal of breath research, vol. 5, p. 027102, June 2011.

[352] E. R. Crosson, K. N. Ricci, B. A. Richman, F. C. Chilese, T. G. Owano, R. A. Provencal, M. W. Todd, J. Glasser, A. A. Kachanov, B. A. Paldus, T. G. Spence, and R. N. Zare, "Stable Isotope Ratios Using Cavity Ring-Down Spectroscopy: Determination of 13 C/ 12 C for Carbon Dioxide in Human Breath," Analytical Chemistry, vol. 74, pp. 2003–2007, May 2002.

[353] M. F. Witinski, D. S. Sayres, and J. G. Anderson, "High precision methane isotopologue ratio measurements atambient mixing ratios using integrated cavity output spectroscopy," Applied Physics B, vol. 102, pp. 375–380, Mar. 2010.

[354] M. Cuntz, "Carbon cycle: a dent in carbon's gold standard.," Nature, vol. 477, pp. 547–8, Sept. 2011.

[355] M. Bock, J. Schmitt, L. Möller, R. Spahni, T. Blunier, and H. Fischer, "Hydrogen isotopes preclude marine hydrate CH4 emissions at the onset of Dansgaard-Oeschger events.," Science, vol. 328, pp. 1686–9, June 2010.

[356] P. B. Niles, W. V. Boynton, J. H. Hoffman, D. W. Ming, and D. Hamara, "Stable isotope measurements of martian atmospheric CO2 at the Phoenix landing site.," Science, vol. 329, pp. 1334–7, Sept. 2010.

[357] D. A. Long, M. Okumura, C. E. Miller, and J. T. Hodges, "Frequency-stabilized cavity ring-down spectroscopy measurements of carbon dioxide isotopic ratios," Applied Physics B, vol. 105, pp. 471–477, May 2011.

[358] G. Herzberg, Spectra of diatomic molecules. Van Nostrand, 1950.

[359] G. Herzberg, The spectra and structures of simple free radicals: an introduction to molecular spectroscopy. Cornell University Press, 1971.

[360] J. M. Brown and A. Carrington, Rotational Spectroscopy of Diatomic Molecules. Cambridge University Press, 2003.

[361] H. Lefebvre-Brion and R. W. Field, The Spectra and Dynamics of Diatomic Molecules. Academic Press, 2004.

[362] R. W. Field, "Diatomic Molecule Electronic Structure beyond Simple Molecular Constants," Berichte der Bunsengesellschaft für physikalische Chemie, vol. 86, pp. 771–779, Sept. 1982.

[363] P. R. Scott and W. G. Richards, "The Electronic Structure of Diatomic Transition-metal Molecules," in Molecular Spectroscopy (D. J. Millen, ed.), ch. 2, p. 320, Royal Society of Chemistry, 1976.

[364] H. Schall, M. Dulick, and R. W. Field, "The electronic structure of LaF: A multiconfiguration ligand field calculation," The Journal of Chemical Physics, vol. 87, p. 2898, Sept. 1987.

[365] J. T. Hougen, "The Calculation of Rotational Energy Levels and Rotational Line Intensities in Diatomic Molecules," in NIST/NBS Monograph 115, 1970.

[366] P. F. A. Klinkenberg, T. A. M. Van Kleef, and P. E. Noorman, "SPECTRAL STRUCTURE OF DOUBLY AND TREBLY IONIZED HAFNIUM," Physica, vol. 27, pp. 1177–1188, 1961.

[367] T. Wall, J. Kanem, J. Hudson, B. Sauer, D. Cho, M. Boshier, E. Hinds, and M. Tarbutt, "Lifetime of the A(vˆ{}=0) state and Franck-Condon factor of the A-X(0-0) transition of CaF measured by the saturation of laser-induced fluorescence," Physical Review A, vol. 78, p. 062509, Dec. 2008.

[368] L. Veseth, "Hund's coupling case (c) in diatomic molecules. I. Theory," Journal of Physics B: Atomic and Molecular Physics, vol. 6, pp. 1473–1483, Aug. 1973.

[369] R. S. Mulliken and A. Christy, "Lambda-type doubling and electron configurations in diatomic molecules," Physical Review, vol. 38, no. July 1, pp. 87–119, 1931.

[370] J. M. Brown and A. J. Merer, "Lambda-Type Doubling Parameters for Molecules in II Electronic States of Triplet and Higher Multiplicity," Journal of Molecular Spectroscopy, vol. 74, pp. 488–494, 1979.

[371] J. Brown, A. S.-C. Cheung, and A. J. Merer, "Λ-Type doubling parameters for molecules in Δ electronic states," Journal of Molecular Spectroscopy, vol. 124, pp. 464–475, Aug. 1987.

[372] B. J. Barker, I. O. Antonov, V. E. Bondybey, and M. C. Heaven, "Communication: Spectroscopic measurements for HfF(+) of relevance to the investigation of fundamental constants.," The Journal of Chemical Physics, vol. 134, p. 201102, May 2011.

[373] D. Zimmermann, P. Baumann, D. Kuszner, and A. Werner, "Isotope shift and hyperfine structure in the atomic spectrum of hafnium by laser spectroscopy," Physical Review A, vol. 50, no. 2, pp. 1112–1120, 1994.

[374] A. Anastassov, Y. Gangrsky, B. K. Kul'djanov, K. P. Marinova, B. N. Markov, and S. G. Zemlyanoi, "Isotope shifts and hyperfine splitting in HfI," Zeitschrift für Physik A, vol. 348, pp. 177–181, 1994.

[375] W. Z. Zhao, F. Buchinger, J. E. Crawford, S. Fedrigo, S. Gulick, J. K. P. Lee, O. Constantinescu, M. Hussonnois, and J. Pinard, "Hyperfine structure and isotope shifts in the 5d6s2 a2D3/2–5d6s(a3D)6p z4F5/2 transition of Hf II," Hyperfine Interactions, vol. 108, pp. 483–495, 1997.

[376] F. Wang and T. C. Steimle, "Tungsten monocarbide, WC: Pure rotational spectrum and (13)C hyperfine interaction.," The Journal of Chemical Physics, vol. 136, p. 044312, Jan. 2012.

[377] K. Namiki, S. Saito, J. S. Robinson, and T. C. Steimle, "The Pure Rotational Spectra of TiO (X 3 \Delta 1) and TiN (X 2 \Sigma +)," Journal of Molecular Spectroscopy, vol. 191, pp. 176–182, 1998.

[378] A. N. Petrov, N. S. Mosyagin, and A. V. Titov, "Theoretical study of low-lying electronic terms and transition moments for HfF+ for the electron electric-dipole-moment search," Physical Review A, vol. 79, pp. 1–7, Jan. 2009.

[379] N. S. Mosyagin, A. Zaitsevskii, and A. V. Titov, "Shape-consistent relativistic effective potentials of small atomic cores," International Review of Atomic and Molecular Physics, vol. 1, no. 1, pp. 63–72, 2010.

[380] A. B. Alekseyev, H.-P. Liebermann, and R. J. Buenker, "Spin-orbit multireference configuration interaction method and applications to systems containing heavy atoms," in Recent Advances in Relativistic Molecular Theory (K. Hirao and Y. Ishikawa, eds.), (Singapore), pp. 65–105, World Scientific, 2004.

[381] A. V. Titov, N. S. Mosyagin, A. B. Alekseyev, and R. J. Buenker, "{GRECP/MRD-CI} calculations of spin-orbit splitting in ground state of {Tl} and of spectroscopic properties of {TlH}," International Journal of Quantum Chemistry, vol. 81, no. 6, pp. 409–421, 2001.

[382] J. F. Stanton, J. Gauss, M. E. Harding, P. G. Szalay, and Others, "Cfour: http://www.cfour.de." 2011.

[383] I. Shavitt, "The Method of Configuration Interaction," in Methods of Electronic Structure Theory (H. F. Schaefer˜III, ed.), vol. 3 of Modern Theoretical Chemistry, part 6, pp. 189–275, New York: Plenum Press, 1977.

[384] B. O. Roos, R. Lindh, P. øA Malmqvist", V. Veryazov, and P. O. Widmark, "Main group atoms and dimers studied with a new relativistic ANO basis set," Journal of Physical Chemistry A, vol. 108, p. 2851, 2005.

[385] V. Goncharov and M. C. Heaven, "Spectroscopy of the ground and low-lying excited states of ThO+.," The Journal of chemical physics, vol. 124, p. 64312, Feb. 2006.

[386] R. G. Denning, "Electronic structure and bonding in actinyl ions and their analogs," The Journal of Physical Chemistry A, vol. 111, pp. 4125–43, May 2007.

[387] L. Castro, A. Yahia, and L. Maron, "Are 5f electrons really active in organoactinide reactivity? Some insights from DFT studies.," ChemPhysChem, vol. 11, pp. 990–4, Apr. 2010.

[388] M. L. Neidig, D. L. Clark, and R. L. Martin, "Covalency in f-element complexes," Coordination Chemistry Reviews, vol. 257, pp. 394–406, Jan. 2013.

[389] E. R. Meyer, J. L. Bohn, and M. Deskevich, "Candidate molecular ions for an electron electric dipole moment experiment," Physical Review A, vol. 73, pp. 1–10, June 2006.

[390] B. J. Barker, I. O. Antonov, M. C. Heaven, and K. A. Peterson, "Spectroscopic investigations of ThF and ThF(+).," The Journal of Chemical Physics, vol. 136, p. 104305, Mar. 2012.

[391] E. Purcell and N. Ramsey, "On the Possibility of Electric Dipole Moments for Elementary Particles and Nuclei," Physical Review, vol. 78, pp. 807–807, June 1950.

[392] A. D. Sakharov, "Violation of CP Invariance, C Asymmetry, and Baryon Asymmetry of the Universe," ZhETF Pis ma Redaktsiiu, vol. 5, 1967.

[393] A. D. Sakharov, "Violation of CP Invariance, C Asymmetry, and Baryon Asymmetry of the Universe," Journal of Experimental and Theoretical Physics Letters, vol. 5, 1967.

[394] M. Trodden, "Electroweak baryogenesis," Reviews of Modern Physics, vol. 71, pp. 1463–1500, Oct. 1999.

[395] I. B. Khriplovich and S. K. Lamoreaux, CP Violation Without Strangeness: Electric Dipole Moments of Particles, Atoms, and Molecules. Springer-Verlag, 1997.

[396] J. L. Feng, "Naturalness and the Status of Supersymmetry," Annual Review of Nuclear and Particle Science, vol. 63, pp. 351–382, Oct. 2013.

[397] E. D. Commins, "Electric Dipole Moments of Leptons," Advances In Atomic, Molecular, and Optical Physics, vol. 40, pp. 1–55, 1999.

[398] E. N. Fortson, "The search for a permanent electric dipole momentstill active, still important," AIP Conference Proceedings, vol. 596, pp. 39–46, Nov. 2001.

[399] M. Pospelov and A. Ritz, "Electric dipole moments as probes of new physics," Annals of Physics, vol. 318, pp. 119–169, July 2005.

[400] M. Swallows, T. Loftus, W. Griffith, B. Heckel, E. Fortson, and M. Romalis, "Techniques used to search for a permanent electric dipole moment of the ˆ{199}Hg atom and the implications for CP violation," Physical Review A, vol. 87, p. 012102, Jan. 2013.

[401] V. A. Dzuba, V. V. Flambaum, and C. Harabati, "Relations between matrix elements of different weak interactions and interpretation of the parity-nonconserving and electron electric-dipole-moment measurements in atoms and molecules," Physical Review A, vol. 84, p. 052108, Nov. 2011.

[402] M. Pospelov and A. Ritz, "CKM benchmarks for electron electric dipole moment experiments," Physical Review D, vol. 89, p. 056006, Mar. 2014.

[403] M. Le Dall and A. Ritz, "CP-violation and electric dipole moments," Hyperfine Interactions, vol. 214, pp. 87–95, Jan. 2013.

[404] J. Engel, M. J. Ramsey-Musolf, and U. van Kolck, "Electric dipole moments of nucleons, nuclei, and atoms: The Standard Model and beyond," Progress in Particle and Nuclear Physics, vol. 71, pp. 21–74, July 2013.

[405] J. Beringer et al. (Particle Data Group), "Review of Particle Physics," Physical Review D, vol. 86, p. 010001, July 2012.

[406] W. Altmannshofer, R. Harnik, and J. Zupan, "Low energy probes of PeV scale sfermions," Journal of High Energy Physics, vol. 2013, p. 202, Nov. 2013.

[407] D. McKeen, M. Pospelov, and A. Ritz, "Electric dipole moment signatures of PeV-scale superpartners," Physical Review D, vol. 87, p. 113002, June 2013.

[408] S. A. R. Ellis and G. L. Kane, "Theoretical Prediction and Impact of Fundamental Electric Dipole Moments," arXiv:1405.7719, p. 33, May 2014.

[409] W. Chao and M. J. Ramsey-Musolf, "Electroweak Baryogenesis, Electric Dipole Moments, and Higgs Diphoton Decays," arXiv:1406.0517, p. 22, June 2014.

[410] D. McKeen, M. Pospelov, and A. Ritz, "Modified Higgs branching ratios versus CP and lepton flavor violation," Physical Review D, vol. 86, p. 113004, Dec. 2012.

[411] T. Chupp and M. Ramsey-Musolf, "Electric Dipole Moments: A Global Analysis," arXiv:1407.1064, p. 15, July 2014.

[412] N. Ramsey, "A Molecular Beam Resonance Method with Separated Oscillating Fields," Physical Review, vol. 78, pp. 695–699, June 1950.

[413] W. Itano, J. Bergquist, J. Bollinger, J. Gilligan, D. Heinzen, F. Moore, M. Raizen, and D. Wineland, "Quantum projection noise: Population fluctuations in two-level systems," Physical Review A, vol. 47, pp. 3554–3570, May 1993.

[414] D. Nelson, A. Schupp, R. Pidd, and H. Crane, "Search for an Electric Dipole Moment of the Electron," Physical Review Letters, vol. 2, pp. 492–495, June 1959.

[415] P. G. H. Sandars, "The electric dipole moment of an atom," Physics Letters, vol. 14, pp. 194–196, Feb. 1965.

[416] P. G. H. Sandars, "Enhancement factor for the electric dipole moment of the valence electron in an alkali atom," Physics Letters, vol. 22, pp. 290–291, Aug. 1966.

[417] E. D. Commins, J. D. Jackson, and D. P. DeMille, "The electric dipole moment of the electron: An intuitive explanation for the evasion of Schiffs theorem," American Journal of Physics, vol. 75, no. 6, p. 532, 2007.

[418] B. C. Regan, E. D. Commins, C. J. Schmidt, and D. DeMille, "New Limit on the Electron Electric Dipole Moment," Physical Review Letters, vol. 88, pp. 18–21, Feb. 2002.

[419] P. G. H. Sandars, "Measurability of the Proton Electric Dipole Moment," Physical Review Letters, vol. 19, pp. 1396–1398, Dec. 1967.

[420] D. M. Kara, I. J. Smallman, J. J. Hudson, B. E. Sauer, M. R. Tarbutt, and E. A. Hinds, "Measurement of the electron's electric dipole moment using YbF molecules: methods and data analysis," New Journal of Physics, vol. 14, no. 10, p. 103051, 2012.

[421] E. R. Meyer and J. L. Bohn, "Prospects for an electron electric-dipole moment search in metastable ThO and ThFˆ{+}," Physical Review A, vol. 78, p. 010502(R), July 2008.

[422] D. DeMille, F. Bay, S. Bickman, D. Kawall, L. Hunter, D. Krause, Jr., S. Maxwell, and K. Ulmer, "Search for the electric dipole moment of the electron using metastable PbO," AIP Conference Proceedings, vol. 596, pp. 72–83, Nov. 2001.

[423] S. Eckel, P. Hamilton, E. Kirilov, H. W. Smith, and D. DeMille, "Search for the electron electric dipole moment using Ω-doublet levels in PbO," Physical Review A, vol. 87, p. 052130, May 2013.

[424] A. N. Petrov, N. S. Mosyagin, T. A. Isaev, and A. V. Titov, "Theoretical study of HfFˆ{+} in search of the electron electric dipole moment," Physical Review A, vol. 76, pp. 3–6, Sept. 2007.

[425] T. Fleig and M. K. Nayak, "Electron electric-dipole-moment interaction constant for HfFˆ{+} from relativistic correlated all-electron theory," Physical Review A, vol. 88, p. 032514, Sept. 2013.

[426] L. V. Skripnikov, "Private Communication," 2013.

[427] A. N. Petrov, "Hyperfine and Zeeman interactions of the a(1)[ˆ3Σˆ+_1] state of PbO," Physical Review A, vol. 83, p. 24502, 2011.

[428] H. Loh, J. Wang, M. Grau, T. S. Yahn, R. W. Field, C. H. Greene, and E. A. Cornell, "Laser-induced fluorescence studies of HfF+ produced by autoionization.," The Journal of Chemical Physics, vol. 135, p. 154308, Oct. 2011.

[429] H. Loh, J. Wang, M. Grau, T. S. Yahn, R. W. Field, C. H. Greene, and E. a. Cornell, "Laser-induced fluorescence studies of HfF+ produced by autoionization.," The Journal of chemical physics, vol. 135, p. 154308, Oct. 2011.

[430] W. Paul, "Electromagnetic traps for charged and neutral particles," Reviews of Modern Physics, vol. 62, pp. 531–540, July 1990.

[431] D. J. Berkeland, J. D. Miller, J. C. Bergquist, W. M. Itano, and D. J. Wineland, "Minimization of ion micromotion in a Paul trap," Journal of Applied Physics, vol. 83, p. 5025, May 1998.

[432] L. S. Cutler, C. A. Flory, R. P. Giffard, and M. D. McGuire, "Doppler effects due to thermal macromotion of ions in an rf quadrupole trap," Applied Physics B Photophysics and Laser Chemistry, vol. 39, pp. 251–259, Apr. 1986.

[433] C. Meis, M. Desaintfuscien, and M. Jardino, "Analytical calculation of the space charge potential and the temperature of stored ions in an rf quadrupole trap," Applied Physics B Photophysics and Laser Chemistry, vol. 45, pp. 59–64, Feb. 1988.

[434] J. H. Parks and A. Szoke, "Simulation of collisional relaxation of trapped ion clouds in the presence of space charge fields," The Journal of Chemical Physics, vol. 103, p. 1422, July 1995.

[435] C. Champenois, "About the dynamics and thermodynamics of trapped ions," Journal of Physics B: Atomic, Molecular and Optical Physics, vol. 42, p. 154002, Aug. 2009.

[436] J. Oberheide, P. Wilhelms, and M. Zimmer, "New results on the absolute ion detection efficiencies of a microchannel plate," Measurement Science and Technology, vol. 8, pp. 351–354, Apr. 1997.

[437] R. C. Taylor, "Maximizing the quantum efficiency of microchannel plate detectors: The collection of photoelectrons from the interchannel web using an electric field," Review of Scientific Instruments, vol. 54, p. 171, Feb. 1983.

[438] B. Deconihout, F. Vurpillot, M. Bouet, and L. Renaud, "Improved ion detection efficiency of microchannel plate detectors," Review of Scientific Instruments, vol. 73, p. 1734, Mar. 2002.

[439] M. Jagger and K. Richards, "You Can't Always Get What You Want," 1969.

[440] J. L. Kinsey, "Laser-Induced Fluorescence," Annual Review of Physical Chemistry, vol. 28, pp. 349–372, 1977.

[441] L. W. Grossman, G. S. Hurst, M. G. Payne, and S. L. Allman, "Saturated photodissociation of CsI," Chemical Physics Letters, vol. 50, pp. 70–73, 1977.

[442] V. S. Antonov, I. N. Knyazev, V. S. Letokhov, V. M. Matiuk, V. G. Movshev, and V. K. Potapov, "Stepwise laser photoionization of molecules in a mass spectrometer: a new method for probing and detection of polyatomic molecules," Optics Letters, vol. 3, pp. 37–39, 1978.

[443] R. Weinkauf, K. Walter, U. Boesl, and E. Schlag, "Mass-selected molecular ion spectra: (1+1)-Photodissociation spectroscopy of CH3I+ and CD3I+," Chemical Physics Letters, vol. 141, no. 4, pp. 267–276, 1987.

[444] K. Walter, R. Weinkauf, U. Boesl, and E. W. Schlag, "Molecular ion spectroscopy: Mass selected, resonant two-photon dissociation spectra of CH3I+ and CD3I+," The Journal of Chemical Physics, vol. 89, p. 1914, Aug. 1988.

[445] N. Mikami, T. Sasaki, and S. Sato, "Trapped ion photodissociation spectroscopy: the electronic spectrum of the hydrogen-bonded complex cation [C6H5OHN(CH3)3]+," Chemical Physics Letters, vol. 180, no. 5, pp. 431–435, 1991.

[446] B. Roth, J. Koelemeij, H. Daerr, and S. Schiller, "Rovibrational spectroscopy of trapped molecular hydrogen ions at millikelvin temperatures," Physical Review A, vol. 74, p. 040501, Oct. 2006.

[447] W. G. Rellergert, S. T. Sullivan, S. J. Schowalter, S. Kotochigova, K. Chen, and E. R. Hudson, "Evidence for sympathetic vibrational cooling of translationally cold molecules," Nature, vol. 495, pp. 490–494, Mar. 2013.

[448] C. M. Seck, E. G. Hohenstein, C.-Y. Lien, P. R. Stollenwerk, and B. C. Odom, "Rotational state analysis of AlH+ by two-photon dissociation," Journal of Molecular Spectroscopy, vol. 300, pp. 108–111, June 2014.

[449] H. A. H. BOOT and R. B. R.-S.-HARVIE, "Charged Particles in a Non-uniform Radio-frequency Field," Nature, vol. 180, pp. 1187–1187, Nov. 1957.

[450] T. Bergeman, G. Erez, and H. Metcalf, "Magnetostatic trapping fields for neutral atoms," Physical Review A, vol. 35, pp. 1535–1546, Feb. 1987.

[451] K. Bergmann, H. Theuer, and B. Shore, "Coherent population transfer among quantum states of atoms and molecules," Reviews of Modern Physics, vol. 70, pp. 1003–1025, July 1998.

[452] N. V. Vitanov, T. Halfmann, B. W. Shore, and K. Bergmann, "LASER-INDUCED POPULATION TRANSFER BY ADIABATIC PASSAGE TECHNIQUES," Annual Review of Physical Chemistry, vol. 52, pp. 763–809, Nov. 2003.

[453] N. Mukherjee and R. N. Zare, "Stark-induced adiabatic Raman passage for preparing polarized molecules.," The Journal of chemical physics, vol. 135, p. 024201, July 2011.

[454] W. Dong, N. Mukherjee, and R. N. Zare, "Optical preparation of H2 rovibrational levels with almost complete population transfer.," The Journal of chemical physics, vol. 139, p. 074204, Aug. 2013.

[455] E. A. Donley, T. P. Heavner, F. Levi, M. O. Tataw, and S. R. Jefferts, "Double-pass acousto-optic modulator system," Review of Scientific Instruments, vol. 76, p. 063112, June 2005.

[456] W. Zhang, M. J. Martin, C. Benko, J. L. Hall, J. Ye, C. Hagemann, T. Legero, U. Sterr, F. Riehle, G. D. Cole, and M. Aspelmeyer, "Reduction of residual amplitude modulation to 1x10ˆ{-6} for frequency modulation and laser stabilization.," Optics letters, vol. 39, pp. 1980–3, Apr. 2014.

[457] J. L. Hall and M. Zhu, "An introduction to phase-stable optical sources," Laser Manipulation of Atoms and Ions/Manipolazione Col Laser Di Atomi E Ioni (Proceedings of the International School of Physics), Enrico Fermi Course CXVIII., vol. CXVIII, 1993.

[458] C. Zener, "Non-Adiabatic Crossing of Energy Levels," Proceedings of the Royal Society A: Mathematical, Physical and Engineering Sciences, vol. 137, pp. 696–702, Sept. 1932.

[459] S. Shevchenko, S. Ashhab, and F. Nori, "Landau–Zener–Stückelberg interferometry," Physics Reports, vol. 492, pp. 1–30, July 2010.

[460] Y. Kayanuma, "Phase coherence and nonadiabatic transition at a level crossing in a periodically driven two-level system," Physical Review B, vol. 47, pp. 9940–9943, Apr. 1993.

[461] B. M. Garraway and N. V. Vitanov, "Population dynamics and phase effects in periodic level crossings," Physical Review A, vol. 55, pp. 4418–4432, June 1997.

[462] Y. Kayanuma and Y. Mizumoto, "Landau-Zener transitions in a level-crossing system with periodic modulations of the diagonal energy," Physical Review A, vol. 62, p. 061401, Oct. 2000.

[463] D. Suqing, L.-B. Fu, J. Liu, and X.-G. Zhao, "Effects of periodic modulation on the Landau–Zener transition," Physics Letters A, vol. 346, pp. 315–320, Oct. 2005.

[464] M. Wubs, K. Saito, S. Kohler, Y. Kayanuma, and P. Hänggi, "LandauZener transitions in qubits controlled by electromagnetic fields," New Journal of Physics, vol. 7, pp. 218–218, Oct. 2005.

[465] J. O. Hornkohl, C. G. Parigger, and L. Nemes, "Diatomic Hönl-London factor computer program," Applied Optics, vol. 44, no. 18, p. 3686, 2005.

[466] A. Hansson and J. K. Watson, "A comment on Hönl-London factors," Journal of Molecular Spectroscopy, vol. 233, pp. 169–173, Oct. 2005.

[467] E. R. Meyer, A. E. Leanhardt, E. A. Cornell, and J. L. Bohn, "Berry-like phases in structured atoms and molecules," Physical Review A, vol. 80, p. 062110, Dec. 2009.

[468] E. R. Meyer, Structure and spectroscopy of candidates for an electron electric dipole moment experiment. PhD thesis, University of Colorado - Boulder, 2010.

[469] I. Rabi, N. Ramsey, and J. Schwinger, "Use of Rotating Coordinates in Magnetic Resonance Problems," Reviews of Modern Physics, vol. 26, pp. 167–171, Apr. 1954.

[470] M. V. Berry, "Quantal Phase Factors Accompanying Adiabatic Changes," Proceedings of the Royal Society A: Mathematical, Physical and Engineering Sciences, vol. 392, pp. 45–57, Mar. 1984.

[471] M. V. Berry, "Quantum Phase Corrections from Adiabatic Iteration," Proceedings of the Royal Society A: Mathematical, Physical and Engineering Sciences, vol. 414, pp. 31–46, Nov. 1987.

[472] J. Anandan, "The geometric phase," Nature, vol. 360, pp. 307–313, Nov. 1992.

[473] E. D. Commins, "Berrys geometric phase and motional fields," American Journal of Physics, vol. 59, p. 1077, Dec. 1991.

[474] A. Vutha and D. DeMille, "Geometric phases without geometry," arXiv:0907.5116, July 2009.

[475] D. Budker, D. F. Kimball, and D. P. DeMille, Atomic physics: an exploration through problems and solutions. Oxford University Press, 2008.

[476] S. R. Williams, A. Jayakumar, M. R. Hoffman, B. B. Blinov, and E. N. Fortson, "Method for measuring the 6S_{1/2}5D_{3/2} magnetic-dipole-transition moment in Baˆ{+}," Physical Review A, vol. 88, p. 012515, July 2013.

[477] P. Rosenbusch, "Magnetically trapped atoms for compact atomic clocks," Applied Physics B, vol. 95, pp. 227–235, Feb. 2009.

[478] F. Schmidt-Kaler, S. Gulde, M. Riebe, T. Deuschle, A. Kreuter, G. Lancaster, C. Becher, J. Eschner, H. H ffner, and R. Blatt, "The coherence of qubits based on single Ca+ ions," Journal of Physics B: Atomic, Molecular and Optical Physics, vol. 36, pp. 623–636, Feb. 2003.

[479] D. Harber, H. Lewandowski, J. McGuirk, and E. Cornell, "Effect of cold collisions on spin coherence and resonance shifts in a magnetically trapped ultracold gas," Physical Review A, vol. 66, p. 053616, Nov. 2002.

[480] V. Ivannikov, Analysis of a trapped atom clock with losses. PhD thesis, Swinburn University of Technology, 2013.

[481] C. W. Chou, D. B. Hume, T. Rosenband, and D. J. Wineland, "Optical Clocks and Relativity," Science, vol. 329, pp. 1630–1633, Sept. 2010.

[482] C. Tamm, B. Lipphardt, H. Schnatz, R. Wynands, S. Weyers, T. Schneider, and E. Peik, "ˆ{171}\hbox{Yb}ˆ{+} Single-Ion Optical Frequency Standard at 688 THz," IEEE Transactions on Instrumentation and Measurement, vol. 56, pp. 601–604, Apr. 2007.

[483] N. Huntemann, M. Okhapkin, B. Lipphardt, S. Weyers, C. Tamm, and E. Peik, "High-Accuracy Optical Clock Based on the Octupole Transition in ˆ{171}Ybˆ{+}," Physical Review Letters, vol. 108, p. 090801, Feb. 2012.

[484] P. O. Schmidt, T. Rosenband, C. Langer, W. M. Itano, J. C. Bergquist, and D. J. Wineland, "Spectroscopy using quantum logic.," Science, vol. 309, pp. 749–52, July 2005.

[485] S. Ding and D. N. Matsukevich, "Quantum logic for the control and manipulation of molecular ions using a frequency comb," New Journal of Physics, vol. 14, p. 023028, Feb. 2012.

[486] J. Mur-Petit, J. J. García-Ripoll, J. Pérez-Ríos, J. Campos-Martínez, M. I. Hernández, and S. Willitsch, "Temperature-independent quantum logic for molecular spectroscopy," Physical Review A, vol. 85, p. 022308, Feb. 2012.

[487] C. Hempel, B. P. Lanyon, P. Jurcevic, R. Gerritsma, R. Blatt, and C. F. Roos, "Entanglement-enhanced detection of single-photon scattering events," Nature Photonics, vol. 7, pp. 630–633, July 2013.

[488] D. Kawall, "Searching for the electron EDM in a storage ring," Journal of Physics: Conference Series, vol. 295, p. 012031, May 2011.

[489] L. Kaledin, J. Mccord, and M. Heaven, "Laser Spectroscopy of TiO: Accurate Term Energies for the Singlet States and Ligand Field Assignment of States in the Range 0 to 4 eV," Journal of Molecular Spectroscopy, vol. 173, pp. 499–509, Oct. 1995.

[490] J. Lee, E. R. Meyer, R. Paudel, J. Bohn, and A. E. Leanhardt, "An electron electric dipole moment search in the X ˆ3Delta_1 ground state of tungsten carbide molecules," Journal of Modern Optics, vol. 56, pp. 2005–2012, Oct. 2009.

[491] J. Benhelm, G. Kirchmair, C. Roos, and R. Blatt, "Experimental quantum-information processing with ˆ{43}Caˆ{+} ions," Physical Review A, vol. 77, p. 062306, June 2008.